EXPERIMENTAL AND NUMERICAL INVESTIGATIONS INTO THERMAL AND HYDRAULIC CHARACTERISTICS OF ARTIFICIAL GROUND FREEZING

Mahmoud Abdel Rahman Alzoubi

Department of Mining and Materials Engineering

McGill University, Montreal

December 2018

A THESIS SUBMITTED TO MCGILL UNIVERSITY
IN PARTIAL FULFILLMENT OF THE REQUIREMENTS
OF THE DEGREE OF DOCTOR OF PHILOSOPHY

Acknowledgements

During the journey towards the completion of my Ph.D., I have been overwhelmed by the tremendous support, help, and encouragement from many people whom I would like to express my sincere gratitude. One particular person, however, stayed with me throughout the days and nights of this project. So, to my wife, Ruba, thank you for everything; without your passion and endless support, this work could not be done.

To my advisor Prof. Agus P. Sasmito, words sometimes are not enough to express the person's gratitude. Thank you for making yourself available for discussion, every time I knocked on your door, despite your busy schedule. Your feedback and advice, motivated me to challenge myself and increase my expectation. Our business trips to Saskatoon and Cardiff City will be remembered fondly. You have been my advisor on the academic level and a sincere friend on a personal level, so thank you so much.

To Prof. Hassani, thank you for your endless support to ease the flow of this project at the highest levels; without your behind-the-scene contributions, this work could face a lot of difficulties. Your wisdom and your kindness will never be forgotten.

To my colleagues at Mine Multiphysics lab, Saad, Bhargav, Aurelien, and Matthew, our daily discussions have, in some way, furthered my understanding in many directions. To Aurelien, your tremendous contribution to the development of the experimental setup, and your continuous feedback is highly appreciated. I will miss the weekly meeting with you and prof. Sasmito. To Saad and Bhargav, our football arguments over lunch or throughout the day have converted the lab into a lovely place to work.

To my colleagues in the mining department, thank you for your support and help. To the administrative staff, your efforts to ease our university life are highly appreciated.

To the collaborators outside of McGill University, Mr. Greg Newmann (Newmans Geotechnique Inc.) and Mr. Martin Wacker (Cameco Corporation), thank you for your valuable feedback and suggestions. Your remarkable contribution to the project is highly appreciated.

Finally, to my parents, Abdel Rahman and Maryam, although far distances set us apart, your prayers and warm wishes kept me always on the correct route; I love you and miss you. To my brother and sisters, thank you for your regular phone and video calls, and for your huge support; I love you.

This project was generously funded by the Ultra Deep Mining Network (UDMN) (241695 Tri-Council (NCE – UDMN) 2-003). The simulations were conducted at McGill HPC facility under Calcul-Quebec and Compute-Canada with contribution from CFI-JELF. The financial supports from McGill Engineering Doctoral Award (MEDA) and Fonds de recherche du Québec - Nature et technologies (FRQNT) are also acknowledged.

To my wife, Ruba,
for your sacrifices, patience, support, friendship, and "humongous" love.

To my children, Hashem and Salma,
for the laughs and happiness that have enlightened my days and nights throughout this journey.

Abstract

The artificial ground freezing (AGF) system has been extensively employed as an excavation-support method in mining and civil engineering projects. Over the last few decades, AGF system has become one of the most favorable ground-support procedures in critical, long-term environmental projects such as underground uranium mines and hazardous-waste management sites. Despite its advantages, most of the conventional AGF systems require continuous energy input for extended periods of time to maintain sufficient frozen body. Essentially, the AGF process involves transient, multi-phase, conjugate heat transfer and fluid flow in a porous ground and bayonet freeze pipes. These complex phenomena and interactions are not well understood, making it difficult to predict the performance, the thermal ground response and, thus, optimize the system. It is also important to explore and devise new ideas that could lead to a more cost-effective and sustainable AGF system.

This dissertation focuses on the thermal and hydraulic characteristics of AGF systems. It starts with reviewing current research and technology of AGF system to identify the research gaps and formulate research directions. Further, a controlled novel laboratory-scale experiment that mimics the AGF process is conceived and developed. The apparatus is thermally controlled and equipped with advanced measurement instrumentation and control systems. It provides a deep understanding of the AGF process and generates a comprehensive database for thorough model validation. The rig is further used to introduce and demonstrate a novel concept of freezing-on-demand (FoD) for the first time to save energy while maintaining safe operation in AGF system.

A mathematical model that effectively incorporates the multi-physics, multi-scale transport phenomena in the porous ground structure and the freeze pipes is derived, analyzed, and validated against the experimental data. The validated model is extended to mine field conditions to study the impact of various design and operating parameters, such as pipe spacing, groundwater seepage, ground temperature and freeze brine temperature. The growth of the frozen body and closure time is analyzed by quantifying the net energy flux and groundwater streamlines. The heatlines visualization is further implemented for the first time in AGF process to better understand the heat transfer mechanism that governs the ice growth. The model's framework is then employed to evaluate the energy consumption of the AGF system operates under continuous and FoD modes. The results suggest that the concept of the FoD could reduce energy consumption by up to 46%, as compared to the conventional counterpart which highlights its potential for practical applications.

Résumé

Le système de Congélation Artificielle des Sols (CAS) est une méthode de soutènement d'excavations couramment utilisée dans les projets miniers et civils. Depuis quelques une vingtaine d'années, la CAS est devenue la technique de soutènement de prédilection pour les projets qui on des impacts environnementaux probables critiques et à long terme, tel que les mine d'uranium et les sites de gestion de déchets dangereux. Malgré ses avantages, la majorité des systèmes de CAS conventionnels nécessitent une source énergétique constante et continue sur de longues périodes afin de maintenir une congélation du sol sécuritaire. Le processus de CAS est un produit de l'écoulement des fluides ainsi que du transfert de chaleur transitoire, multi-phase et conjugué qui ont lieu dans les tubes de réfrigération en baïonnette et dans le sol poreux. La compréhension limitée de ces phénomènes et interactions complexes complique la prédiction de la performance du système et de la réponse thermique du sol, et en conséquent nuit à l'optimisation de ces systèmes. L'exploration de nouvelles idées et nouveaux paradigmes pourrait aussi amener des améliorations au niveau des coûts et des impacts environnementaux des systèmes de CAS.

Cette dissertation se concentre sur les caractéristiques thermales et hydrauliques des systèmes CAS. Au début, une revue des recherches et technologies des systèmes de CAS cerne les lacunes de recherches et formule une direction de recherche. À cette fin, une nouvelle plateforme expérimentale à échelle de laboratoire reproduisant les conditions et processus de CAS est conçue et créée. Cet équipement permet un contrôle thermique étendu et contient une instrumentation avancée de lecture thermique qui permet une compréhension en profondeur des processus de CAS ainsi qu'une base de données compréhensive pour une validation approfondie de modèles numérique. La plateforme expérimentale est de plus utilisée pour introduire et démontrer le nouveau concept de Congélation sur Demande (CsD) afin de diminuer la demande énergétique tout en maintenant la sécurité du système.

Le modèle mathématique choisi incorpore efficacement les phénomènes de transport multi-échelle et multi-physiques dans les structures poreuses du sol et dans les tubes de congélation. Ce modèle est dérivé, analysé et validé grâce aux données expérimentales. La portée du modèle validé est étendue aux dimensions et conditions présentes dans les opérations minières souterraines afin d'étudier l'impact des paramètres de conception et d'opération variés, tel que l'espacement entres les tubes de congélation, l'infiltration souterraine, la température du sol et la température du liquide de congélation. L'analyse de la croissance de la masse congelée et de son temps de fermeture découle de la quantification du flux énergétique net et des lignes de courant de l'eau souterraine. De plus, les lignes de chaleur sont utilisées pour la première fois dans le contexte de CAS afin d'aider à la com-

préhension des mécanismes de transferts de chaleur qui gouvernent la croissance du corps congelé. Le cadre du modèle est ensuite utilisé pour évaluer et comparer la consommation énergétique du système de CAS en mode continu contre une opération en CsD. Les résultats suggèrent que le concept de CsD pourrait réduire la consommation d'énergie jusqu'à 46% par rapport à une utilisation conventionnelle. Cette amélioration souligne le potentiel de CsD pour des applications pratiques.

Contribution of Authors

I, Mahmoud Alzoubi (the Ph.D. candidate), carried out all experimentation; conceived all the related codes (i.e., Matlab code, scheme algorithms, User Defined Functions (UDFs), and simulations journalling); performed all the computations and simulations; completed all the data analysis; and wrote and completed all the manuscripts. However, this dissertation was made possible due to the contributions of my co-authors. Aurélien Nie-Rouquette (Master graduate, McGill University) contributed to the experimental part of this thesis; he was a constant source of help and provided a great insight during the design and commissioning stages of the experiment. Prof. Ferri Hassani (McGill University) and Dr. Ali Madiseh (Assistant Professor, University of British Columbia) were involved in defining the concept of the freezing-on-demand (Chapter 6). Finally, my supervisor Prof. Agus Sasmito supported me and encouraged me to investigate the aspects of the artificial ground freezing, and guided me throughout the entirety of the project.

Contents

Preface

This thesis presents the study on the experimental and numerical investigation of artificial ground freezing systems. The following publications are based on research carried out for this doctoral thesis.

Journal papers

1. **Alzoubi, M. A.** and Sasmito, A. P. (2018). *A review of thermal and hydraulic aspects of the artificial ground freezing system*, to be submitted to Science of the Total Environment, 2018, in preparation. (SCI - Q1; IF: 4.61 (JCR: 2017))

2. **Alzoubi, M. A.**, Nie-Rouquette, A., Zueter, A., and Sasmito, A. P. (2018). *Freezing on Demand: A New Concept for Mine Safety and Energy Savings in Wet Underground Mines*, recommended for submission to the special issue of International Journal of Mining Science and Technology, 2018, in preparation. (Scopus Indexed; SJR: 1.323 (JCR: 2017))

3. **Alzoubi, M. A.**, Nie-Rouquette, A., Sasmito, A. P., Madiseh, A., and Hassani, F. P. (2018). *On the concept of the Freezing-on-Demand (FoD) in artificial ground freezing for energy savings*, submitted to Applied Energy, 2018, under review. (SCI - Q1; IF: 7.9 (JCR: 2017))

4. **Alzoubi, M. A.** and Sasmito, A. P. (2018). *Heat transfer analysis in artificial ground freezing under high seepage: Validation and heatlines visualization*, submitted to International Journal of Thermal Sciences, 2018, under review. (SCIE - Q1; IF: 3.361 (JCR: 2017))

5. **Alzoubi, M. A.**, Nie-Rouquette, A., and Sasmito, A. P. (2018). *Conjugate heat transfer in artificial ground freezing using enthalpy-porosity method: Experiments and model validation*, International Journal of Heat and Mass Transfer, 126:740-752. (SCI - Q1; IF: 3.891 (JCR: 2017))

6. **Alzoubi, M. A.** and Sasmito, A. P. (2017). *Thermal performance optimization of a bayonet tube heat exchanger*, Applied Thermal Engineering, 111:232-247. (SCIE - Q1; IF: 3.771 (JCR: 2017))

SCI: Science Citation Index
SCIE: Science Citation Index Expanded
SJR: SCImago Journal Rank
IF: Impact Factor
JCR: Journal Citation Reports

Conference papers

1. **Alzoubi, M. A.**, Nie-Rouquette, A., Zueter, A., and Sasmito, A. P. (2018). *Freezing on Demand: A New Concept for Mine Safety and Energy Savings in Wet Underground Mines*, Proceedings of the 4$^{\text{th}}$ International Symposium on Mine Safety Science and Engineering (ISMSSE2018), Beijing, China, Accepted. (Scopus Indexed)

2. **Alzoubi, M. A.**, Sasmito, A. P., Madiseh, A., and Hassani, F. P. (2018). *Freezing on Demand (FoD): An Energy Saving Technique for Artificial Ground Freezing*, Proceedings of the 10$^{\text{th}}$ International Conference on Applied Energy (ICAE2018), Hong Kong, China, Energy Procedia, in press. (Scopus Indexed)

3. Fong, M., **Alzoubi, M. A.**, Sasmito, A. P., and Kurnia, J. C. (2018). *Performance Evaluation of Ground-Coupled Seasonal Thermal Energy Storage with High Resolution Weather Data: Case Study of Calgary, Canada*, Proceedings of the 10$^{\text{th}}$ International Conference on Applied Energy (ICAE2018), Hong Kong, China, Energy Procedia, in press. (Scopus Indexed)

4. **Alzoubi, M. A.** and Sasmito, A. P. (2018). *Development and Validation of Enthalpy-Porosity Method for Artificial Ground Freezing under Seepage Conditions*, Proceedings of the ASME 5$^{\text{th}}$ Joint US-European Fluids Engineering Summer Conference (FEDSM2018), Montreal, QC, Canada, in press. (Scopus Indexed)

5. **Alzoubi, M. A.**, Sasmito, A. P., Madiseh, A., and Hassani, F. P. (2017). *Intermittent freezing concept for energy saving in artificial ground freezing systems*, Proceedings of the 9$^{\text{th}}$ International Conference on Applied Energy, (ICAE2017), Cardiff, UK, Energy Procedia, 142:3920-3925. (Scopus Indexed)

6. **Alzoubi, M. A.**, Akhtar, S., Fong, M., and Sasmito, A. P. (2017). *Characterization of an Open-loop Seasonal Thermal Energy Storage System*, Proceedings of the 9$^{\text{th}}$ International Conference on Applied Energy, (ICAE2017), Cardiff, UK, Energy Procedia, 142:3401-3406. (Scopus Indexed)

Conference posters

1. Nie-Rouquetter, A., **Alzoubi, M. A.**, Shao, K., and Sasmito, A.P. (2017). *Selective Ground Freezing using Air Insulation - Experimental and Numerical Investigation*, CIM Congress, Montreal, QC, Canada.

Oral presentations

1. **Alzoubi, M. A.**, Sasmito, A.P., Madiseh, A., Hassani, F.P., and Newman, G. (2017). *Freezing-on-Demand Concept for Energy Saving in Artificial Ground Freezing System*, CIM Congress, Montreal, QC, Canada.

2. Nie-Rouquette, A., **Alzoubi, M. A.**, Sasmito, A.P. (2017). *Experimental and numerical investigation of selective artificial ground freezing with air insulation*, CIM Maintenance, Engineering and Reliability / Mine Operators Conference (MEMO 2017), Saskatoon, SK, Canada.

3. Akhtar, S., **Alzoubi, M. A.**, Fong, M., and Sasmito, A.P.(2017). *Numerical Investigation and Optimization Study of a Novel Seasonal Energy Storage System for Air-Conditioning Application*, ASME Power and Energy Conference, Charlotte, NC, USA

List of Figures

List of Tables

List of Symbols

A	area
A_{pv}	interfacial area
a	molar Helmholtz energy
AGF	artificial ground freezing
C	constant
C_0	empirical coefficient
C_E	Ergun's coefficient
C_m	mushy constant
c_p	specific heat capacity
D, d	diameter
E	energy
Eu	Euler number
F	area
FoD	freezing on demand
FoM	figure of merit
f_d	friction factor
G_κ	the generation of turbulence kinetic energy
$\mathbf{g}$	gravitational acceleration

H	heat function
ΔH	latent heat of fusion
h	specific enthalpy
$\hbar$	heat transfer coefficient
$\mathbf{I}$	identity matrix
K	permeability
K_r	relative permeability
k	thermal conductivity
L, ℓ	length
L	latent heat of fusion (Eqns. (2.3)-(2.6))
m	material constant
$\dot{m}$	mass flow rate
Nu	Nusselt number
P, p	pressure
Pe	Péclet number
Pr	Prandtl number
Q	heat rate
$q, \dot{q}$	heat flux
P_{pump}	pumping power
R	universal gas constant
R^2	coefficient of determination
r	radius
Re	Reynold's number
S	source term

$\dot{S}'''_{gen}$	entropy generation
S_H	source term
S/N	signal-to-noise ratio
S_p	Sparrow number
T	temperature
t	time
$\mathbf{U}, \mathbf{u}, u$	velocity
V	volume
$\mathbf{v}$	velocity
$\dot{V}$	volumetric flow rate
VFD	variable frequency drive
Y	the individually measured response value
Z	the compressibility factor
z	constant

Greek Letter

α	reduced Helmholtz energy (Eqn. (3.8)), thermal diffusivity (Eqn. (5.16))
β	thermal expansion coefficient
γ	liquid fraction within pore fluid
δ	reduced density (Eqn. (3.8)), liquid fraction in a volume element (Eqn. (4.13)).
ϵ	rate of dissipation
ε	porosity
η	efficiency
Θ	volume-averaged quantity

θ reduced temperature (Eqn. (3.8)), local quantity (Eqn. (2.1)), diffusive coefficient ((4.1))

κ turbulent kinetic energy

μ viscosity

ρ density

σ turbulent Prandtl number

$\boldsymbol{\tau}$ stress tensor

φ dependent variable (Eqn. (4.1)), porosity (Eqns. (5.3)-(5.7))

ξ liquid fraction

χ saturation degree

ψ volume-averaged quantity (Eqn. (4.9)), stream function (Eqn. (5.8)), porosity (Eqns. (6.2)-(6.10))

Ψ local quantity

ω material constant

Superscripts

L Latent

S Sensible

T transpose

Subscripts

0 ideal gas

app apparent

c coolant, critical

e effective

f fluid

g	ground
i	inlet, inner
in	inlet
$init$	initial
LTB	larger-the-better
lat	latent
ℓ	liquid, length (Eqn. (4.26))
m	mushy
o	outer, outlet
out	outlet
p	particle
r	radial direction
ref	reference
res	residual
s, s	solid, static
STB	smaller-the-better
sen	sensible
T	total
t	tube, turbulent
w	wall
v	void

Chapter 1

Introduction

Contents

1.1 Background and motivation

The deposit at McArthur River uranium mine is the largest, high-grade uranium deposit in the world with almost 500 million pounds reserves of U_3O_8 at an average grade of 17% [1]. The uranium ore is located in the Athabasca Basin in northern Saskatchewan, Canada, between a sandstone layer and a basement-rock layer at 530 - 600 [m] below the surface, as depicted in Fig. 1.1. The raise bore mining method has been utilized to safely mine this high-grade ore body [2]. The uranium ore is located beneath a large aquifier, which makes it subject to a large volume of groundwater flow under high pressure of 6000 [kPa] [3]. Moreover, the groundwater near the uranium ore zone is contaminated with a high concentration of radon gas [4]. Thus, it should be contained and isolated from other fresh groundwater resources. These particular characteristics of McArthur mine represent significant risks for the natural resources and the overall mining operations. Therefore, the artificial ground freezing (AGF) method was proposed as a robust solution to the complication associated with the uranium mining process.

The idea of controlled freezing for temporary ground support was introduced by Friedrich Poetsch in the 19th century to secure the construction of deep shafts [5, 6]. Since then, the AGF method has been employed as an excavation-support method in mining [7] and civil

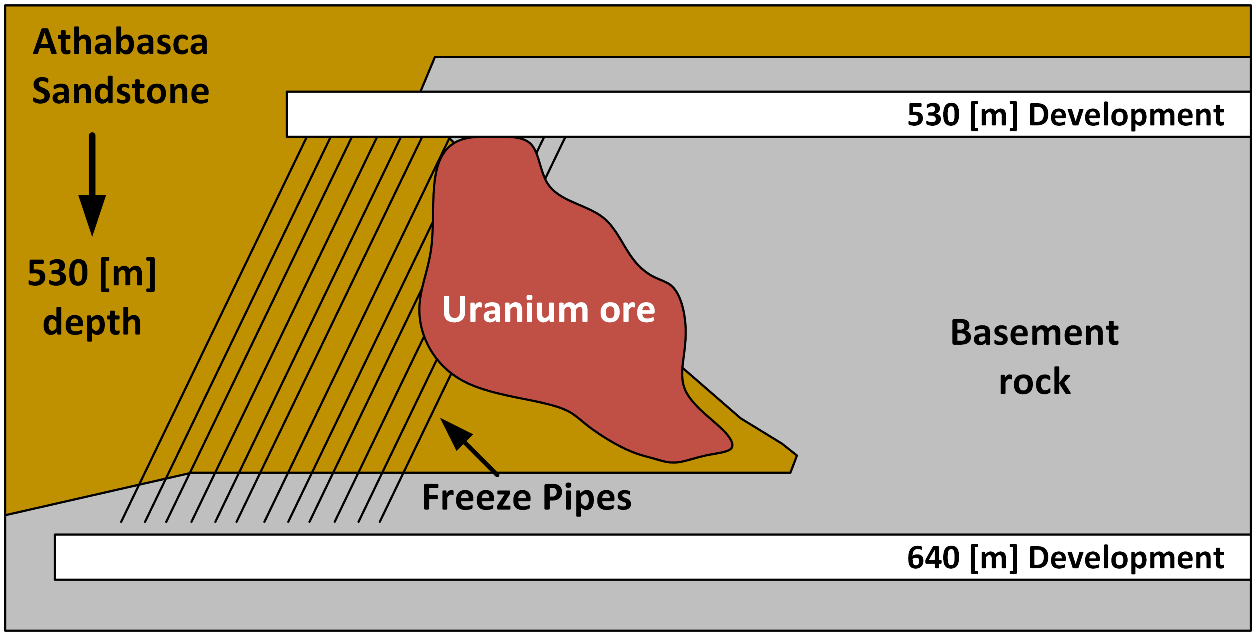

Figure 1.1 – Schematic diagram of the uranium ore at McArthur River mine, Saskatchewan, Canada (after [4]).

engineering projects [8] found in wet environment. However, the fundamental comprehension of the complicated coupling between the transient, multi-phase heat transfer and fluid mechanics of the AGF process under various hydrological conditions is not well understood. The AGF process is basically a phase-change problem in a porous medium, that is governed by combination of conduction, convection, and phase-change heat transfer. The process begins when a sub-zero brine extracts the heat from the surrounding ground, forcing the groundwater to transfer into ice.

The heat extraction rate depends on the thermophysical properties of the ground such as porosity, permeability, and particle size. It also depends on the design and operating parameters such as coolant's flow rate, coolant's temperature, quantity and geometry of the freeze pipes, and the spacing between two freeze pipes. Thus, the AGF system is a site-specific process and a function of the design and operating parameters.

The transport phenomena associated with the AGF process is inherently a multi-level process, as depicted in Fig. 1.2. One could deal with the performance of the AGF system at a mechanistic-level by examining the design and operating parameters of a freeze pipe with a view to optimizing its performance. Moreover, at the same level of analysis, a conjugate heat transfer problem between the brine's flow rate and the surrounding ground structure could be conducted in order to describe and quantify the ground's response toward the freezing process. At pore-level, it is typical to discuss the macro-scale analysis of heat interaction between the soil matrix, water, and ice, considering the local volume-averaged formulations and the local thermal equilibrium hypothesis. The last level deals with the transformation of the groundwater into ice, where the phase-change interface is considered as a mushy zone. These levels should be handled as a whole unit aiming toward an optimized AGF system.

From an energy consumption point of view, conventional AGF systems are usually designed with a continuous-freezing procedure in order to overcome the safety concerns, by maintaining a certain thickness of the frozen body. In order to support this practice, the AGF system consumes a tremendous amount of energy which, in turn, leads to a large carbon footprint. Therefore, it is crucial to propose more cost-effective and sustainable practices for the AGF system.

1.2 Objectives

The artificial ground freezing process, as just discussed, is a challenging fundamental problem, that is intrinsically a multi-scale and multi-physics process, including multi-phase heat transfer and fluid flow in a porous ground structure. There are various challenges face any AGF process. The seepage of the groundwater and the intensive energy consumption are among the most challenging obstacles - the consequences of these impediments could be daunting. For instance, the seepage of the groundwater could delay, or in some cases, hamper the creation of a merged frozen body. Therefore, it is of great interest to comprehensively understand the associated physical phenomena of the AGF process, which could lead to a safe and efficient AGF system.

Generally, there are two main questions that could be raised concerning the design of the AGF systems: (i) How to ensure the creation of a safe, reliable frozen body under severe groundwater seepage, and (ii) How to reduce the energy consumption, while sustaining the safety requirements. To answer these compulsory questions adequately, the AGF problem should be addressed using various approaches. Therefore, the work presented in this thesis attempts to tackle the thermal and hydraulic aspects of the AGF process experimentally and numerically.

Concerning the experimental approach, the development of a state-of-the-art laboratory scale experimental setup is crucial to quantify the ground's behavior towards the AGF process. In order to provide a controlled setup, the rig should be adequately insulated to minimize the heat gain from the surrounding environment. Moreover, the design of the setup should be able to provide operational flexibility, such that the rig is capable of conducting several parametric studies. Furthermore, in order to track the transient response of the

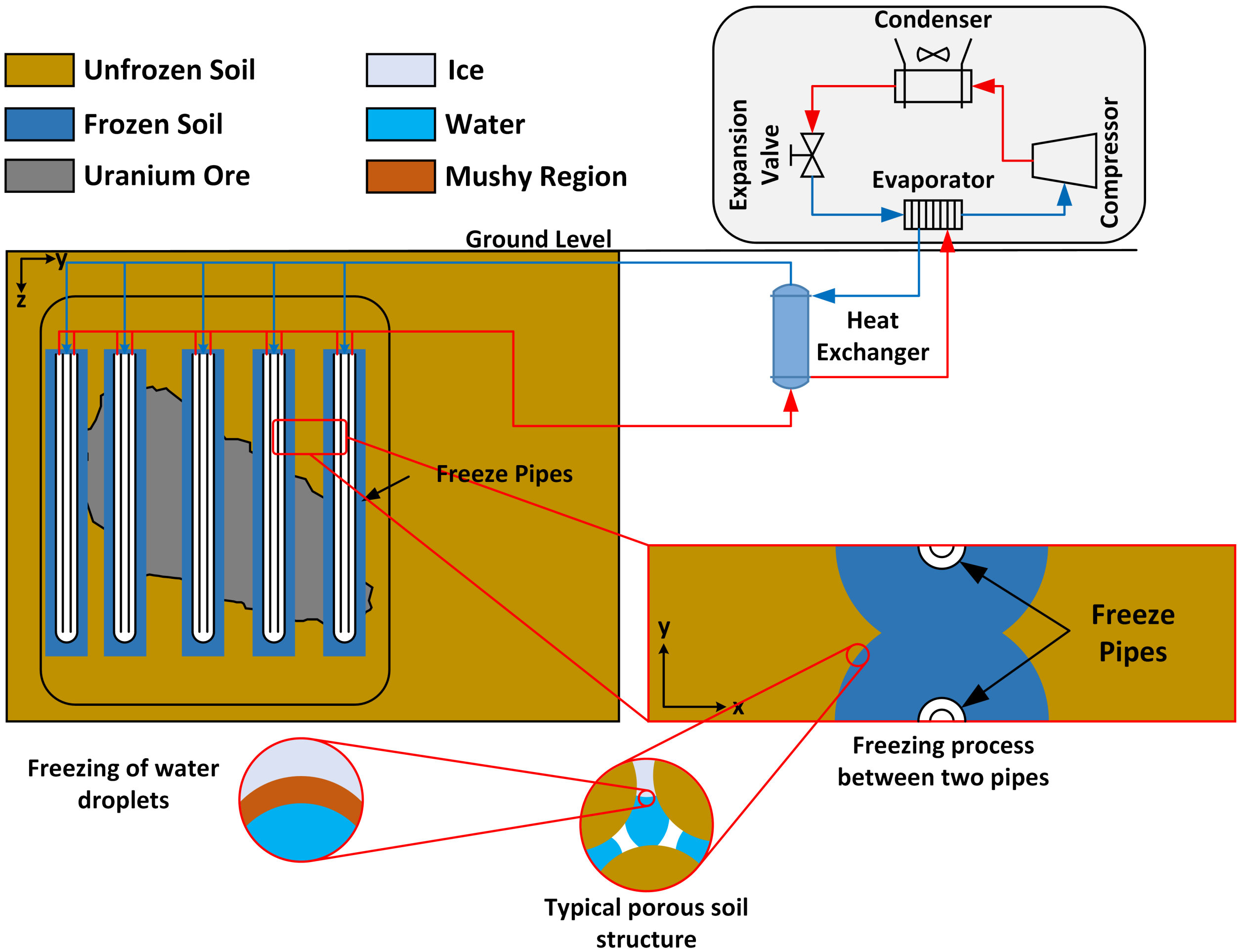

Figure 1.2 – The AGF process occurs at various scales, ranging from system-level operation into a pore-scale process of the transformation of pore-water into pore-ice.

ground toward the AGF process, the platform should be equipped with sufficient amount of thermocouples and flow-meters to record the coolant's flow rate and temperature, and the ground's temperature.

Regarding the numerical approach, the mathematical model that will be proposed should satisfy specific criteria. First, the developed model should be reliable. That is, to assess a mathematical model, the computational results of that model should be validated against the measurements of an experiment that is carried out under a controlled environment. Secondly, the model should be adaptable, which means that one can extend the framework of the model into field geometry without compromising the accuracy of the model's outcomes. Finally, the model should predict the ground's response toward any new conceptual idea. It should be used as an engineering tool for current and future development of the AGF system.

1.3 Thesis outline

This dissertation is structured as a manuscript-based doctoral thesis. Five articles are either published or under review based on the discussions in chapters 2, 3, 4, 5, and 6. These chapters form a harmonious structure and associated by a brief preface at the beginning of each chapter. The chapters are placed in chronological order (except Chapter 2)and without any modification from published/submitted version of the paper other than the layout.

The first chapter is the primary guideline of this thesis. It first discusses the background of the artificial ground freezing systems and their critical roles in various applications. Then, it addresses the fundamental and applied objectives of this work. Finally, it gives a brief dialogue of each chapter.

The second chapter aims to give a comprehensive review of the work done in the context of AGF. In particular, it examines the thermal and hydraulic aspects associated with the artificial ground freezing process. In the beginning, it reviews two popular types of the AGF systems; it analyzes the main components, the pros and cons, and the main applications of each type. After that, it provides a detailed overview of the experimental research, the design of the lab-scale experiments that have been developed, and their main objectives. Finally, the chapter examines the fundamental aspects of the AGF process and compares the methods used in literature to model the freezing process in a porous medium.

The third chapter deals with the thermal analysis of the bayonet tube heat exchanger (i.e., the freeze pipe). The primary objective of this chapter is to examine the design and operating conditions of a typical bayonet tube that could lead to optimum performance. It first specifies the physical system and details the conservation equations that characterize the fluid flow and the heat transfer. The overall model is then validated against experimental data from the literature. Later, the framework of the validated model is extended to a field geometry with a view to studying the impact of various design and operating parameters on the overall performance of the freeze pipe. Finally, an optimization analysis is conducted with an objective to reach an optimum combination of design and operating parameters that provide the optimum performance in terms of pressure drop, heat transfer, entropy generation, and the figure of merit; Taguchi method is used as an experimental design methodology and optimization.

The fourth chapter is the cornerstone of this dissertation. It highlights, in details, the contribution of building a state-of-the-art controlled laboratory-scale AGF experimental setup that. It first provides comprehensive information regarding the physical model and its dimensions, the material properties, the experiment procedure, and the reproducibility of the experimental data. After that, an extensive analysis of the conjugate, multi-phase mathematical model that governs the freezing process in a porous medium is provided. The model development section highlights the conservation equations that govern the convective flow in the freeze pipe and the heat transfer in the porous ground structure in light of implementing the local volume-averaged formulations and the local thermal equilibrium hypothesis. Later, the results of the mathematical model are validated against our experiments at various operating conditions; good agreement between model predictions and experimental data was achieved with an average $R^2 = 0.972$. Finally, parametric studies were conducted to evaluate the impact of operating parameters - coolant's flow rate, coolant's inlet temperature, and ground's initial temperature - on the closure time.

The fifth chapter discusses the overall effect of the seepage of the groundwater on the AGF process in terms of the closure time and the shape of the frozen body. In the beginning, a two-dimensional model is developed and validated against experimental data. The framework of the validated model is then extended to a typical design and operating conditions of an AGF system that is used in underground uranium mines. Various parametric studies are conducted to study the influence of the seepage's velocity and temperature, the coolant's temperature, and the spacing between two freeze pipes on the growth rate, the closure time, and the shape of the frozen wall. Finally, in this chapter, we use the concept of the heat-functions to visualize the net energy flow in forced-convective heat transfer problems that include phase-change processes. The utilization of this concept provides a deeper understanding of the impact of the groundwater seepage along with other design and operating parameters on the development of the frozen body between two freeze pipes.

The sixth chapter introduces a novel concept of the freezing on demand (FoD) as an operational technique to reduce the intensive energy consumption of the AGF systems. It first discusses the utilization of our experimental setup to demonstrate the proof-of-concept of the FoD approach. After that, it illustrates the three-dimensional, conjugate model, as well as the initial and boundary conditions that govern the intermittent freezing cycles. Later, it examines the impact of the distance between two freeze pipes, the brine's temperature, and the ground's initial temperature on the process of the FoD. Finally, it analyzes the energy consumption of three different freezing procedures: continuous freezing, FoD that starts after a specific period, and FoD that begins at a particular temperature.

The last chapter presents the main conclusions of this work. It highlights the primary findings of individual sections and draws an outlook concerning the main objectives of this study. In the end, it provides certain perspectives of the limitation of the current work and the recommendation for future studies.

References

[1] GP Newman and Derek Maishman. Artificial ground freezing of the mcarthur river uranium ore deposit. In *International symposium on ground freezing and frost action in soils. Belgium: Universite catholique de Louvain (UCL)*, pages 317–321, 2000.

[2] BW Jamieson. Mining the high grade mcarthur river uranium deposit. Technical report, International Nuclear Information System (INIS), 2002.

[3] Greg P Newman. Case study: thermal analysis of artificial ground freezing at the mcarthur river uranium mine. *Geotechnical News Vancouver*, 21(2):60–62, 2003.

[4] Greg Newman, Lori Newman, Denise Chapman, and Travis Harbicht. Artificial ground freezing: An environmental best practice at cameco's uranium mining operations in northern saskatchewan, canada. In *11th International Mine Water Association Congress–Mine Water–Managing the Challenges*, 2011.

[5] Friedrich Hermann Poetsch. *Das Gefrierverfahren: Methode für schnelles, sicheres und lothrechtes abteufen von schächten im schwimmsande und überhaupt im wasserreichen gebirge für herstellung tiefgehender brückenpfeiler und für tunnelbauten im rolligen gebirge*. Craz & Gerlach, 1887.

[6] Helmut HaB and Peter Schafers. Application of ground freezing for underground construction in soft ground. In *Geotechnical Aspects of Underground Construction in Soft Ground: Proceedings of the 5th International Symposium TC28. Amsterdam, the Netherlands, 15-17 June 2005*, page 405. CRC Press, 2013.

[7] Manon Vitel, Ahmed Rouabhi, Michel Tijani, and Frédéric Guérin. Thermo-hydraulic modeling of artificial ground freezing: Application to an underground mine in fractured sandstone. *Computers and Geotechnics*, 75:80–92, 2016.

[8] E Pimentel, S Papakonstantinou, and G Anagnostou. Numerical interpretation of temperature distributions from three ground freezing applications in urban tunnelling. *Tunnelling and Underground Space Technology*, 28:57–69, 2012.

Chapter 2

A state-of-the-art review of thermal and hydraulic aspects of the artificial ground freezing system

Contents

Preface (Linking Paragraph)

This chapter is the start-point of this work. It reviews the state-of-the-art achievements in the literature regarding the thermal and hydraulic aspects of the artificial ground freezing systems. It aims to provide a detailed overview of the published works and highlights, in some way, the research gap, which shapes the structure of the current work that will be discussed in the following chapters. A review article is to be submitted based on the discussion of this chapter:

Alzoubi, M. A. and Sasmito, A. P. (2018). *A review of thermal and hydraulic aspects of the artificial ground freezing system*, to be submitted to Science of the Total Environment, 2018, in preparation.

Abstract

The artificial ground freezing (AGF) system has been widely spread as an excavation-support method in civil and mining projects. Over the last decades, the AGF system became the most favorable ground-support method in the containment of hazardous-waste in various environmental projects, e.g., Giant mine remediation and Fukushima nuclear reactor. Driven by its reliability, compatibility with a wide range of ground types, and low impact on the environment, the AGF systems are expected to play a critical role in these projects. Despite promising expectations, the intensive energy consumption required to maintain the frozen ground is the main drawback of the system, especially for long-term projects. To optimize the energy consumption, and further develop these systems, it is crucial to understand the nature of the system's applications and the technical aspects of the AGF method. The objective of this paper is to provide an overview of the artificial ground freezing systems, review the most common types of AGF systems, their basic configurations, and their main applications. It also examines the thermal and hydraulic aspects associated with AGF process and a series of experimental and computational studies undertaken to analyze the effect of certain parameters on the overall performance of the AGF system.

2.1 Introduction

Inspired by the natural ground-freezing phenomena in Arctic regions, Siebe Gorman & Co developed in 1862 the first artificial ground freezing in Swansea, South Wales, UK; it was mainly applied for a shaft sinking in a coal mine [1]. A few years later, the German mining engineer Friedrich Poetsch improved the system and patented it in 1883 [2]. The AGF method was selected because it was the only *safe* method to construct a 50 [m] depth shaft in a fully saturated sand structure [3]. The system, since then, has been extensively used as a temporary excavation-support method in various applications.

Exploiting the impenetrable nature of ice, and the strength of frozen ground, AGF systems are employed to create a hydraulic boundary, that enhances and stabilizes the ground structure, and restrict the flow of the groundwater. These roles are heavily implemented in civil engineering, shaft sinking, underground uranium mines, and containment of hazardous waste. The basic principle of the AGF process is to lower the ground's temperature to a degree below the freezing point of the groundwater. This is achieved by providing a coolant with a sub-zero temperature through the targeted area to extracts the heat from the ground's strata, transforming the groundwater, gradually, into ice.

As compared to other geotechnical support methods, the AGF system is not limited to a project's scale or a specific type of the ground. It can really cope with small projects such as undisturbed sampling of Pleistocene sand [4, 5], or with mega projects such as underground uranium mines [6, 7]. It can work with fine-grained sand such as slit and clay sand [8], or within fractured sedimentary rocks such as sandstones rocks [9]. Moreover, as a temporary process, the impact of AGF method on the environment is minimal; there are no additive foreign-materials to the ground like cement or chemical grouting, and once the AGF process finished, ground thawing starts, allowing the strata to return to original conditions.

Over the last few decades, there has been a growing interest in AGF systems especially in perpetuity projects, such as hazardous waste management [10–13]. This is mainly driven by the desire to have an environmentally-friendly, reliable systems. The main concern associated with the AGF systems is the tremendous operational cost and energy consumption [14, 15]. In line with that, several studies have been conducted to assess the thermal and hydraulic aspects of the AGF process. Studies of the AGF method have investigated design fundamental, system and process optimization, transient behavior, and field performance. The approaches, however, vary depending on the discussions point-of-view and the authors' backgrounds. Hence, it is essential to summarize and discuss the main findings of these studies.

This paper comprehensively reviews the thermal and hydraulic aspects of the artificial ground freezing system. In the following, a brief description of the review methodology is presented in the first part. The discussion of the main types of the AGF systems is followed in the second part. After that, the classical and current applications of AGF systems are explained in the third section. Later, a detailed analysis of the technical aspects of the AGF process is presented. Finally, conclusions are drawn with emphasis on the future directions of the development of the AGF systems.

2.2 Methodology

The literature is rife with broad-based studies on the AGF freezing systems. Thus, it is hard to encompass the outcomes of these studies in a single article. Therefore, in this paper we consider the articles that fit within the following criteria:

- The article should discuss either thermal or hydraulic aspects of the AGF system.
- The mechanical aspect of the AGF process, such as the structural behavior of the grounds toward freezing, is excluded from this study.
- The article should be peer-reviewed.
- Qualitative and quantitative studies could be included in this article.

The main searching strategy is based on a concept/keyword technique. Table 2.1 shows an example of the structure to search for the usage of liquid nitrogen in AGF systems; the logical operator between the concepts is "AND", while "OR" operator is used between the keywords. The notion behind this procedure is to accommodate the largest number of articles that are highly relevant to this work. We searched Scopus and Web of Science databases, targeting the articles that could answer any of the following research questions:

- What are the main applications of the AGF process?
- What are the primary types of the AGF systems?
- How to characterize the heat transfer and the groundwater flow during the AGF process?
- How to optimize the AGF process and the AGF system?

Table 2.1: The structure of the key/word technique that targets articles discuss the usage of liquid nitrogen in AGF systems.

	Concept 1	Concept 2
Keyword 1	(artificial ground freezing)	(liquid nitrogen)
Keyword 2	(ground freezing)	LN_2
Keyword 3	(frozen ground)	(cryogenic liquid nitrogen)
Keyword 4	AGF	(liquified nitrogen)

2.3 Types of AGF systems

The AGF systems comprise three, strongly-coupled aspects (namely: thermal, hydraulic, and mechanical aspects), as shown in Fig. 2.1. As discussed in the methodology section, this article only considers the impact of the thermal and hydraulic aspects on the design and performance of the AGF systems. Mainly, there are two types of AGF systems. The conventional system often referred to as the closed-loop system, indirect freezing method, or brine method. In this method, a mechanical refrigeration plant is utilized to cool down the brine, which is then pumped into a network of freeze pipes to extract heat from the ground before returning into the freezing plant, as illustrated in Fig. 2.2(a). The other type is frequently called as direct freezing, open-loop system, or cryogenic cooling system. In this system, a liquefied gas, typically nitrogen, is pumped directly into the freeze pipes' circuit; the vaporized fluid is then allowed to exhaust into the atmosphere, as shown in Fig. 2.2(b). Regardless of the type, the primary objectives of any AGF system are basically identical,

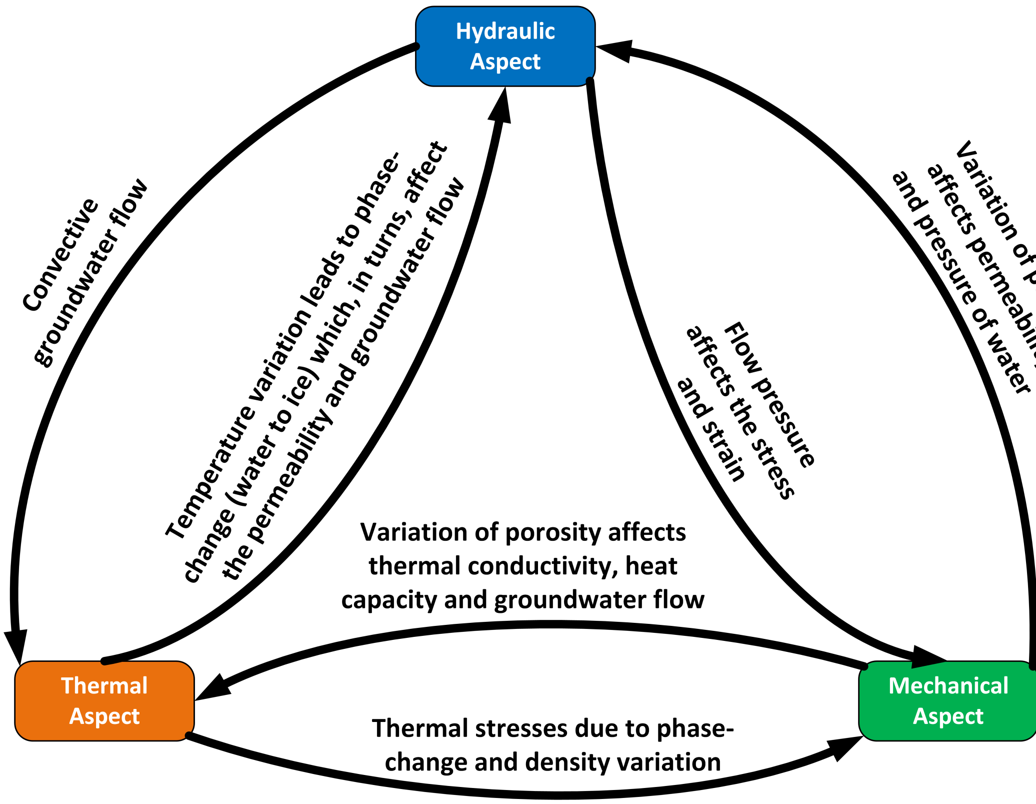

Figure 2.1 – Coupling of thermal, hydraulic, and mechanical aspects during the AGF process.

such as: (i) create a certain volume of a frozen ground within (ii) specific time, taking into considerations (iii) the flow of the groundwater, as illustrated in Fig. 2.3.

2.3.1 Open-loop AGF system

Liquid nitrogen has a temperature of -195.8 [°C] at atmospheric pressure (101.325 [kPa]), as depicted in Fig. 2.4. As it evaporates, it draws 199.18 [kJ/kg] of energy from its surroundings, and around 133.13 [kJ/kg] of heat gain to heat up the cold gas to the exhaust temperature of -70 [°C], this temperature is economically favorable for the resultant nitrogen gas [16, 17]. Further, nitrogen is abundant; it is the main component of air (78% by volume). Thus, it has been utilized as a cooling medium in AGF systems. To produce liquid nitrogen, an off-site facility is required, where nitrogen is cooled down, liquefied, and separated from other air constituents. The liquefied nitrogen is then delivered to the site and stored in an insulated storage vessel to be used in the AGF process.

On-site, the liquid nitrogen is circulated through a network of freeze pipes. A pumping system is not a requirement; the pressure of the liquefied nitrogen is sufficient to force the

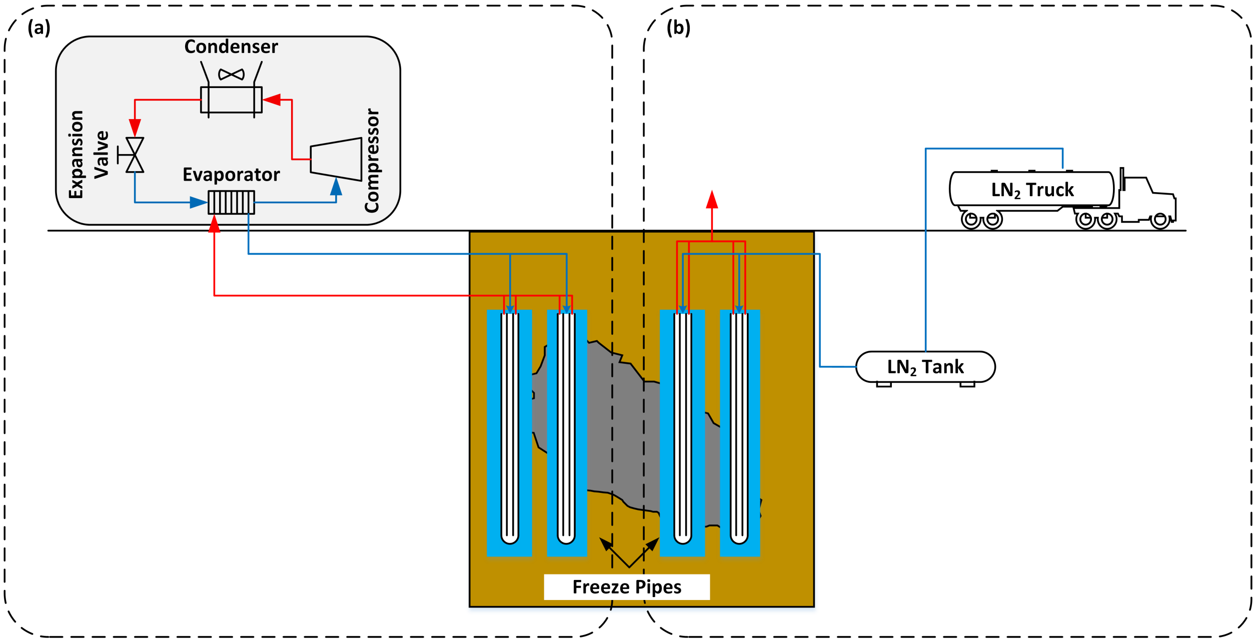

Figure 2.2 – Schematic diagram of the AGF systems: (a) an indirect, closed-loop method using a cold, sub-zero brine; and (b) a direct, open-loop system using liquid nitrogen as a cryogenic liquid refrigerant.

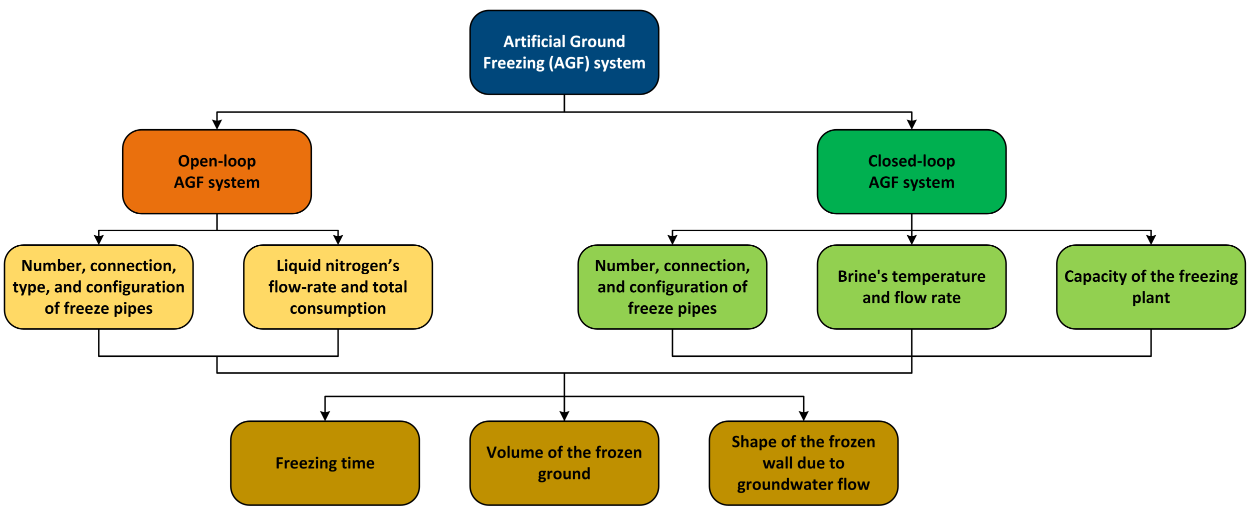

Figure 2.3 – Basic design considerations and the primary objectives of different types of AGF system

liquid through the freeze pipes. On the other hand, however, it is impractical to collect the nitrogen and liquefy it again. Therefore, the resultant gas is exhausted to the atmosphere. Due to its low temperature (-195.8 [°C]), nitrogen is typically circulated between multi freeze

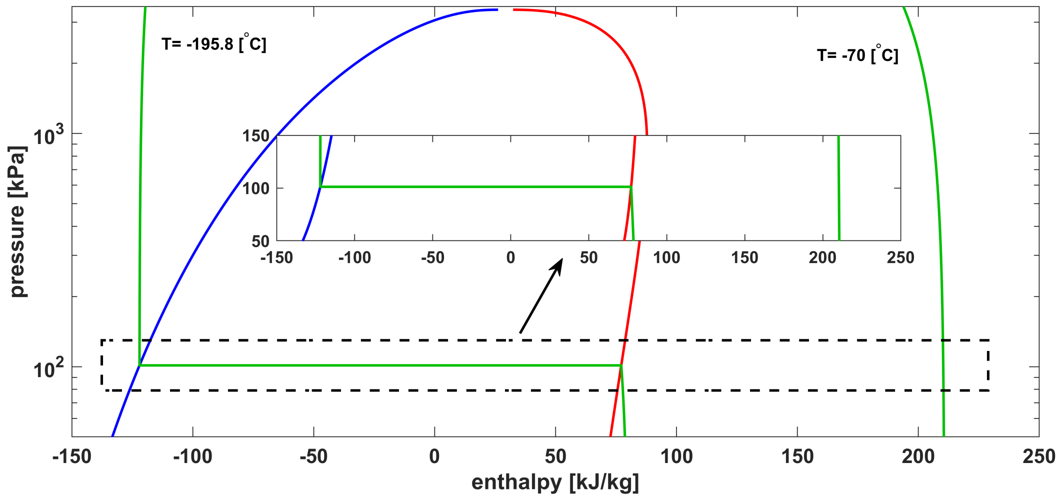

Figure 2.4 – Pressure-enthalpy diagram of nitrogen showing the evaporation temperature at ambient pressure

pipes before it is released to the ambient. Two types of freeze pipes are used with the open-loop AGF system: (i) regular bayonet tube freeze pipes where nitrogen extracts the heat from the ground through the wall of the freeze pipes, as observed in Fig. 2.5(a), and (ii) perforated freeze pipe, where nitrogen is directly injected into the ground, as illustrated in Fig. 2.5(b). The usage of each type depends on the ground structure; porous soil is the major prerequisite for the perforated freeze pipes.

The open-loop AGF system was used for the first time to stop a sewage leakage in France in 1964 [18]. Since then, the system has been used in several applications. Due to the large temperature gradient between the liquid nitrogen and the surrounding ground structure, the open-loop system is mainly considered to reduce the freezing time. Thus it is used in emergency situations, such as hazardous-waste management [11, 18–22]. Also, it is used to create strong structures for undisturbed local sampling [4, 5, 23–27]. Furthermore, the open-loop AGF system is used once the conventional, closed-loop system fails, such as destroyed parts of underground tunnels [28–37], or when the strata face high groundwater seepage [37–40]. Table 2.2 lists several examples of main applications of the open-loop AGF system.

The open-loop AGF system has many advantages. The system is simple to establish, independent of expensive freezing plants, and has low moving parts (pumping system is not required). On the contrary, the disadvantages of the open-loop AGF system are: (i) the irregular shape of the freeze wall; and (ii) the tremendous amount of liquefied nitrogen that is required on-site. Correlating the consumption of the liquid nitrogen with the volume of

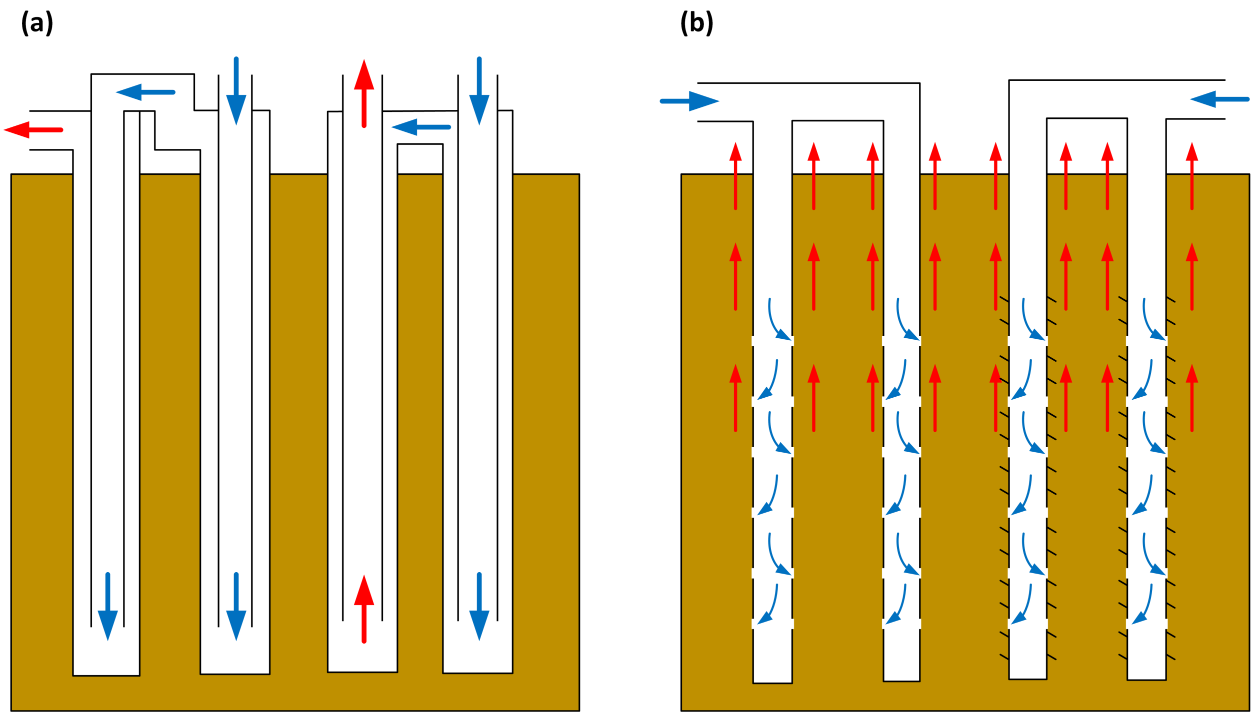

Figure 2.5 – Two types of freeze pipes connections. (a) regular freeze pipes, where nitrogen is circulated between the pipes in different ways; (b) perforated freeze pipes (left), the first type is drilled into the ground using the bore-whole method; the second type (right) is a perforated auger, where it is screwed into the ground.(after [16])

the frozen ground has a significant degree of uncertainty. It depends on many factors, such as ground's thermophysical properties (thermal conductivity, porosity, saturation level, and thermal diffusivity), the design of the freeze pipes (i.e., diameter, length, wall thickness, and network connection), ground's initial temperature, and project's lifetime. Therefore, it is impossible to make exact calculations for practical application. Veranneman and Rebhan [16] bundled the consumption of the nitrogen of several projects within upper and lower limits as a function of the frozen ground's volume, the consumption is converted from [m^3] to [ton] (1 [ton]=1000 [kg]) by assuming liquid nitrogen density at -195.8 [°C] and atmospheric pressure is 806 [kg/m^3]), as presented in Fig. 2.6. The data is updated with other projects [29–31, 39, 41]. Although the data fit within limits, the uncertainty, in some cases, is one order of magnitude. This arouses a huge concern regarding the feasibility of using the liquid nitrogen in the AGF process [1, 42].

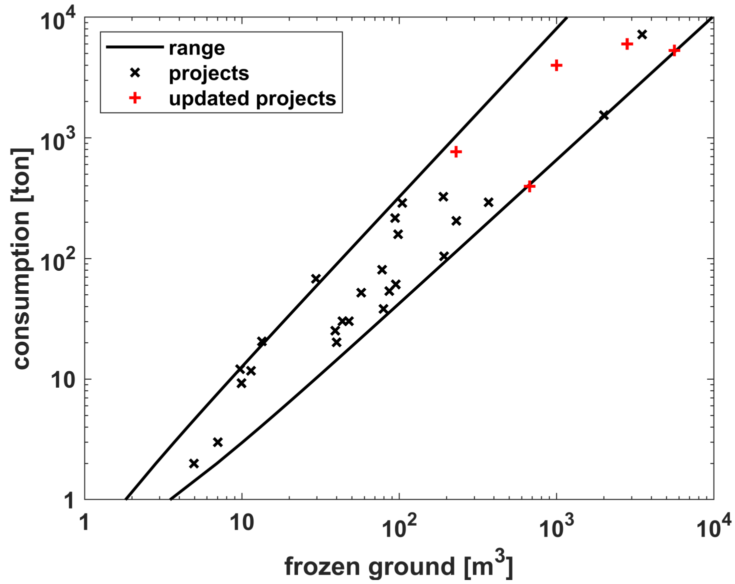

Figure 2.6 – The consumption of the liquid nitrogen in tons as a function of the volume of the frozen ground. (after [16])

2.3.2 Closed-loop AGF system

The close-loop AGF systems have been extensively used in several applications. Table 2.2 lists various examples of the most common projects that employed the closed-loop AGF system as a geotechnical support method. In this type of AGF system, various chemical solutions could be used as sub-zero brine and circulated in a closed-loop to extract the heat from the ground. At the surface, the brine is cooled down to a desired sub-zero temperature within an industrial refrigeration plant (known as the freezing plant). The plant is typically a mechanical, vapor-compression cycle that usually uses ammonia as a working fluid, as shown in Fig. 2.2(a). There are several options of chemical solutions that could be used as a sub-zero brine, such as magnesium chloride, $MgCl_2$, sodium chloride, $NaCl$, calcium chloride, $CaCl_2$, calcium magnesium acetate, CMA, potassium acetate, KAc, glycerine, and ethylene glycol [43–46], as depicted in Fig. 2.7. Among other chemical solutions, calcium chloride, $CaCl_2$, is usually used in closed-loop AGF systems. Although, potassium acetate, KAc, and ethylene glycol have lower freezing points, but there are other factors, than low temperature, should be considered in selecting the brine. The first of these factors is the capability of the freezing plant. In most of the cases, as mentioned earlier, ammonia is commonly used as working fluid. The optimum evaporating temperature of the ammonia is at -40 [°C] [47, 48]. Therefore, at this operating condition, one should expect a brine flow with a temperature equal to or higher than -40 [°C]. Additionally, calcium chloride, $CaCl_2$, reaches -40 [°C] at solution concentration at a lower concentration around 27% , as compared to 63%, 54%, and 40% for the glycerine, ethylene glycol, and potassium acetate, respectively. These differences in concentrations translate into considerably higher costs.

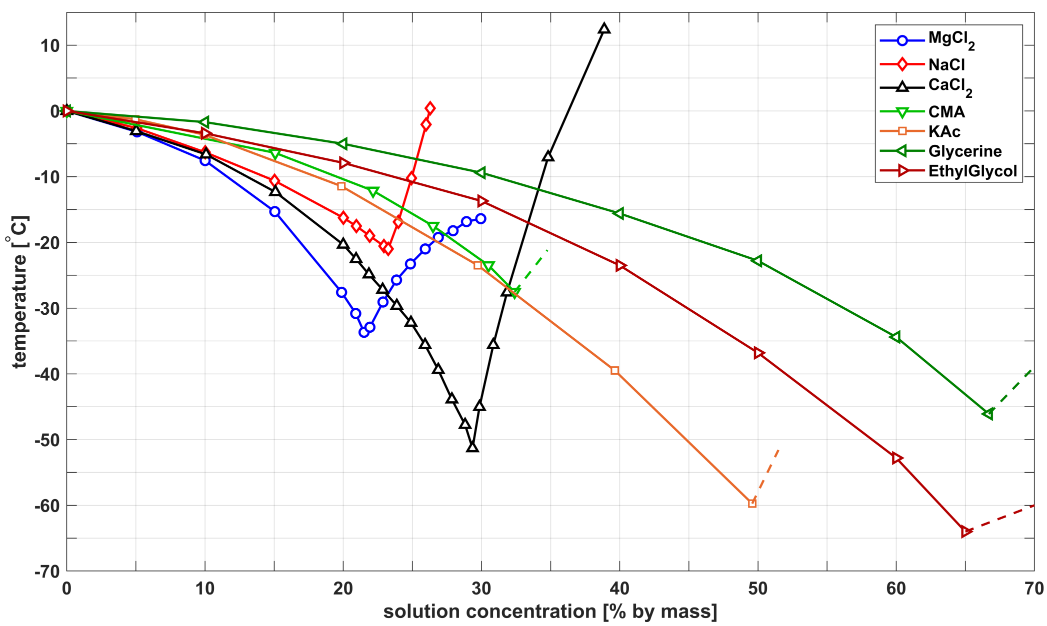

Figure 2.7 – Characteristics of several chemical solutions. (edited from [44, 45])

The configuration of the freeze pipes depends mainly on the nature of the applications. For example, in shaft sinking [49–52], the freeze pipes are installed either vertically or inclined, in a circular shape. In tunneling projects, the orientation is mostly horizontal with either circular [53–55] or semi-circular shapes [56–59] - depends on the ground's physical properties. In other applications, however, such as mining [6, 60] or waste management [10, 11, 15, 18, 22, 61], a larger area is needed to be frozen. Therefore, a wall configuration is mainly used.

The distribution system of the freeze pipe could be connected either in parallel or hybrid (in series and in parallel), as illustrated in Fig. 2.8. In the first type, each pipe works independently, that is, each pipe receives and returns the brine from and into a main hub. In the second type, the pipes are grouped in pairs or more, where the second pipe's inlet is the first pipe's outlet. In this way, the brine's energy is utilized in a better way as compared to the first type [1].

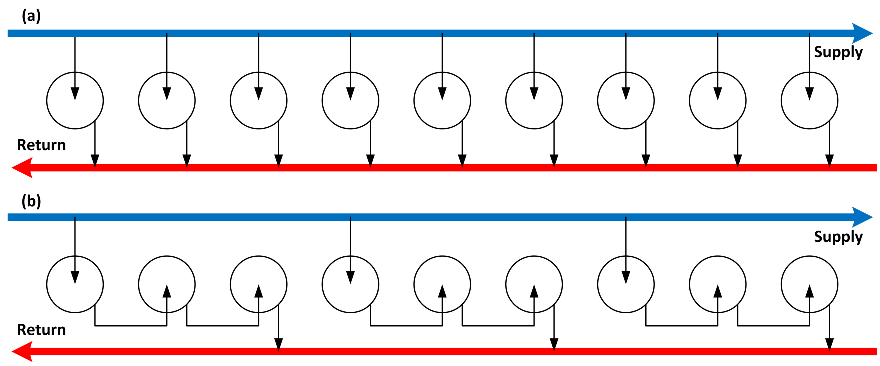

Figure 2.8 – The distribution system of wall-type freeze pipes. (a) parallel connection; (b) hybrid connection with 3-series × 3-parallel connection

2.4 Laboratory-scale experiments

The experimental research of either open-loop or closed-loop AGF systems is scarce; only a few studies have been published in the literature. The model used by Gioda et al. [64] simulates an open-loop AGF system. The experimental setup consists of a vertical cylinder with a diameter and height of 1.0 [m]; a single steel freeze pipe was installed at the center, as depicted in Fig. 2.9 and Table 2.3. The rig was fully insulated with polyurethane foam. The tank was filled with coarse sand with a D_{50} of 0.52 [mm]. Before that, the tank was filled up to 10 [cm] by water to ensure fully saturated sand. Nine thermocouples were installed at mid-height of the tank. Each three were positioned apart with an angle of 120°. The sand was set at an initial temperature between 18 and 19 [°C]. The flow of the liquid nitrogen was regulated to provide a constant temperature of -183 [°C].

Ständer [65] developed a lab-scale closed-loop AGF system with horizontal freeze pipes. The rig consists of a polymethyl methacrylate (PMMA) tank, that was filled with medium sand with a D_{50} of 0.4 - 0.7 [mm]. Five freeze pipes were installed horizontally at the middle of the tank, as shown in Fig. 2.10. At the bottom of the tank, a small reservoir of water was installed, allowing the water to infiltrate vertically into the sand through a filter plate. The tank's initial temperature was set at 10 [°C], and the coolant was circulated in the freeze pipes at a temperature of -30 [°C], as listed in Table 2.3.

Frivik and Comini [67] built an insulated, rectangular tank with three freeze pipes installed vertically in the tank, as illustrated in Fig. 2.11. The experiment mimics groundwater seepage by supplying water at a constant pressure across the tank. Thermocouples were placed at three levels between two freeze pipes. They reported a coolant temperature of -40 [°C]; more detailed are discussed in Table 2.3.

Table 2.2: Examples of several projects that implemented the AGF systems

Ref.	Application	Example	Comments
Open-loop System			
[11]	Hazardous-waste management (short-term)	Wastewater treatment	A tunnel below a wastewater treatment plant collapsed. AGF with liquid nitrogen was implemented to seal the leakage.
[26]	Sampling	Pleistocene sand samples	Open AGF system was used to freeze the sand between depths of 1.8 and 3.8 [m] for 270 [hr] to preserve and study the samples.
[37]	High seepage velocity	tunnel in Nanjing, China	The construction site faced high groundwater seepage velocity. An open AGF system was used temporarily for 7 days to accelerate the freezing process.
Closed-loop System			
[60, 62]	Underground wet mines	McArthur River and Cigar Lake uranium mines	The nature and geographical location of these mines require a special mining method. AGF systems have been used for decades in these site to isolate the working area from a high pressure flow.
[14]	Hazardous-waste management (long-term)	Giant mine remediation	A closed-loop AGF has been constructed to contain the residual arsenic trioxide stored at the former Giant Mine site in the Canadian Northwest Territories.
[15]	Hazardous-waste management (long-term)	Fukushima nuclear plant	After the accident at the Fukushima Daiichi Nuclear Power Plant (FDNPP) in March 2011, A closed-loop AGF has been constructed around the reactors to intercept groundwater fluxes to and from the buildings.
[63]	Shaft sinking	Potash and salt mines	A closed-loop AGF system with freezing plant capacity up to 10 [MW] was employed to construct an ultra-deep mine shaft with a final depth of more than 2000 [m]
[3]	Tunneling	multi-projects of tunneling in Germany	Four projects used closed-loop AGF systems for construction of underground tunnels with different freeze pipes configurations.

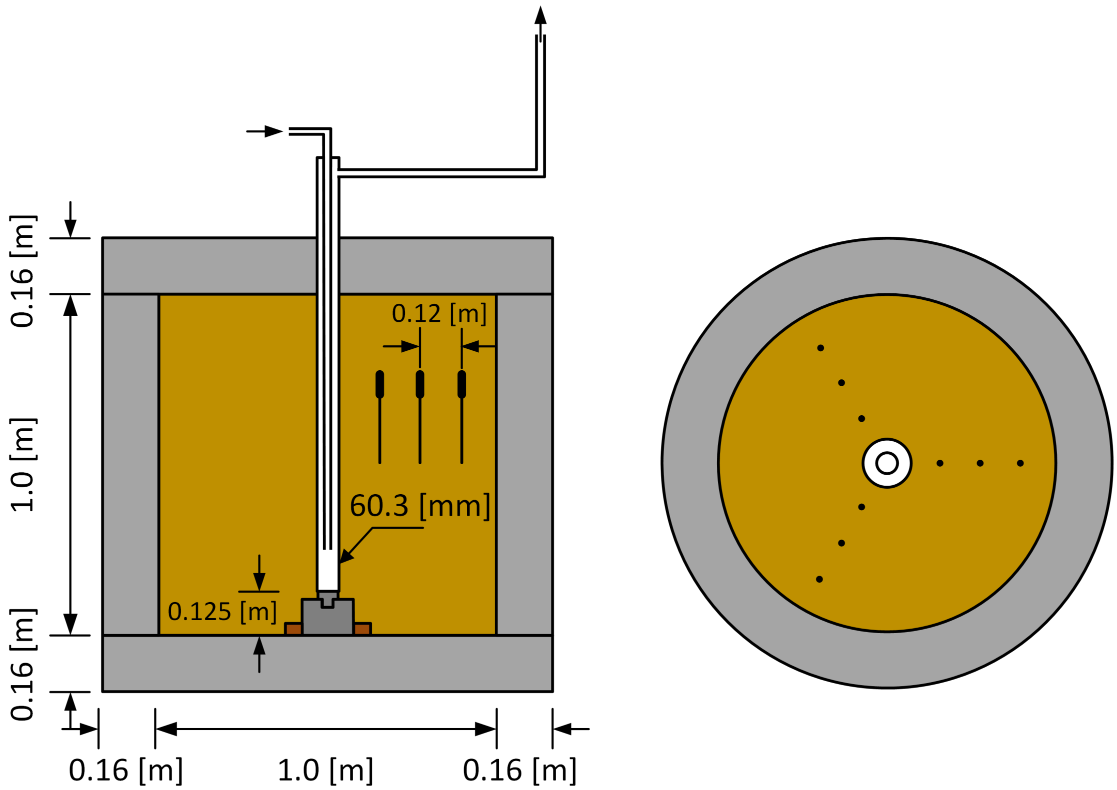

Figure 2.9 – Simplified schematic diagram of Gioda et al. experimental setup. (after [64])

Pimentel et al. [66] developed a tank with three vertical freeze pipes, as observed in Fig. 2.12. The tank was insulated by polyvinyl chloride (PVC) with a thickness of 2 [cm]. The tank was filled with saturated sand with a D_{50} of 1.0 [mm]. The groundwater seepage was simulated by providing a horizontal water flow through the tank. A homogeneous flow was obtained by providing a constant pressure head across the tank. The coolants temperature varied between -18 and -25 [°C], while the sand's initial temperature was set at 18 or 21 [°C] (see Table 2.3.

Alzoubi et al. [68] developed a lab-scale physical model to simulate the AGF process in underground mines. The setup consists of a vertical aluminum cylinder that contains two vertical freeze pipes. The tank is fully insulated and filled with saturated sand with a D_{50} of 0.212 [mm], as depicted in Fig. 2.13. Several parametric studies have been conducted at several operating conditions. The range of initial ground's temperature and coolant's temperature are listed in Table 2.3.

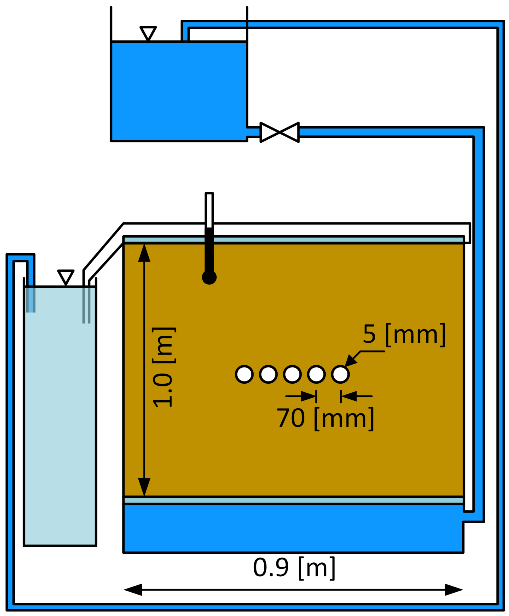

Figure 2.10 – Simplified schematic diagram of Ständer experimental setup. (after [65], from [66])

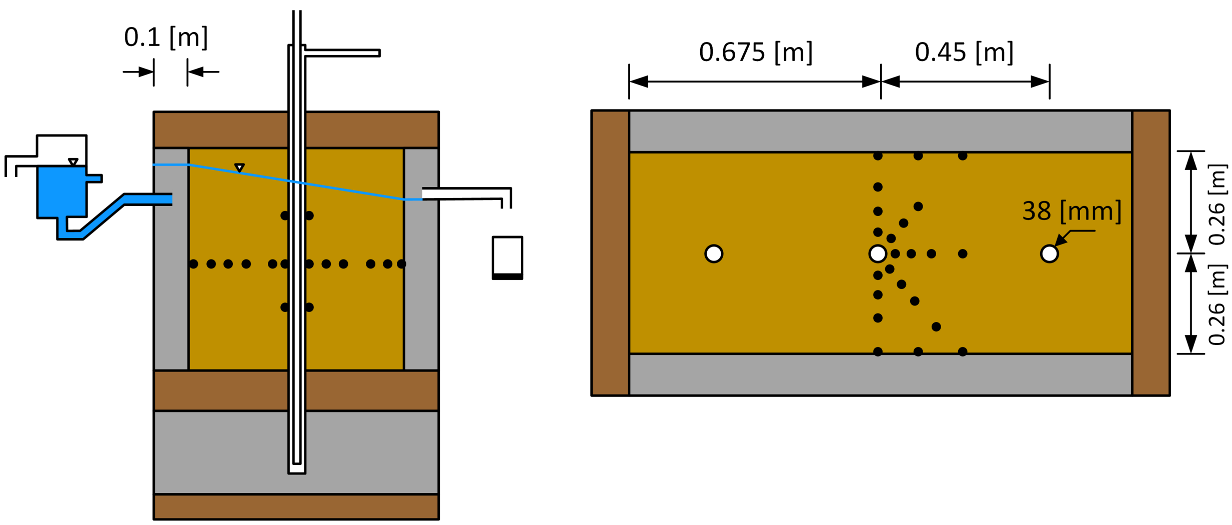

Figure 2.11 – Simplified schematic diagram of Frivik and Comini experimental setup. (after [67])

2.5 The process of the artificial ground freezing

Freezing phenomenon in a porous medium is a challenging fundamental and numerical problem. The complication of the problem arises primarily from the difficulty of tracking the

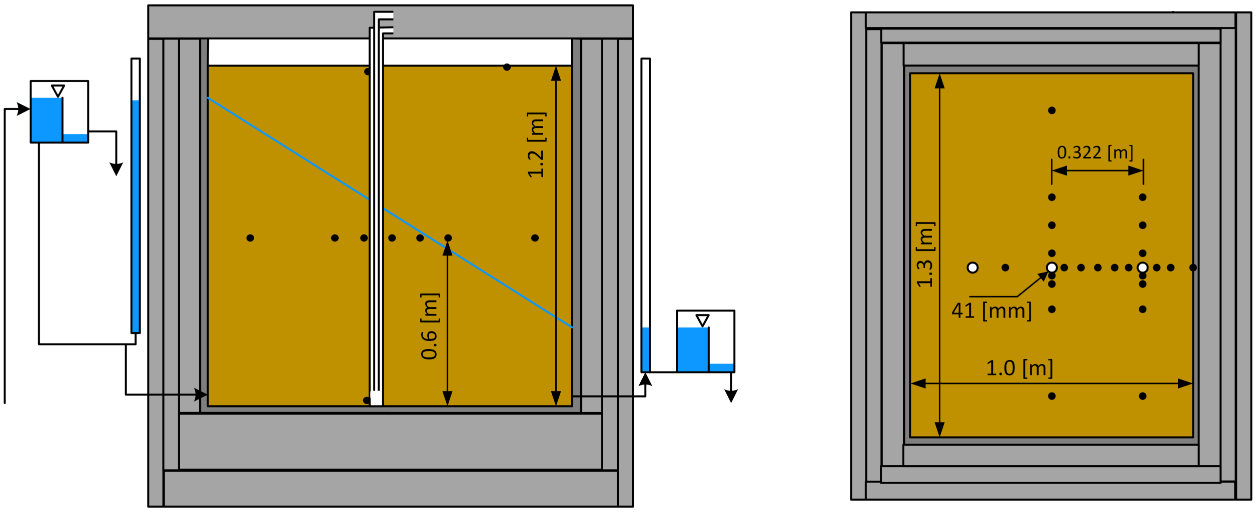

Figure 2.12 – Simplified schematic diagram of Pimentel et al. experimental setup. (after [66])

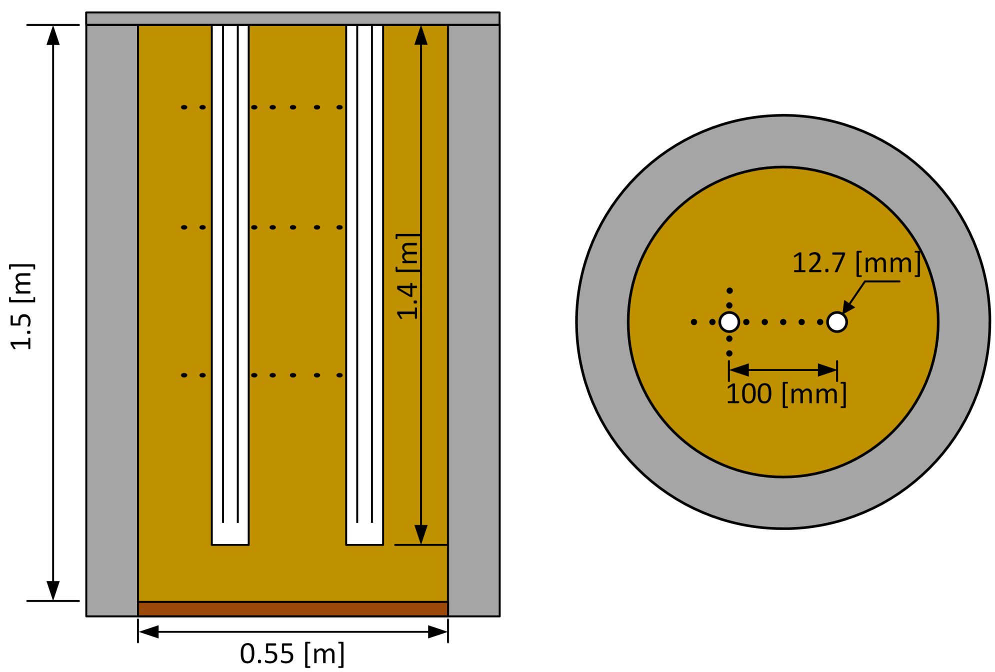

Figure 2.13 – Simplified schematic diagram of Alzoubi et al. experimental setup. (after [68])

movement of the solid-liquid interface, the discontinuity of the water-ice thermophysical properties, and the presence of the porous structure. Concerning the physical and numerical modelings, several approaches have been developed to solve this moving boundary problem. The main concepts of these procedures have been adapted from the solid-liquid phase-change

Table 2.3: Summary of the available AGF experimental research

Ref.	AGF type	Size [cm]	No. of pipes	Pipes' orientation	Pipes' spacing [cm]	Ground's temp. [°C]	Brine's temp. [°C]
[64]	open-loop	100×100	1	vertical	-	18-19	-183
[65]	closed-loop	$100 \times 90 \times 30$	5	horizontal	7	10	-30
[67]	closed-loop	$135 \times 52 \times 52$	3	vertical	45	8	-40
[68]	closed-loop	150×55	2	vertical	10	5-20	-20 to -30

of pure material. Among other numerical methods, this paper focuses on the mathematical and numerical models that rely on the fixed-grid methods [69]. This technique, in contrast to the moving boundary approach [70, 71] or Lattice Boltzmann modeling [72], solves the system of partial differential equations over the entire domain. Therefore, there is no need to track the solid-liquid interface, or to employ deforming mesh.

The porous structure of the ground consists of solid matrix (sand particles) and interconnected pores that could be filled with water (in case of fully-saturated sand), air (in case of dry sand), or both (in the case of unsaturated sand). The analysis of fluid flow and heat transfer in a porous medium could be addressed at the microscopic level (pore-level) or macroscopic level (local volume-averaged). In this section, we attempt to analyze the fundamental aspects of the fluid flow, conduction, and convection of the artificial ground freezing process, by discussing the local volume-averaged conservation equations of mass, momentum, and energy in a porous medium [73, 74].

Several studies have been conducted to address the ground freezing process. The discussions include analytical or numerical approaches using one-dimensional, two-dimensional or three-dimensional mathematical models - in some cases the models are validated against lab-scale experimental setup. The main objectives of these studies were defined, for example, as: estimating the closure time, the effect of the groundwater seepage on the growth rate of the frozen body, or optimization analysis of freeze pipes' spacing. Table 2.4 provides a list of references that discussed the AGF process.

The survey reveals that all studies adopted the volume-averaged assumption in their calculation, which is indeed a valid approximation, taking into consideration the size of the sands particle and the slow AGF process. Using the volume-averaged technique means that the conservation equations are integrated over a representative volume element, V, where for any local quantities, θ, the volume-averaged value,Θ, is defined as:

$$\Theta = \frac{1}{V}\int_V \theta dV \tag{2.1}$$

Also, the most common approach applied in the solution of the phase-change of the AGF process is a formulation that uses the classical apparent heat capacity method. This method is widely used in heat transfer problems, where conductive heat transfer is the dominant mechanism. The conservation equation of energy, using the apparent heat capacity, is expressed as:

$$\rho c_{p,\,app}\left[\frac{\partial T}{\partial t}+\nabla\cdot(\mathbf{u}T)\right]=\nabla\cdot(k_e\nabla T) \tag{2.2}$$

The apparent heat capacity, $c_{p,\,app}$, could be defined as [75]:

$$c_{p,\,app}=\frac{\displaystyle\int_{T_s}^{T_\ell} c_p\,(T)\,dT+L\,(T)}{T_\ell-T_s} \tag{2.3}$$

Bonacina et al. [76], on the other hand, proposed a simplified version with a constant function for the latent heat of fusion, such that the apparent heat capacity, $c_{p,\,app}$, could be defined as:

$$c_{p,\,app}=\frac{L}{2\,(T_\ell-T_s)}+\frac{c_{p\ell}+c_{ps}}{2} \tag{2.4}$$

The enthalpy-porosity approach, on the contrary, is implemented in fewer studies. This method basically relies on separating the enthalpy of a liquid into sensible and latent terms [69]:

$$h=h_{sen}+h_{lat}=\int_{T_{ref}}^{T}\rho c_p dT+\rho L \tag{2.5}$$

This definition enables to redefine the conservation equation of energy in the following form [77]:

$$\frac{\partial}{\partial t}\,(\rho h_{sen})+\nabla\cdot(\rho h_{sen}\mathbf{u})=\nabla\cdot(k_e\nabla T)-\rho L\left[\frac{\partial\gamma}{\partial t}+\nabla\cdot(\mathbf{u}\gamma)\right] \tag{2.6}$$

The enthalpy method is commonly used in other phase-change porous-medium problems, where it is prefered over the apparent heat capacity method. Agyenim et al. [78] conducted a comprehensive review of the phase-change formulation for latent-heat thermal energy storage systems; one of the conclusions of their survey was that the enthalpy methods is preferable by the researchers over other approaches. Furthermore, König-Haagen et al. [79] performed an extensive study to examine the corresponding accuracy of the most used macroscopic energy formulations within the frame of the fixed-grid formulation; they concluded that, as a rule of thumb, the enthalpy formulations showed more robust and precise outcomes, as compared to the apparent heat capacity method. It is important to highlight here that the formulations of the energy equations mentioned above are for a pure substance. In the case of the phase change in a porous medium, proper modifications with the local volume-averaged technique and the porosity should be implemented. More details could be obtained from [68].

Table 2.4: Summary of the available studies that discussed AGF process. A: Analytical; N: Numerical; E: Experiment.

Ref.	Modeling Nature	Method
[68]	3D model; enthalpy-porosity approach, solving mass, momentum, and energy equations	N & E
[80, 81]	2D model; enthalpy-porosity approach, solving mass, momentum, and energy equations	N
[82]	2D model; enthalpy-porosity approach, solving mass, momentum, and energy equations; considering groundwater seepage	N
[34, 53, 83–95]	2D model; apparent c_p method; solving heat conduction equation	N
[17, 67, 96–98]	2D model; apparent c_p method; solving mass and heat conduction equations; considering groundwater seepage	N & E
[99]	1D-A & 2D-N model; apparent c_p method; solving heat conduction equation	A & N
[49, 100–111]	1D cylindrical coordinates; solving heat conduction equation	A
[112–114]	3D model; apparent c_p method; solving heat conduction equation	N
[115, 116]	2D model; hydraulic conductivity and apparent c_p method; solving mass, momentum, and heat conduction equation	N
[56, 66]	3D model; apparent c_p method; considering groundwater seepage	N & E
[46, 117, 118]	1D & conjugate-2D model; apparent c_p method; solving mass and heat conduction equations	N
[59, 119]	3D conjugate model; apparent c_p method; solving mass and heat conduction equations; considering groundwater seepage	N
[98, 120–123]	2D model; apparent c_p method; solving mass and heat conduction equations; considering groundwater seepage	N

Moreover, a review of the most implemented effective thermal conductivity, k_e, is conducted. A summary of the most used formulations is listed in Table 2.5. Apparently, the parallel arrangement and the geometric mean formulations are among the most used methods to calculate the effective thermal conductivity, k_e, in the porous ground structure. In general, the effective thermal conductivity, k_e, depends on: (i) the thermal conductivities of each phase, (ii) the porosity, ε, of the ground, and (iii) the distribution of the phases within a volume element. For all cases considered in Table 2.5, $k_f < k_p$, and therefore $k_f < k_e < k_p$.

The parallel distribution, as defined in Table 2.5, means that the phases are thermally in parallel with respect to the direction of the heat flow. This weighted arithmetic mean leads, at the same porosity, ε, to a higher effective thermal conductivity, k_e, as compared to the intermediate weighted geometric mean approach, as depicted in Fig. 2.14(b). However, the comparison between the two approaches varies with porosity. For instance, at a low porosity of 0.1, the geometric mean approach gave an underestimated value of the effective thermal conductivity, as compared to the parallel arrangement formulation, as shown in Fig. 2.14(a). On the other hand, the deviation between the two approaches is higher at a higher porosity of 0.9. Overall, both approaches give the same values when $k_p/k_f \rightarrow 1.0$. The choice of either approaches should be based on the nature of the problem. Interested readers could find more information about various methods to calculate the effective thermal conductivity, k_e, and comparisons between different approaches at [73, 124].

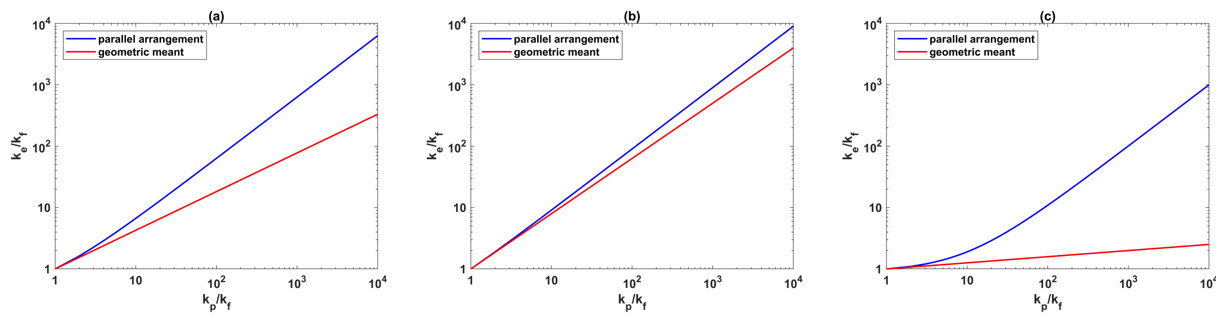

Figure 2.14 – Effective thermal conductivity, k_e, predicted by different approaches at ground porosity, ε, of (a) 0.1, (b) 0.37, and (c) 0.9

The formulation of the conservation equations of mass and momentum is also reviewed. The review shows that the structure of the conservation equation of mass is identical in all studies. Based on the local volume-averaged assumption, and using the superficial velocity,$\mathbf{u} = \varepsilon \mathbf{u}_\ell$, the conservation equation of mass is defined as below:

$$\frac{\partial}{\partial t}(\rho) + \nabla \cdot (\rho \mathbf{u}) = 0 \tag{2.7}$$

Concerning the liquid flow and the phase-change in the porous ground structure, several approaches have been adopted to address the zero velocity condition as the liquid water turns into ice. The first approach is based on the concept of the relative hydraulic conductivity proposed by [129]. This approach has been discussed further by [130, 131] and later implemented by several studies [46, 59, 67, 98, 117–119, 121, 132, 133], where the water flow is assumed to satisfy Darcy's law as:

$$\mathbf{u} = -K_r \frac{K}{\mu_\ell} \nabla p \tag{2.8}$$

Table 2.5: Summary of some predictions for effective thermal conductivity

Ref.	Approach	Expression
[68, 82, 114, 115, 121, 123, 125]	Parallel arrangement	$k_e = \varepsilon k_f + (1-\varepsilon)\, k_p$
[80]	Veinberg model [126]	$k_e = k_p - \varepsilon \left[\dfrac{k_p - k_f}{k_f^{1/3}} \right] k_e^{1/3}$
[34, 46, 53, 56, 92, 98, 110, 116–119]	Geometric mean	$k_e = k_f^{\varepsilon} k_p^{1-\varepsilon}$
[59, 127, 128]	Variational formulation	$k_e = k_f \left[1 + \dfrac{3\,(1-\varepsilon)\,(k_p/k_f - 1)}{3 + \varepsilon\,(k_p/k_f - 1)} \right]$

The relative permeability, K_r, is a scalar term varies between 0 and 1, and depends on the saturation degree, χ. The value of the relative permeability is controlled by the degree of freezing. The creation of ice is associated with a smaller free-path pore size, which, in turn, mitigates the water velocity. Of several formulations (check [73]), the below definition is the one that is used in the studies mentioned above [130, 134]:

$$K_r(\chi) = \sqrt{\chi} \left[1 - \left(1 - \chi^{1/z} \right)^{z} \right]^2 \tag{2.9}$$

Various simplifications have been made to define the saturation degree, χ, as a function of temperature only, by introducing fitting parameters; two examples are given below for illustrations:

Example 01 [59, 119, 132, 133]

$$\chi = \left[1 + \left(\frac{T_0 - T}{\omega} \right)^{\frac{1}{1-m}} \right]^{-m} \tag{2.10}$$

where T_0 is the freezing temperature; ω and m are material constants.

Example 02 [81, 121]

$$\chi = (1 - \chi_{res}) \exp \left[\left(\frac{T_0 - T}{\omega} \right)^2 \right] + \chi_{res} \tag{2.11}$$

where χ_{res} is the residual saturation, which is the minimum value that water saturation, χ, could reach.

One of the main factors that influence the relative permeability is the history of the process. This means that the value of the relative permeability, K_r, as the saturation degree, χ, increases (during thawing process) differs from that observed as, χ, decreases (during freezing process). That is, the results show multi-values of the relative permeability at the same saturation degree (i.e., one has hysteresis). Furthermore, the value of the relative permeability stays zero until the saturation degree exceeds particular non-zero value. It is important to highlight here that the value of the relative permeability depends, also, on the absolute permeability, K, at the same saturation degree. These behaviors are illustrated in Fig. 2.15.

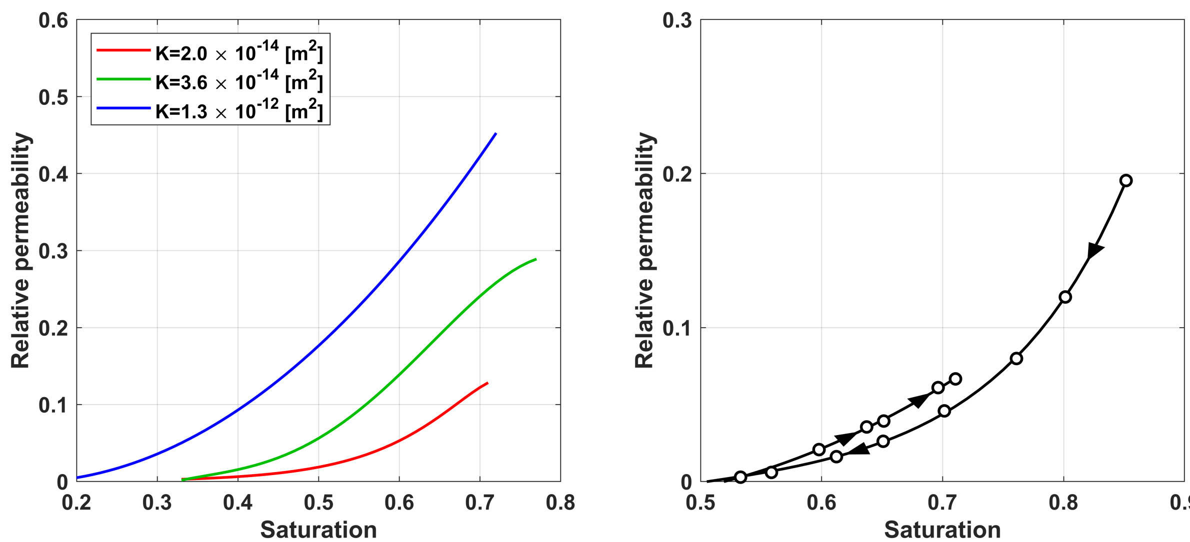

Figure 2.15 – The dependence of the relative permeability, K_r, on the absolute permeability, K, (left). A general form of the relative permeability as a function of the saturation degree showing the hysteresis behavior (right). (after [73])

Despite its popularity in the ground freezing literature, the concept of relative permeability was critiqued by [73, 74, 135] because of its complexity and dependence on various factors such as local saturation, matrix structure, surface tension, density ratio, and others, that are determined experimentally.

The second approach proposes a buffering area between liquid water and ice, known as the mushy zone [77, 80]. The approach supposes that the mushy region behaves as a porous medium, as depected in Fig. 2.16 (left). The momentum equation is defined as [68, 80]:

$$\frac{1}{\varepsilon}\frac{\partial}{\partial t}\left(\rho_\ell \mathbf{u}\right)+\frac{1}{\varepsilon^2}\left[\nabla\cdot\left(\rho_\ell \mathbf{u}\mathbf{u}\right)\right]=-\nabla p-\frac{1}{\varepsilon}\nabla\cdot\left(\mu_\ell\left(\nabla\mathbf{u}+\nabla\mathbf{u}^T\right)\right)$$
$$-\frac{C_F}{K^{1/2}}\rho_\ell|\mathbf{u}|\mathbf{u}-\frac{\mu_\ell}{K}\mathbf{u}-\mathbf{u}C_m\frac{\left(1-\gamma\right)^2}{\gamma^3} \quad (2.12)$$

The second term on the right-hand side accounts for the macroscopic viscous shear in the liquid and is often called Brinkman's extension [80]. The third and the fourth terms on the right-hand side of Eq. 2.12 accounts for Forchheimer term and Darcy's term, respectively. These two terms make up the total resistance to the fluid flow in the porous medium.

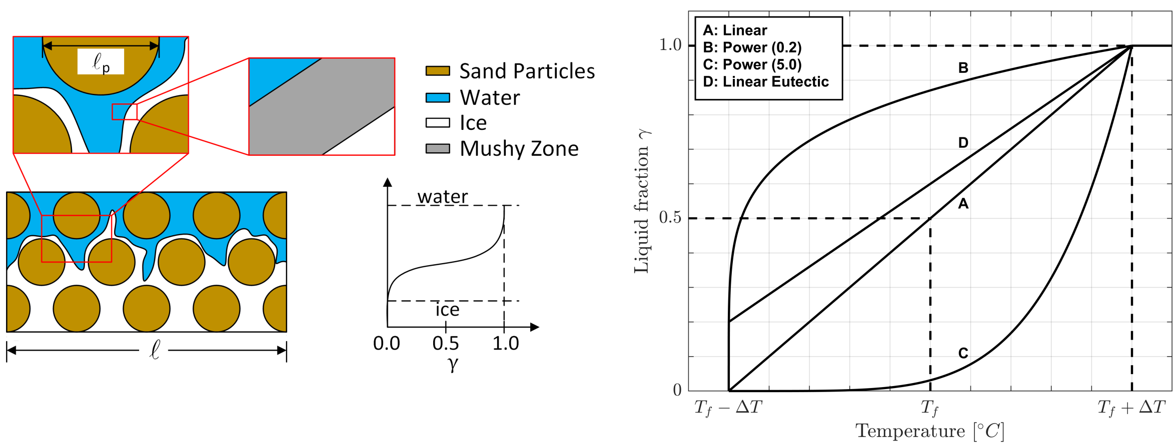

Figure 2.16 – A schematic of a representative elementary volume (REV) during AGF process, considering the phase-change interface as a mushy zone (left) (after [80]). Possible forms for liquid fraction, γ, within the mushy zone (right). (after [69, 136])

The last term in Eq. (2.12) is basically a modified Darcy source term that affects water velocity as follows. In the liquid zone, the mushy source term takes a value of zero; the single-phase momentum equation is then approximated by Darcy law. Within the mushy zone, the source term increases from zero to a large value as the local liquid fraction, γ, decreases from its liquid value of 1 to its solid value of 0. As the local liquid fraction approaches zero, the mushy source term dominates all other terms, and force the velocity, $\mathbf{u}$, to a value close to 0. The value of the liquid fraction, γ, could be defined, within the mushy zone, as shown in Fig. 2.16 (right) and Table 2.6 [136]. The selection of different formulation could influence, to a certain point, the interaction between the solid region and the mushy zone. Generally, the temperature range of the mushy zone, $2\Delta T$, during AGF process is significantly small, where $2\Delta T \approx 0.1[^\circ C]$. This small value will reduce the influence of liquid fraction formulation on the freezing process. However, in specific cases, such as rock fracture, the temperature range within the mushy zone could reach 6 [$^\circ C$]. In such problems, further examination to select the proper formulation should be considered.

Table 2.6: Suggested formulation of the liquid fraction, γ, within the mushy zone as illustrated in Fig. 2.16. (after [136])

Curve	Type	Equation of γ	Condition
A	Linear	$\gamma = \frac{T - (T_f - \Delta T)}{2\Delta T}$	
B	Power	$\gamma = \left(\frac{T - (T_f - \Delta T)}{2\Delta T}\right)^n$	$n = 0.2$
C	Power	$\gamma = \left(\frac{T - (T_f - \Delta T)}{2\Delta T}\right)^n$	$n = 5.0$
D	Linear eutectic	$\gamma = \frac{(1-\gamma_e)\,T + \gamma_e\,(T_f + \Delta T) - (T_f - \Delta T)}{2\Delta T}$	$\gamma_e = 0.2$

2.6 Conclusions

Over the last few decades, studies have investigated the fundamentals of the artificial ground freezing (AGF) systems, examined their design aspect, conducted optimization analyses of the AGF process and its transient behavior, and observed the overall performance of the AGF systems. The studies included analytical, numerical, and experimental examinations. The current review revealed an intensive summary of the up-to-date achievements concerning thermal and hydraulic aspects of the AGF systems; it discussed the main type of the AGF systems and their main applications, the laboratory-scale experimental setup that have been developed, and some of the main fundamental aspects concerning the AGF process. The following conclusions can be drawn from the reviewed studies:

- There are two types of AGF systems. The commonly used one is the closed-loop, brine system. Although the freezing time of this type is considerably slow, as compared to the open-looped, liquid nitrogen system, it provides regular frozen body, higher flexibility, in terms of the size and shape of the frozen wall, and better control. On the other hand, the open-looped system is the optimum answer to short-term projects, such as ground sampling, or in case of a sudden emergency, such as hazardous-waste leakage.

- The reliability of mathematical models should be assessed by validating their results against the measurements of a controlled experiment. However, according to this review, the number of the studies that conducted experimental analysis by developing a laboratory-scale setup is very limited.
- Concerning the fundamental aspect of AGF process, the majority of the reviewed studies developed their models based on the formulation of the apparent heat capacity method. However, based on various reports, the modern enthalpy-porosity approach provides more robust and accurate results, compared to the apparent heat capacity method. Therefore, the authors believe that this method should be implemented in the formulation of the mathematical models concerning the AGF process to obtain more accurate results.
- Finally, AGF process is a challenging, multi-scale problem. However, the amount of studies concerning the fundamental aspect of this subject is limited. Most of the studies in the literature are either technical reports where observational remarks are listed, or in situ studies with fields measurements. There has been a growing interest in the AGF systems, especially in long-term projects such as hazardous-waste management. Therefore, there should be a higher potential in the research that focuses on the fundamentals, design, and applied aspects of the AGF system.

References

[1] John S Harris. *Ground freezing in practice.* Thomas Telford, 1995.

[2] Friedrich Hermann Poetsch. *Das Gefrierverfahren: Methode für schnelles, sicheres und lothrechtes abteufen von schächten im schwimmsande und überhaupt im wasserreichen gebirge für herstellung tiefgehender brückenpfeiler und für tunnelbauten im rolligen gebirge.* Craz & Gerlach, 1887.

[3] Helmut HaB and Peter Schafers. Application of ground freezing for underground construction in soft ground. In *Geotechnical Aspects of Underground Construction in Soft Ground: Proceedings of the 5th International Symposium TC28. Amsterdam, the Netherlands, 15-17 June 2005*, page 405. CRC Press, 2013.

[4] David C Sego, Peter K Robertson, S Sasitharan, BL Kllpatrick, and VS Pillai. Ground freezing and sampling of foundation soils at duncan dam. *Canadian Geotechnical Journal*, 31(6):939–950, 1994.

[5] BA Hofmann, DC Sego, and PK Robertson. In situ ground freezing to obtain undisturbed samples of loose sand. *Journal of geotechnical and geoenvironmental engineering*, 126(11):979–989, 2000.

[6] Greg P Newman. Case study: thermal analysis of artificial ground freezing at the mcarthur river uranium mine. *Geotechnical News Vancouver*, 21(2):60–62, 2003.

[7] Xiaoyou Yun, Baoyao Tang, Murdock Greg, McGill Brian, and Mattie Brian. Radon bearing water protection in underground uranium mining–a case study. *International Journal of Mining Science and Technology*, 27(4):599–603, 2017.

[8] Jie Zhou and Yiqun Tang. Experimental inference on dual-porosity aggravation of soft clay after freeze-thaw by fractal and probability analysis. *Cold Regions Science and Technology*, 153:181–196, 2018.

[9] Shen Yanjun, Wang Yongzhi, Zhao Xiaodong, Yang Gengshe, Jia Hailiang, and Rong Tenglong. The influence of temperature and moisture content on sandstone thermal conductivity from a case using the artificial ground freezing (agf) method. *Cold Regions Science and Technology*, 2018.

[10] JG Dash. Ice technology for hazardous waste management. *Waste Management*, 11(4):183–189, 1991.

[11] David Andrew Brown. Hull wastewater flow transfer tunnel: recovery of tunnel collapse by ground freezing. *Proceedings of the Institution of Civil Engineers-Geotechnical Engineering*, 157(2):77–83, 2004.

[12] John S Wettlaufer, J Gregory Dash, and Norbert Untersteiner. *Ice physics and the natural environment*, volume 56. Springer Science & Business Media, 2013.

[13] Anna M Wagner and Edward Yarmak Jr. Using frozen barriers for containment of contaminants. Technical report, Office of the Assistant Chief of Staff for Installation Management Washington United States, 2017.

[14] Cynthia G Jardine, Laura Banfield, S Michelle Driedger, and Christopher M Furgal. Risk communication and trust in decision-maker action: a case study of the giant mine remediation plan. *International Journal of Circumpolar Health*, 72(1):21184, 2013.

[15] Adrian H Gallardo and Atsunao Marui. The aftermath of the fukushima nuclear accident: Measures to contain groundwater contamination. *Science of The Total Environment*, 547:261–268, 2016.

[16] G Veranneman and D Rebhan. Ground consolidation with liquid nitrogen (ln2). *Engineering Geology*, 13(1-4):473–484, 1979.

[17] Per E. Frivik. State-of-the-art report. ground freezing: thermal properties, modelling of processes and thermal design. *Engineering Geology*, 18:115–133, 1981.

[18] Iskandar K. Iskandar. Effect of freezing on the level of contaminants in uncontrolled hazardous waste sites. part 1. literature review. *Cold Regions Research and Engineering Laboratory*, 86(19):1–33, 1986.

[19] F Gallavresi. Ground freezing—the application of the mixed method (brine—liquid nitrogen). *Engineering Geology*, 18(1-4):361–375, 1981.

[20] Iskandar K. Iskandar. Ground freezing controls hazardous waste. *Military Engineer*, 79:455–456, 1987.

[21] Rafael D Simon and George A Cooper. Cryogenic drilling: A new drilling method for environmental remediation. *Groundwater Monitoring & Remediation*, 16(3):79–85, 1996.

[22] Hanadi S Rifai, Philip B Bedient, and Gretchen L Shorr. Monitoring hazardous waste sites: characterization and remediation considerations. *Journal of Environmental Monitoring*, 2(3):199–212, 2000.

[23] Grace W Su, Joseph SY Wang, and Kris Zacny. In situ freeze-capturing of fracture water using cryogenic coring. *Vadose Zone Journal*, 3(4):1479–1482, 2004.

[24] Naval Goel, Joao Tadeu V De Sousa, Joseph Flenniken, Subhash Shah, and Bill Liddell. Fabrication and testing of apparatus for laboratory simulation of alaska frozen rock encountered during hydrate gas reservoir coring. *Journal of cold regions engineering*, 18(2):53–69, 2004.

[25] Paul C Schmall and Bernd Braun. Ground freezing—a viable and versatile construction technique. In *Current Practices in Cold Regions Engineering*, pages 1–11. 2006.

[26] Michael P Esposito III, Ronald D Andrus, and William M Camp III. Ground freezing and sampling of pleistocene sand near charleston, south carolina. *Journal of Geotechnical and Geoenvironmental Engineering*, 140(1):185–193, 2013.

[27] Youngseok Kim, Bumsik Hwang, and Wanjei Cho. Development of ground freezing system for undisturbed sampling of granular soils. *Advances in Civil Engineering*, 2018, 2018.

[28] Hans L Jessberger. Theory and application of ground freezing in civil engineering. *Cold Regions Science and Technology*, 3(1):3–27, 1980.

[29] DC Arnold. Ground treatment for the three valleys tunnel. *Tunnels & tunnelling*, 17(10):35–38, 1985.

[30] C Selosse. Special techniques used for the structural phases of the saint michel station on line b of the regional express railway. *Travaux*, 613:34–38, 1986.

[31] Carlo Crippa and Vittorio Manassero. Artificial ground freezing at sophiaspoortunnel (the netherlands)—freezing parameters: Data acquisition and processing. *GeoCongress 2006: Geotechnical Engineering in the Information Technology Age*, 254, 2006.

[32] Cungang Lin, Shiming Wu, and Zhongmiao Zhang. One technique for shield tail brushes' repair using liquid nitrogen freezing method in the artesian aquifer. In *ICPTT 2011: Sustainable Solutions for Water, Sewer, Gas, and Oil Pipelines*, pages 858–867. 2011.

[33] F Kirsch and Th Richter. Ground freezing for tunnelling under historical structures-icsmge. *Alexandria/Egypt Disponível em: www. gudconsult. de consultado em Abril*, 2011.

[34] Spyridon Papakonstantinou, Georgios Anagnostou, and Erich Pimentel. Evaluation of ground freezing data from the naples subway. *Proceedings of the Institution of Civil Engineers-Geotechnical Engineering*, 166(3):280–298, 2013.

[35] François Bergeron and Philippe Pasquier. Simulation of ground heat exchanger for cryogenic applications. In *COMSOL Conference Boston*, 2013.

[36] Youngjin SON, Hangseok CHOI, and Tae Young KO. Estimation of the amount of refrigerant in artificial ground freezing for subsea tunnel. In *The World Congress on Advances in Structural Engineering and Mechanics (ASEM17)*. Seoul, Korea, 2017.

[37] Jun Hu, Yong Liu, Yuping Li, and Kai Yao. Artificial ground freezing in tunnelling through aquifer soil layers: a case study in nanjing metro line 2. *KSCE Journal of Civil Engineering*, pages 1–7, 2018.

[38] B Braun, J Shuster, and E Burnham. Ground freezing for support of open excavations. *Engineering Geology*, 13(1-4):429–453, 1979.

[39] IS Zhitomirsky, VN Fenchenko, VI Borisenko, PA Schparber, and AL Schreiman. Simulation and optimization of high-speed freezing of water-bearing rocks using liquid nitrogen. *Cryogenics*, 24(12):676–678, 1984.

[40] P. C. Schmall, D. K. Mueller, and K. E. Wigg. Ground freezing in adverse geology and difficult ground conditions. pages 431–436, 2006.

[41] ACJ Baker and AN James. Three valleys water committee: Tunnel connection to thames water reservoirs. *Proceedings of the Institution of Civil Engineers*, 88(6):929–954, 1990.

[42] Orlando B Andersland and Branko Ladanyi. *Frozen Ground Engineering*. John Wiley & Sons, 2004.

[43] P de PORCELLINIS, JL Rojo, and Cimentaciones Especiales. Brine substitute liquids for soil freezing at very low temperatures. *Engineering Geology*, 18:203–210, 1981.

[44] Dennis R Cordray, Lisa R Kaplan, Peter M Woyciesjes, and Theodore F Kozak. Solid-liquid phase diagram for ethylene glycol+ water. *Fluid phase equilibria*, 117(1-2):146–152, 1996.

[45] Stephen A Ketcham, L David Minsk, Robert R Blackburn, and Edward J Fleege. Manual of practice for an effective anti-icing program: a guide for highway winter maintenance personnel. Technical report, FHWA-RD-9-202. Army Cold Regions Research and Engineering Laboratory, 1996.

[46] Manon Vitel, Ahmed Rouabhi, Michel Tijani, and Frédéric Guérin. Modeling heat transfer between a freeze pipe and the surrounding ground during artificial ground freezing activities. *Computers and Geotechnics*, 63:99–111, 2015.

[47] Piyanon Mumanachit, DT Reindl, and GF Nellis. Comparative analysis of low temperature industrial refrigeration systems. *international journal of refrigeration*, 35(4):1208–1221, 2012.

[48] Zhaorui Zhao, Ziwen Xing, Feng Hou, Yafen Tian, and Shaoming Jiang. Theoretical and experimental investigation of a novel high temperature heat pump system for recovering heat from refrigeration system. *Applied Thermal Engineering*, 107:758–767, 2016.

[49] John T Holden. Improved thermal computations for artificially frozen shaft excavations. *Journal of Geotechnical and Geoenvironmental Engineering*, 123(8):696–701, 1997.

[50] C.S. Jahan, C. Quamruzzaman, Q.H. Mazumder, and T.A.H.F.M.A. Haque. Artificial ground freezing method for shaft construction in maddhapara hardrock mine, bangladesh: Minimization of its cost. *Pakistan Journal of Scientific and Industrial Research*, 47(2):112–117, 2004.

[51] J.M. McCann, D.K. Mueller, P.C. Schmall, and J.D. Nickerson. Brightwater conveyance system: ground freezing for access shaft excavation through soft ground. pages 297–307, 2009.

[52] Renshu Yang, Qianxing Wang, and Liyun Yang. A closed-form elastic solution for irregular frozen wall of inclined shaft considering the interaction with ground. *Inter-*

national Journal of Rock Mechanics and Mining Sciences, 100(Supplement C):62 – 72, 2017.

[53] Chang-Yu Ou, Chung-Cheng Kao, and Ching-I Chen. Performance and analysis of artificial ground freezing in the shield tunneling. *Journal of GeoEngineering*, 4(1):29–40, 2009.

[54] TSK Lam and PLR Pang. Geotechnical control for artificial ground freezing works in tunnel projects in hong kong. *CRC Handbook of Phase Equilibria and Thermodynamic Data of Polymer Solutions at Elevated Pressures*, 4:117–122, 2015.

[55] Xiangdong Hu, Tao Fang, Jin Chen, Hui Ren, and Wang Guo. A large-scale physical model test on frozen status in freeze-sealing pipe roof method for tunnel construction. *Tunnelling and Underground Space Technology*, 72:55–63, 2018.

[56] E Pimentel, S Papakonstantinou, and G Anagnostou. Numerical interpretation of temperature distributions from three ground freezing applications in urban tunnelling. *Tunnelling and Underground Space Technology*, 28:57–69, 2012.

[57] G. Meschke, M.-M. Zhou, M. Zaki Abd Elrehim, and A. Marwan. Computational modelling and optimization of artificial ground freezing in tunnelling. pages 1397 – 1402, 2015.

[58] Gianpiero Russo, Andrea Corbo, Filippo Cavuoto, and Silvia Autuori. Artificial ground freezing to excavate a tunnel in sandy soil. measurements and back analysis. *Tunnelling and Underground Space Technology*, 50:226–238, 2015.

[59] Ahmed Marwan, Meng-Meng Zhou, M Zaki Abdelrehim, and Günther Meschke. Optimization of artificial ground freezing in tunneling in the presence of seepage flow. *Computers and Geotechnics*, 75:112–125, 2016.

[60] Greg Newman, Lori Newman, Denise Chapman, and Travis Harbicht. Artificial ground freezing: An environmental best practice at cameco's uranium mining operations in northern saskatchewan, canada. In *11th International Mine Water Association Congress–Mine Water–Managing the Challenges*, 2011.

[61] I.K. Iskandar and T.F. Jenkins. Potential use of artificial ground freezing for contaminant immobilization. In *Proceedings of the International Conference on New Frontiers for Hazardous Waste Management (September 15-18), Pittsburgh. Washington, DC: US Environmental Protection Agency*, pages 128–137, 1985.

[62] Wacker Martin, Guy Morand, and Barry W. Schmitke. Cigar lake's jet boring mining method. In *World Nuclear Association Annual Symposium, London*, 2004.

[63] Eduard Dorn and Oleg Kaledin. Modern and innovative shaft sinking and construction technology with examples from current projects/moderne und innovative schachtbautechnik am beispiel aktueller abteufprojekte. *Geomechanics and Tunnelling*, 6(5):574–581, 2013.

[64] Giancarlo Gioda, Livio Locatelli, and Francesco Gallavresi. A numerical and experimental study of the artificial freezing of sand. *Canadian geotechnical journal*, 31(1):1–11, 1994.

[65] Wolfgang Ständer. *Mathematische Ansätze zur Berechnung der Frostausbreitung in ruhendem Grundwasser im Vergleich zu Modelluntersuchungen für verschiedene Gefrierrohranordnungen im Schactund Grundbau*, volume 28. Technische Hochschule Fridericiana, Institut für Bodenmechanik und Felsmechanik, 1967.

[66] E Pimentel, A Sres, and G Anagnostou. Large-scale laboratory tests on artificial ground freezing under seepage-flow conditions. *Geotechnique*, 62(3):227, 2012.

[67] PE Frivik and G Comini. Seepage and heat flow in soil freezing. *Journal of Heat Transfer*, 104(2):323–328, 1982.

[68] Mahmoud A Alzoubi, Aurelien Nie-Rouquette, and Agus P Sasmito. Conjugate heat transfer in artificial ground freezing using enthalpy-porosity method: Experiments and model validation. *International Journal of Heat and Mass Transfer*, 126:740–752, 2018.

[69] VR Voller, CR Swaminathan, and Brian G Thomas. Fixed grid techniques for phase change problems: a review. *International Journal for Numerical Methods in Engineering*, 30(4):875–898, 1990.

[70] John Crank. *Free and moving boundary problems*. Oxford University Press, 1987.

[71] Tomasz A Kowalewski and Dominique Gobin. *Phase change with convection: modelling and validation*. Springer, 2004.

[72] MC Sukop. Dt thorne, jr. lattice boltzmann modeling lattice boltzmann modeling. 2006.

[73] Maasoud Kaviany. *Principles of heat transfer in porous media*. Springer Science & Business Media, 2012.

[74] Donald A Nield, Adrian Bejan, et al. *Convection in porous media*, volume 5. Springer, 2017.

[75] M Salcudean and Z Abdullah. On the numerical modelling of heat transfer during solidification processes. *International journal for numerical methods in engineering*, 25(2):445–473, 1988.

[76] Comini Bonacina, G Comini, A Fasano, and M 1973 Primicerio. Numerical solution of phase-change problems. *International Journal of Heat and Mass Transfer*, 16(10):1825–1832, 1973.

[77] Vaughan R Voller and C Prakash. A fixed grid numerical modelling methodology for convection-diffusion mushy region phase-change problems. *International Journal of Heat and Mass Transfer*, 30(8):1709–1719, 1987.

[78] Francis Agyenim, Neil Hewitt, Philip Eames, and Mervyn Smyth. A review of materials, heat transfer and phase change problem formulation for latent heat thermal energy storage systems (lhtess). *Renewable and sustainable energy reviews*, 14(2):615–628, 2010.

[79] Andreas König-Haagen, Erwin Franquet, Eric Pernot, and Dieter Brüggemann. A comprehensive benchmark of fixed-grid methods for the modeling of melting. *International Journal of Thermal Sciences*, 118:69–103, 2017.

[80] C Beckermann and R Viskanta. Natural convection solid/liquid phase change in porous media. *International Journal of Heat and Mass Transfer*, 31(1):35–46, 1988.

[81] Virgil J Lunardini. Freezing of soil with an unfrozen water content and variable thermal properties. Technical report, COLD REGIONS RESEARCH AND ENGINEERING LAB HANOVER NH, 1988.

[82] Mehdi Musivand Arzanfudi and Rafid Al-Khoury. Freezing-thawing of porous media: An extended finite element approach for soil freezing and thawing. *Advances in Water Resources*, 119:210–226, 2018.

[83] OC Zienkiewicz, CJ Parekh, and AJ Wills. The application of finite elements to heat conduction problems involving latent heat. *Rock mechanics*, 5(2):65–76, 1973.

[84] S Del Giudice, G Comini, and RW Lewis. Finite element simulation of freezing processes in soils. *International Journal for Numerical and Analytical Methods in Geomechanics*, 2(3):223–235, 1978.

[85] Hans L Jessberger and Eugen Makowski. Optimization of the freeze pipe arrangement and the necessary refrigeration plant capacity by a femcomputer program. *Engineering Geology*, 18(1-4):175–188, 1981.

[86] F Talamucci. Freezing processes in porous media: formation of ice lenses, swelling of the soil. *Mathematical and computer modelling*, 37(5-6):595–602, 2003.

[87] Zhang Xuefu, Lai Yuanming, Yu Wenbing, Zhang Shujuan, and Xiao Jianzhang. Forecast analysis of the refreezing of kunlun mountain permafrost tunnel on qing–tibet railway in china. *Cold regions science and technology*, 39(1):19–31, 2004.

[88] Shuangyang Li, Yuanming Lai, Mingyi Zhang, and Shujuan Zhang. Minimum ground pre-freezing time before excavation of guangzhou subway tunnel. *Cold Regions Science and Technology*, 46(3):181–191, 2006.

[89] Anton Sres and Georg Anagnostou. Numerical modelling and the implementation of artificial ground freezing. In *Proceedings of the Tenth International Symposium on Numerical Models in Geomechanics (NUMOG X), Rhodes, Greece, 25-27 April 2007*, pages 311–317. Taylor & Francis Group, 2007.

[90] Zhen Liu and Xiong Yu. Coupled thermo-hydro-mechanical model for porous materials under frost action: theory and implementation. *Acta Geotechnica*, 6(2):51–65, 2011.

[91] Parham Eslami-nejad and Michel Bernier. Freezing of geothermal borehole surroundings: A numerical and experimental assessment with applications. *Applied Energy*, 98:333–345, 2012.

[92] Young Seok Kim, Jae-Mo Kang, Jangguen Lee, Sung-Seo Hong, and Kwang-Jin Kim. Finite element modeling and analysis for artificial ground freezing in egress shafts. *KSCE Journal of Civil Engineering*, 16(6):925–932, 2012.

[93] Stephen William Rees, Peter John Cleall, Yu-Chao Li, and Kangjie Shao. Freezing soil effects on earth-contact heat transfer. *Building Services Engineering Research and Technology*, 34(3):259–274, 2013.

[94] Weibo Yang, Lei Kong, and Yongping Chen. Numerical evaluation on the effects of soil freezing on underground temperature variations of soil around ground heat exchangers. *Applied Thermal Engineering*, 75:259–269, 2015.

[95] Jun Hu, Yong Liu, Hong Wei, Kai Yao, and Wei Wang. Finite-element analysis of heat transfer of horizontal ground-freezing method in shield-driven tunneling. *International Journal of Geomechanics*, 17(10):04017080, 2017.

[96] PE Frivik and E Thorbergsen. Thermal design of artificial soil freezing systems. *Engineering Geology*, 18(1-4):189–201, 1981.

[97] Xianjun Tan, Weizhong Chen, Guojun Wu, and Jianping Yang. Numerical simulations of heat transfer with ice–water phase change occurring in porous media and application to a cold-region tunnel. *Tunnelling and Underground Space Technology*, 38:170–179, 2013.

[98] Shibing Huang, Yunlin Guo, Yanzhang Liu, Lihua Ke, Guofeng Liu, et al. Study on the influence of water flow on temperature around freeze pipes and its distribution optimization during artificial ground freezing. *Applied Thermal Engineering*, 135:435–445, 2018.

[99] Hasan G Askar and Paul P Lynn. Infinite elements for ground freezing problems. *Journal of Engineering Mechanics*, 110(2):157–172, 1984.

[100] FJ Sanger and FH Sayles. Thermal and rheological computations for artificially frozen ground construction. *Engineering Geology*, 13(1-4):311–337, 1979.

[101] M Ramos, J Aguirre-Puente, and R Posado Cano. Soil freezing problem: an exact solution. *Soil technology*, 9(1-2):29–38, 1996.

[102] Holden J. T. Heat transfer in artificial ground freezing. In *Proceedings of the International Symposium on Ground Freezing and Frost Action*, pages 107–112, 1984.

[103] Chi Zhang, Wei-hao Yang, Jia-gen Qi, and Tao Zhang. Analytic computation on the forcible thawing temperature field formed by a single heat transfer pipe with unsteady outer surface temperature. *Journal of Coal Science and Engineering (China)*, 18(1):18–24, 2012.

[104] Xiang-dong Hu and Luo-yu Zhang. Analytical solution to steady-state temperature field of two freezing pipes with different temperatures. *Journal of Shanghai Jiaotong University (Science)*, 18(6):706–711, 2013.

[105] Xiang-dong Hu, Wang Guo, Luo-yu Zhang, Jin-tai Wang, and Xue Dong. Mathematical models of steady-state temperature fields produced by multi-piped freezing. *Journal of Zhejiang University-SCIENCE A*, 17(9):702–723, 2016.

[106] Xiang-dong Hu, Jin-zhu Yu, Hui Ren, Yang Wang, and Jin-tai Wang. Analytical solution to steady-state temperature field for straight-row-piped freezing based on superposition of thermal potential. *Applied Thermal Engineering*, 111:223–231, 2017.

[107] Xiangdong Hu, Zequn Hong, and Tao Fang. Analytical solution to steady-state temperature field with typical freezing tube layout employed in freeze-sealing pipe roof method. *Tunnelling and Underground Space Technology*, 79:336–345, 2018.

[108] Xiang-dong Hu, Tao Fang, and Luo-yu Zhang. Analytical solution to temperature distribution in frozen soil wall with wavy boundaries by single-row-and double-row-piped freezing. *Cold Regions Science and Technology*, 145:208–228, 2018.

[109] Xiang-dong Hu, Tao Fang, and Yan-guang Han. Mathematical solution of steady-state temperature field of circular frozen wall by single-circle-piped freezing. *Cold Regions Science and Technology*, 148:96–103, 2018.

[110] Ting Li, Yang Zhou, Xiang-you Shi, Xiao-xue Hu, and Guo-qing Zhou. Analytical solution for the soil freezing process induced by an infinite line sink. *International Journal of Thermal Sciences*, 127:232–241, 2018.

[111] Tao Wang, Guoqing Zhou, Jianzhou Wang, and Lei Zhou. Stochastic analysis of uncertain thermal parameters for random thermal regime of frozen soil around a single freezing pipe. *Heat and Mass Transfer*, pages 1–8, 2018.

[112] Liu Zhiqiang and Lai Yuanming. Numerical analysis for the ventilated embankment with thermal insulation layer in qing–tibetan railway. *Cold Regions Science and Technology*, 42(3):177–184, 2005.

[113] Haiqing Song, Haibing Cai, Zhishu Yao, Chuanxin Rong, and Xiaojian Wang. Finite element analysis on 3d freezing temperature field in metro cross passage construction. *Procedia engineering*, 165:528–539, 2016.

[114] I Panteleev, A Kostina, M Zhelnin, A Plekhov, and L Levin. Intellectual monitoring of artificial ground freezing in the fluid-saturated rock mass. *Procedia Structural Integrity*, 5:492–499, 2017.

[115] Hywel Rhys Thomas, Peter John Cleall, Y Li, C Harris, and M Kern-Luetschg. Modelling of cryogenic processes in permafrost and seasonally frozen soils. *Geotechnique*, 59(3):173–184, 2009.

[116] Yared W Bekele, Hiroyuki Kyokawa, Arne M Kvarving, Trond Kvamsdal, and Steinar Nordal. Isogeometric analysis of thm coupled processes in ground freezing. *Computers and Geotechnics*, 88:129–145, 2017.

[117] Manon Vitel, Ahmed Rouabhi, Michel Tijani, and Frédéric Guérin. Thermo-hydraulic modeling of artificial ground freezing: Application to an underground mine in fractured sandstone. *Computers and Geotechnics*, 75:80–92, 2016.

[118] Ahmed Rouabhi, E Jahangir, and H Tounsi. Modeling heat and mass transfer during ground freezing taking into account the salinity of the saturating fluid. *International Journal of Heat and Mass Transfer*, 120:523–533, 2018.

[119] Manon Vitel, Ahmed Rouabhi, Michel Tijani, and Frédéric Guérin. Modeling heat and mass transfer during ground freezing subjected to high seepage velocities. *Computers and Geotechnics*, 73:1–15, 2016.

[120] BD Kay, M Fukuda, H Izuta, and MI Sheppard. The importance of water migration in the measurement of the thermal conductivity of unsaturated frozen soils. *Cold Regions Science and Technology*, 5(2):95–106, 1981.

[121] Jeffrey M McKenzie, Clifford I Voss, and Donald I Siegel. Groundwater flow with energy transport and water–ice phase change: numerical simulations, benchmarks, and application to freezing in peat bogs. *Advances in Water Resources*, 30(4):966–983, 2007.

[122] Leonid Bronfenbrener and Regina Bronfenbrener. Modeling frost heave in freezing soils. *Cold Regions Science and Technology*, 61(1):43–64, 2010.

[123] Christophe Grenier, Hauke Anbergen, Victor Bense, Quentin Chanzy, Ethan Coon, Nathaniel Collier, François Costard, Michel Ferry, Andrew Frampton, Jennifer Frederick, et al. Groundwater flow and heat transport for systems undergoing freeze-thaw: Intercomparison of numerical simulators for 2d test cases. *Advances in Water Resources*, 114:196–218, 2018.

[124] WMJH Woodside and JH Messmer. Thermal conductivity of porous media. i. unconsolidated sands. *Journal of applied physics*, 32(9):1688–1699, 1961.

[125] Erfan A Amiri, James R Craig, and Barret L Kurylyk. A theoretical extension of the soil freezing curve paradigm. *Advances in Water Resources*, 111:319–328, 2018.

[126] AK Veinberg. Permeability, electrical conductivity, dielectric constant and thermal conductivity of a medium with spherical and ellipsoidal inclusions. In *Soviet Physics Doklady*, volume 11, page 593, 1967.

[127] Roman Lackner, Andreas Amon, and Hannes Lagger. Artificial ground freezing of fully saturated soil: thermal problem. *Journal of Engineering Mechanics*, pages 117–122, 2005.

[128] Roman Lackner, Christian Pichler, and Andreas Kloiber. Artificial ground freezing of fully saturated soil: viscoelastic behavior. *Journal of Engineering Mechanics*, pages 211–220, 2008.

[129] Morris Muskat and Milan W Meres. The flow of heterogeneous fluids through porous media. *Physics*, 7(9):346–363, 1936.

[130] Yechezkel Mualem. A new model for predicting the hydraulic conductivity of unsaturated porous media. *Water resources research*, 12(3):513–522, 1976.

[131] M Th Van Genuchten. A closed-form equation for predicting the hydraulic conductivity of unsaturated soils. *Soil science society of America journal*, 44(5):892–898, 1980.

[132] S Nishimura, A Gens, S Olivella, and RJ Jardine. Thm-coupled finite element analysis of frozen soil: formulation and application. 2008.

[133] MM Zhou and G Meschke. A three-phase thermo-hydro-mechanical finite element model for freezing soils. *International Journal for Numerical and Analytical Methods in Geomechanics*, 37(18):3173–3193, 2013.

[134] L Luckner, M Th Van Genuchten, and DR Nielsen. A consistent set of parametric models for the two-phase flow of immiscible fluids in the subsurface. *Water Resources Research*, 25(10):2187–2193, 1989.

[135] Martin A Diaz Viera, Pratap Sahay, Manuel Coronado, and Arturo Ortiz Tapia. *Mathematical and numerical modeling in porous media: applications in geosciences*. CRC Press, 2012.

[136] VR Voller and CR Swaminathan. Eral source-based method for solidification phase change. *Numerical Heat Transfer, Part B Fundamentals*, 19(2):175–189, 1991.

Chapter 3

Thermal performance optimization of a bayonet tube heat exchanger

Contents

Preface (Linking Paragraph)

The freeze pipes are one of the most critical components of any artificial ground freezing (AGF) system, and they rule, as the primary heat exchangers, the AGF process. Therefore, it is proper to analyze their design, geometry, and operating parameters, which, in turn, should improve the overall performance of the AGF system. This chapter examines, at a mechanistic level, the performance of the freeze pipes. The outcomes of this chapter will be considered in the design of the experimental setup and in the framework of the mathematical models that will be illustrated in the next chapters. The below article has been published based on the discussion of this chapter:

Alzoubi, M. A. and Sasmito, A. P. (2017). *Thermal performance optimization of a bayonet tube heat exchanger*, Applied Thermal Engineering, 111:232-247.

Abstract

A bayonet tube heat exchanger is typically a pair of concentric tubes, the outer of which has a closed end that creates a clearance pass between the inner and annulus tube. This paper evaluates the impact of key parameters and operating conditions on the performance of a bayonet tube by utilizing computational fluid dynamic approach and Taguchi statistical method. A validated two-dimensional model, that considers conservation of mass, momentum and energy, was employed together with an L_{25} orthogonal array (OA) of Taguchi matrix of five factors and five level designs to determine the optimum combination of parameters as well as their interactions. The result indicates that pipe total length and length of clearance area play an important role in determining the bayonet tube performance in term of pressure drop and heat transfer. The optimum combination of design and operating parameters were obtained with the objective of maximizing the efficiency and performance of the bayonet tube.

3.1 Introduction

Bayonet tube heat exchanger consists of two concentric tubes. A working fluid, that could be gas, liquid or phase change material, is pumped either into the inner tube or in the annulus tube, based on the application. Ideally, the fluid is pumped into the inner tube which then flows back in the annulus tube through the closed-ended clearance. Heat transfer in the bayonet tube occurs mainly at two surfaces: (i) the surface between the inner and annular flow streams, and (ii) the surface between the annular flow stream and the surroundings [1, 2].

Bayonet tube has a simple design compared to the other types of heat exchangers. It needs only one penetration point in the working domain to fit in [3]. It can work in a highly corrosive environment and handle ultra-high temperature conditions, by using proper materials [4–6]. Furthermore, bayonet tube is preferably used in applications where the domain is accessed from one side only such as underground tunneling projects.

Bayonet tube heat exchanger has wide range of applications. For instance, it is used as a freezing pipe in underground mines [7, 8] and tunneling projects [9, 10] to create a frozen zone around the excavation area. It is also worked, in nuclear plants, as a steam generator in lead-cooled fast reactors [11–14], or as a direct heat exchanger for liquid metal cooled reactor, where it removes the decay heat of the primary coolant [15]. In other applications, bayonet tube is utilized as a molten-salt tubular-receiver in solar power tower [1], as a decomposition reactor in hydrogen production [16–19], or as an evaporator in an alkali metal thermal-toelectric converter [20]. Furthermore, bayonet tube is frequently employed for heat removal in fluidized bed coal combustors and gasifiers [21], and it also works as a heat exchanger for externally-fired combined cycle energy generation processes [5, 6]. In medicine, typically in cryosurgery surgeries, the cold tip of the bayonet tube acts as a freezer to destroy abnormal or diseased tissue in particular small spots [22]. The principle of the bayonet tube is also applied in salt-cavern leaching process for gas storage [23]. In spite of all these applications, there are no international standards to control the manufacturing of bayonet tube [24, 25], whence, more research and development is required in this area.

Different aspects related to bayonet tube design has been studied in several literature. One of these aspects is to minimize material stresses and tube failures (e.g. [6, 11, 24, 26–29]). Tube failure is mainly caused by: (i) the tolerance of temperature difference between the annulus tube and the surrounding [2], (ii) water interruption due to system shutdown [27], or (iii) scaling and fouling that occurs at the inlet face of the annulus tube [6, 27].

Another topic that has been concerned is enhancing the tube surfaces structure in order to imporve the overall heat transfer rate. For example, installing internal fins [4] or rings [30], at the outer wall of the inner tube, or external fins, at the outer wall of annulus tube [15], showed an increase in the heat transfer rate, compared to a bare bayonet tube. However, any surface enhancement should be applied in the annulus tube, where most of the heat transfer occurs [31, 32]. A special care, therefore, should be taken concerning the shape, spacing, and diameter of these surface-enhancements due to their direct influence on the pressure drop across bayonet tube.

Proceeding to another aspects, fluid flow orientation and bayonet tube installation have been discussed in detail in the literature. The installation of bayonet tube could be horizontal or vertical, depending on the accessibility of the domain and/or the operation requirements. However, vertical orientation is better for film boiling, at the same operation and design conditions, as comapred to horizontal installation [33]. The working fluid is, usually, injected into the inner tube. However, it could also be injected into the annulus tube, in particular cases, to fulfill process requirements [16]. A study performed by Kayansayan [34] observed that, at identical design conditions, an evaporator, with a flow enters the annulus tube, shows higher heat transfer rate, as compared to a flow enters the inner tube. In both scenarios, a counter flow of the annulus tube and the surrounding fluid provides higher heat transfer rate, as compared to a parallel flow [35–39]. In total, six different, possible flow configurations can be achieved between the primary (outside the tube) and the secondary flow (inside the tube) [40, 41].

The dominant heat transfer in a bayonet tube occurs in the form of conduction and convection. However, radiation heat transfer should be taken into consideration for ultra-high temperature applications, where primary and secondary fluids' temperatures are higher than 550 $°C$ [42–44]. In particular, heat loss due to radiation is highly significant when the fluid temperature is above 800 $°C$ [45].

Bayonet tube geometry is one of the most important aspects that should be addressed carefully during the design stage. To date, few studies in the literature discussed this topic in detail [46–53]. The focus of these literature was, mainly, on the effect of bayonet tube length, clearance length, and tube cross-sectional area ratios on pressure drop, and heat transfer rate. No work, however, had discussed the interaction between different parameters, and the impact of this interaction on the performance of the bayonet tube.

Design of experiments Taguchi method has in recent years become popular tool for engineering optimization due to its simplicity and robustness. It has the capability to determine the most significant factor influencing the performance of a bayonet tube, it is therefore of interest to apply this method to assess and evaluate the key parameters affecting the performance of such heat exchanger and determine the optimum conditions for its operation. Therefore, the aim of the study presented here is threefold: (i) to investigate, by means of a mathematical model, the impact of tube geometry, as well as operating parameters, on the performance of bayonet tube; (ii) to optimize bayonet performance based on pressure drop, heat transfer, entropy generation, and figure of merit; and (iii) to evaluate interaction between each design and operating factor with regards to the tube performance.

3.2 Model development

A cross section of a bare flat-end bayonet tube is considered in this study, as illustrated in Fig. 3.1. A general model would have to be 3D. In order to reduce the bayonet tube to a 2D geometry which describe a cross section, the model is limited to a tube in which the fluid flow and heat transfer in θ direction are small. Further, it is assumed that flow split in the clearance area is identical; thus the domain under consideration is set as a 2D axi-symmetry geometry. The annulus and inner tube materials are copper and acrylic, respectivly. Only heat transfer at the outer wall of annulus tube will be taken into account. Neglecting the heat transfer between the annulus flow stream and the inner flow stream is a reasonable approximation, provided that the thermal conductivity of acrylic (k=0.19 $[W/(m.K)]$ [54]) is three order of magnitude lower than the thermal conductivity of copper(k=385 $[W/(m.K)]$ [55]).

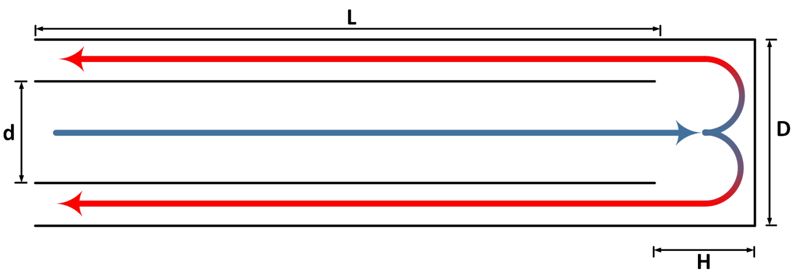

Figure 3.1 – Schematic diagram of a bayonet tube

3.2.1 Governing equations

In this paper, a two-dimensional cylindrical coordinates flow model comprising conservation of momentum, mass, and energy is solved. Detailed description of all parameters can be found in the Nomenclature. The governing equations are given as follows:
Conservation equation of mass:

$$\frac{\partial \rho}{\partial t} + \frac{1}{r}\frac{\partial}{\partial r}(r\rho u_r) + \frac{\partial}{\partial z}(\rho u_z) = 0 \tag{3.1}$$

Conservation equation of momentum:

r-direction:

$$\rho\frac{\partial u_r}{\partial t} + \rho u_r\frac{\partial u_r}{\partial r} + \rho u_z\frac{\partial u_r}{\partial z} = -\frac{\partial P}{\partial r} + \frac{1}{r}\frac{\partial}{\partial r}(r\tau_{rr}) + \frac{\partial}{\partial z}(\tau_{rz}) \tag{3.2}$$

z-direction:

$$\rho\frac{\partial u_z}{\partial t} + \rho u_r\frac{\partial u_z}{\partial r} + \rho u_z\frac{\partial u_z}{\partial z} = -\frac{\partial P}{\partial z} + \frac{1}{r}\frac{\partial}{\partial r}(r\tau_{zr}) + \frac{\partial}{\partial z}(\tau_{zz}) \tag{3.3}$$

where

$$\tau_{rr} = \mu\left(2\frac{\partial u_r}{\partial r} - \frac{2}{3}\left[\frac{1}{r}\frac{\partial}{\partial r}(ru_r) + \frac{\partial u_z}{\partial z}\right]\right) \tag{3.4}$$

and

$$\tau_{zz} = \mu\left(2\frac{\partial u_z}{\partial z} - \frac{2}{3}\left[\frac{1}{r}\frac{\partial}{\partial r}(ru_r) + \frac{\partial u_z}{\partial z}\right]\right) \tag{3.5}$$

and

$$\tau_{rz} = \tau_{zr} = \mu\left(\frac{\partial u_z}{\partial r} + \frac{\partial u_r}{\partial z}\right) \tag{3.6}$$

Conservation equation of thermal energy:

$$\rho\frac{\partial}{\partial t}(C_pT) + \rho u_r\frac{\partial}{\partial r}(C_pT) + \rho u_z\frac{\partial}{\partial z}(C_pT) = \frac{1}{r}\frac{\partial}{\partial r}\left(rk\frac{\partial T}{\partial r}\right) + \frac{\partial}{\partial z}\left(k\frac{\partial T}{\partial z}\right) \tag{3.7}$$

3.2.2 Constitutive relations

Gas.—A dry air, with thermophysical properties evaluated based on real gas model, for more accurate results, is used as working fluid in this study. The equation of state is explicit in the non-dimensional Helmholtz energy [56]:

$$\alpha\left(\delta,\theta\right)=\frac{a\left(\rho,T\right)}{RT}=\alpha^{0}\left(\delta,\theta\right)+\alpha^{r}\left(\delta,\theta\right) \tag{3.8}$$

where a is the molar Helmholtz energy, R is the universal gas constant, α is the reduced Helmholtz energy, α^0 is the ideal gas contribution to the Helmholtz energy, α^r is the residual contribution to the Helmholtz energy, $\delta = \rho/\rho_c$ is the reduced density, ρ_c is the critical density, $\theta = T_c/T$ is the reduced temperature, and T_c is the critical temperature. The constitutive relations of the working fluid are described in the Appendix.

Heat Transfer.—For a typical circular tube, the definition of Nusselt number is written as

$$\overline{Nu}_p=\frac{qL_c}{Ak\Delta T} \tag{3.9}$$

where q is the averaged heat flux across the outer surface of the tube, $A = \pi DL$ is the surface area of the tube, and L_c is the characteristic length which is the tube diameter in this case. The formula for concentric tubes, however, differs from the single tube formula. The heat transfer occurs only at the outer wall of the annulus tube, whence Nusselt number is given by the diameter of annulus tube as

$$\overline{Nu}=\frac{q\left(D-d_o\right)}{\pi DLk\left(T_w-\overline{T}_f\right)} \tag{3.10}$$

where $\overline{Nu}$ is an average effective Nusselt number, D is the inner diameter of the annulus tube, d_o is the outer diameter of inner tube, T_w is wall temperature, and $\overline{T}_f = (T_i + T_o)/2$ is the average fluid temperature between inlet T_i and outlet T_o.

Flow Characteristics.—The evaluation of the pressure drop across the bayonet tube is presented as an Euler number or Cavitation number. Following Minhas et al.'s study [48], Euler number and Reynolds number are defined as

$$Eu=\frac{\Delta P_T}{\frac{1}{2}\rho\left(u_c\right)^2} \tag{3.11}$$

and

$$Re_e=\frac{4\dot{m}}{\mu\pi\left(D+d_o\right)}\left(\frac{D}{d_i}\right)=Re_a\left(\frac{D}{d_i}\right) \tag{3.12}$$

where u_c denotes the characteristic or average velocity

$$u_c=\frac{4\dot{m}}{\rho\pi\left(D^2-d_o^2\right)}\left(\frac{D}{d_i}\right)^2=u_a\left(\frac{D}{d_i}\right)^2 \tag{3.13}$$

where d_i is the inner tube inlet diameter, $\dot{m}$ is mass flow rate, and u_a is the velocity in the annulus tube. Applying energy balance between the tube inlet and outlet, ΔP_T can be estimated as

$$\Delta P_T = \Delta P_s + \frac{1}{2}\rho u_i^2 \left[1 - \left(\frac{F_i}{F_a}\right)^2\right] \tag{3.14}$$

where ΔP_s is the static pressure drop across the tube, u_i is the velocity in the inner tube, and F_i and F_a are the inner and annulus tubes cross sectional area, respectively.

$$F_i = \frac{\pi}{4} d_i^2 \tag{3.15}$$

and

$$F_a = \frac{\pi}{4}\left(D^2 - d_o^2\right) \tag{3.16}$$

Entropy Generation.—Heat transfer, across finite temperature difference, and pressure drop, due to friction inside the concentric tubes, are the main two sources of exergy destruction or entropy generation in bayonet tube, which yields the following expression for 2D cylindrical coordinates [57]

$$\dot{S}'''_{gen} = \underbrace{\frac{k}{T^2}\left[\left(\frac{\partial T}{\partial r}\right)^2 + \left(\frac{\partial T}{\partial z}\right)^2\right]}_{\dot{S}'''_{gen} \text{ due to temperature difference}} + \underbrace{\frac{\mu}{T}\left\{2\left[\left(\frac{\partial u_r}{\partial r}\right)^2 + \left(\frac{\partial u_z}{\partial z}\right)^2\right] + \left(\frac{\partial u_z}{\partial r} + \frac{\partial u_r}{\partial z}\right)^2\right\}}_{\dot{S}'''_{gen} \text{ due to friction}} \tag{3.17}$$

Figure of Merit (FoM).—This term is a quantity that is used to characterize the heat transfer performance of a bayonet tube with respect to its pumping power, and is written as [58]

$$FoM = \frac{\dot{Q}_{total}}{P_{pump}} \tag{3.18}$$

where $\dot{Q}_{total}$ is the total heat rate

$$\dot{Q}_{total} = \dot{m} C_p \left(T_{out} - T_{in}\right) \tag{3.19}$$

and P_{pump} is the pumping power required to drive the air flow through the bayonet tube

$$P_{pump} = \frac{1}{\eta}\dot{V}\Delta P_t \tag{3.20}$$

where η is the pump efficiency (assumed to be 75%), $\dot{V}$ is the volumetric flow rate, and ΔP_t is the pressure drop across bayonet tube.

3.2.3 Boundary and initial conditions

The boundary conditions of bayonet tube simulation are stated as follow:

Initial Condition.—Initial temperature and initial velocity at $t = 0$.

$$T = T_{init}, \mathbf{u} = \mathbf{u}_{init} \tag{3.21}$$

Tube Inlet.—Dirichlet boundary conditions for mass flow rate and inlet temperature.

$$\dot{m} = \dot{m}_{in}, T = T_{in} \tag{3.22}$$

Wall: Annulus Tube.—Dirichlet boundary conditions for temperature and no slip conditions.

$$T = T_{wall}, \mathbf{u} = 0 \tag{3.23}$$

Wall: Inner Tube.—Dirichlet boundary conditions for heat flux and no slip conditions.

$$q = 0, \mathbf{u} = 0 \tag{3.24}$$

Tube Outlet.—Dirichlet boundary condition for pressure, and Neumann boundary condition for temperature.

$$P = P_{out}, \mathbf{n} \cdot \nabla T = 0 \tag{3.25}$$

3.2.4 Taguchi statistical method

Taguchi statistical method is an experimental design methodology developed by Genichi Taguchi particularly to improve the quality of manufactured products. More recently, this technique has been adapted as an engineering tool for design development and experiment optimization. It is mainly used to investigate the effect of each parameter on the mean response independently. It also investigates and models the interaction between different parameters to show the influence of each parameter on the mean response for other parameters at different levels [59]. In this study, five key parameters determining the performance of bayonet tube are evaluated; those parameters are wall temperature (T_{wall}), effective Reynolds number (Re_e), tube length to annulus diameter ratio (L/D), cap clearance to annulus diameter ratio (H/D), and inner tube to annulus tube area ratio (F_i/F_a). Five values are evaluated for each parameter, as presented in Table 3.1. With this variations, more than thousand simulations are needed should each possible combination is evaluated. Therefore, to minimize the required computational time and resources, an L25 orthogonal array (OA), Using Minitab 17 software, was employed in the experiment matrix, as shown in Table 3.2.

For optimum design of the bayonet tube, Nusselt number ($\overline{Nu}$) and figure of merit (FoM) should be maximized, whence the signal-to-noise (S/N) ratio is evaluated based on larger-the-better [59]:

$$S/N_{LTB} = -10\log_{10}\left[\frac{1}{n}\sum_{i=1}^{n}\left(\frac{1}{y_i^2}\right)\right] \tag{3.26}$$

On the other contrary, the pressure drop, across the bayonet tube, and total entropy generation should be at the minimum to achieve the optimum design. Therefore, the signal-to-noise (S/N) ratio is evaluated based on smaller-the-better [59]:

$$S/N_{STB} = -10\log_{10}\left[\frac{1}{n}\sum_{i=1}^{n}\left(y_i^2\right)\right] \tag{3.27}$$

Table 3.1: Combination of Taquchi parameters and levels

	Parameter	Level 1	Level 2	Level 3	Level 4	Level 5
A	Wall Temperature [$°C$]	40	50	60	70	80
B	Reynolds number [—]	100	500	1000	1500	2000
C	L/D [m/m]	10	20	30	40	50
D	H/D [m/m]	0.6	0.8	1.0	1.5	2.0
E	F_i/F_a [m^2/m^2]	0.2	0.3	0.474	0.7	1.0

3.3 Numerical methodology

The mathematical model for the bayonet tube is implemented in the commercial fluid dynamics software Fluent 16.1 along with a user-defind function (UDF). The latter is used to solve for entropy generation equation (see Equation (3.17)). The computational domain (see Fig. 3.1) is created, meshed, and resolved, with a direct numerical simulation (DNS), using a finite volume method software - ANSYS package 16.1. The kolmogorov length scale for all cases has been calculated based on the formula $\eta = L/Re^{3/4}$, where η is kolmogorov length scale, L is the characteristic length (i.e. tube length), and Re is the Reynolds number. The minimum cell length values, in all cases, are kept below kolmogorov length scale, as summarized in Table 3.3, in order to have a refined mesh, that is sufficient enough, to capture such small length scales; η ranges from 8.6×10^{-4} to 0.0043 [m].

Table 3.2: Orthogonal array for L_{25} with five parameters and five levels experimental design

Simulation No.	T_{wall} [$^{\circ}C$]	Re_e [—]	L/D [m/m]	H/D [m/m]	F_i/F_a [m^2/m^2]
1		100	10	0.6	0.2
2		500	20	0.8	0.3
3	40	1000	30	1.0	0.474
4		1500	40	1.5	0.7
5		2000	50	2.0	1.0
6		100	20	1.0	0.7
7		500	30	1.5	1.0
8	50	1000	40	2.0	0.2
9		1500	50	0.6	0.3
10		2000	10	0.8	0.474
11		100	30	2.0	0.3
12		500	40	0.6	0.474
13	60	1000	50	0.8	0.7
14		1500	10	1.0	1.0
15		2000	20	1.5	0.2
16		100	40	0.8	1.0
17		500	50	1.0	0.2
18	70	1000	10	1.5	0.3
19		1500	20	2.0	0.474
20		2000	30	0.6	0.7
21		100	50	1.5	0.474
22		500	10	2.0	0.7
23	80	1000	20	0.6	1.0
24		1500	30	0.8	0.2
25		2000	40	1.0	0.3

The numerical model is solved with the Semi-Implicit Pressure-Linked Equation (SIMPLE) algorithm; second-order upwind discretization for the conservation of momentum and energy; first-order upwind discretization for the transient formulation; all the relative residuals of 10^{-6}; and the built-in National Institute of Standards and Technology (NIST) formulation, based on Equation (3.8), for fluid thermo-physical properties.

Table 3.3: kolmogorov length sale and minimum cell length values at the minimum and maximum Re and L combinations

Re	L $[m]$	η $[m]$	l_0 $[m]$
100	0.257	8.1×10^{-3}	2.8×10^{-5}
2000	0.257	8.6×10^{-4}	8.1×10^{-6}
100	1.285	4.1×10^{-2}	5.7×10^{-4}
2000	1.285	4.3×10^{-3}	5.7×10^{-5}

3.4 Results and discussion

3.4.1 Validation

The model used here is validated with experimental data from Minhas et al [48]. In their experiment, a 2.57 [cm] copper tube with a length varying from 25.7 to 102.8 [cm] was used as an outer pipe of the bayonet tube. On the other hand, acrylic tubes with different diameters, that satisfy area ratio between 0.2 and 1.0, were used as inner tubes. The pressure and flow rate of the air, that came directly from a settling chamber into the inner tube, were controlled and regulated by a control valve and a flow regulator, respectively. The exhaust air, however, was discharged into the ambient at atmospheric pressure. In addition, the pressure and temperature of the air were measured at the inlet and outlet of the apparatus using a pressure gage, differential pressure transducer and thermocouples, respectively.

Minhas et al. [48] performed, also, a numerical model and validated it with their experimental data. In that model, constant fluid thermophysical properties, that calculated at fluid average temperature ($T_f = (T_i + T_o)/2$), were used. Furthermore, the computational domain was divided into 11 zones; the Reynolds-averaged Navier-Stokes (RANS) turbulent flow model was used only at the impingement region. However, the justification behind the definition of turbulent region boundaries was not provided by the authors. The model derived here, on the other hand, uses real gas model along with direct numerical simulation (DNS), with a minimum cell length lower than the kolmogorov length scale η, in order to capture all possible turbulence in the tube. Good agreement between experiments and the model was observed, as compared to Minhas et al.'s numerical model, which can be discerned from Fig. 3.2.

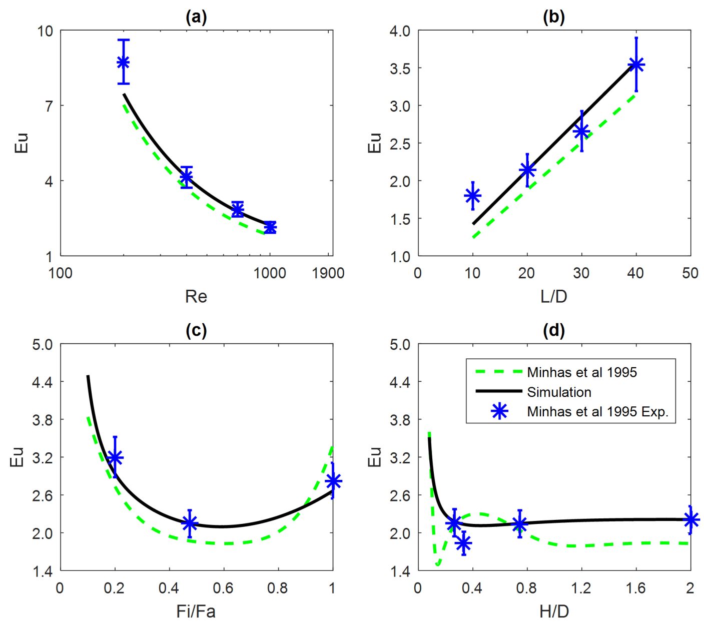

Figure 3.2 – Numerical model validation against Minhas et al [48] experimental and numerical; (a) the influence of Reynolds number; (b) the effect of length to diameter ratio; (c) the impact of clearance to diameter ratio; and (d) the effect of surface area ratio

3.4.2 Flow characteristics

One of the main factors that determines the performance of a bayonet tube is the pressure drop. The flow stream velocity and fluid density are the main parameters affecting ΔP, as stated in Equation (3.11). Therefore, an increase in Reynolds number and tube length is mirrored by an increase in the pressure drop across the tube. Fig. 3.3-a depicts the influence of different parameters on the pressure drop. Clearly, Reynolds number has the highest influence on ΔP due to the exponential proportion between the pressure drop and stream velocity ($\Delta P \propto u^2$). This influence becomes more prominent between Re_e=1500 and Re_e=2000 where more turbulence is to be expected in the clearance area and annulus tube. Furthermore, the tube length has a proportional relation with pressure drop due to the increase in Darcy friction loss.

$$\Delta P = f_D \frac{L}{D} \frac{\rho u^2}{2} \tag{3.28}$$

In contrast to Reynolds number and tube length, an increase in wall temperature leads to a decrease in the pressure drop, due to the reduction in air density and wall friction. On the other contrary, clearance length to diameter ratio (H/D) has a minor impact on the pressure drop as compared to Reynolds number and tube length. Nonetheless, it is of interest to see how (H/D) affect the ΔP. At the shortest distance $(H/D = 0.6)$, a partially developed vortex is created via the reflected flow stream in the clearance area. As the clearance distance increases $(H/D = 0.8)$, the vortex becomes fully developed, which, in turn, leads to a decrease in the pressure drop, as shown in Figures 3.4-b and 3.3-a. At $H/D = 1.0$, a second, partially-developed, due to the obstruction of the inner wall, vortex, that contributes to a higher pressure drop, is created, as inferred in Fig. 3.4-c. Clearly, the increase of the clearance distance has an impact on the pressure drop, provided that more vortices are developed with higher H/D ratio, thus a higher pressure drop is achieved with higher H/D (i.e. $H/D = 1.5$ and 2.0). In addition to the previous parameters, the area ratio (F_i/F_a) also affects the pressure drop, since the air flowing through the clearance area will encounter a resistance while passing into the annulus tube. At low area ratio (0.2 and 0.3), the pressure drop increase, slowly, due to the sudden increase in the cross-sectional area between the inner and annulus pipes. However, the influence of this increase is minimized at $(F_i/F_a = 0.474)$. As the area ratio increases $(F_i/F_a = 0.7$ and $1.0)$, the pressure drop steeply increases due to the significant reduction in the cross-sectional area of the annulus tube.

The signal to noise (S/N) ratio for each parameter is presented in Fig. 3.3-b. As can be seen, Reynolds number and tube length have the most significant effect on the pressure drop. However, as discussed earlier, the relation between the fluid stream velocity, pipe length, and the pressure drop is governed by Equation (3.28) where $(\Delta P \propto u^2)$ and $(\Delta P \propto L)$. Therefore, the influence of varying the stream velocity on the pressure drop is higher than the influence of increasing the pipe length. Wall temperature, on contrary, shows no significant effect on the pressure drop, due to the fact that the temperature difference, in this particular case, between the tube wall and the fluid stream ranges from 20 $[^\circ C]$ and 60 $[^\circ C]$, therefore the density changes is insignificant. Further, the influence of the clearance length to diameter ratio (H/D) and area ratio (F_i/F_a) on the pressure drop is marginal, as compared to the contribution of the fluid stream velocity and friction loss along the tube wall. However, the mean of S/N ratio drastically dropped once $F_i/F_a > 0.474$, where the reduction of the cross-sectional area of the annulus tube is high enough to contribute to ΔP.

Fig. 3.5 shows interaction plot for each factor for which parallel plot denotes no interaction while crossing indicates significant interaction. Here, several features are apparent; foremost among them is the interaction of Reynolds number which shows the most significant influence as compared to other factors, followed by L/D ratio. Overall, other factors; wall temperature, H/D, and area ratio, have marginals influence at low Re_e and L/D. However, the interaction becomes more apparent at higher Re_e and L/D.

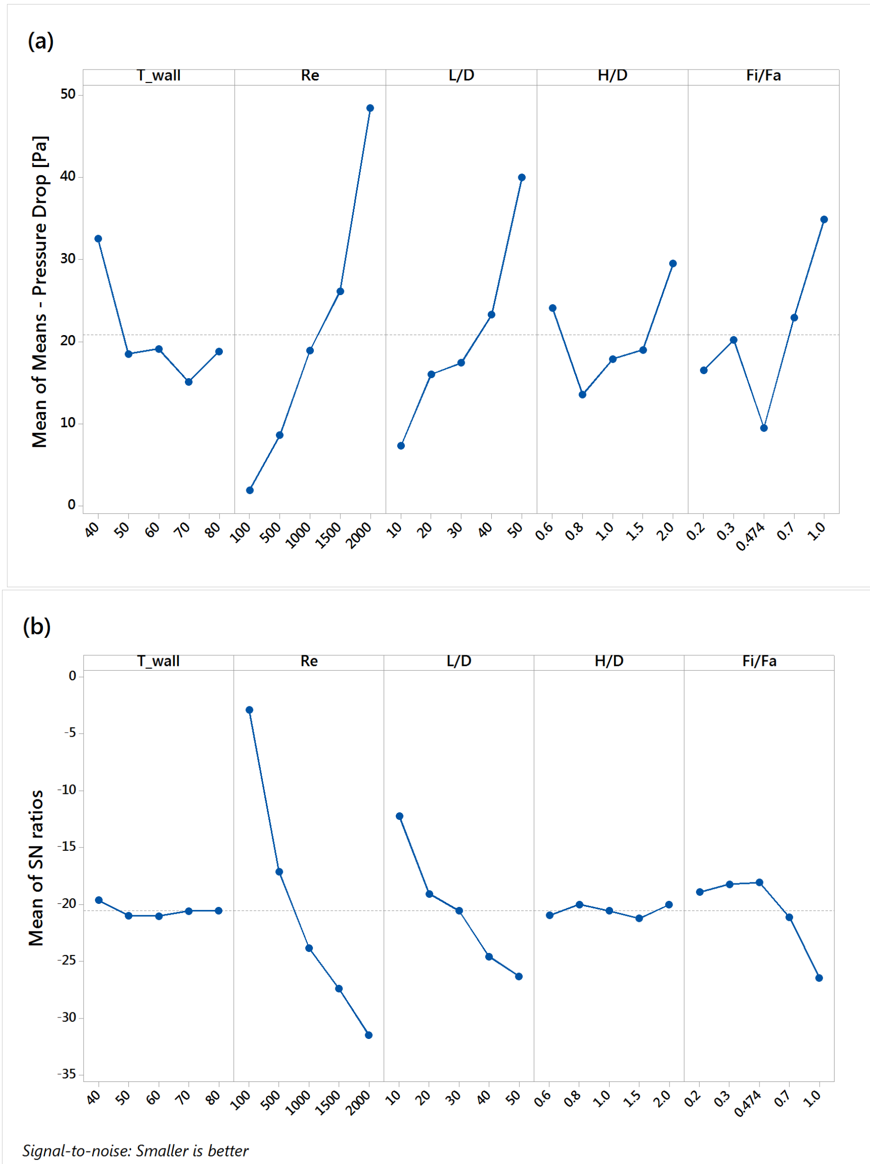

Figure 3.3 – Response of (a) mean and (b) S/N ratio (smaller is better) of various geometries and operating parameters with respect to pressure loss

3.4.3 Heat transfer characteristics

Another factor that rules the bayonet tube performance is the heat transfer presented by the averaged Nusselt number ($\overline{Nu}$). As shown in Fig. 3.7-a, The tube length (L/D) and the Reynolds number (Re) show the highest impact on the averaged Nusselt number, as compared to other parameters. This can be adequately explained by the fact that Nusselt number, for forced convection, is a function of Reynolds number $Nu = f(Re, Pr)$. Further, ($\overline{Nu} \propto q$); $q = h\Delta T$, where h is the convection heat transfer coefficient, which typically, increases with increasing (Re). The influence of the tube length, on the other hand, is

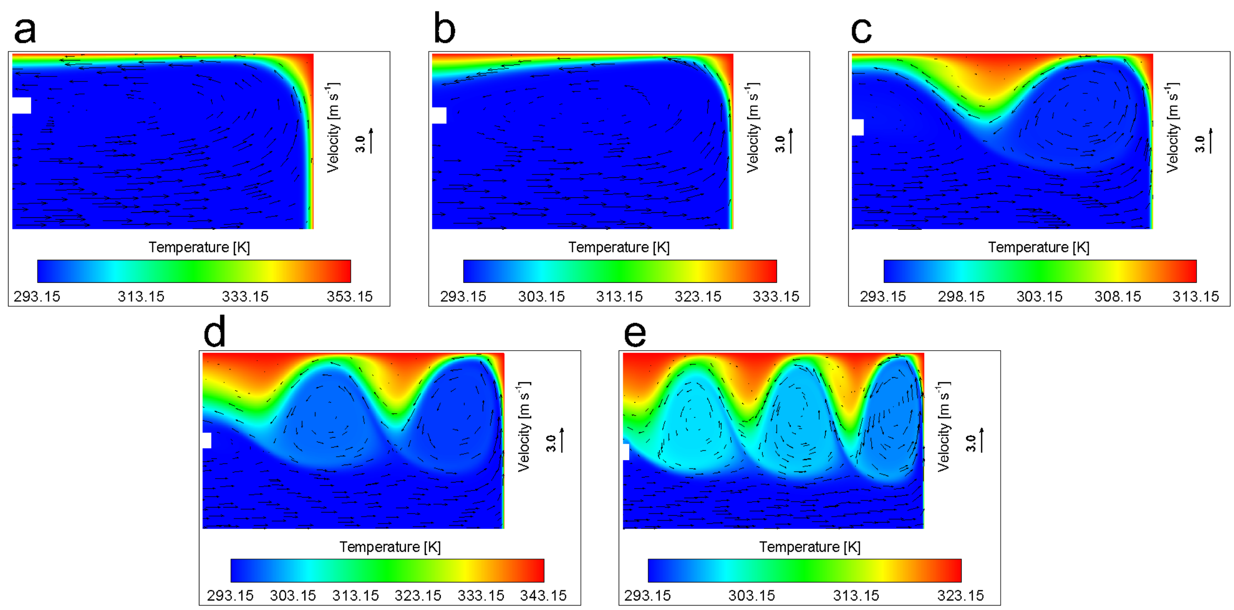

Figure 3.4 – Local distributions of temperature and velocity vector at the clearance are for various H/D ratio: (a) 0.6; (b) 0.8; (c) 1.0; (d) 1.5; and (e) 2.0

somewhat higher than Reynolds number, which can be attributed to the definition of $(\overline{Nu})$ as in Equation(3.9). Basically, there are two main regions contribute to the $(\overline{Nu})$: the clearance area and the annulus tube. The highest *local* Nu is achieved at the clearance region where the air stream impinges to the wall, changes its direction, and creates turbulence flow. Recalling the influence of (H/D) ratio on vortices formation in the previous section, Fig. 3.4 depicts stagnant regions, in the clearance area, due to vortices creation. The low-velocity regions is expected to decrease the convective heat transfer coefficient, thus lowering the Nusselt number, as illustrated in Fig. 3.6. The local Nu, on the other contrary, is drastically decreased when the fluid stream becomes laminar; at the entrance of the annulus tube. Overall, the contribution of the local Nu in the annulus tube increases with increasing L/D ratio, which is mirrored by the decrease in the $(\overline{Nu})$.

Fig. 3.7-b presents the signal to noise (S/N) ratio for each parameter to the averaged Nusselt number. For instance, Reynolds number plays key role for high $(\overline{Nu})$; typically, the higher the Re, the higher the $(\overline{Nu})$. This is due to the fact that Nusselt number is directly proportional to Reynolds number. However, a steep increase in the $(\overline{Nu})$ is observed between Re 100 and 500, as can be inferred from Fig. 3.7-b. This is to be predicted, because an increase in Reynolds number, in the clearance area, is mirrored by an increase in the turbulence, thus contributing to a higher $(\overline{Nu})$. Similarly, lower (L/D) ratio gives rise to the $(\overline{Nu})$ due to the dominant contribution of the local Nu in the clearance area, as compared to

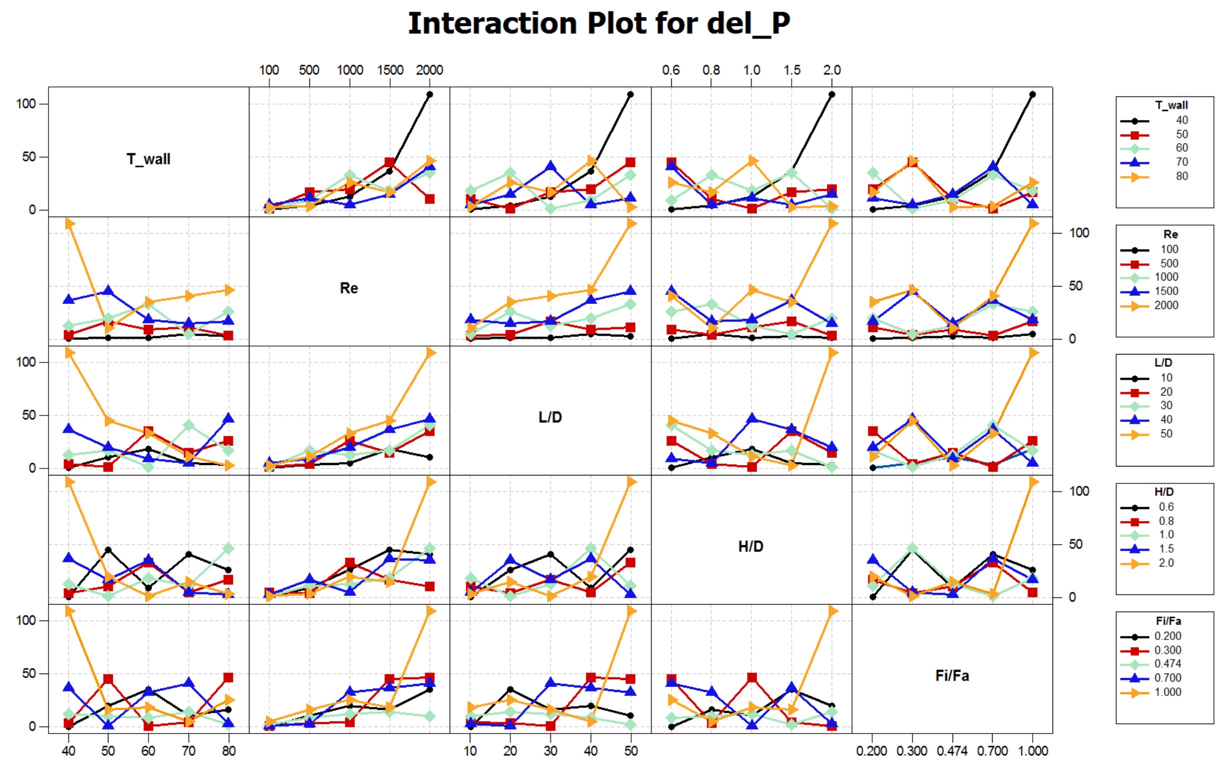

Figure 3.5 – The interactions of various parameters with respect to pressure loss

the local Nu in the annulus tube. While other factors, i.e. wall temperature, (H/D) ratio, and area ratio have marginal effect to the $(\overline{Nu})$.

Looking at the interaction of each factor in Fig. 3.8, it is found that significant interaction is obtained between wall temperature and (H/D) ratio, wall temperature and area ratio, and (H/D) ratio and area ratio. It is also noted, however, that these parameters interact significantly only at a higher Reynolds number and low (L/D) ratio.

3.4.4 Entropy generation characteristics

Another point of interest is to evaluate the impact of the total entropy generation (S_g''') on the thermal performance. As was mentioned in the Model Development section, the main losses, in any heat exchanger, are, usually, characterized by: (i) heat transfer across *temperature difference* and (ii) pressure drop due to *friction*. In essence, these two terms are quantified by the total entropy generation. While discussing these, it is instructive to recall the structure of the total entropy generation formulation, defined by Equation (3.17), to see the influence

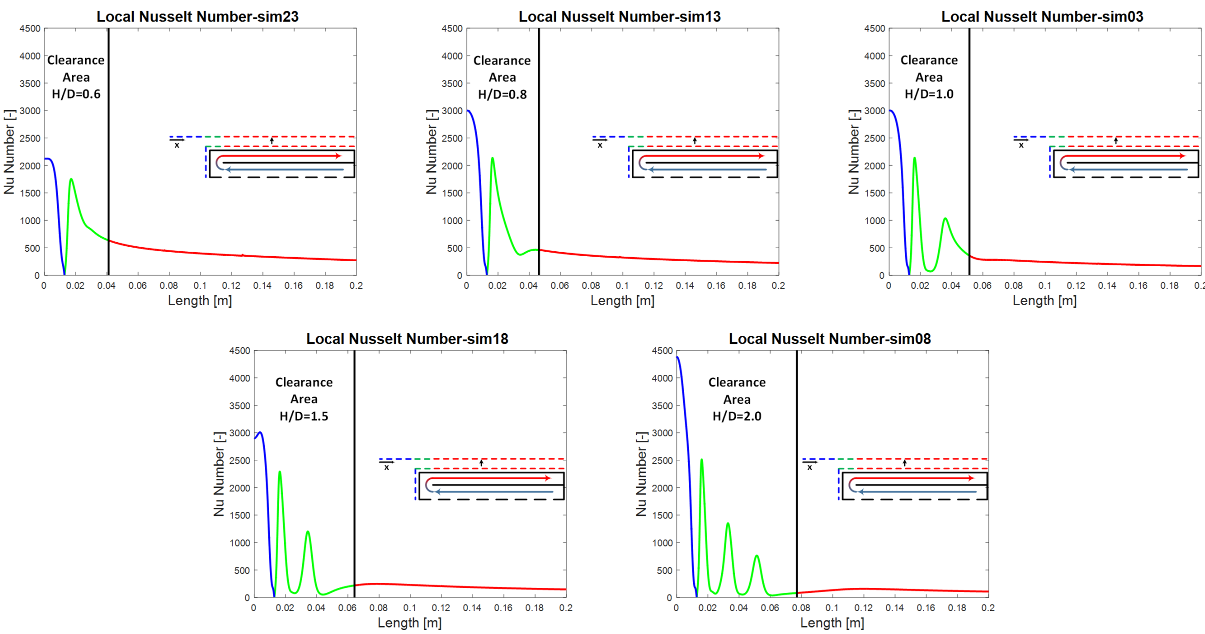

Figure 3.6 – Local distribution of Nu number along bayonet tube walls: Impingement wall (blue line), clearance wall (green line), and annulus wall (red line) for various H/D ratios

of different parameters on (S_g'''). The first term in the equation accounts for temperature difference and the second term describes the friction losses. Intuitively, one would expect that wall temperature and Reynolds number have a higher impact on (S_g'''), as compared to the other factors. This is indeed the case, as can be inferred from Fig. 3.9-a, which depicts the impact of different factors on (S_g'''). As wall temperature increases, a higher heat transfer is expected, which in turn leads to an increase in the entropy generation. Similarly, when Re increases, the chances for more turbulence in the clearance area increases, where the highest S_g''', due to high heat transfer and friction loss, is observed, as depicted in Fig. 3.10.

Looking further to the sensitivity response of S/N ratio for each parameter in Fig. 3.9-b, it reveals that Re is the most significant parameter influencing the entropy generation, followed by wall temperature. Lower Reynolds number and wall temperature lead to a lower (S_g'''), due to the fact that at lower Re and T_w, lower heat transfer losses is observed in the tube, which, in turns, leads to a lower total entropy generation. On the other contrary, area ratio has less significant effect; whereas L/D and H/D ratios have the least significant effect on the total entropy generation. This is due to the fact that, the contribution of the friction losses is lower than the heat transfer contribution by two to three order-of-magnitude.

Proceeding to the interaction of each factor, Fig. 3.11 demonstrates the interaction of each factor to the total (S_g'''). Significant interaction is shown between the different parameters. It is also noted that the influence of L/D ,H/D, and area ratios, at low wall

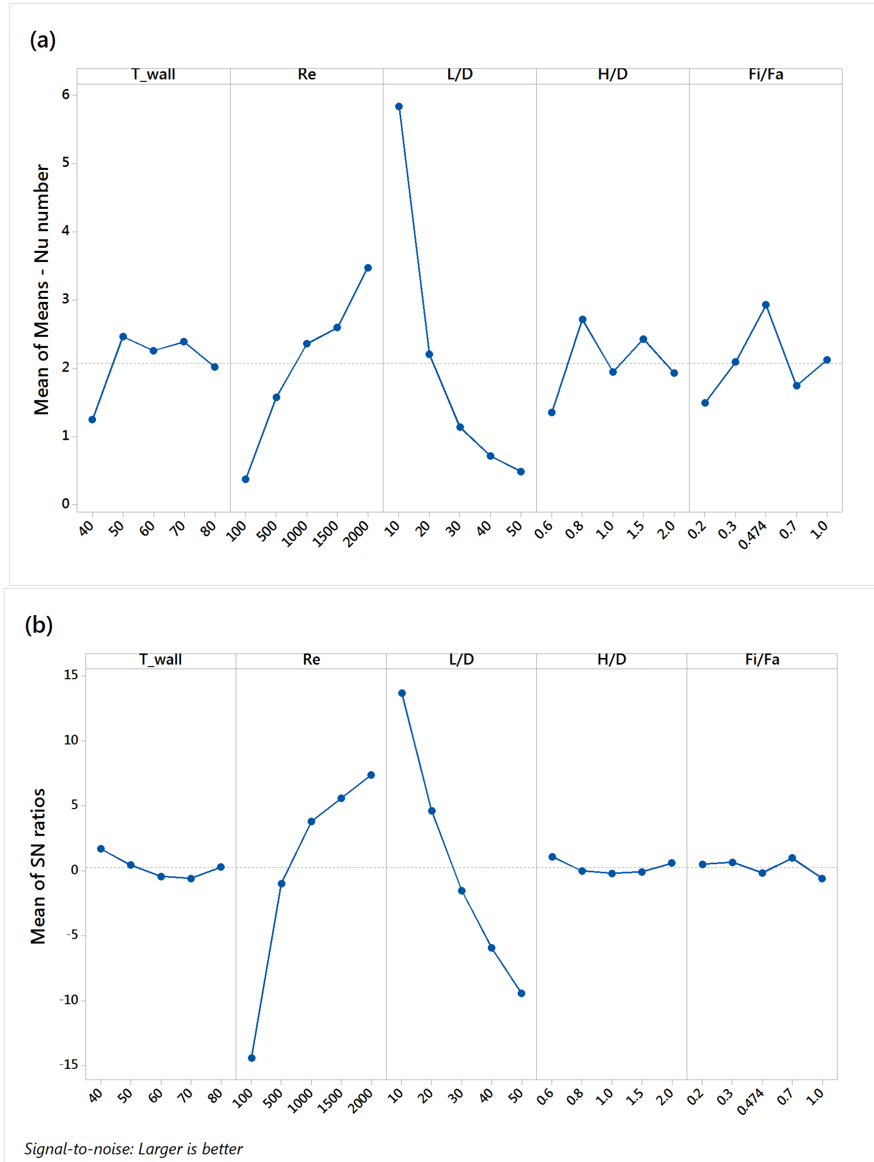

Figure 3.7 – Response of (a) mean and (b) S/N ratio (larger is better) of various geometries and operating parameters with respect to Nusselt number

temperature and Reynolds number, is marginal, since the latter two parameters have the highest impact on the total (S_g''').

Before addressing the final factor in this study, let's discuss the effect of the length of the clearance area (H/D ratio) on the entropy generation. The H/D ratio has a marginal influence on the total S_g''' as compared to the wall temperature and Re. However, the local entropy generation at the clearance area changes drastically at different H/D ratio. This can be expected, due to the fact that, most of the turbulence and heat transfer occurs in this region. Consequently, it is a nontrivial task to determine the influence of the H/D ratio

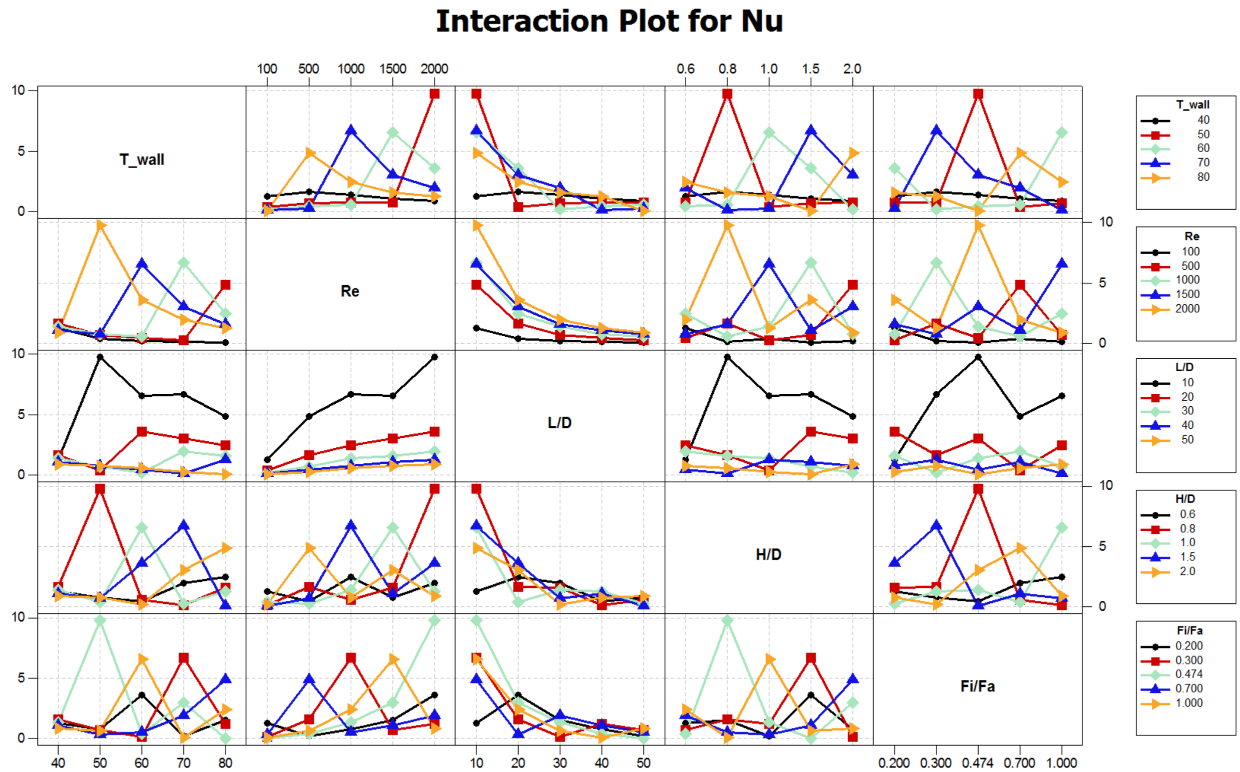

Figure 3.8 – The interactions of various parameters with respect to Nusselt number

on the local entropy generation. It is useful to recall previous discussions, in particular: the impact of H/D ratio and vortices generation on pressure drop, Nusselt number, and Reynolds number, to see how H/D ratio influence the local S_g'''. The conclusion from the vortices creation analysis was that: the more the vortices, the more the turbulence, friction loss, and stagnant regions. Returning to Fig. 3.6, the local Nusselt number is directly linked to the flow behaviour and wall temperature, which in turn affects the behaviour of the dominant part of S_g'''; the first term of the right-hand-side of Equation (3.17), as discerned from Fig. 3.10-i. Furthermore, the turbulence and friction losses, in the clearance area, create zones with high entropy generation, as can be inferred from Fig. 3.10-ii. Nonetheless, the contribution of this term is marginal as compared to the entropy generation due to heat transfer.

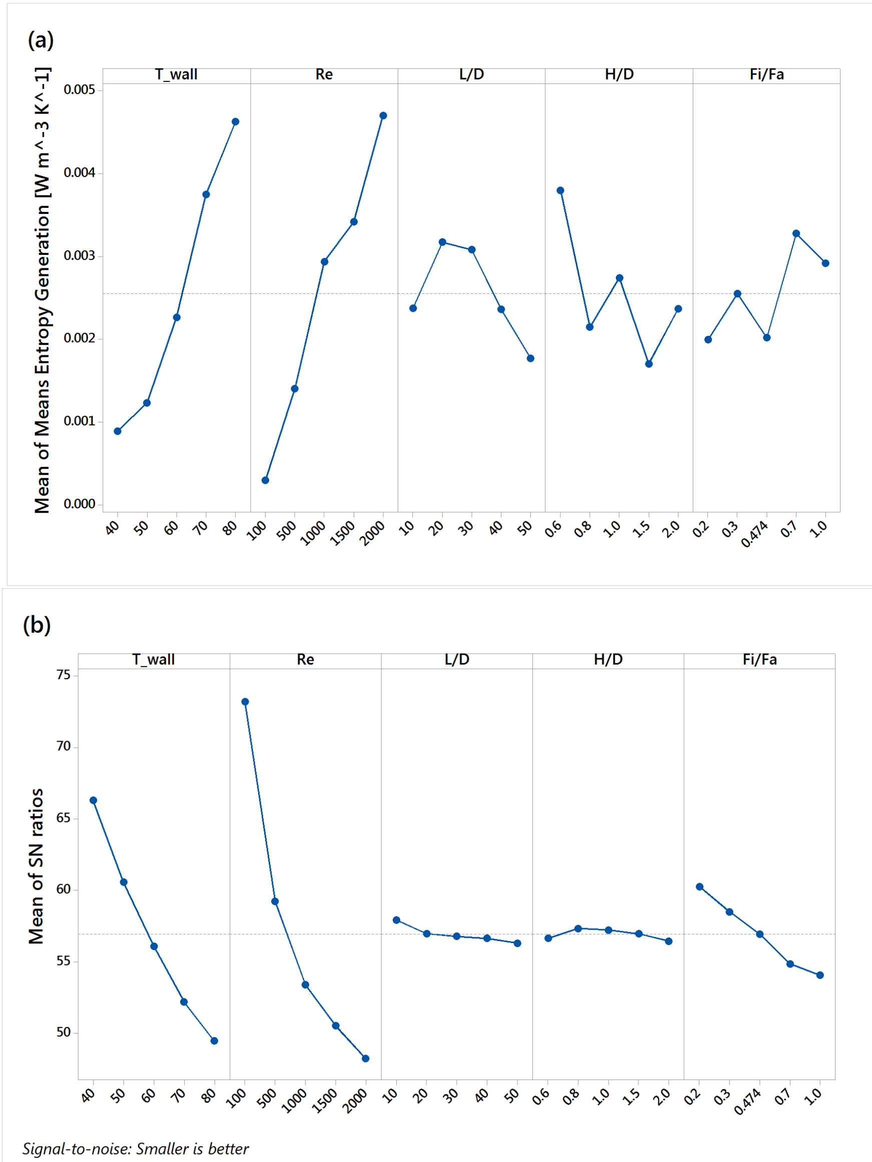

Figure 3.9 – Response of (a) mean and (b) S/N ratio (smaller is better) of various geometries and operating parameters with respect to entropy generation

3.4.5 Figure of Merit characteristics

Another factor that influence the performance of a bayonet tube is Figure of Merit (FoM), which as prescribed in Equation (3.18), has a linear proportion to Q_{total} and P_{pump}. Reynolds number, in contrast to other factors, particularly wall temperature, has a major impact on the FoM, as depicted in Fig. 3.12-a. Recalling the influence of Reynolds number on pressure drop and heat transfer from the previous sections, Q_{total} and P_{pump} are linearly proportion to Re. However, the influence of Reynolds number on the P_{pump} is higher, since the latter is, as stated in Equation (3.20), a combination of volumetric flow rate $(\dot{V})$ and pressure drop.

Therefore, the higher the Reynolds number, the lower the FoM.

The signal to noise (S/N) ratio for each parameter is presented in Fig. 3.12-b. As can be seen, lower Re and L/D ratio is more desirable. High Reynolds number and pipe length impose higher pressure drop, which is inversely proportion to the FoM. On the other hand, high wall temperature is beneficial to the FoM. The reason for the latter is affirmative, higher wall temperature, with a constant fluid temperature, provides more heat transfer to the flow, which increases the Q_{total} and therefore the FoM.

Turning our attention to the interaction of each factor, Fig. 3.13 depicts a significant interaction between all parameters at different levels. However, the influence of these parameters becomes marginal at higher Reynolds number, since the latter has the highest impact on the FoM.

3.4.6 Optimization analysis

Thus far, the Taguchi S/N results, the impact of parameters, and interaction between them have been discussed. Now, a further look, to the optimum combination of design and operating parameters, is required for optimum performance of bayonet tube. Fig. 3.14 and Table 3.4 depict the optimum performance with respect to four different factors. Each optimum design point, depend on the aim of the optimization analysis, requires different combination of design and operating parameters, as explained below:

Pressure Drop.—One needs to optimize the design based on pressure drop in application where pumping power/production cost is of paramount important,e.g. mass production or cheap product.

Nusselt Number.—If the quality of the final product is the ultimate goal of the process, and it solely depends on the quality and quantity of heat transfer, Nusselt number should be the objective function.

Total Entropy Generation.—When the total thermodynamic efficiency of the process is important, one needs to optimize the design based on entropy generation minimization.

Figure of Merit (FoM).—When one needs to balance between heat transfer performance and pumping power (cost), the design can be optimized based on figure of merit. This term is only summarized in Table 3.4. It is noted that for optimum pressure drop the best combination of design and operating parameters are: 40 $[°C]$ wall temperature, 100 Reynolds number, 10 L/D ratio, 0.8 H/D ratio, and 0.474 area ratio. The Nusselt number, however, is very low, which can be expected due to low Reynolds number and temperature difference, between the wall and the flow stream, as inferred from Fig. 3.14-*a*&*d*. Further, the best combination of parameters for optimum Nusselt number are: 40 $[°C]$ wall temperature, 2000

Reynolds number, 10 L/D ratio, 0.6 H/D ratio, and 0.7 area ratio. However, the pressure drop, as compared to other optimized cases, is at the maximum value of 3.11 [Pa]. This can be adequately explained as higher Reynolds number gives rise to a higher pressure drop, along bayonet tube, as depicted in Fig. 3.14-b&e. In addition, the optimum total entropy generation, which is discerned from Fig. 3.14-c&f, is achieved with parameters similar to optimum Nusselt number, but with decreasing area ratio into 0.2. It is notable that pressure drop and Nusselt number are as low as 0.42 [Pa] and 1.3, respectively. This is expected, due to the mechanism of entropy generation formulation, as expressed by Equation (3.17). At the optimum Figure of Merit, the best combination of design and operating parameters are: 80 [$°C$] wall temperature, 100 Reynolds number, 10 L/D ratio, 2.0 H/D ratio, and 0.3 area ratio. Clearly, a compromised performance is achieved with these parameters, where pressure drop is 0.38 [Pa], as compared to a ΔP=0.33 [Pa] in the optimum pressure case, while Nusselt number is 3.2, as compared to a Nu=5.0 in the optimum Nusselt number case.

Table 3.4: Optimum combination of design and operating parameters; the optimum values are highlighted in bold

	Optimum ΔP	**Optimum Nu**	**Optimum S_g'''**	**Optimum FoM**
T_{wall}	40	40	40	80
Re_e	100	2000	100	100
L/D	10	10	10	10
H/D	0.8	0.6	0.8	2.0
F_i/F_a	0.474	0.7	0.2	0.3
ΔP	**0.33**	3.11	0.42	0.38
Nu	1.4	**5.0**	1.3	3.2
S_g'''	7.1×10^{-5}	4.1×10^{-4}	$\mathbf{4.7 \times 10^{-5}}$	4.4×10^{-4}
FoM	4.7×10^{4}	4.9×10^{3}	4.4×10^{4}	$\mathbf{1.7 \times 10^{5}}$

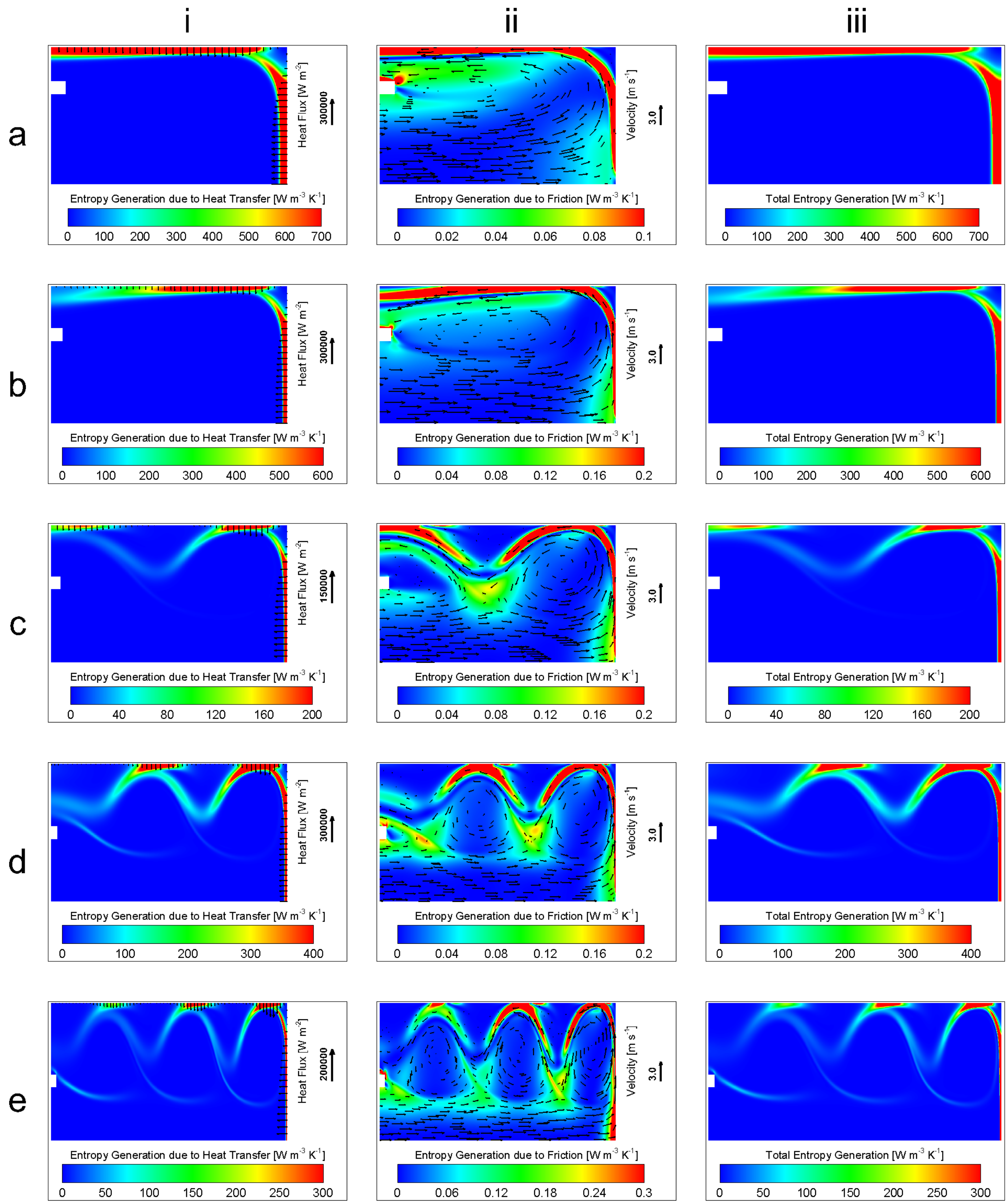

Figure 3.10 – Local distributions of entropy generation (i) due to heat transfer; (ii) friction loss; and (iii) total entropy at impingement area for various H/D ratios: (a) 0.6; (b) 0.8; (c) 1.0; (d) 1.5; and (e) 2.0

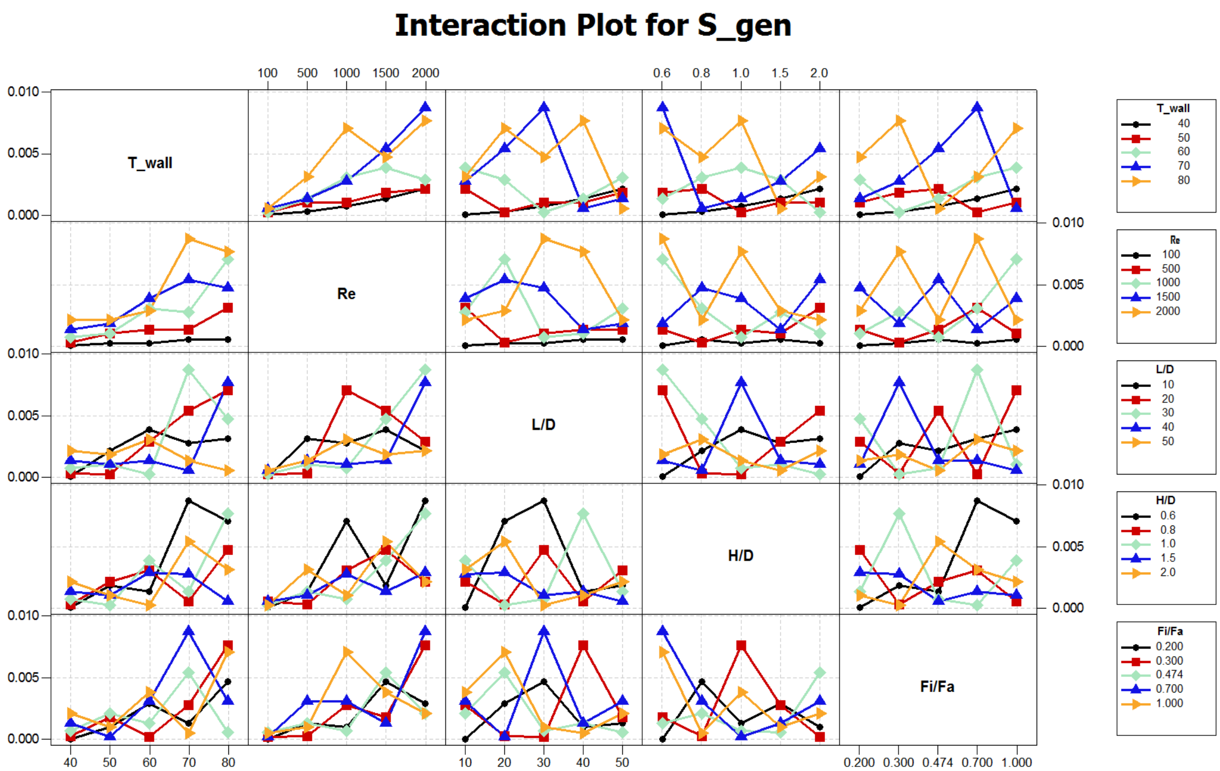

Figure 3.11 – The interactions of various parameters with respect to entropy generation

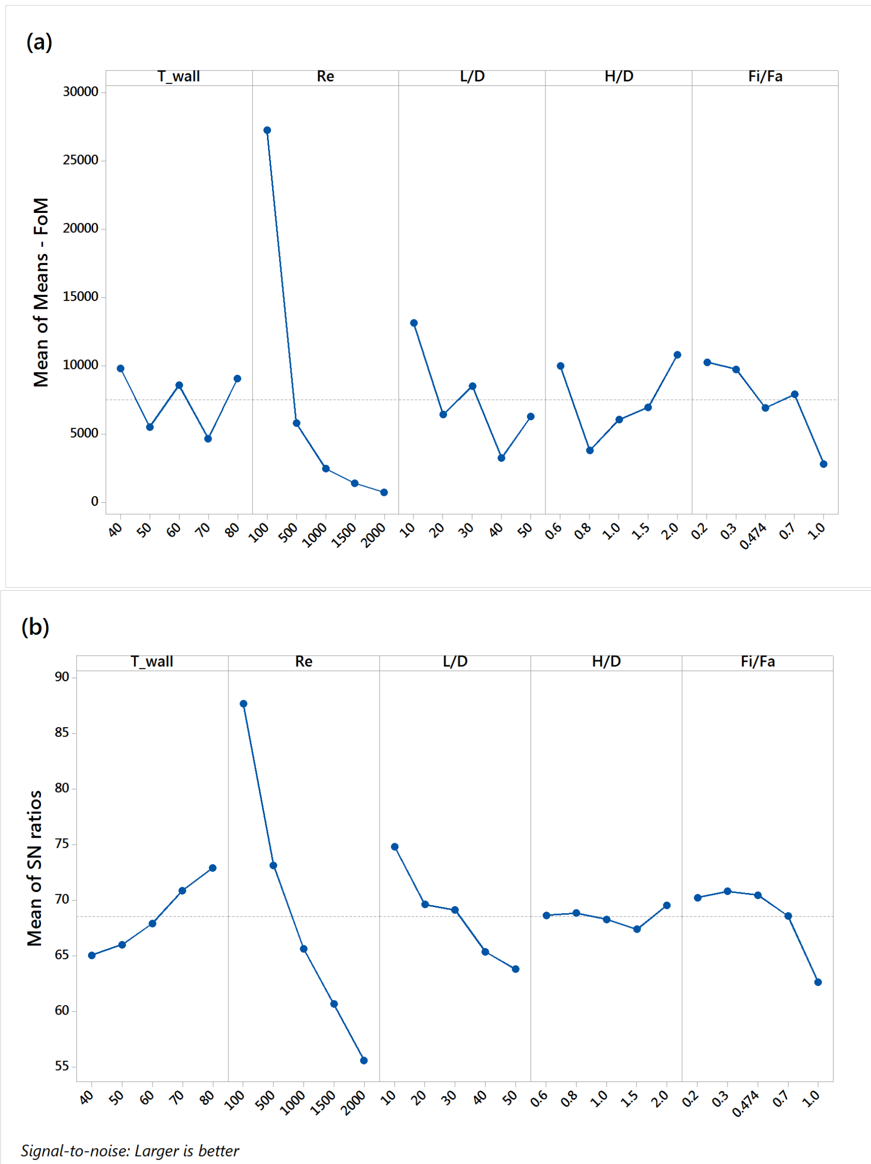

Figure 3.12 – Response of (a) mean and (b) S/N ratio (larger is better) of various geometries and operating parameters with respect to FoM

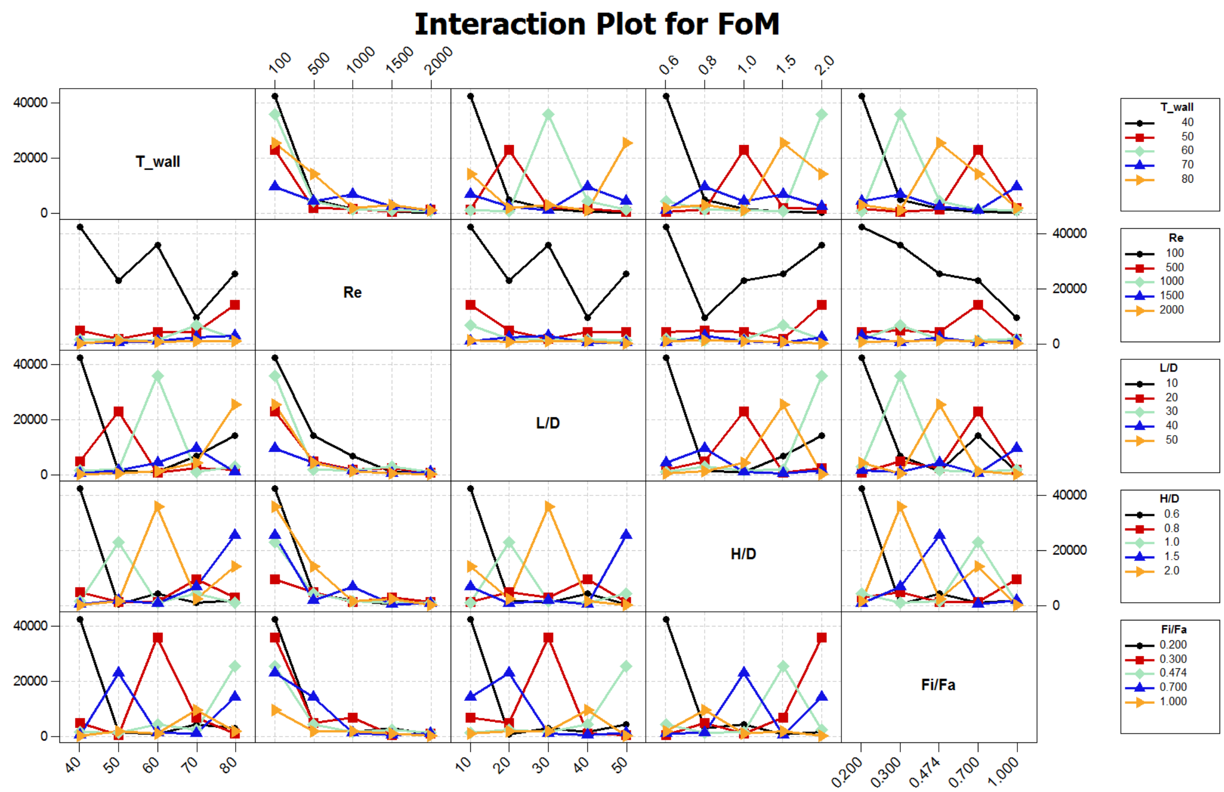

Figure 3.13 – The interactions of various parameters with respect to FoM

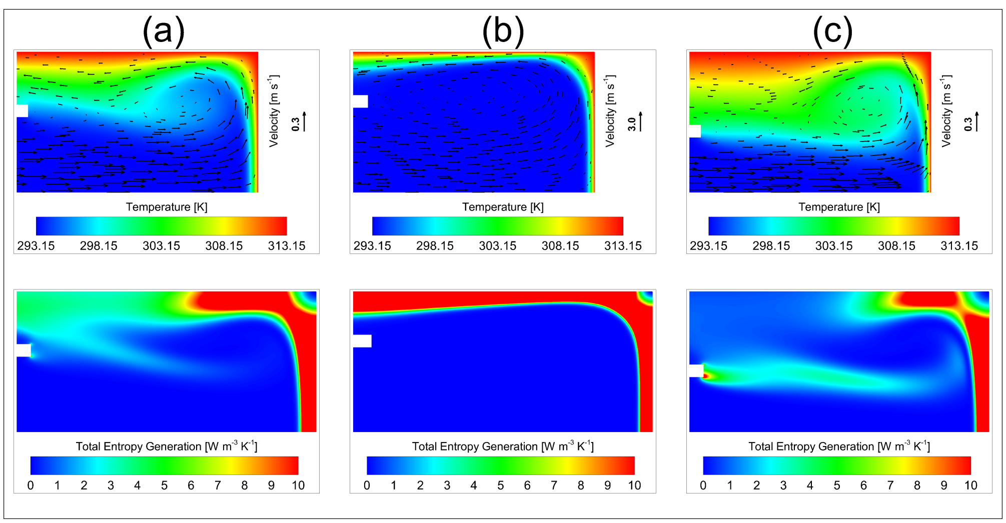

Figure 3.14 – Local distributions of velocity vectors, temperature, and entropy generation at the clearance area for optimized cases with respect to (a) pressure; (b) Nusselt number; and (c) Entropy generation

3.5 Conclusions

A two-dimensional model for a bayonet tube heat exchanger that takes into account conservation of mass, momentum, and energy has been derived, analyzed, and validated. A computational study, based on this model, has been carried out with a view to studying how tube geometry and operating parameters impact the performance of the bayonet tube.

It has been shown that a range of parameters - wall temperature, Reynolds number, tube length to diameter ratio, clearance length to diameter ratio, area ratio - influence the performance of the bayonet tube in terms of pressure drop, Nusselt number, total entropy generation, and figure of merit. It should also be noted that different combination of design and operating parameters are selected for different optimum design point, whence careful and precise decision has to be considered when designing a bayonet tube to ensure that all factors have been considered for an optimal performance. Furthermore, there was significant interaction between the parameters. However, the most influence parameters, in most cases, were Reynolds number and tube length to diameter ratio. Future work will focus on more precise optimization procedure in order to alleviate current limitation of discrete level optimization parameters.

References

[1] MR Rodríguez-Sánchez, A Sánchez-González, C Marugán-Cruz, and D Santana. New designs of molten-salt tubular-receiver for solar power tower. *Energy Procedia*, 49:504–513, 2014.

[2] Frank Boni. The design of a liquid metal heated bayonet tube steam generator. *Journal of the American Society for Naval Engineers*, 70(2):231–244, 1958.

[3] AJ Baum. Optimum design of a bayonet tube heat exchanger. In *Proc. 6th Int. Heat Transfer. Conf., Toronto*, volume 4, pages 285–289, 1978.

[4] L Almanza-Huerta, A Hernandez-Guerrero, M Krarti, and JM Luna. Parametric analysis of a bayonet tube with a special type of extended surface. In *ASME 2010 International Mechanical Engineering Congress and Exposition*, pages 781–790. American Society of Mechanical Engineers, 2010.

[5] AJ Jolly, T O'Doherty, and CJ Bates. COHEX: a computer model for solving the thermal energy exchange in an ultra high temperature heat exchanger.Part A: computational theory. *Applied Thermal Engineering*, 18(12):1263–1276, 1998.

[6] AJ Jolly, T O'Doherty, and CJ Bates. COHEX: a computer model for solving the thermal energy exchange in an ultra high temperature heat exchanger. Part B: validation and results. *Applied Thermal Engineering*, 19(4):389–398, 1999.

[7] Manon Vitel, Ahmed Rouabhi, Michel Tijani, and Frédéric Guérin. Modeling heat transfer between a freeze pipe and the surrounding ground during artificial ground freezing activities. *Computers and Geotechnics*, 63:99–111, 2015.

[8] C.S. Jahan, C. Quamruzzaman, Q.H. Mazumder, and T.A.H.F.M.A. Haque. Artificial ground freezing method for shaft construction in maddhapara hardrock mine, bangladesh: Minimization of its cost. *Pakistan Journal of Scientific and Industrial Research*, 47(2):112–117, 2004.

[9] E Pimentel, S Papakonstantinou, and G Anagnostou. Numerical interpretation of temperature distributions from three ground freezing applications in urban tunnelling. *Tunnelling and Underground Space Technology*, 28:57–69, 2012.

[10] Gang Zheng, Tianqi Zhang, and Yu Diao. Mechanism and countermeasures of preceding tunnel distortion induced by succeeding EPBS tunnelling in close proximity. *Computers and Geotechnics*, 66:53–65, 2015.

[11] Lorenzo Damiani, Massimo Montecucco, and Alessandro Pini Prato. Conceptual design of a bayonet-tube steam generator for the ALFRED lead-cooled reactor. *Nuclear Engineering and Design*, 265:154–163, 2013.

[12] Lorenzo Damiani, Alessandro Pini Prato, and Roberto Revetria. Innovative steam generation system for the secondary loop of "ALFRED" lead-cooled fast reactor demonstrator. *Applied Energy*, 121:207–218, 2014.

[13] F Belloni, G Bandini, and M Polidori. Investigation on the heat exchange efficiency of bayonet tube steam generator of lead-cooled ALFRED reactor with RELAP5 code. In *International Congress on Advances in Nuclear Power Plants 2011 (ICAPP 2011)*, pages 2103–2111, 2011.

[14] Roberto Ponciroli, Andrea Bigoni, Antonio Cammi, Stefano Lorenzi, and Lelio Luzzi. Object-oriented modelling and simulation for the ALFRED dynamics. *Progress in Nuclear Energy*, 71:15–29, 2014.

[15] Andrea De Santis, Damiano Vitale Di Maio, Gianfranco Caruso, and Fabio Manni. Innovative radiation-based direct heat exchanger (DHX) for liquid metal cooled reactors. *Nuclear Engineering and Design*, 263:164–171, 2013.

[16] Maximilian B Gorensek and William A Summers. Hybrid sulfur flowsheets using PEM electrolysis and a bayonet decomposition reactor. *International Journal of Hydrogen Energy*, 34(9):4097–4114, 2009.

[17] Vijaisri Nagarajan, Valery Ponyavin, Yitung Chen, Milton E Vernon, Paul Pickard, and Anthony E Hechanova. Numerical study of sulfur trioxide decomposition in bayonet type heat exchanger and chemical decomposer with porous media zone and different packed bed designs. *International Journal of Hydrogen Energy*, 33(22):6445–6455, 2008.

[18] Vijaisri Nagarajan, Valery Ponyavin, Yitung Chen, Milton E Vernon, Paul Pickard, and Anthony E Hechanova. CFD modeling and experimental validation of sulfur trioxide

decomposition in bayonet type heat exchanger and chemical decomposer for different packed bed designs. *International Journal of Hydrogen Energy*, 34(6):2543–2557, 2009.

[19] Ting Ma, Min Zeng, Yanpeng Ji, Haibin Zhu, and Qiuwang Wang. Investigation of a novel bayonet tube high temperature heat exchanger with inner and outer fins. *International Journal of Hydrogen Energy*, 36(5):3757–3768, 2011.

[20] Shuang Ying Wu, Bao Xi Cao, Lan Xiao, and You Rong Li. Effect of mass flow rate of working fluid on performance of capillary porous wick evaporator with bayonet tube for AMTEC. In *Applied Mechanics and Materials*, volume 190, pages 1302–1305. Trans Tech Publ, 2012.

[21] A Mathur, SC Saxena, and ZH Qureshi. Heat transfer to a bayonet heat exchanger immersed in a gas-fluidized bed. *International Communications in Heat and Mass Transfer*, 10(3):241–252, 1983.

[22] Bernard L Segal and David G Kilpatrick. *Engineering in The Practice of Medicine*. Williams & Wilkins, 1967.

[23] Ahmed Rouabhi, M Tijani, O Stab, Y Charnavel, and T You. A semi-analytical approach for modelling heat transfer during salt-cavern leaching process. *International Journal for Numerical and Analytical Methods in Geomechanics*, 32(13):1617–1634, 2008.

[24] H Fuchs. Performance of bayonet tube boilers. *American Institute of Chemical Engineers*, 26:187, 1986.

[25] C Luzzatto, A Morgana, S Chaudourne, T O'Doherty, and G Sorbie. A new concept composite heat exchanger to be applied in high-temperature industrial processes. *Applied Thermal Engineering*, 17(8):789–797, 1997.

[26] Ting Ma, Yitung Chen, Min Zeng, and Qiuwang Wang. Stress analysis of internally finned bayonet tube in a high temperature heat exchanger. *Applied Thermal Engineering*, 43:101–108, 2012.

[27] M Mansoor and A Tauqir. Failure of heat-exchanger tubes due to localized scaling and microstructural transformation. *Journal of Failure Analysis and Prevention*, 8(5):434–440, 2008.

[28] A Usman and A Nusair Khan. Failure analysis of heat exchanger tubes. *Engineering Failure Analysis*, 15(1):118–128, 2008.

[29] Min Zeng, Ting Ma, Bengt Sundén, Mohamed B Trabia, and Qiuwang Wang. Effect of lateral fin profiles on stress performance of internally finned tubes in a high temperature heat exchanger. *Applied Thermal Engineering*, 50(1):886–895, 2013.

[30] T O'Doherty, AJ Jolly, and CJ Bates. Optimisation of heat transfer enhancement devices in a bayonet tube heat exchanger. *Applied Thermal Engineering*, 21(1):19–36, 2001.

[31] T O'Doherty, AJ Jolly, and CJ Bates. Analysis of a bayonet tube heat exchanger. *Applied Thermal Engineering*, 21(1):1–18, 2001.

[32] WILLIAM TESSIN. Heat transfer in bayonet-type tubes. *Journal of the American Society for Naval Engineers*, 64(4):707–718, 1952.

[33] Yih-Yun Hsu and JW Westwater. Film boiling from vertical tubes. *AIChE Journal*, 4(1):58–62, 1958.

[34] N Kayansayan. Thermal design method of bayonet-tube evaporators and condensers. *International Journal of Refrigeration*, 19(3):197–207, 1996.

[35] Norman L Hurd. Mean temperature difference in the field or bayonet tube. *Industrial & Engineering Chemistry*, 38(12):1266–1271, 1946.

[36] Isao Todo. Dynamic response of bayonet-type heat exchangers - 2. response to flow rate changes. *Bulletin of JSME*, 21(154):644–651, 1978.

[37] Isao Todo. Response of parallel-flow and counterflow heat exchangers to sinusoidal flow rate changes of large amplitude. *Bulletin of JSME*, 25(210):1994–2001, 1982.

[38] Isao Todo. Response of multipass heat exchangers to sinusoidal flow rate changes of large amplitude. *Bulletin of JSME*, 27(223):87–94, 1984.

[39] Isao Todo. Response of bayonet-type heat exchangers to sinusoidal flow rate changes of large amplitude. *Bulletin of JSME*, 28(243):2084–2091, 1985.

[40] Abel Hernandez-Guerrero and Agustin Macias-Machin. How to design bayonet heat exchangers. *Chemical Engineering (New York)*, 98(4):122–126, 1991.

[41] Isao Todo. Dynamic response of bayonet-type heat exchangers - 1. response to inlet temperature changes. *Bulletin of JSME*, 19(136):1135–1140, 1976.

[42] Chung-Hsiung Li. Effect of radiation heat transfer on a bayonet tube heat exchanger. *AIChE Journal*, 32(2):341–343, 1986.

[43] Chung Hsiung Li. Analytical solution of the heat transfer equation for a bayonet tube heat exchanger. *American Society of Mechanical Engineers*, 3:1–9, 1981.

[44] Shripad P Mahulikar, Heinz Herwig, Jing-Wei Zhou, and Yash M Sodhani. Surface radiative transfer in gas-to-gas cocurrent microheat exchanger. *AIChE Journal*, 57(1):40–50, 2011.

[45] Richard B Peterson and John A Vanderhoff. Analysis of a bayonet-type counterflow heat exchanger with axial conduction and radiative heat loss. *Numerical Heat Transer, Part A Applications*, 40(3):203–219, 2001.

[46] GSH Lock and Maolin Wu. Heat transfer characteristics of a bayonet tube using air under laminar conditions. *International Journal of Heat and Mass Transfer*, 36(2):287–291, 1993.

[47] GSH Lock and Harpal Minhas. Bayonet tube heat exchanger. *Applied Mechanics Reviews*, 50(8):445–473, 1997.

[48] Harpal Minhas, GSH Lock, and Maolin Wu. Flow characteristics of an air-filled bayonet tube under laminar conditions. *International Journal of Heat and Fluid Flow*, 16(3):186–193, 1995.

[49] Harpal Minhas and GSH Lock. Transitional forced convection in a bayonet tube. *International Communications in Heat and Mass Transfer*, 22(5):721–728, 1995.

[50] Harpal Minhas and GSH Lock. Estimating the influence of prandtl number on heat transfer in a bayonet tube. *International Communications in Heat and Mass Transfer*, 23(7):1011–1017, 1996.

[51] H Minhas and GSH Lock. Numerical analysis of heat transfer in an air-filled bayonet tube under laminar conditions. *International Journal of Heat and Mass Transfer*, 39(4):761–769, 1996.

[52] Harpal Minhas and GSH Lock. Forced convection in an air-filled bayonet tube during the laminar-turbulent transition. *International Journal of Heat and Mass Transfer*, 40(8):1885–1894, 1997.

[53] Harpal Minhas and GSH Lock. Laminar-turbulent transition in a bayonet tube. *International Journal of Heat and Fluid Flow*, 17(2):102–107, 1996.

[54] J. Brandrup, E.H. Immergut, and W. McDowell. *Polymer Handbook*. Wiley, 1975.

[55] Hugh D Young and Francis Weston Sears. *University Physics*. Addison-Wesley, 1992.

[56] E.W. Lemmon, R.T. Jacobsen, S.G. Penoncello, and D.G. Friend. Thermodynamic properties of air and mixtures of nitrogen, argon, and oxygen from 60 to 2000 k at pressures to 2000 mpa. *Journal of Physical and Chemical Reference Data*, 29(3):331–362, 2000.

[57] Adrian Bejan. *Entropy Generation Minimization: The Method of Thermodynamic Optimization of Finite-size Systems and Finite-time Processes*. CRC press, 1995.

[58] Jundika C Kurnia, Agus P Sasmito, and Arun S Mujumdar. Laminar heat transfer performance of power law fluids in coiled square tube with various configurations. *International Communications in Heat and Mass Transfer*, 57:100–108, 2014.

[59] William Y Fowlkes and Clyde M Creveling. *Engineering Methods for Robust Product Design Using Taguchi Methods in Technology and Product Development*. Addison-Wesley, 1995.

Chapter 4

Conjugate heat transfer in artificial ground freezing using enthalpy-porosity method: Experiments and model validation

Contents

Preface (Linking Paragraph)

This chapter is a continuation of the previous two chapters. Based on the literature review in Chapter 2 it was appear that the contribution to the experimental research concerning the artificial ground freezing systems is minimal. Also, most of the previous works formulate their models of the AGF process either by only considering the conduction energy equation or based on the classical apparent heat capacity method. Therefore, this chapter introduce the development of a lab-scale experiment that mimics the AGF process, along with a three-dimensional

conjugate heat transfer model that take into consideration the design recommendations from Chapter 3. The results of this chapter will be implemented in the studies of the next two chapters. The below article has been published based on the discussion of this chapter:
Alzoubi, M. A., Nie-Rouquette, A., and Sasmito, A. P. (2018). *Conjugate heat transfer in artificial ground freezing using enthalpy-porosity method: Experiments and model validation*, International Journal of Heat and Mass Transfer, 126:740-752.

Abstract

Artificial ground freezing (AGF) system is a temporary excavation-support method that is used in underground mines and tunneling projects to improve and stabilize ground structure, and to control groundwater seepage. The conjugate heat transfer between the bayonet freeze pipes and the ground plays a vital role in determining ice wall formation, heat extraction rate and closure time. In this study, a controlled laboratory scale AGF experimental rig is conceived and developed at Mine Multiphysics laboratory, McGill University. It is equipped with more than 80 temperature readings, thorough properties characterization, and an advanced instrumentation system to quantify the conjugate heat transfer process. We also developed a three-dimensional conjugate mathematical and numerical model of the bayonet freeze pipes and porous ground structure using enthalpy-porosity method. The model is further validated against global heat balance and local temperature distributions from our experiments at various operating conditions. Good agreement between model predictions and experimental data was achieved with $R^2 = 0.972$. The results indicate that higher coolant Reynolds number gives rise to a higher Nusselt number and, thus, higher heat extraction rate which is mirrored by a shorter closure time. Coolant Reynolds number is found to have a higher effect on the heat transfer performance as compared to coolant temperature and ground's initial temperature. Finally, the model is a reliable tool that can be extended and employed for design and optimization of industrial AGF system.

4.1 Introduction

Artificial ground freezing (AGF) was developed by Friedrich Poetsch in the 19th century to stabilize the construction of deep shafts in saturated soil [1]. The system, since then, has been used intensively in several applications such as underground mines [2], shaft sinking [3], civil and tunneling [4, 5], maintaining the permafrost structure by implementing thermosyphon concept [6], and hazardous-waste management [7]. The AGF process has many advantages, as compared to other geotechnical support methods such as cement and chemical grouting, dewatering, and compressed air. It is compatible with wide range of soil types [8], has low effect on the ground structure (during and after the freezing process) [8, 9], has a small impact on the environment [10], and it is a reliable method for high-risk applications – such as uranium mines [11] and harmful-wastes management [12, 13]. The concept of an AGF system is to circulate a sub-zero coolant in a network of pipes to freeze the surrounding saturated-soil. As the coolant flows through the pipes, it extracts heat from the ground and induces the gradual freezing of the groundwater. The quantity of extracted heat depends on the thermal interaction between the coolant's flow and the porous ground.

Several contributions have been made in literature to examine the AGF process analytically [14–16] and numerically [17–19]. Sanger and Sayles [14] solve the AGF process for vertical pipes by dividing the process into two main stages: (i) the frozen body is growing around the separate pipes; and (ii) the circular frozen body merged to form a continuous curtain. It was assumed that a neighbor freeze pipe does not affect the growth of the frozen body. Holden [15] extended Sanger and Sayles model by considering the contribution of a neighbor freeze pipe to the growth of frozen body in the first stage. Zhou et al. [16] studied AGF process for shaft sinking application. The study considered one freeze pipe and modeled it as an infinite line source using similarity type of general solution. Further analysis could also be performed using proper orthogonal decomposition (POD) reduced-order model in order to save the computational time [20]. Rouabhi et al. [17] studied the heat transfer in a porous ground structure during the salt-cavern leaching process. The process considered a single freeze pipe that is installed vertically in the ground. They built a 2D axisymmetric model using a semi-analytical approach to simulate the transient heat transfer. Papakonstantinou et al. [18] examined the AGF process for horizontal pipes installation that is usually used in tunneling projects. They validated their numerical model against in-situ temperature measurements. Vitel et al. [19] developed a conjugate 2D axisymmetric model to simulate AGF process for a singular freeze pipe. They studied the effect of coolants' properties on the efficiency of the freeze pipe in terms of the ice growth. In these studies [14–19], conductive heat transfer has been assumed as the primary mechanism for energy transfer, whereas convective heat transfer is low enough to be neglected. However, under certain conditions, such as high porosity or groundwater seepage, convective heat transfer become more significant and should be considered in the calculations [21, 22].

Recent studies, such as [2, 23–26], included the convective heat transfer in the mathematical models. Vitel et al. [2] extended their previous work [19] by studying the performance of AGF process in fractured sandstone. They studied the effect of fractures on the ice growth within the AGF process. Ou et al. [23] examined the performance of AGF process in tunneling project. They studied the time that is required to achieve the minimum thickness of ice wall. Another study from Vitel et al. [24] modeled the transient heat transfer of AGF under high seepage velocities. The study showed the influence of groundwater seepage on the growth of the frozen body. Marwan et al. [25] used the ant colony method in their work to optimize the spacing between horizontal freeze pipes in tunneling projects. The optimization method along with their numerical model reduced the freezing time as compared to an equal spacing of freeze pipes. Rouabhi et al. [26] investigated the effect of the salinity of groundwater on the performance of AGF process. They found that water salinity affects the capillary pressure in porous media and on the latent heat of fusion. These studies used the effective (apparent) heat capacity assumption; an approach used to simulate the latent heat of fusion as a part of the fluid heat capacity. This procedure, however, requires careful consideration of the temperature, velocity, and latent heat evolution in the phase-change zone [27]. Alternatively, Voller and Prakash [28] proposed a modeling methodology called enthalpy-porosity method, where the water-ice phase-change interface is modeled as a mushy zone. The transformation from water to ice in this zone is considered as a porous medium, where a modified Darcy source term (called here: mushy source term) is used to simulate motion in the phase-change region. This approach shows some advantages in terms of simplifying the numerical modeling requirements without compromising the accuracy of the results.

The reliability of mathematical models can be assessed by validating computational results with the measurements of an experiment that is carried out under controlled environment. Several experiments have been conducted to mimic the AGF system. Ständer [29] performed one of the first systematic experiment on AGF. The tests were performed either with a single freeze pipe or with a group of freeze pipes, which were arranged in a circle to mimic the underground tunnel usage of AGF. The results were presented by means of contours showing the ice growth around the freeze pipes. Victor [30] used a similar setup as Ständer, but with seepage flow included. The experiment of Pimentel et al. [31, 32] is, to our knowledge, the only reference that has been used to validate the mathematical models of the recent, respective studies. Pimentel et al. examined the adverse effect of groundwater seepage on AGF process. Their experimental setup consisted of three vertical freeze pipes contained within an insulated container with inner dimensions of (1.2 [m] $\times$ 1.3 [m] $\times$ 1.0 [m]). Several experiments were conducted with and without groundwater seepage conditions. In order to simulate the seepage, two constant-head water tanks were installed at the opposite faces of the tank, perpendicular to the freeze pipes. However, the influence of other operating parameters on the AGF process, such as coolant's temperature and flow rate, is yet to be studied.

The primary objective of this study is to implement, contrary to the previous studies, the enthalpy-porosity methods to quantify the heat transfer of AGF process, and to examine the influence of key operating parameters on the performance of AGF process in terms of ice growth. Additionally, this paper provides comprehensive documentation of the physical geometries of a laboratory-scale setup, the thermo-physical properties of coolant and soil structure, boundary and initial conditions, and the results of parametric studies. The data presented here is a reliable source for the assessment of analytical or numerical models of multi-phase heat transfer in porous media with solidification.

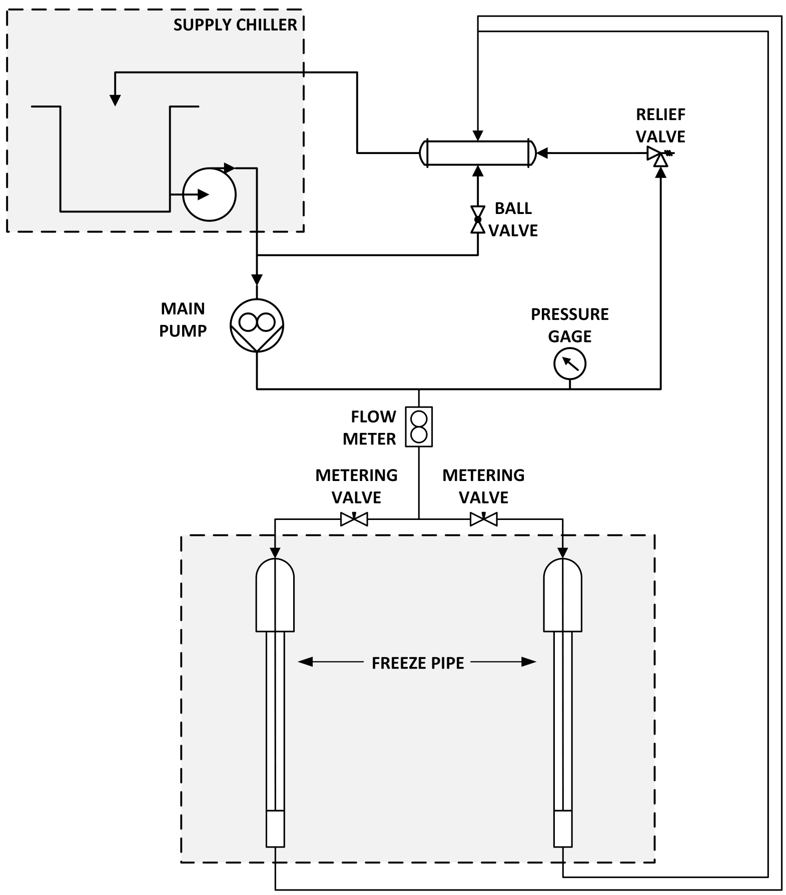

Figure 4.1 – Flowchart of the experimental setup showing the main components

4.2 Experimental setup

In order to conduct AGF process in a controlled environment and determined initial and boundary conditions, a laboratory-scale experimental setup has been designed and built. The physical model of the setup and the properties of the coolant and ground are discussed in the following sections.

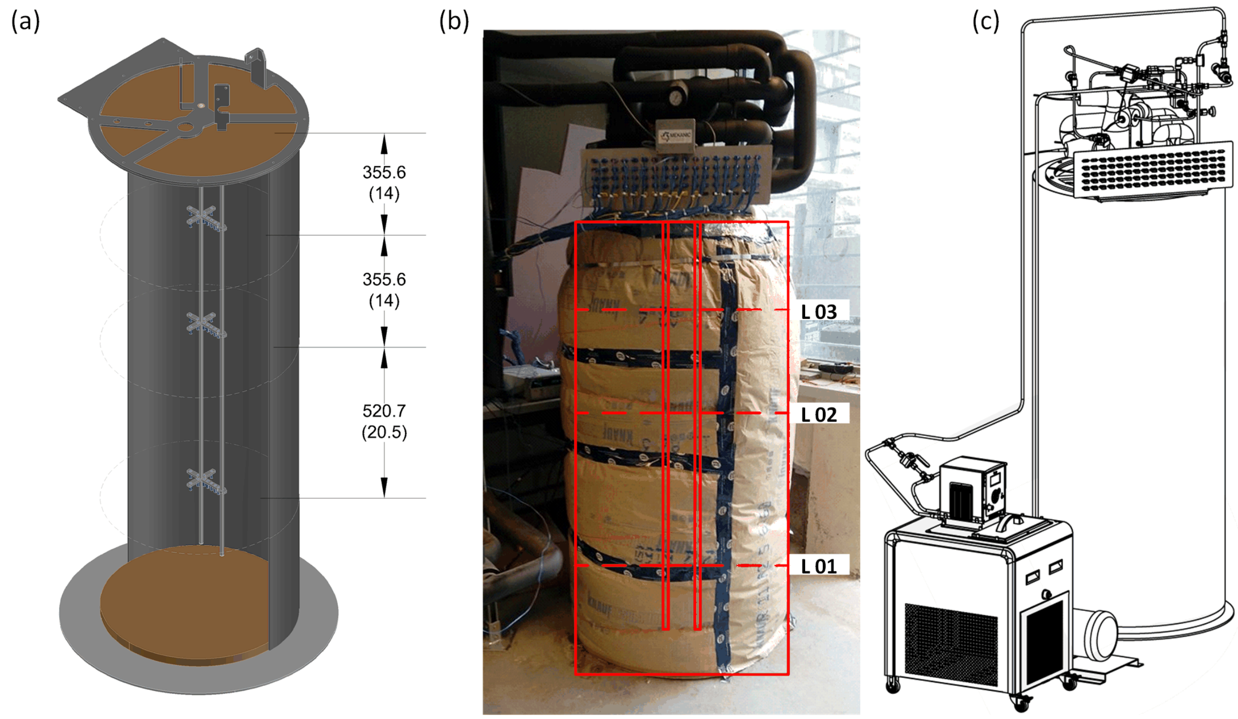

Figure 4.2 – The structure of the experimental setup showing: (a) thermocouple positions within the soil structure; (b) the physical setup labeled with levels' positions; and (c) 3D schematic of the setup.

4.2.1 Physical model

Figs. 4.1 and 4.2 (c) show the process diagram and the 3D schematic of the experimental setup, respectively. The rig consists of two main parts: a supply chiller that can provide the system with coolant's temperature as low as -30 [°C], and an aluminum ground structure in which two stainless steel 316 bayonet freeze pipes are installed. A positive displacement pump (controlled by a variable frequency drive (VFD)) provides the flow, which is regulated with control valves, pressure gage, and flow meters. The working fluid is 57% diluted Ethylene Glycol. The coolant flows through a primary circuit before being directed into the targeted experiment (smaller loop on Fig. 4.1). This loop aims to maintain a steady, cold temperature in the coolant's flow. The temperature is measured using calibrated thermocouples types T, J, and K. More than 80 thermocouples record the temperature of the inlet and outlet glycol's flow, and the ground structure at three different levels, as illustrated in Figs. 4.2 (a) and 4.3. The dimensions of the physical model are shown in Table 4.1. Additionally, the rig is equipped with three band-type heaters that supply the ground structure with a constant wall temperature. The thermocouples and the flowmeters are connected to a data acquisition (DAQ) system to collect their readings. To minimize the heat gain, the rig and the connection pipes are fully insulated with fiberglass and rubber foam, respectively, as shown in Fig. 4.2 (b). A LabVIEW program controls the chiller, VFD, and heaters while also recording the temperature and flow rates. The tank is filled with fully saturated sand and then covered with two layers (1" thickness) of foam insulation.

Table 4.1: Dimensions of the tank and the freeze pipes

Quantities	Value
Tank	
Total hight [mm] (in)	1,638.30 (64.500)
Sand hight [mm] (in)	1,552.58 (61.125)
Outer diameter [mm] (in)	549.28 (21.625)
Wall thickness [mm] (in)	6.35 (0.250)
Base thickness [mm] (in)	9.53 (0.375)
Freeze pipe	
Length [mm] (in)	1,400.18 (55.125)
Annulus tube outer diameter [mm] (in)	12.70 (0.500)
Inner tube outer diameter [mm] (in)	6.35 (0.250)
Clearance length [mm] (in)	12.70 (0.500)
Outer tube thickness [mm] (in)	0.89 (0.035)
Inner tube thickness [mm] (in)	0.89 (0.035)
Clearance cap thickness - outer tube [mm] (in)	1.60 (0.063)

4.2.2 Material properties

Medium sand with a maximum particle size of 1[mm], was used in this study. The thermo-physical properties of fully-saturated frozen and unfrozen sand samples were measured in the lab. The properties of the dry sand particles were then calculated based on the lab results, as shown in Table 4.2. 57% diluted Glycol is used as a working fluid. The coolant was selected for practical reasons: freezing temperature as low as -50 [°C], and compatibility with the supply chiller. The physical and thermal properties were measured in the lab and compared with literature values. Fig. 4.4 shows the temperature dependent properties of the coolant.

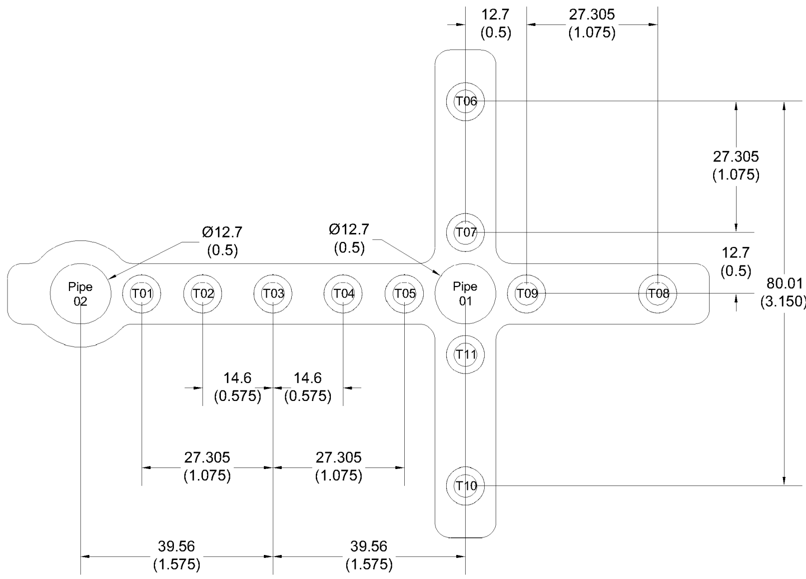

Figure 4.3 – The layout of thermocouples around the freeze pipes.

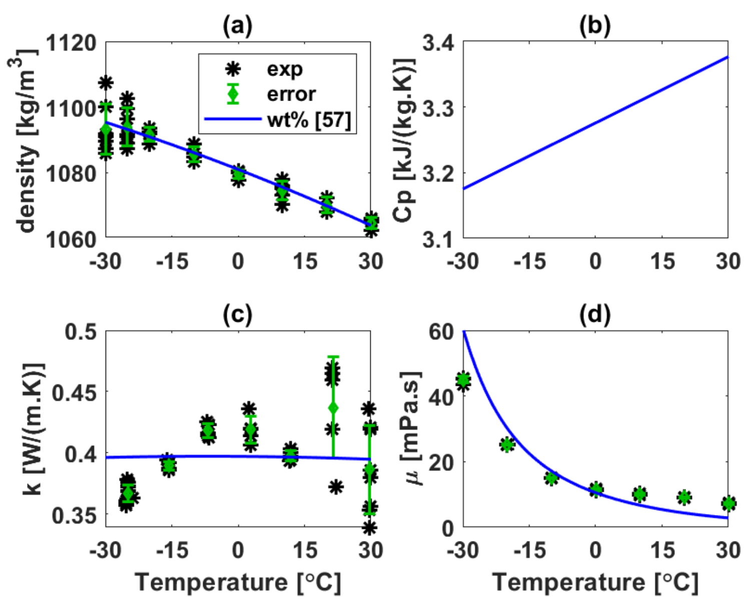

Figure 4.4 – The experimental results of temperature dependent (a) density, (b) specific heat capacity, (c) thermal conductivity, and (d) viscosity of the coolant that is used in this study as compared to literature values of 57 % glycol

4.2.3 Data reproducibility test

In order to verify the reliability and repeatability of the rig's data, three identical experiments in terms of initial, boundary, and operating conditions were conducted. The inlet and outlet temperatures, the ground's temperature at level-02 (see Fig. 4.2), and the flow rate were

Table 4.2: Properties of the sand particle that is used in this study

Quantities	Value
Particle diameter (D_{50}) [mm]	0.212
Quartz content [%]	90.5
Thermal conductivity [W/(m.K)]	3.73
Density [kg/m^3]	2,634.50
Specific heat capacity [J/(kg.K)]	945.92
Porosity [%]	37
Permeability [m^2]	4.94×10^{-12}

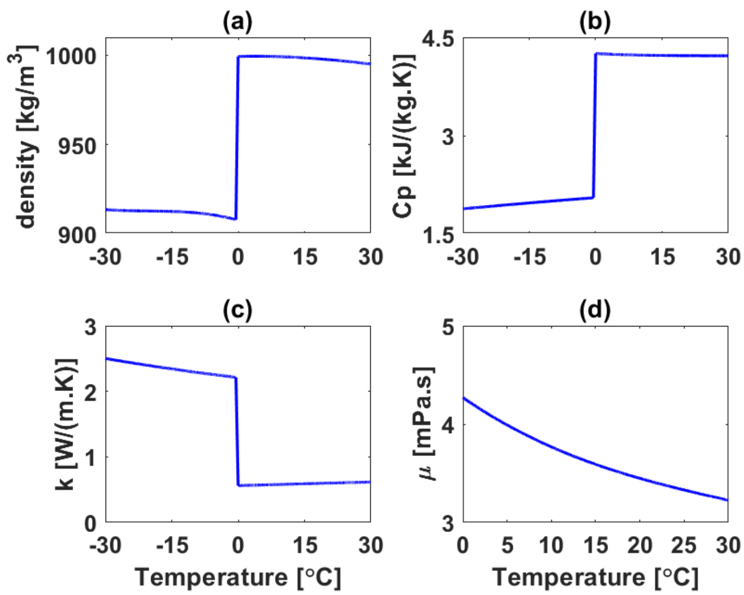

Figure 4.5 – Water temperature dependent properties: (a) density, (b) specific heat capacity, (c) thermal conductivity, and (d) viscosity

examined and monitored. The result showed very good reproducibility, as depicted in Fig. 4.6. The outlet temperature shows a small deviation in one experiment which is due to extreme outdoor conditions. However, these conditions have a minimal effect on the overall performance.

4.2.4 Parametric studies

During the freezing process, certain operating conditions, such as soil properties, and groundwater content, are, by nature, immutable. Thus, coolant's flow rate, coolant's inlet temper-

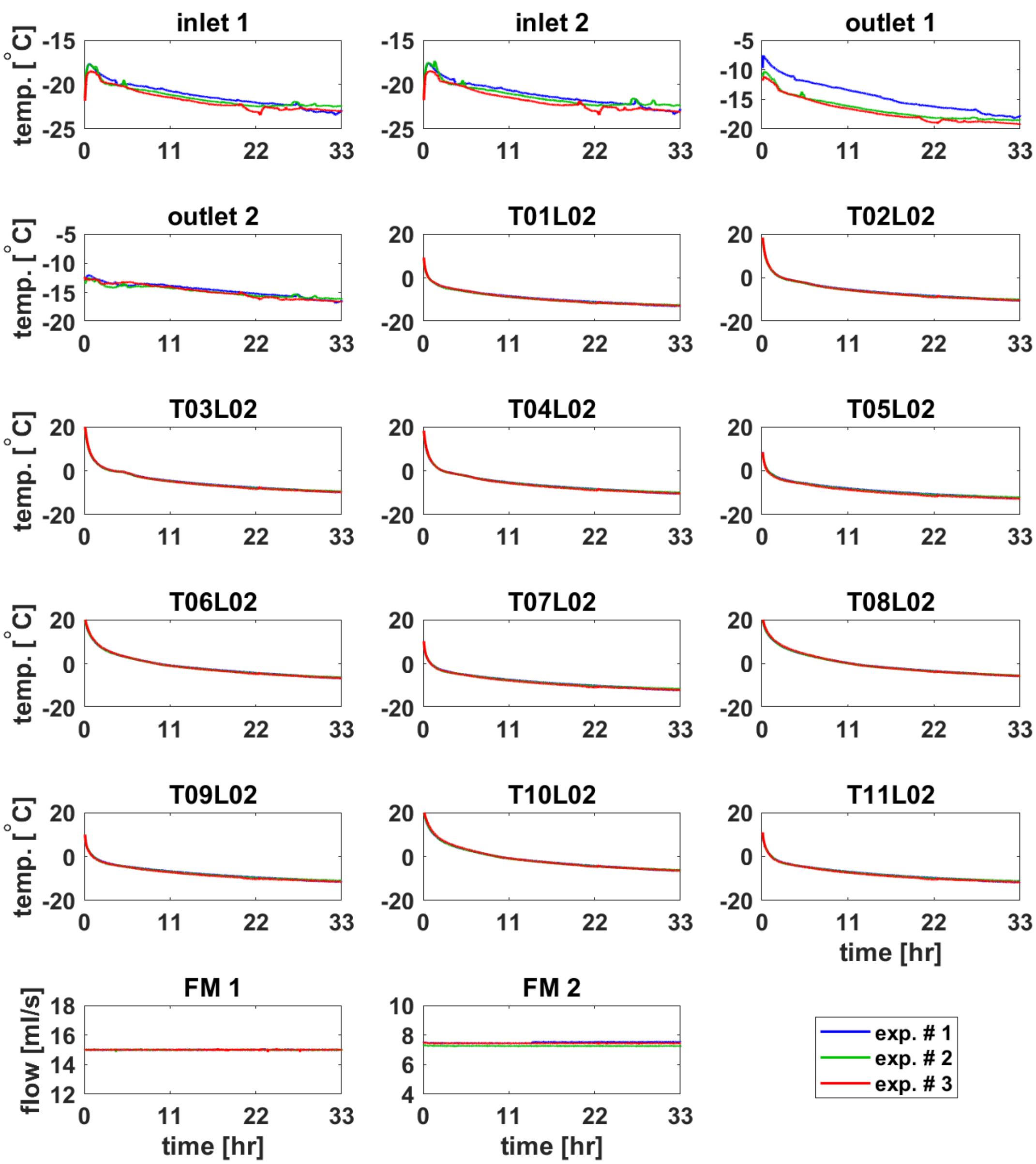

Figure 4.6 – The ground's temperature at level-02 (see Fig. 4.2), inlet and outlet temperature of two freeze pipes, and the flow rate readings show a very good consistency throughout the repeatability test.

ature, and ground's initial temperature become the only parameters that can be controlled. In this study, these three key parameters were evaluated at three different levels to determine the performance of an AGF process in terms of closure time, as presented in Table 4.3. The closure time is defined here as the period of time that is needed to create a closed frozen wall between two freeze pipes with a core temperature below the freezing point. The parametric studies were carried out by varying one parameter while keeping other parameters constants. The main criterion to stop the experiment was to have a merged frozen wall between the freeze pipes. Therefore, some experiments stopped after 25 [hr], while others stopped after 55 [hr], depends on the selected initial and boundary conditions.

Table 4.3: Operating parameters for parametric studies.The base case is highlighted in bold

Coolant Temp. [°C]	Ground Temp. [°C]	$\dot{Q}$ [ml/s]
-10	20	2.5
-15	**25**	**5**
-20	30	10

4.3 Model development

The AGF system consists of two main domains: (i) the flow of sub-zero brine in the freeze pipe (bayonet tube), and (ii) porous ground structure surrounding the pipe as shown in Fig. 4.7. The two domains are separated by the freeze pipe's wall, where they interact thermally. The main unknowns in this conjugate problem are the coolant's temperature T_c, and the ground's temperature T_g, respectively. In the next sections, the governing equations of each domain will be illustrated separately. Detailed description of all parameters can be found in the Nomenclature.

4.3.1 Governing equations

The conservation law of a dependent variable φ, can be written in a generalized differential equation form [33]:

$$\frac{\partial}{\partial t}(\rho\varphi) + \nabla\cdot(\rho\mathbf{v}\varphi) = \nabla\cdot(\theta\nabla\varphi) + S \tag{4.1}$$

The dependent variable φ can stand for different quantities, such as velocity, enthalpy, and temperature. The term $\left[\frac{\partial}{\partial t}(\rho\varphi)\right]$ is the rate-of-change of the dependent variable, $[\nabla\cdot(\rho\mathbf{v}\varphi)]$ is the convective term, $[\nabla\cdot(\theta\nabla\varphi)]$ is the diffusive term, and S is the source term. Based on the value of φ, the diffusive coefficient θ and the source term S should have appropriate meanings.

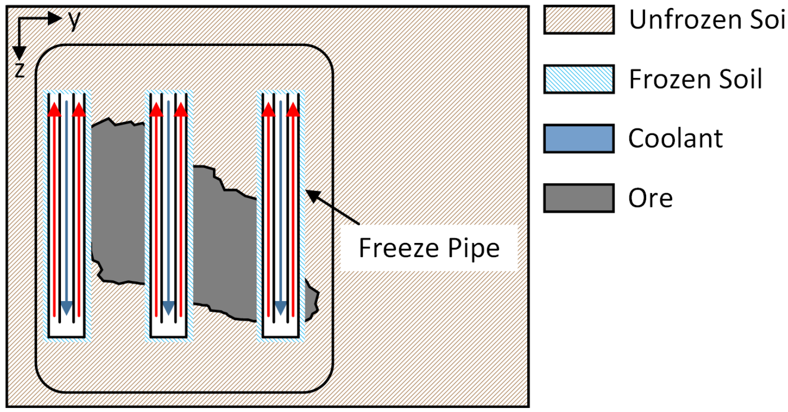

Figure 4.7 – Schematic diagram of a typical artificial ground freezing system.

Bayonet freeze pipe

The freeze pipe consists of two concentric tubes. Ideally, the coolant is pumped into the inner pipe which then flows back in the annulus pipe through the closed-ended clearance. The formulation of the flow in the freeze pipe is based on the following assumptions:

- Incompressible, fully developed flow.
- Single-phase, turbulent flow.
- The pipe is filled with the coolant at any time t.
- The coolant properties are temperature-dependent.

Based on Eqn. (4.1), the conservation equations of mass, momentum, and energy of the coolant's flow could be formulated as below [34]:
— Conservation equation of mass:

$$\frac{\partial}{\partial t}(\rho) + \nabla \cdot \left(\rho \overline{\mathbf{U}}\right) = 0 \tag{4.2}$$

— Conservation equation of momentum:

$$\frac{\partial}{\partial t}\left(\rho \overline{\mathbf{U}}\right) + \nabla \cdot \left(\rho \overline{\mathbf{U}}\ \overline{\mathbf{U}}\right) = \nabla \cdot \left((\mu + \mu_t)\left(\nabla \overline{\mathbf{U}} + \nabla \overline{\mathbf{U}}^T\right)\right) - \nabla P + \rho \mathbf{g} \tag{4.3}$$

where the velocity $\overline{\mathbf{U}}$ is the averaged velocity.
— Conservation equation of energy:

The dependent variable in the energy equation, here, is the specific enthalpy h. To satisfy the general form in Eqn. (4.1), the diffusion term is generally written as $\left[\nabla \cdot \left(\frac{k}{c_p}\nabla h\right)\right]$. For incompressible fluids, however, $\nabla h = c_p \nabla T$. With this substitution, the turbulence energy equation could be written as below:

$$\frac{\partial}{\partial t}(\rho h) + \nabla \cdot \left(\rho h \overline{\mathbf{U}}\right) = \nabla \cdot \left[\left(k + \frac{c_p \mu_t}{Pr_t}\right) \nabla T\right] \tag{4.4}$$

— Turbulence Model:

The current study uses the standard k-epsilon formulation. The model considers a two-equation model that solves for turbulent kinetic energy κ, and rate of dissipation ϵ. The equations for turbulent kinetic energy is given by:

$$\frac{\partial}{\partial t}(\rho \kappa) + \nabla \cdot \left(\rho \kappa \overline{\mathbf{U}}\right) = \nabla \cdot \left[\left(\mu + \frac{\mu_t}{\sigma_\kappa}\right) \nabla \kappa\right] + G_\kappa - \rho \epsilon \tag{4.5}$$

whereas the rate of dissipation is:

$$\frac{\partial}{\partial t}(\rho \epsilon) + \nabla \cdot \left(\rho \epsilon \overline{\mathbf{U}}\right) = \nabla \cdot \left[\left(\mu + \frac{\mu_t}{\sigma_\epsilon}\right) \nabla \epsilon\right] + C_{1\epsilon} G_\kappa \frac{\epsilon}{\kappa} - C_{2\epsilon} \rho \frac{\epsilon^2}{\kappa} \tag{4.6}$$

where σ_κ and σ_ϵ are the turbulent Prandtl numbers for κ and ϵ, respectively. G_κ is the generation of turbulence kinetic energy due to the mean velocity gradients. The formulation of the turbulent viscosity μ_t combines κ and ϵ as below:

$$\mu_t = \rho C_\mu \frac{\kappa^2}{\epsilon} \tag{4.7}$$

$C_{1\epsilon}, C_{2\epsilon}$ and C_μ are constants. More details of the turbulence model could be found in [35].

Porous ground

As a general practice in the porous medium, the conservation equations of mass, momentum, and energy are described at a small length scale, ℓ, which is smaller than the linear dimension of the system, L, yet larger than the linear dimension of the solid particle, ℓ_p, as depicted in Fig. 4.8.

$$\ell_p < \ell << L \tag{4.8}$$

This practice requires the use of the local volume averaging technique, where the conservation equations are integrated over a small elementary volume, V. For any local quantity, ψ, the volume averaged value, Ψ, is defined as [37]:

$$\Psi_\alpha = \frac{1}{V_\alpha(t)} \int_{V_\alpha(t)} \psi_\alpha dV \tag{4.9}$$

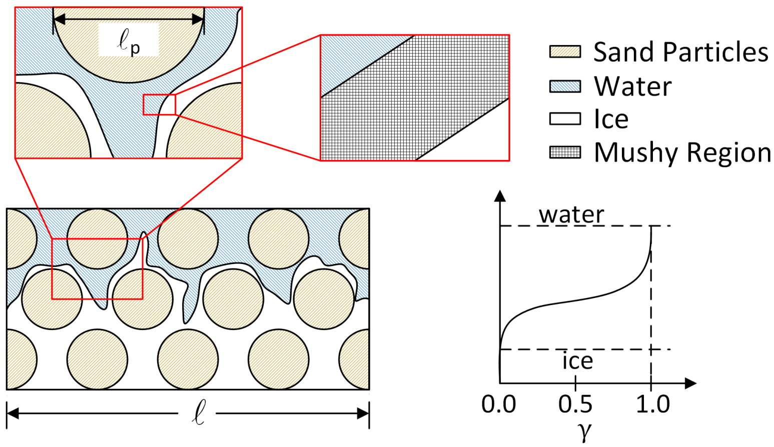

Figure 4.8 – Schematic of a volume element of a saturated porous medium. (after [36])

where α designate the phases: $\alpha = p$ for soil particles, $\alpha = \upsilon$ for void, $\alpha = \ell$ for liquid water, and $\alpha = s$ for solid water (ice). In addition,the mathematical model used here considers the Darcian (superficial) velocity $\mathbf{u}$ in its formation:

$$\mathbf{u} = \varepsilon \mathbf{u}_\ell \tag{4.10}$$

where $\mathbf{u}_\ell$ is the actual liquid velocity.

Before discussing the conservation equations, it is appropriate to illustrate certain volume fractions. In saturated soil structure, a volume element is mainly occupied by soil particles V_p and pores V_υ, that is ($V = V_s + V_\upsilon$). During AGF process, the pore groundwater could exist in liquid form (water), V_ℓ, or solid form (ice), V_s. Hence, the fluid fraction, ε, the liquid fraction within pore fluid, γ, and liquid fraction in an elementary volume, δ, could be defined as [36]:

$$\varepsilon = \frac{V_\upsilon}{V}; \quad 0 < \varepsilon \ < 1 \tag{4.11}$$

$$\gamma(t) = \frac{V_\ell(t)}{V_\upsilon}; \quad 0 < \gamma < 1 \tag{4.12}$$

$$\delta(t) = \frac{V_\ell(t)}{V} = \varepsilon\gamma(t); \quad 0 < \delta < \varepsilon \tag{4.13}$$

Within unfrozen soil region, the water is completely in the liquid form so that $\gamma = 1$ and $\delta = \varepsilon$. On the other hand, in frozen soil region, the pores are totally filled with ice, so $\gamma = \delta = 0$.

Considering the above mentioning descriptions, the conservation equations for ground structure could be written as:

— Conservation equation of mass:

$$\frac{\partial}{\partial t}(\rho) + \nabla \cdot (\rho \mathbf{u}) = 0 \tag{4.14}$$

— Conservation equation of momentum:

$$\frac{1}{\varepsilon}\frac{\partial}{\partial t}(\rho_\ell \mathbf{u}) + \frac{1}{\varepsilon^2}\left[\nabla \cdot (\rho_\ell \mathbf{u}\mathbf{u})\right] = \frac{1}{\varepsilon}\nabla \cdot \left(\mu_\ell \left(\nabla \mathbf{u} + \nabla \mathbf{u}^T\right)\right) - \nabla P + S_D + S_E + S_B + S_m \tag{4.15}$$

where S_D, S_E, S_B and S_m are Darcy, inertial (Ergun), buoyancy, and mushy source terms, respectively. They are given by

$$S_D = -\frac{\mu_\ell}{K}\mathbf{u} \tag{4.16}$$

$$S_E = -\frac{C_E}{K^{1/2}}\rho_\ell |\mathbf{u}|\mathbf{u} \tag{4.17}$$

The Darcy term S_D along with the inertial (Ergun) term S_E make up the total resistance to the flow. The inertial contribution, however, becomes more significant with groundwater seepage. At no-seepage, or at low seepage velocity, the inertial term is sufficiently low to be safely neglected. C_E stands for the Ergun coefficient; its value is basically based on the micro-structure of the porous medium [36]. The soil's permeability K is formulated, based on the Carman-Koseny equation, as a function of the liquid fraction δ and the characteristic length of a soil particle ℓ_p [21]:

$$K = \frac{\ell_p^2 \varepsilon^3}{180\left(1-\varepsilon\right)^2} \tag{4.18}$$

$$S_B = \rho_\ell \mathbf{g} \tag{4.19}$$

The buoyancy source term S_B is used to induce the natural convection within the voids.

$$S_m = -\mathbf{u} C_m \frac{\left(1-\gamma\right)^2}{\gamma^3} \tag{4.20}$$

The mushy source term S_m is a modified Darcy source term that is introduced to control the freezing process within the mushy zone. It has a zero value within the liquid region, where $\gamma = 1$, as depicted in Fig. 4.8. Within the mushy region, however, the value of γ decrease from 1 to 0, such that the value of S_m starts to dominates transient, convective, and diffusive terms. As γ approaches zero the mushy source term dominates all other terms in the momentum equation, Eqn. (4.15), and forces the superficial velocity to a value close to zero. Usually, a small constant is added to the source term's denominator in numerical simulations to avoid division by zero [22]. The mushy constant C_m is determined based on the morphology of the porous medium. In the current study, the value of this constant is set to a value of 5×10^6.

— Conservation equation of energy:

Based on the local volume averaging treatment, each phase in the porous medium is treated as a continuum, which generates two equations of energy for each phase coupled at the soil-void interface, A_{pv}. This assumption is known as the local thermal non-equilibrium (LTNE) hypothesis. The LTNE approach is imposed when the difference between the two local averaged temperatures, $T_p - T_v$, and the difference between the gradient of phase-averaged temperatures are significant. Hence, the conservation equation of energy for each phase could be written as:

soil particles:

$$(1-\varepsilon)\frac{\partial}{\partial t}(\rho_p h_p) = \nabla \cdot ((1-\varepsilon) k_p \nabla T_p) + \hbar_{pv} A_{pv} (T_p - T_v) \tag{4.21}$$

void:

$$\varepsilon \frac{\partial}{\partial t}(\rho_v h_v) + \nabla \cdot (\rho_l h_l \mathbf{u}) = \nabla \cdot (k_v \nabla T_v) + \hbar_{pv} A_{pv} (T_v - T_p) \tag{4.22}$$

Throughout AGF process, the voids, v, within a volume element could be occupied by liquid water, ice, or both. Therefore, the fusion term in the energy equation of the voids takes into account the sensible enthalpy, h_ℓ^S, as well as the latent heat of fusion, h_ℓ^L:

$$h_\ell = h_\ell^S + h_\ell^L \tag{4.23}$$

The groundwater properties are averaged over the liquid fraction within the void fluid as below:

$$(\rho_v h_v) = (\gamma \rho_\ell h_\ell + (1-\gamma)\rho_s h_s) \tag{4.24}$$

where:

$$k_v = \gamma k_\ell + (1-\gamma) k_s \tag{4.25}$$

$\hbar_{pv}$ is the overall convection heat transfer coefficient, which is determined experimentally. A_{pv} is the interfacial area between the soil particles and the void.

Returning to the LTE approach, when the temperature differences between soil particles, liquid water, and solid water at the void level ℓ_p, are much smaller than those occurring over the system level L

$$\Delta T_{\ell_p} < \Delta T_\ell << \Delta T_L \tag{4.26}$$

the local thermal equilibrium (LTE) can be implemented to solve the conservation equation of energy in a porous medium [21]. Basically, the LTE hypothesis considers that the local averaged temperatures of sands particle, T_P the voids, T_v, are equal. In general, the LTE assumption is valid when the time scale, t, satisfy [21]:

$$\frac{\varepsilon\left(\rho c_p\right)_v \ell^2}{t}\left(\frac{1}{k_v}+\frac{1}{k_p}\right)<<1 \tag{4.27}$$

and

$$\frac{(1-\varepsilon)\left(\rho c_p\right)_p \ell^2}{t}\left(\frac{1}{k_v}+\frac{1}{k_p}\right)<<1 \tag{4.28}$$

Also, the length scale must satisfy [21]:

$$\frac{\varepsilon k_v \ell}{A_{pv} L^2}\left(\frac{1}{k_v}+\frac{1}{k_p}\right)<<1 \tag{4.29}$$

and

$$\frac{(1-\varepsilon) k_p \ell}{A_{pv} L^2}\left(\frac{1}{k_v}+\frac{1}{k_p}\right)<<1 \tag{4.30}$$

In addition, Minkowycz et al. [38] discussed the validity of LTE assumption in terms of Sparrow number, S_p

$$S_p=Nu\left(\frac{k_v}{k_e}\right)\left(\frac{L}{\ell_p}\right)^2 \tag{4.31}$$

where Nu is defined as a constant; ~ 1.0. They stated that a sufficiently large Sparrow number is indicative of the presence of an LTE condition.

Based on these definitions, one can combine Eqns. (4.21) and (4.22), and formulate a single LTE conservation equation of energy as below:

$$\frac{\partial}{\partial t}\left[\varepsilon\left(\gamma \rho_\ell h_\ell^S+(1-\gamma) \rho_s h_s\right)+(1-\varepsilon) \rho_p h_p\right]+ \nabla \cdot\left(\rho_\ell h_\ell^S \mathbf{u}\right)=\nabla \cdot\left(k_e \nabla T\right)+S_H \tag{4.32}$$

where k_e is the effective thermal conductivity of the porous ground. There are several ways to calculate k_e. Kaviany [21] listed several approaches to predict the effective thermal conductivity of a porous ground structure. We examined several approaches that predict k_e; the parallel-arrangement approach agreed best with experimental data. Therefore, it is used in this study:

$$k_e=\varepsilon k_v+(1-\varepsilon) k_p \tag{4.33}$$

The source term S_H is used to induce the latent heat of fusion during the phase-change - it is given by:

$$S_H=-\left[\left(\varepsilon \rho_\ell h_\ell^L \frac{\partial \gamma}{\partial t}\right)+\left(\nabla \cdot\left[\rho_\ell \mathbf{u} \gamma h_\ell^L\right]\right)\right] \tag{4.34}$$

It should be noted here that the source term S_H is equal to zero when no phase-change takes place (i.e. when $(\partial\gamma/\partial t)$ and $(\nabla \cdot \gamma)$ equal to zero). In the mushy region, however, the temporal and transient liquid fraction start to change, which activate the source term in Eqn. (4.32).

4.3.2 Initial and boundary conditions

The initial and boundary conditions of the conjugate heat transfer problem between the freeze pipe and the surrounding porous structure are:

- *Initial condition* —Initial temperature and initial velocity at $t = 0$

$$T_g = T_c = T_{init}, \quad \overline{\mathbf{U}} = \mathbf{u} = \mathbf{u}_{init} \tag{4.35}$$

- *Freeze pipe inlet* —Dirichlet boundary conditions for mass flow rate and inlet temperature.

$$\dot{m} = \dot{m}_{in}, \quad T = T_{in} \tag{4.36}$$

- *Freeze pipe outlet* —Dirichlet boundary condition for pressure, and Neumann boundary condition for temperature.

$$P = P_{out}, \quad \mathbf{n} \cdot \nabla T = 0 \tag{4.37}$$

- *Freeze pipe's wall: inner and outer* —Dirichlet boundary condition of no slip wall.

$$\mathbf{u}_w = 0 \tag{4.38}$$

- *Freeze pipe's wall: outer* —Thermally coupled boundary conditions defined as below:

$$q_w = \pm k_w \frac{\partial T}{\partial x} \tag{4.39}$$

$$k_c \frac{\partial T_c}{\partial n} = k_w \frac{\partial T}{\partial n}; \quad T_c = T \tag{4.40}$$

$$k_g \frac{\partial T_g}{\partial n} = k_w \frac{\partial T}{\partial n}; \quad T_g = T \tag{4.41}$$

  where $n=$ normal to the surface in question.

4.4 Numerical simulations

The computational domain was created and meshed using ANSYS software package 16.12. A mesh-independent solution was ensured by comparing with results obtained using a coarse mesh consisting of 5×10^3 elements, followed by several mesh-adaptation until the difference in computed ground's temperature was below 1%, with a final mesh size of 6.3×10^5. The LTE hypothesis was implemented in this study after satisfying the criteria mentioned in Eqns. (4.27) - (4.31). The time scale, t, and length scale, L, are in the order of 10^{-6} and 10^{-5}, respectively; Sparrow number, S_p, on the other hand, is in the order of 10^6 which is large enough to consider the LTE hypothesis. The governing equations together with initial and boundary conditions were solved using ANSYS Fluent 16.2 software, that is based on finite volume method. Additionally, user-defined functions (UDFs) was used to specify the transient inlet temperature, inlet velocity, and the temperature dependent properties of water (see Fig. 4.5) and brine (see Fig. 4.4). The numerical model has solved with the Semi-Implicit Pressure-Linked Equation (SIMPLE) algorithm and second-order upwind discretization. The convergence criteria were set to 1×10^{-5} for all equations.

4.5 Model validation

The mathematical model was validated against experimental results. The actual inlet temperatures of the glycol have some deviation as compared to the nominal inlet temperatures due to some heat gain through the pipe distribution system, as shown in Fig. 4.9. However, the mathematical model has been validated using the actual inlet temperature using user-defined functions (UDFs). The flow rate was measured at the inlet of the main pipe and the inlet of one of the freeze pipes. The flow rate at the other freeze pipe was assumed to be the difference between the flow meters' readings. The equations of the fitted curves, that shown in Fig. 4.10, were fed into the simulation, as boundary conditions in Eqn. (4.36), using UDF file. The model monitors the ground's temperature at three different levels in addition to the coolant's outlet temperatures of each freeze pipe. Good agreement between the model and the experimental data was observed, which can be discerned from Fig. 4.11; a comprehensive validation for all 7 cases is listed in Appendix A. The numerical results of the outlet temperatures (outlet temp. 1 and outlet temp. 2 in Fig. 4.11) show small deviations from the experimental results (maximum 1.5 [°C]). The reason behind these small deviations is that the thermocouples that measure the outlet temperatures are located at the top of the tank (see Fig. 4.2 (c)). Although the pipes connections are well insulated, in some extreme cases, they capture some heat from the ambient.

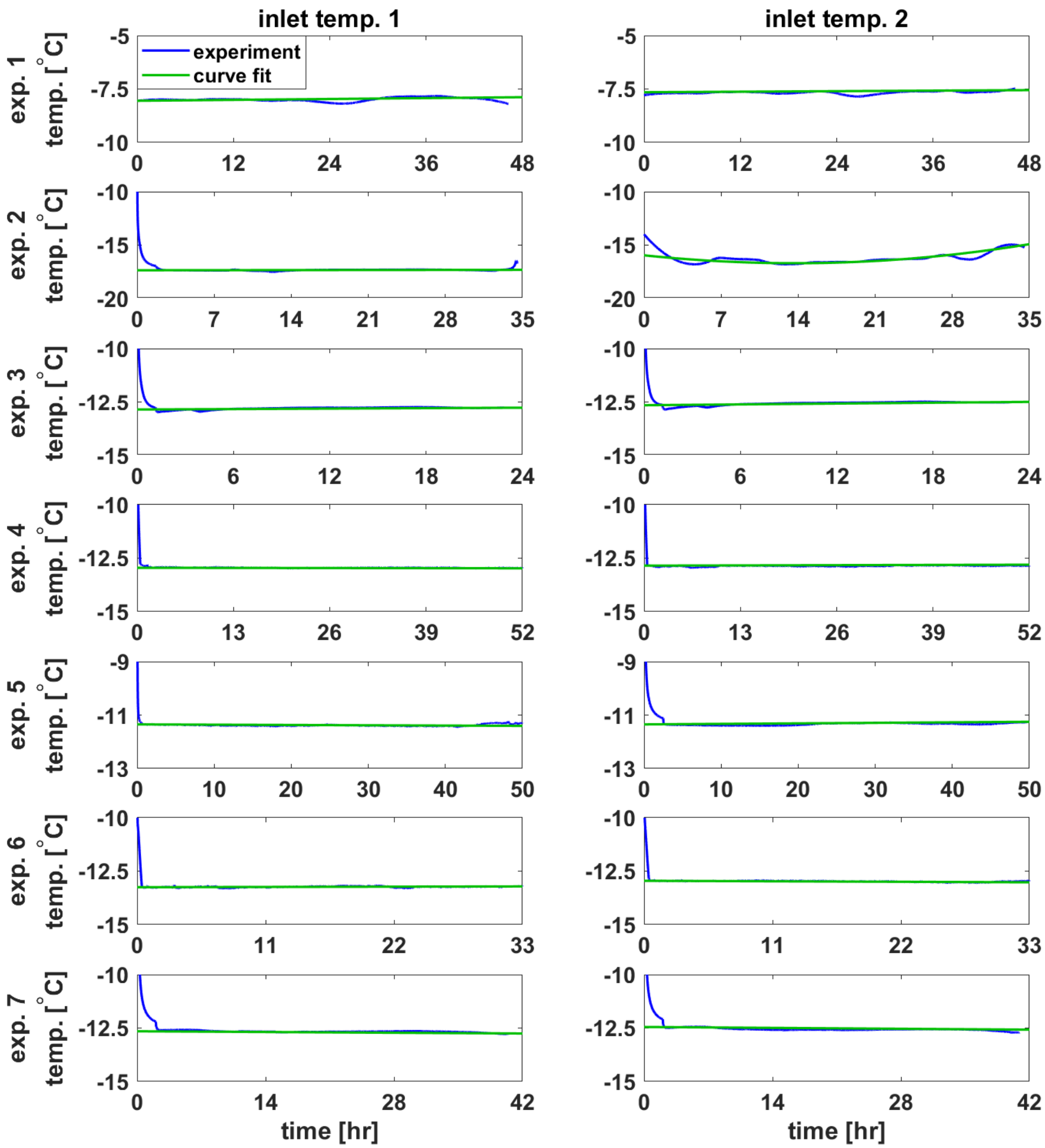

Figure 4.9 – The coolant's inlet temperatures of each experiment. exp. 1: inlet temperature at -10 [°C]; exp. 2: inlet temperature at -20 [°C]; exp. 3 ground's initial temperature at 20 [°C]; exp. 4: ground's initial temperature at 30 [°C]; exp. 5: coolant's flow rate at 2.5 [ml/s]; exp. 6: coolant's flow rate at 10 [ml/s]; and exp. 7: is the base case (see Table 4.3)

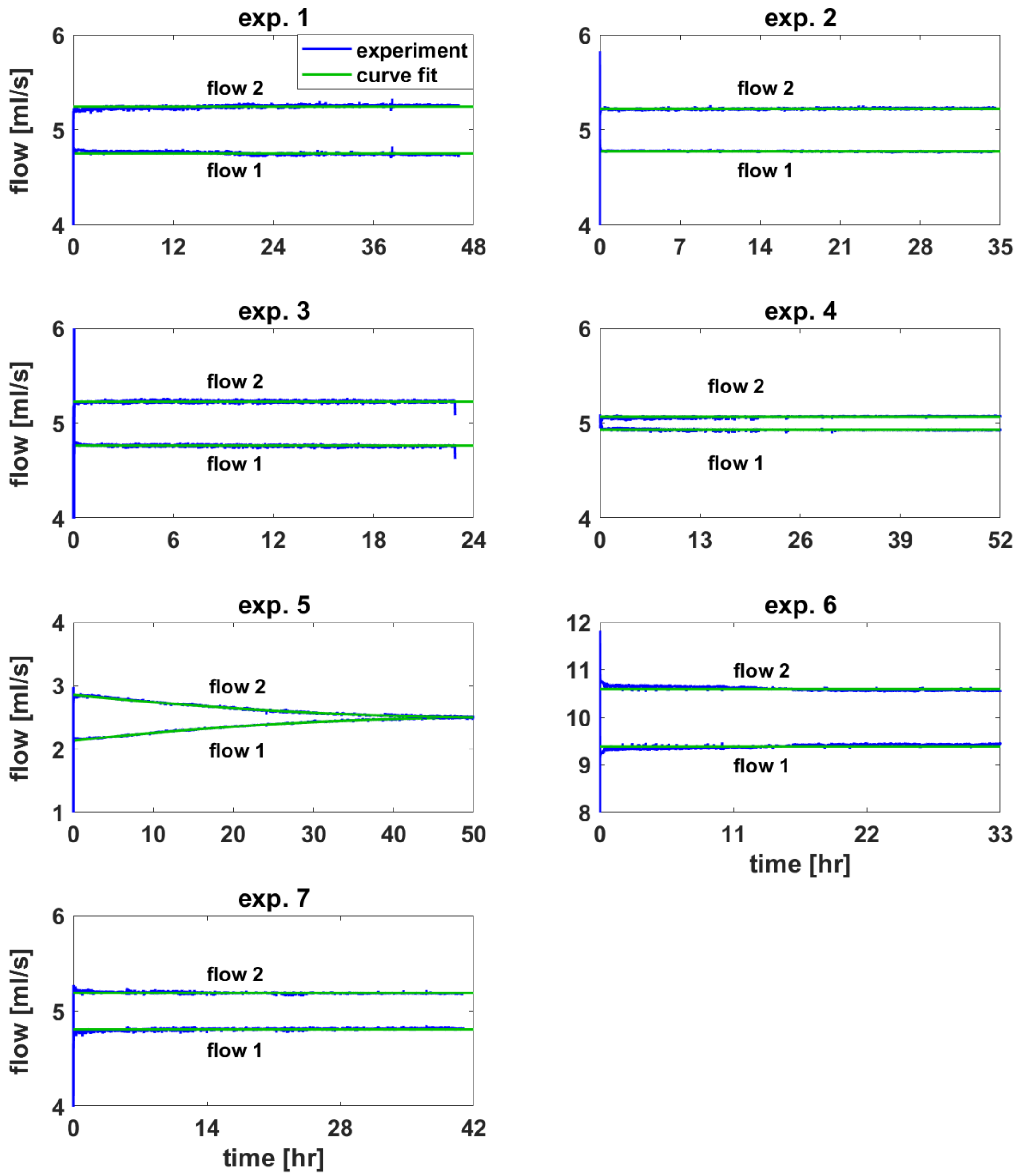

Figure 4.10 – The inlet flow rates of each experiment. exp. 1: inlet temperature at -10 [°C]; exp. 2: inlet temperature at -20 [°C]; exp. 3 ground's initial temperature at 20 [°C]; exp. 4: ground's initial temperature at 30 [°C]; exp. 5: coolant's flow rate at 2.5 [ml/s]; exp. 6: coolant's flow rate at 10 [ml/s]; and exp. 7: is the base case (see Table 4.3)

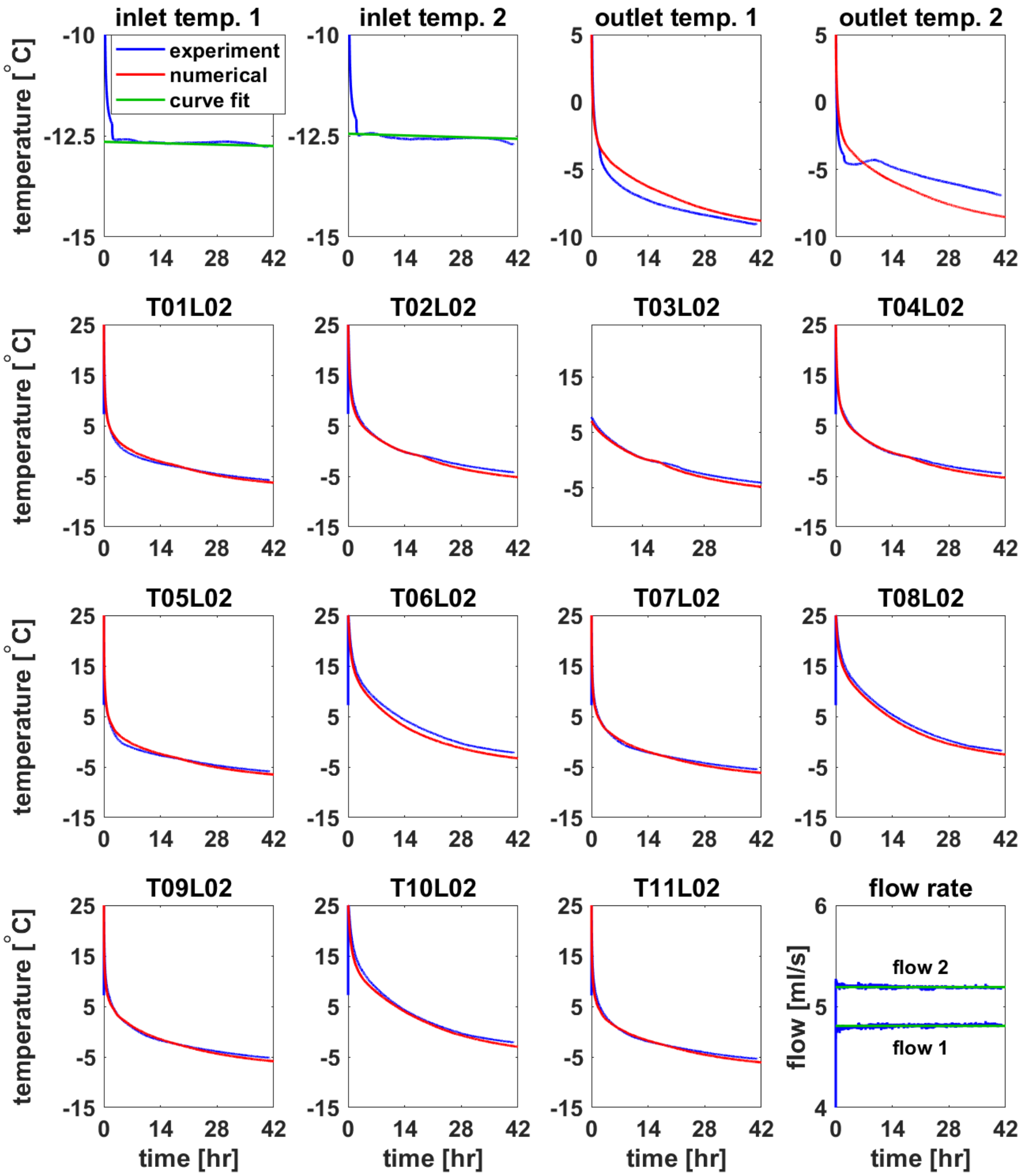

Figure 4.11 – The validation of the mathematical model with the base-case experiment (see Table 4.3). The results show the coolant's outlet temperatures with ($R^2 = 0.881$), the ground's temperature at level-02 (Fig. 4.2) with ($R^2 = 0.991$), and the curve fit of the coolant's inlet temperature and flow rate.

4.6 Results and discussion

4.6.1 Coolant's flow rate

The coolant's flow is one of the primary parameters that control the heat transfer in AGF process. The sub-zero coolant absorbs the heat from the surrounding saturated ground while flows in the freeze pipes. Once the ground's temperature reaches the freezing point, the pore liquid water transfers gradually into ice. The closure time is highly affected by the coolant's flow rate, as illustrated in Figs. 4.12 (a) and 4.13 (a). At flow rate of 2.5 [ml/s], the closure time was 41.64 [hr]. The time decreases into 21.33 [hr] and 12.46 [hr] as the flow rate was doubled into 5.0 [ml/s] and 10 [ml/s], respectively. It is clear that the closure time reduced almost 50% when the flow rate is doubled. To illustrate this, it is instructive to recall the definition of the convective heat transfer, which is the dominating mechanism of heat transfer in the freeze pipe. According to Newton's law of cooling, the rate of convective heat transfer per unit area (i.e. convective heat flux) is proportional to the temperature difference between the wall and the fluid's flow ($\dot{q} \propto \Delta T$) [39]. In order to quantify this relation, the heat transfer coefficient, $\hbar$, is introduced, and the relationship between the heat flux and the temperature difference becomes $\dot{q} = \hbar \Delta T$. The heat transfer coefficient, $\hbar$, is a function of the Nusselt number, which, in case of turbulent flow, is a function of Reynold's and Prandtl numbers, $Nu = f(Re, Pr)$. Hence, the convective heat transfer, $\dot{q}$, increased with increasing the flow rate. In the ground, on the other hand, a phase change process occurs due to the sub-zero flow in the pipe. This process includes three main stages: (i) sensible cooling of the pore liquid water, (ii) phase change from water to ice at constant temperature (i.e., freezing temperature), and (ii) sensible cooling of the pore ice. In the second stage, the latent heat of fusion is released by liquid water to solidify. The time needed for this stage to finish highly depends on the heat removal rate from the convective heat transfer in the bayonet freeze pipe, as inferred in Fig. 4.13 (a). Hence, by combining these mechanisms in this conjugate heat transfer problem, the closure time reduced almost 50 % once the flow rate is doubled.

4.6.2 Coolant's inlet temperature

The temperature difference between two medium or zones is another parameter that drives the heat transfer. In AGF process, the temperature difference between the ground structure and the sub-zero coolant force the heat flux from the ground structure toward the freeze pipes. Figs 4.12 (b) and 4.13 (b) show the influence of the coolant's temperature on the closure time and the ground response. At coolant's temperature of -20 [°C], the closure time is 10.68 [hr]. The time increases to 21.33 [hr] at coolant's temperature of -15 [°C], and to

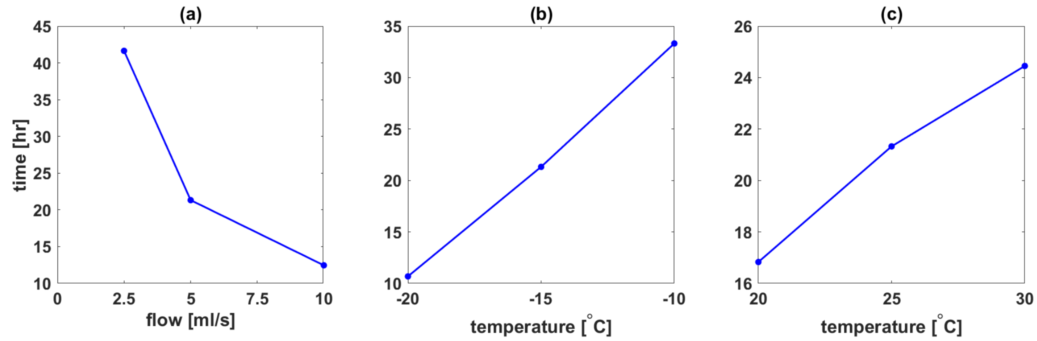

Figure 4.12 – The effect of (a) the coolant's flow rate; (b) coolant's inlet temperature; and (c) ground's initial temperature on the closure time.

33.32 [hr] at coolant's temperature of -10 [°C]. It is almost a linear relationship with a slope of 2.26. Based on the relationship between heat flux and temperature, $\dot{q} \propto T$, the linear relationship between the coolant's temperature and the closure time is clear. The convective and diffusive term in Eqn. (4.4) emphasize the linear influence of the coolant's temperature on the total energy, and as a result, on the closure time.

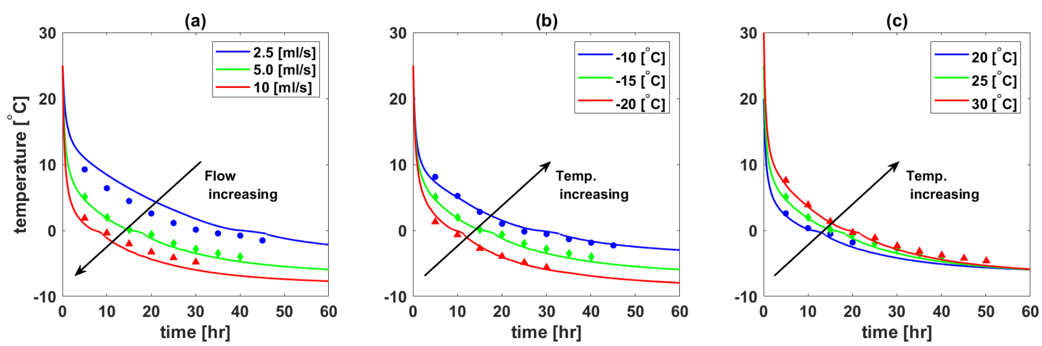

Figure 4.13 – The effect of (a) coolant's flow rate; (b) coolant's inlet temperature; and (c) ground's initial temperature on the ground temperature between two pipes (T03 in Fig. 4.3). Line: model; symbols: experiments

4.6.3 Ground's initial temperature

The ground's initial temperature is a site-base operating condition that influences the time of the AGF process. This parameter, however, has the least effect on the closure time and ground's behavior, as inferred in Figs 4.12 (c) and 4.13 (c). At the initial temperature of 20 [°C], the closure time is 16.83 [hr]. The time increases to 21.33 [hr] and 24.45 [hr] at the initial temperature of 25 [°C] and 30 [°C], respectively. It is almost a linear relationship with a slope of 0.7622. The slope in the time-ground's temperature relation, as well as time-coolant's temperature relation, provide the weight of each parameter as a significant influence on the closure time and ground response. The higher the slope the higher the effect of the parameter on the closure time. During AGF process, the ground's temperature between the freeze pipes reduces significantly due to the continuous freezing. Therefore, the initial ground's temperature has a higher influence on the ground's response at the beginning of AGF process. With time, the ground's temperature, as shown in Fig. 4.13, will converge into the same value, where the coolant's flow rate and temperature become the dominant parameters.

4.7 Conclusions

This chapter highlighted the contribution of building a state-of-the-art laboratory scale experimental setup that mimics the artificial ground freezing process. The scale-down design of the apparatus took into consideration the actual design of the artificial ground freezing. The design was determine to conduct a lab-scale experiment within a short time-frame. The physical model, the material properties, and the initial and boundary conditions were elaborated in details. The enthalpy-porosity technique has been used in the mathematical model to validate the experimental data. The model shows very good agreement with the experimental results. Also, parametric studies were conducted to evaluate the effect of operating parameters on the closure time. The coolant's flow rate has the highest effect on the closure time, as compared to other operating parameters. This chapter could be used as a reference for phase change processes in porous media, especially AGF and permafrost soil.

References

[1] Helmut HaB and Peter Schafers. Application of ground freezing for underground construction in soft ground. In *Geotechnical Aspects of Underground Construction in Soft Ground: Proceedings of the 5th International Symposium TC28. Amsterdam, the Netherlands, 15-17 June 2005*, page 405. CRC Press, 2013.

[2] Manon Vitel, Ahmed Rouabhi, Michel Tijani, and Frédéric Guérin. Thermo-hydraulic modeling of artificial ground freezing: Application to an underground mine in fractured sandstone. *Computers and Geotechnics*, 75:80–92, 2016.

[3] Renshu Yang, Qianxing Wang, and Liyun Yang. A closed-form elastic solution for irregular frozen wall of inclined shaft considering the interaction with ground. *International Journal of Rock Mechanics and Mining Sciences*, 100(Supplement C):62 – 72, 2017.

[4] Yongshui Kang, Quansheng Liu, Yong Cheng, and Xiaoyan Liu. Combined freeze-sealing and new tubular roof construction methods for seaside urban tunnel in soft ground. *Tunnelling and Underground Space Technology*, 58:1–10, 2016.

[5] E Pimentel, S Papakonstantinou, and G Anagnostou. Numerical interpretation of temperature distributions from three ground freezing applications in urban tunnelling. *Tunnelling and Underground Space Technology*, 28:57–69, 2012.

[6] Lei Guo, Zhongqiu Zhang, Xinbin Wang, Qihao Yu, Yanhui You, Chang Yuan, Yanli Xie, and Tingtao Gou. Stability analysis of transmission tower foundations in permafrost equipped with thermosiphons and vegetation cover on the qinghai-tibet plateau. *International Journal of Heat and Mass Transfer*, 121:367–376, 2018.

[7] I.K. Iskandar and T.F. Jenkins. Potential use of artificial ground freezing for contaminant immobilization. In *Proceedings of the International Conference on New Frontiers for Hazardous Waste Management (September 15-18), Pittsburgh. Washington, DC: US Environmental Protection Agency*, pages 128–137, 1985.

[8] John S Harris. *Ground freezing in practice*. Thomas Telford, 1995.

[9] Orlando B Andersland and Branko Ladanyi. *Frozen Ground Engineering*. John Wiley & Sons, 2004.

[10] Francesca Casini, Antonio Gens Solé, Sebastià Olivella Pastallé, and Giulia Viggiani. Artificial ground freezing of a volcanic ash: laboratory tests and modelling. *Environmental Geotechnics*, 3(3):1–14, 2016.

[11] Greg Newman, Lori Newman, Denise Chapman, and Travis Harbicht. Artificial ground freezing: An environmental best practice at cameco's uranium mining operations in northern saskatchewan, canada. In *11th International Mine Water Association Congress–Mine Water–Managing the Challenges*, 2011.

[12] Iskandar K. Iskandar. Effect of freezing on the level of contaminants in uncontrolled hazardous waste sites. part 1. literature review. *Cold Regions Research and Engineering Laboratory*, 86(19):1–33, 1986.

[13] Iskandar K. Iskandar. Ground freezing controls hazardous waste. *Military Engineer*, 79:455–456, 1987.

[14] FJ Sanger and FH Sayles. Thermal and rheological computations for artificially frozen ground construction. *Engineering Geology*, 13(1-4):311–337, 1979.

[15] John T Holden. Improved thermal computations for artificially frozen shaft excavations. *Journal of Geotechnical and Geoenvironmental Engineering*, 123(8):696–701, 1997.

[16] Yang Zhou, Xiao-xue Hu, Ting Li, Dong-hai Zhang, and Guo-qing Zhou. Similarity type of general solution for one-dimensional heat conduction in the cylindrical coordinate. *International Journal of Heat and Mass Transfer*, 119:542–550, 2018.

[17] Ahmed Rouabhi, M Tijani, O Stab, Y Charnavel, and T You. A semi-analytical approach for modelling heat transfer during salt-cavern leaching process. *International Journal for Numerical and Analytical Methods in Geomechanics*, 32(13):1617–1634, 2008.

[18] Spyridon Papakonstantinou, Georgios Anagnostou, and Erich Pimentel. Evaluation of ground freezing data from the naples subway. *Proceedings of the Institution of Civil Engineers-Geotechnical Engineering*, 166(3):280–298, 2013.

[19] Manon Vitel, Ahmed Rouabhi, Michel Tijani, and Frédéric Guérin. Modeling heat transfer between a freeze pipe and the surrounding ground during artificial ground freezing activities. *Computers and Geotechnics*, 63:99–111, 2015.

[20] Ye Wang, Xintong Xia, Yi Wang, Liangbi Wang, and Wenting Hu. Using proper orthogonal decomposition to solve heat transfer process in a flat tube bank fin heat exchanger. *Advances in Geo–Energy Research*, 1(3):158–170, 2017.

[21] Maasoud Kaviany. *Principles of heat transfer in porous media*. Springer Science & Business Media, 2012.

[22] JH Nazzi Ehms, R De Césaro Oliveski, LA Oliveira Rocha, and C Biserni. Theoretical and numerical analysis on phase change materials (pcm): A case study of the solidification process of erythritol in spheres. *International Journal of Heat and Mass Transfer*, 119:523–532, 2018.

[23] Chang-Yu Ou, Chung-Cheng Kao, and Ching-I Chen. Performance and analysis of artificial ground freezing in the shield tunneling. *Journal of GeoEngineering*, 4(1):29–40, 2009.

[24] Manon Vitel, Ahmed Rouabhi, Michel Tijani, and Frédéric Guérin. Modeling heat and mass transfer during ground freezing subjected to high seepage velocities. *Computers and Geotechnics*, 73:1–15, 2016.

[25] Ahmed Marwan, Meng-Meng Zhou, M Zaki Abdelrehim, and Günther Meschke. Optimization of artificial ground freezing in tunneling in the presence of seepage flow. *Computers and Geotechnics*, 75:112–125, 2016.

[26] Ahmed Rouabhi, E Jahangir, and H Tounsi. Modeling heat and mass transfer during ground freezing taking into account the salinity of the saturating fluid. *International Journal of Heat and Mass Transfer*, 120:523–533, 2018.

[27] AD Brent, VR Voller, and KTJ Reid. Enthalpy-porosity technique for modeling convection-diffusion phase change: application to the melting of a pure metal. *Numerical Heat Transfer, Part A Applications*, 13(3):297–318, 1988.

[28] Vaughan R Voller and C Prakash. A fixed grid numerical modelling methodology for convection-diffusion mushy region phase-change problems. *International Journal of Heat and Mass Transfer*, 30(8):1709–1719, 1987.

[29] Wolfgang Ständer. *Mathematische Ansätze zur Berechnung der Frostausbreitung in ruhendem Grundwasser im Vergleich zu Modelluntersuchungen für verschiedene Gefrierrohranordnungen im Schactund Grundbau*, volume 28. Technische Hochschule Fridericiana, Institut für Bodenmechanik und Felsmechanik, 1967.

[30] Herbert Victor. *Die Frostausbreitung beim künstlichen Gefrieren von Böden unter dem Einfluss strömenden Grundwassers*, volume 42. Univ., Inst. f. Bodenmechanik u. Felsmechanik, 1969.

[31] E Pimentel, A Sres, and G Anagnostou. Modelling of ground freezing in tunnelling. In *Underground Space-the 4th Dimension of Metropolises, ITA and World Tunnel Congress, Prague*, pages 331–336, 2007.

[32] E Pimentel, A Sres, and G Anagnostou. Large-scale laboratory tests on artificial ground freezing under seepage-flow conditions. *Geotechnique*, 62(3):227, 2012.

[33] Suhas Patankar. *Numerical heat transfer and fluid flow*. CRC press, 1980.

[34] Mahmoud A Alzoubi and Agus P Sasmito. Thermal performance optimization of a bayonet tube heat exchanger. *Applied Thermal Engineering*, 111:232–247, 2017.

[35] Agus P Sasmito, Erik Birgersson, Hung C Ly, and Arun S Mujumdar. Some approaches to improve ventilation system in underground coal mines environment–a computational fluid dynamic study. *Tunnelling and Underground Space Technology*, 34:82–95, 2013.

[36] C Beckermann and R Viskanta. Natural convection solid/liquid phase change in porous media. *International Journal of Heat and Mass Transfer*, 31(1):35–46, 1988.

[37] N Moussa, B Goyeau, H Duval, and D Gobin. Macroscopic model for solidification in porous media. *International Journal of Heat and Mass Transfer*, 113:704–715, 2017.

[38] WJ Minkowycz, A Haji-Sheikh, and Kf Vafai. On departure from local thermal equilibrium in porous media due to a rapidly changing heat source: the sparrow number. *International Journal of Heat and Mass Transfer*, 42(18):3373–3385, 1999.

[39] A. F. Mills. *Heat Transfer*. Prentice Hall, 1999.

Chapter 5

Heat transfer analysis in artificial ground freezing under high seepage: Validation and heatlines visualization

Contents

Preface (Linking Paragraph)

One of the main safety concerns that challenge the artificial ground freezing system is to isolate the groundwater seepage from the working areas. The impact of the groundwater flow on the creation of a frozen body is significant, and thus should be considered in the simulations of the AGF process. This chapter utilizes the framework of the mathematical model presented in Chapter 4 to quantify the performance of AGF system under various seepage conditions. The work conducted here provides a more profound understanding of the seepage effect by employing the concept of heatlines in the analysis. The below article has been submitted based on the discussion of this chapter:

Alzoubi, M. A. and Sasmito, A. P. (2018). *Heat transfer analysis in artificial ground freezing under high seepage: Validation and heatlines visualization*, submitted to International Journal of Thermal Sciences, 2018, under review.

Abstract

The primary goal of artificial ground freezing (AGF) system is to create a hydraulic barrier encircling working areas and stall groundwater seepage. This goal is achieved once a consolidated frozen wall is developed between the freeze pipes. Groundwater flow, however, has an undesirable effect on the formation and the growth rate of the frozen body - high water flow could hamper, totally, the establishment of a merged frozen wall between two freeze pipes. Therefore, it is of great interest to evolve a reliable prediction of the transient response of the ground structure toward the AGF process under high seepage flow conditions. This work interprets the multiphase heat transfer that accompanying the development of a frozen body between two freeze pipes with and without the presence of the groundwater seepage. A mathematical model has been derived, validated, and implemented to simulate the effect of the coolant's temperature, the spacing between two freeze pipes, and the seepage temperature on the closure time and the shape of the frozen body. The results are presented in terms of temperature fields, phase-change interface, velocity-streamlines, and heatlines. The results indicate that spacing between two pipes and seepage velocity have the highest impact on the closure time and the frozen body width.

5.1 Introduction

Artificial ground freezing (AGF) is employed in many practical engineering applications, for example, in underground mines [1], tunneling [2, 3], and environmental engineering (hazardous waste management) [4–6]. Groundwater seepage may have a strong impact on the AGF process, affecting the development of the frozen body, closure time, and, in specific circumstances, prevent the creation of a close, frozen body between two freeze pipes. Understanding the coupled thermal and hydraulic mechanisms associated with AGF process is crucial in many processes, and is thus of considerable practical and theoretical interest.

A typical AGF system consists of two primary domains: (i) the flow of sub-zero coolant in a network of freeze pipes, and (ii) porous ground structure surrounding the pipes. The heat flow between the adjacent domains occurs through the coupled pipe's wall; this is termed a conjugate problem. The physical processes associated with the conjugate, multi-phase AGF process has been discussed thoroughly in our previous work [7].

The freezing process in the ground is governed by two main mechanisms of energy transfer: conductive heat transfer, and forced-convective heat transfer due to groundwater seepage. Since the first model elaborated by Sagner and Sayles [8], several studies [9–12] addressed the freezing process by solving the conduction energy equation; thus considering the conduction as the principal mechanism of energy transfer. In the last decade or so, various researches discussed a saturated porous medium subject to groundwater seepage [13–20]. These studies modeled the thermal-hydraulic mechanisms by solving the conservation equation of mass and energy. The effect of the groundwater seepage is formulated as a function of the capillary pressure at the phase-change interface. Huang et al. [14] considered the effect of segregation potential in the formulation of the water seepage, which is a function of the average suction in the freezing interface. Yu et al. and McKenzie et al. and [16, 17] modeled the seepage velocity as a function of the water head and the specific yield (the volume of water drained-out from a given porous medium under the forces of gravity), and pressure storativity (the volume of water released from a saturated pore aquifer due to a unit drop in hydraulic head per total volume), respectively. Also, Fowler and Krantz [13] employed the cryostatic suction in the formulation of the groundwater seepage. On the other contrary, in order to model the thermal aspects of the phase-change phenomenon, the latent heat of fusion, in these studies, was added to the specific heat capacity of water; this approach is known as the apparent heat capacity approximation. These approaches, however, require careful consideration of the temperature, velocity, and latent heat progression in the freezing interface [21]. Alternatively, other researchers [7, 22] implemented the enthalpy-porosity approach proposed by Voller and Prakash [23]. This method represents the phase-change interface as a porous zone; the movement of the freezing interface is governed by a modified Darcy source term in the conservation equation of momentum. The enthalpy-porosity is introduced to simplify the modeling requirements without compromising the accuracy of the results. König-Haagen et al. [24] conducted a comprehensive study to evaluate the corresponding accuracy of the most used macroscopic energy formulations. They concluded that, as a role of thumb, the enthalpy-porosity formulations are more robust and precise, as compared to the apparent heat capacity approach.

In conductive heat transfer problems, heat-flux lines and isotherms are commonly used as standard techniques to visualize the heat transfer. Yet, once convective heat transfer is introduced, either naturally or forced by a fluid flow, one cannot generate an accurate picture of net energy flow by only monitoring these visualization tools. Instead, Kimura and Bejan [25] introduced a generalized concept that could be used to visualize the transfer of heat by fluid flow in convective heat transfer problems, which could be extended to include phase-change processes. Named as "Heatlines Visualisation," the approach is an attractive option that could be dealt with as the convection counterpart of the heat-flux lines used in conduction problems. To the best of our knowledge, however, limited literature (for example [26–28]) applied this concept to visualize the net energy flow in forced-convective heat transfer problems that include phase-change processes.

To continue the work on mathematical modeling and computation of the artificial ground freezing, the mechanistic model by Alzoubi et al. [7, 29] is extended to quantify the impact of the groundwater seepage on the progression of the frozen body; in particular, the effect on the closure time and the shape and thickness of the frozen wall. Within this framework, a study is then carried out to evaluate how key factors - spacing between freeze pipes, seepage velocity, coolant's temperature, and seepage's temperature - affect the performance of AGF process. In essence, the mechanistic model considers the two-phase conservation of mass, momentum, and energy. The results are demonstrated in terms of closure time, temperature fields, phase-change iso-therms, streamlines, and heatlines.

In the following, the model development along with its numerical implementation is described in the first part. A brief discussion of the model validation is followed in the second part. The results of a parametric study that highlights the influence of the design and operating conditions of an AGF system is then carried out. Finally, conclusions are drawn with emphasis on the impact of various design and operating parameters on the AGF under seepage conditions.

5.2 Model development

Fig. 5.1(a) shows a schematic diagram of a typical AGF system with parallel freeze pipes configuration. A horizontal cross-section that contains two freeze pipes and the surrounding porous ground structure is considered in this study, as illustrated in Fig. 5.1(b). In order to reduce the AGF model from a general 3D model to a 2D geometry, which describes a cross-section, the model is limited to a plane in which the groundwater flow and heat transfer in the axial direction (z-direction) are small enough to be neglected as compared to the horizontal directions. Further, the freeze pipes in this study are arranged in a uniform parallel configuration. The interaction between each two freeze pipes is assumed to be identical; thus the domain under consideration is set as a 2D symmetry geometry. The dimensions of the computational domain, the thermo-physical properties of the ground, and the initial and boundary conditions are based on Pimental et al. experiment [30, 31].

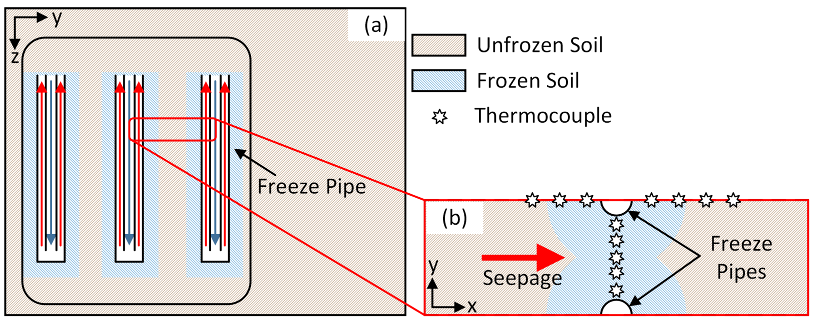

Figure 5.1 – (a) schematic diagram of a typical AGF system. (b) Computational domain that includes two freeze pipes

5.2.1 Governing equations

A mathematical model is developed to study the artificial freezing process within a fully saturated porous medium. The domain comprises a solid matrix containing spaces (pores) filled with one or several water phases. The following discussion intends to describe the mass, momentum, and energy equations that govern the thermal and hydraulic aspects of the AGF process. Detailed description of all parameters can be found in the Nomenclature. The local volume averaging approximation is implemented over a representative elementary volume to formulate the conservation equations through which the porous medium is treated as a continuum, as depicted in Fig. 5.2. Within this volume element, any local quantity θ is converted into a volume-averaged value Θ using the following expression [32]:

$$\Theta = \frac{1}{V}\int_V \theta dV \tag{5.1}$$

Also, the pore velocity is defined, based on Dupuit-Forchheimer relationship [34], as ($\mathbf{u} = \varphi\mathbf{u}_\ell$), φ is the porosity, and $\mathbf{u}_\ell$ is the pore water velocity. The governing equations could be written under the local volume averaging approach as below:

— Conservation equation of mass:

$$\frac{\partial}{\partial t}(\rho) + \nabla\cdot(\rho\mathbf{u}) = 0 \tag{5.2}$$

— Conservation equation of momentum [23, 32]:

$$\frac{1}{\varphi}\frac{\partial}{\partial t}(\rho_\ell\mathbf{u}) + \frac{1}{\varphi^2}\left[\nabla\cdot(\rho_\ell\mathbf{u}\mathbf{u})\right] = \frac{1}{\varphi}\nabla\cdot\left(\mu_\ell\left(\nabla\mathbf{u}+\nabla\mathbf{u}^T\right)\right) - \nabla p - \underbrace{\frac{\mu_\ell}{K}\mathbf{u}}_{S_D} - \underbrace{\frac{C_F}{K^{1/2}}\rho_\ell|\mathbf{u}|\mathbf{u}}_{S_F} - \underbrace{\mathbf{u}C_m\frac{(1-\gamma)^2}{\gamma^3}}_{S_m} \tag{5.3}$$

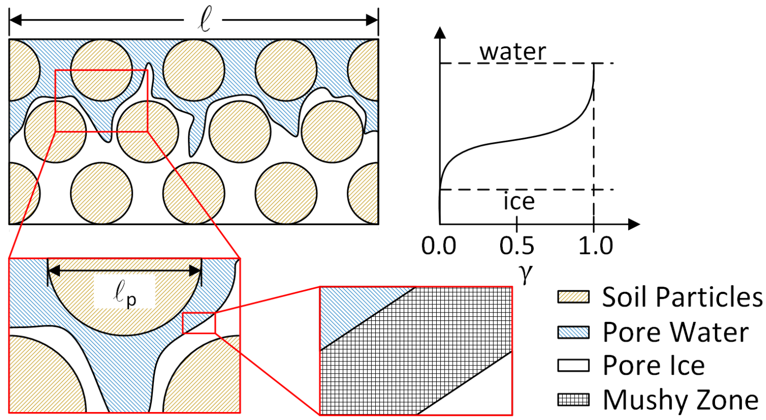

Figure 5.2 – Schematic of the freezing process in a porous medium, considering the phase-change interface as a mushy zone. (after [33])

where S_D, S_F, and S_m are Darcy, Forchheimer, and mushy source terms, respectively. The contribution of the natural convection is insignificant as compared to the contribution of the convective flow. Thus, it has been ignored in this study.

The Darcy and Forchheimer terms represent the total resistance to the flow. The quadratic Forchheimer's term, S_F, is added for high seepage cases. C_F is a friction factor commonly known as Ergun's coefficient [33]. The soil's permeability K is formulated, based on the semi-empirical Carman-Koseny equation [32], as a function of the porosity φ and the diameter of a soil particle D_p:

$$K = \frac{D_p^2 \varphi^3}{C_0 \left(1 - \varphi\right)^2} \tag{5.4}$$

The empirical coefficient C_0 is usually taken to be a constant (180 in this study) and can be adapted for various soil geometries.

The last term in Eq. (5.3), S_m, is a modified Darcy source term that is used to force the superficial velocity, $\mathbf{u}$, to a value close to zero within the mushy zone. A small constant is generally added to the denominator of the source term to avoid division by zero. C_m is a constant that is based on the morphology of the porous structure. The value of this constant was calibrated from 1×10^5 to 1×10^7; the value of 5×10^6 fits best with experimental data, and it is used in this study.

— Conservation equation of energy: In this study, the local thermal equilibrium (LTE) hypothesis is implemented. The justification behind the LTE assumption has been discussed thoroughly in our previous study [7]. The LTE conservation equation of energy could be written as:

$$\frac{\partial}{\partial t}\left(\overline{\rho h}\right) + \nabla\cdot\left(\rho_\ell h_\ell \mathbf{u}\right) = \nabla\cdot\left(k_e \nabla T\right) - \underbrace{\left[\left(\varphi\rho_\ell \Delta H \frac{\partial \gamma}{\partial t}\right) + \left(\nabla\cdot\left[\rho_\ell \mathbf{u}\gamma\Delta H\right]\right)\right]}_{S_H} \tag{5.5}$$

where

$$\overline{\rho h} = \varphi\left(\gamma\rho_\ell h_\ell + (1-\gamma)\rho_s h_s\right) + (1-\varphi)\rho_p h_p \tag{5.6}$$

ℓ, s, and p describe the phases: liquid water, solid water (ice), and soil particle, respectively. h stands for the sensible enthalpy of the liquid water. γ is the water fraction. The effective thermal conductivity, k_e, is defined based on the parallel arrangement approach as [32, 35]:

$$k_e = \varphi\left(\gamma k_\ell + (1-\gamma) k_s\right) + (1-\varphi) k_p \tag{5.7}$$

The source term, S_H, is used to induce the latent heat of fusion, ΔH, during the phase-change process.

5.2.2 The concept of heatlines

The concept of the heatlines is evolved, basically, from the use of stream-function and streamlines to visualize the fluid flow. In two-dimensional Cartesian coordinates, one can define the steam-functions as below:

$$\frac{\partial \psi}{\partial y} = u, \quad -\frac{\partial \psi}{\partial x} = v \tag{5.8}$$

where $\psi(x, y)$ is the stream-function. The flow, by definition, is locally parallel to the constant line of the stream-function, ψ, (i.e., streamlines). Thus, although there is no explicit substitution for the velocity components (u, v) as the source of the local flow attributes, constant streamlines provide a valuable observation of the fluid flow and its characteristics.

Similarly, heat-function and heatlines are introduced as a visualization aid of the transfer of heat by fluid flow. As equation (5.8) should fulfill the conservation equation of mass, heat-functions should satisfy the conservation equation of energy. Hence, the definition of heat-function could be described as [36]:

$$\frac{\partial H}{\partial y} = E_x, \quad -\frac{\partial H}{\partial x} = E_y \tag{5.9}$$

where

$$E_x = \left(\rho u\left[h + \Delta H\right] - k\frac{\partial T}{\partial x}\right), \quad E_y = \left(\rho v\left[h + \Delta H\right] - k\frac{\partial T}{\partial y}\right) \tag{5.10}$$

E_x and E_y describe the net energy flow in the x-direction and y-direction, respectively. According to this definition, the net energy flow is locally parallel to the heatlines (i.e., $H =$ constant). Therefore, heatlines could be used to describe the actual path of the energy flow.

5.2.3 Initial and boundary conditions

The initial and boundary conditions of the current mathematical model are defined as below:

- *Initial condition* —Initial temperature and initial velocity at $t = 0$

$$T_g = T_w = T_{init}, \quad \mathbf{u} = \mathbf{u}_{init} \tag{5.11}$$

- *Freeze pipes' wall* —Dirichlet boundary conditions for temperature and no-slip conditions.

$$T = T_w, \quad \mathbf{u} = 0 \tag{5.12}$$

- *Ground (left and right boundaries)* —Neumann boundary condition for temperature in case of no-seepage scenario.

$$\mathbf{n} \cdot \nabla T = 0 \tag{5.13}$$

  Dirichlet boundary for pressure in case of seepage scenario.

$$p = p_{in} \quad \text{(left boundary)} \mid p = p_{out} \quad \text{(right boundary)} \tag{5.14}$$

- *Ground (top and bottom boundaries)* —Symmetry boundaries (i.e. zero normal velocity, and zero normal gradients of any variable Θ at the symmetry planes.)

$$\mathbf{n} \cdot \mathbf{u} = 0, \quad \mathbf{n} \cdot \nabla\Theta = 0 \tag{5.15}$$

5.3 Numerical simulations

The computational domain was developed and meshed using ANSYS software package 16.1. A mesh-sensitivity procedure was performed to ensure the solution's independence. The domain was meshed at the beginning with a coarse mesh consisting of 1×10^3 elements, followed by several mesh adaptations until the difference in computed ground's temperature was below 1%. In addition, the influence of the ground's boundaries on the AGF process has been investigated; different widths of the computational domain in the x-direction, ranging from 1 [m] to 100 [m] were implemented, and the ground's temperature at the center between the freeze pipes was compared to ensure a boundary condition independence. For example, in the case of 1.0 [m] space between two freeze pipes, a domain with a width of 11 [m] gave less than 1% deviation compared to the 100 [m] width.

The governing equations along with the initial and the boundary conditions were solved using the finite volume method. The transient coolant temperature, water and sand thermophysical properties, and groundwater seepage were specified and implemented into the numerical model using a user-defined functions (UDFs). The numerical model was solved with the Semi-Implicit Pressure-Linked Equation (SIMPLE) algorithm and second-order upwind discretization. The convergence criteria were set to 1×10^{-6} for all equations.

5.4 Model validation

The numerical model is validated against experimental data from Sres [37] and Pimentel et al. [30]. They conducted several experiments with and without seepage conditions. The lab-scale setup is characterized by an insulated container with inner dimensions of (1.2 [m] × 1.3 [m] × 1.0 [m]) that contains three vertical freeze pipes with outer diameters of 0.041 [m]. In order to simulate the groundwater seepage, two constant-head water tanks have been installed at the opposite faces, perpendicular to the freeze pipes arrangement. More than 70 thermocouples have been installed, at three vertical levels, across one freeze pipes in the x-direction, between two freeze pipes in the y-direction, and at the top and bottom of the freeze pipes' wall; more details are available in [31]. The readings of the walls' temperature were

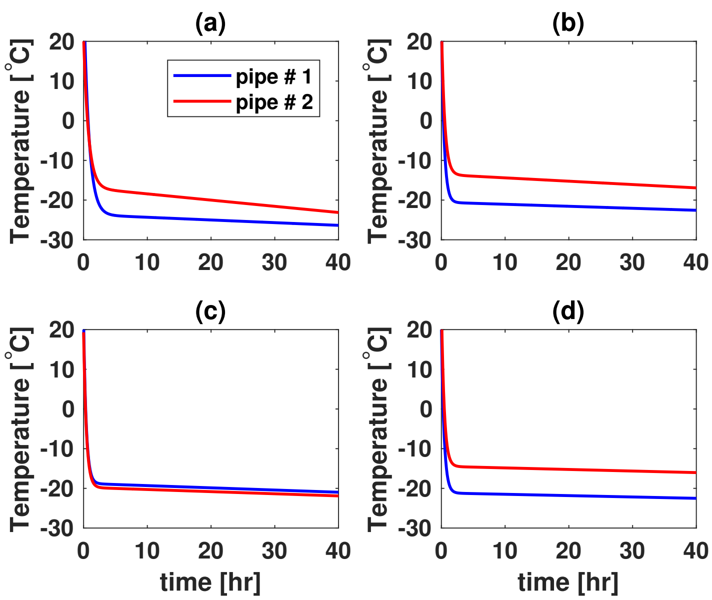

Figure 5.3 – ;
(c) seepage of 1.4 [m/d]; and (d) seepage of 2.0 [m/d].]Wall boundary condition of each freeze pipe under different seepage scenarios: (a) no-seepage; (b) seepage of 1.0 [m/d]; (c) seepage of 1.4 [m/d]; and (d) seepage of 2.0 [m/d]. (Adapted from [31])

curve-fitted, averaged, and used in the model as a transient thermal boundary condition, as shown in Fig. 5.3. The temperature of the groundwater seepage was set at the initial ground temperature (15 [°C] for the no-seepage case, and 20 [°C] for the other cases). Four scenarios of seepage flow ($v = 0, 1.0, 1.4$, and 2.0 [m/d]) have been investigated and validated in this study. For the seepage cases, a velocity inlet boundary condition was employed at the beginning. As soon as the hydraulic condition was stabilized, the groundwater inlet was switched into a pressure inlet condition utilizing the corresponding inlet pressure. This shift mimics the actual scenario of an AGF under seepage condition, where the seepage velocity is affected by the reduction of the cross-sectional area between two freeze pipes due to ice growth. The cooling phase started once the hydraulic condition is stabilized. The properties of the materials involved in this study are listed in Table 5.1. The temperature-dependent properties of water and ice were implemented in the numerical simulation via a UDFs. Good agreement between the model and the experimental data was observed, which can be discerned from Fig. 5.4.

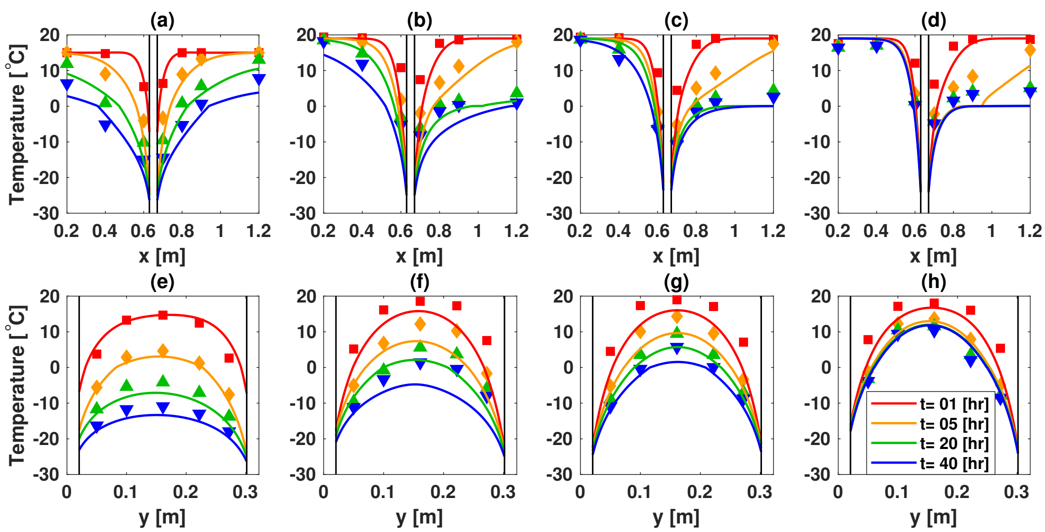

Figure 5.4 – ;
(c) and (g) seepage of 1.4 [m/d]; (d) and (h) seepage of 2.0 [m/d]]Model validation against experimental data [30, 37] at various seepage. (a), (b), (c), and (d) shows thermocouples in x-direction; whereas (e), (f), (g), and (h) shows thermocouples in y-direction. (a) and (e) no-seepage condition; (b) and (f) seepage of 1.0 [m/d] ; (c) and (g) seepage of 1.4 [m/d]; (d) and (h) seepage of 2.0 [m/d]

5.5 Results and discussion

The results of the validated model are utilized to illustrate the effect of groundwater seepage on the progression of the frozen body at different time stage. The discussion compares

Table 5.1: Material properties used in this study

Properties	Value
Thermal conductivity (sand particle) [W/(m.K)]	4.9
Density (sand particle) [kg/m^3]	2664
Specific heat capacity (sand particle) [J/(kg.K)]	826
Porosity [%]	36
Permeability [m^2]	1.8×10^{-11}
Latent heat of fusion [J/kg]	334000
Water liquidus temperature [°C]	0.1
Water solidus temperature [°C]	0.0

the behavior of the heatlines with the behavior of the velocity's streamlines. After that, the framework of the mathematical model is extended to simulate the AGF process with a typical field configuration of parallel freeze pipes. In this study, four key parameters, determining the performance of an AGF process in terms of the thickness and the shape of the frozen body, and closure time, are evaluated with regard to the spacing between two freeze pipes, the velocity of groundwater seepage, brine's temperature, and seepage's temperature, as presented in Table 5.2.

5.5.1 Progression of the frozen body

Fig. 5.5 and Fig. 5.6 depict the growth of the frozen wall under various seepage scenarios (0, 1.0, 1.4, and 2 [m/day]) at different time stages (1,5, 20, and 40 [hr]); Fig. 5.5 describes the temperature contours and the streamlines, while Fig. 5.6 shows the magnitude of the net energy flow and the heatlines at the same conditions. The results are based on the design and operating parameters of the validated model (see Section 5.4).

Fig. 5.5 (a)-(d) describes the temperature contour and the phase-change isotherms at no-seepage condition after 1, 5, 20, and 40 [hr] of freezing, respectively. With no-seepage, the freeze pipes are the primary heat sink, and conductive heat transfer is the main heat transfer mechanism. Therefore, a symmetric frozen body between the freeze pipes is observed in these cases. Correspondingly, the associated heatlines are pointed directly into the freeze pipes, as illustrated in Fig. 5.6 (a)-(d). At the beginning of the AGF process, the heat transfer occurs only around the freeze pipes. Thus, the heatlines are only shown in the middle of the

Table 5.2: The main parameters at three levels. The base case is highlighted in bold

Spacing [m]	Coolant's Temp. [°C]	Seepage Velocity [m/d]	Seepage Temp. [°C]
0.3	-20	0.0	5
1.0	**-25**	**0.05**	**10**
2.0	-30	0.1	15

domain of interest pointed toward the freeze pipes, as observed in Fig. 5.6 a. As more heat is extracted from the ground, the size of the frozen body increases and the heatlines start to expand, as shown in Fig. 5.6 (b). As time advances, the heat extraction reaches the edge of the domain of interest. The energy flows directly toward the freeze pipes, following the path of the heatlines, as shown in Fig. 5.6 (c) and (d). It is important to recall here that since the main mechanism under the no-seepage condition is conduction, these heatlines represent the heat-flux lines. On the contrary, the overall magnitude of the conduction energy flow is less than 3000 [W/m^2]. As we will discuss next, this fact has a direct impact on the growth of the frozen body, especially under high seepage velocity. Once the seepage is introduced, one expects an immediate interaction between the groundwater flow and the growth of the frozen wall. Yet, after 1 and 5 [hr] of freezing under a seepage velocity of 1 [m/day], the frozen body is barely affected by the flow, as depicted in Fig. 5.5 (e) and (f), in comparison with Fig. 5.5 (a) and (b), respectively. On the other hand, Fig. 5.6 (e) shows a modest bending in the heatlines in the frozen body; at this stage, the effect of the seepage on the ice growth is insignificant, which leads to a symmetric frozen body - similar to the no-seepage case. Originally, before AGF process starts, heatlines flows in parallel with the streamlines, as observed in Fig. 5.5 (e) and Fig. 5.6 (e). Once freezing begins, the cold pipes start to extract heat from the ground, forcing the heatline to stop and tilt toward the heat sinks. The deflection of the heatlines is clearer after 5 [hr] of freezing, as displayed in Fig. 5.6 (f). Additionally, some of the heatlines do not approach the freeze pipes. Instead, they slip away with the direction of the seepage. This phenomina is apparent after 20 [hr] of freezing - the curvature is greater, and more heatlines are escaping the frozen zone in the direction of the flow, as inferred in Fig. 5.6 (g). It is noticed here that the convective heat transfer increases significantly at this stage, as compared to the previous two stages. This may be attributed to the fact that the seepage has to pass through a narrower passage between the growing, separate frozen bodies, as depicted in Fig. 5.5 (g). After sufficient time, 40 [hr]

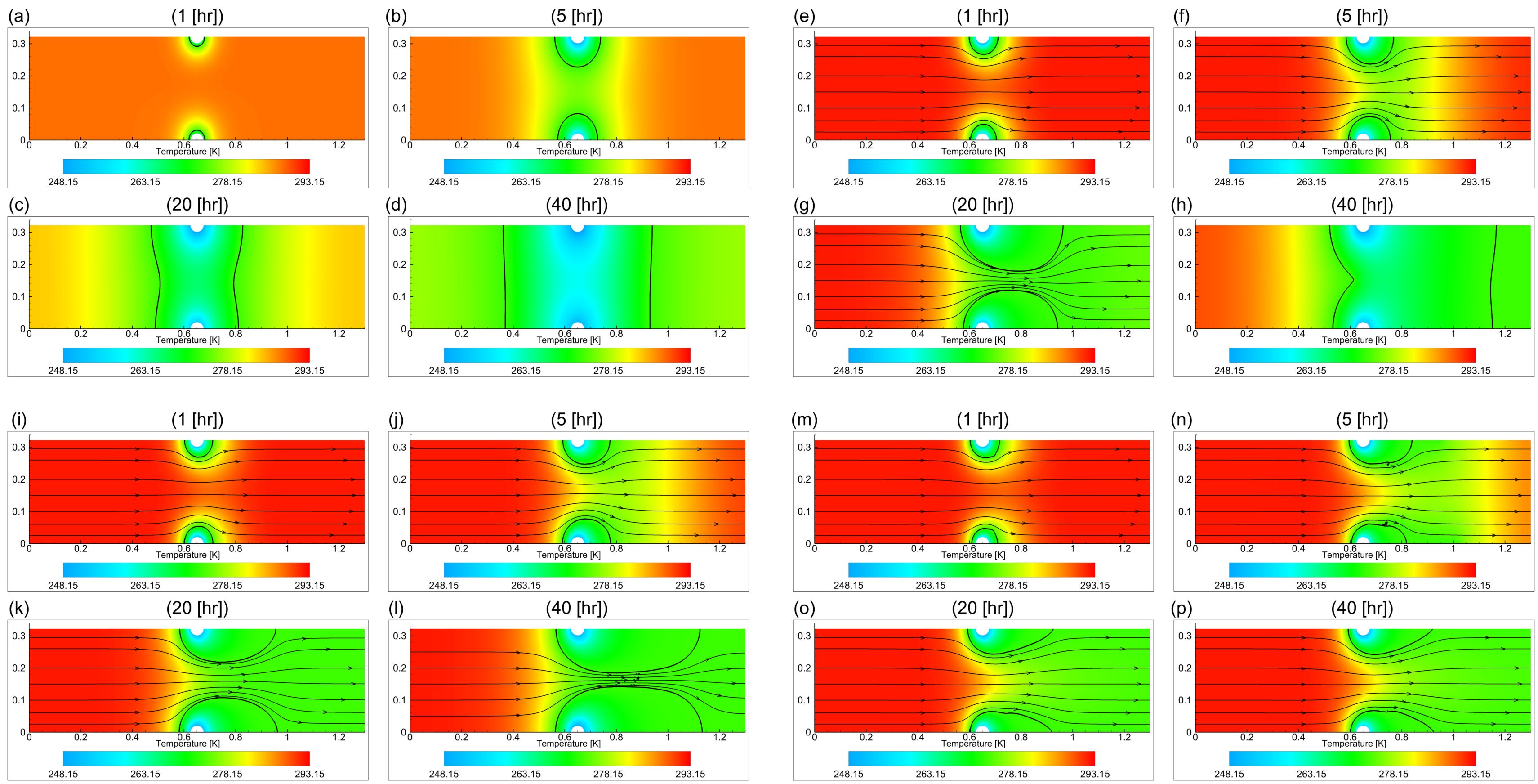

Figure 5.5 – Temperature fields (contours) and streamlines (lines) of the growth of the frozen body at different time stages and various seepage velocities: (a)-(d) no-seepage condition; (e)-(h) seepage of 1.0 [m/d]; (i)-(l) seepage of 1.4 [m/d]; and (m)-(n) seepage of 2.0 [m/d].

in this case, a merged, frozen body is created between the freeze pipes. The convective seepage is not powerful enough to hinder the formation of a closed, frozen wall. However, it is strong enough to cause the frozen wall to swell in the direction of the seepage, as displayed in Fig. 5.5 (h). Accordingly, the conductive heat transfer becomes the dominant mechanism again while the heat-flux lines draw the direction of the energy flow, as shown in Fig. 5.6 (h).

The undesirable effect of the groundwater seepage on the evolution of the frozen body increases at higher velocities. The main behavior, however, is similar to low-velocity scenario. The ice growth under 1.4 [m/day] at 1 and 5 [hr] is almost identical to the ice growth under 1 [m/day] at the same time frame, as shown in Fig. 5.5 (i)-(k), and Fig. 5.6 (i)-(k), as compared to Fig. 5.5 (e)-(g), and Fig. 5.6 (e)-(g), respectively. Several features are apparent from these plots; foremost is that the wall thickness in the 1.0 [m/day] case is larger than the 1.4 [m/day] case. This is due to the fact that the seepage at higher velocity has more convective energy that could interfere with the freeze pipes and reduce their efficiencies. Furthermore, although the 1.4 [m/day] flow suppose to have higher energy, the magnitude of the local net energy flow between the freeze pipes is lower than the 1.0 [m/day], as discerned in Fig. 5.6 (k) and Fig. 5.6 (g), respectively. As discussed previously, the narrower the passage between the freeze pipes, the higher the seepage velocity. However, the magnitude of the global net energy flow in the 1.4 [m/day] case is higher, which force the frozen body to elongate more with the flow. Moreover, after 40[hr] of freezing, the frozen body under 1.4 [m/day] seepage stretched more in the direction of the flow and yet to merge, as depicted in Fig. 5.5 (l) and Fig. 5.6 (l). The flow convective energy at this stage is still higher than the power of the freeze pipes. Therefore, the AGF process should continue in order to create a closed, frozen wall. Fig. 5.5 (m)-(p) and Fig. 5.6 (m)-(p) demonstrate the performance of AGF process under seepage velocity of 2 [m/day]. The overall behavior is drastically changed, as compared to the previous cases. Clearly, high seepage velocity hinders the hydraulic sealing between the freeze pipes. The energy of the freeze pipes is not powerful enough to overcome the high-velocity of the warm groundwater seepage, which could have a significant impact on the overall AGF process. Also, by comparing the magnitude of the net energy flow in the unfrozen areas throughout the freezing process, one can observe a minimal change in the overall magnitude. However, in the previous two cases (1 and 1.4 [m/day]), the magnitude reduced significantly from its initial values. This means that at high seepage velocity of 2 [m/day] the convective and conductive parts of the energy flow, as described in Eq. (5.10), reach an equilibrium stage, where the power of the heat sinks is not adequate to advance the size of the frozen body.

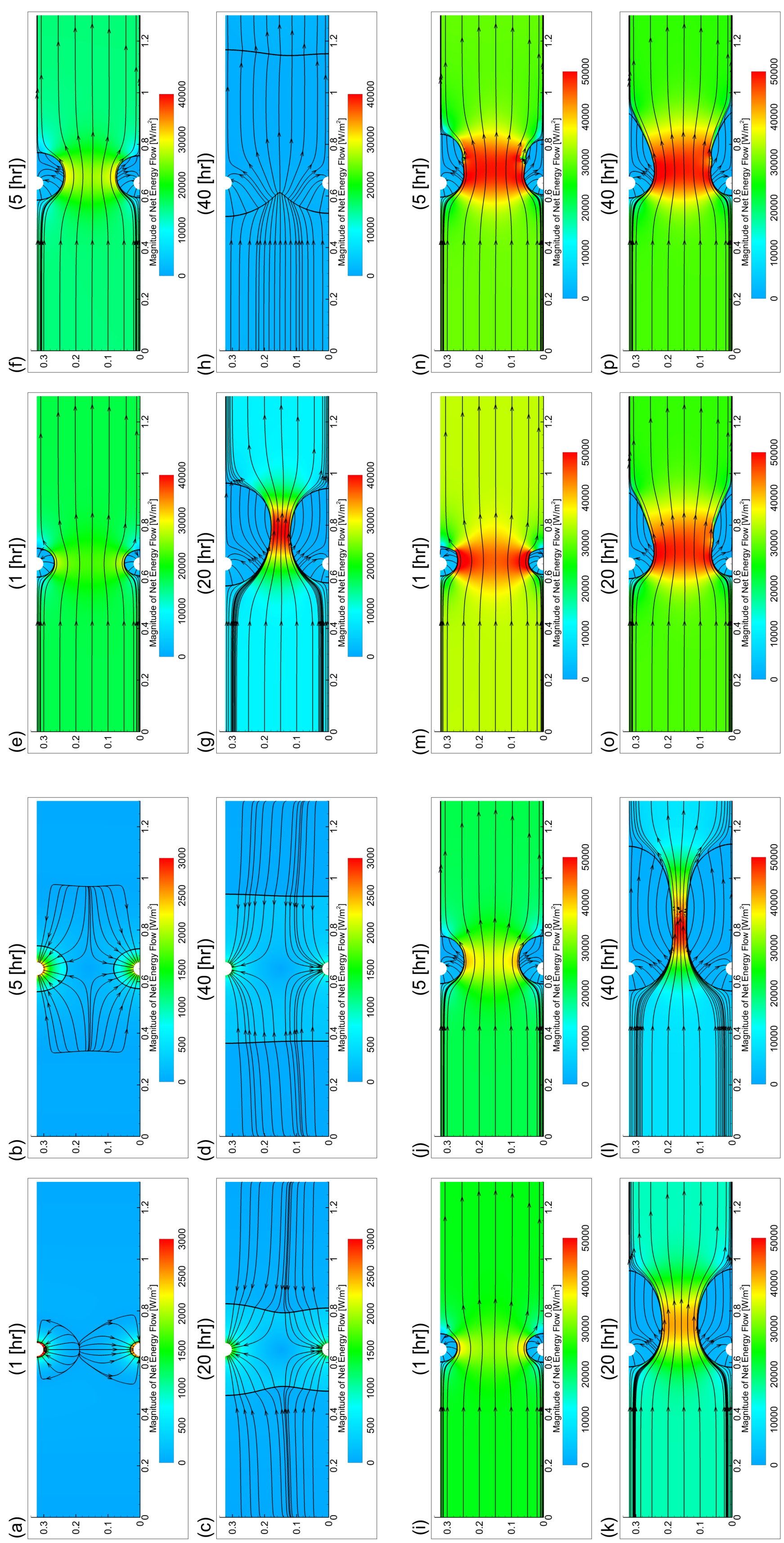

Figure 5.6 – Magnitude of net energy flow (contours) and heatlines (lines) of the growth of the frozen body at different time stages and various seepage velocities: (a)-(d) no-seepage condition; (e)-(h) seepage of 1.0 [m/d]; (i)-(l) seepage of 1.4 [m/d]; and (m)-(n) seepage of 2.0 [m/d].

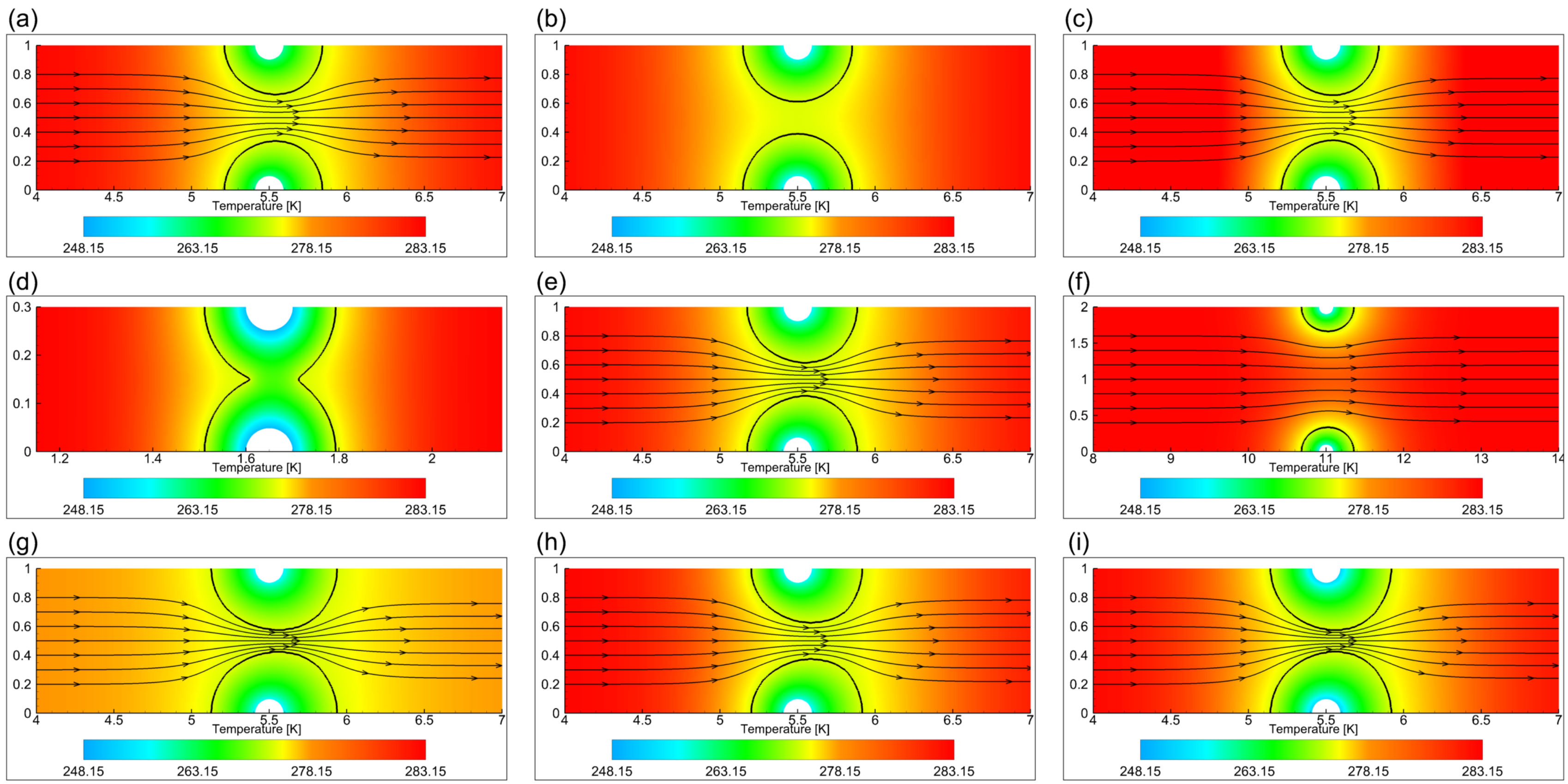

Figure 5.7 – The progression of the frozen body after 3 [day] of freezing under various design and operating parameters: (d), (e), and (f) highlight the effect of pipes spacing; (b), (e), and (h) represent the impact of groundwater seepage; (a), (e), and (i) show the influence of coolant's temperature; and (c), (e), and (g) display the effect of the seepage temperature. Individual plots describe certain parameter: (a) coolant's temperature of -20 [°C]; (b) no-seepage condition; (c) seepage temperature of 15 [°C]; (d) spacing of 0.3 [m]; (e) spacing of 1.0 [m] (**base case**); (f) spacing of 2.0 [m]; (g) seepage temperature of 5 [°C]; (h) seepage of 0.1[m/d]; and (i) coolant's temperature of -30 [°C].

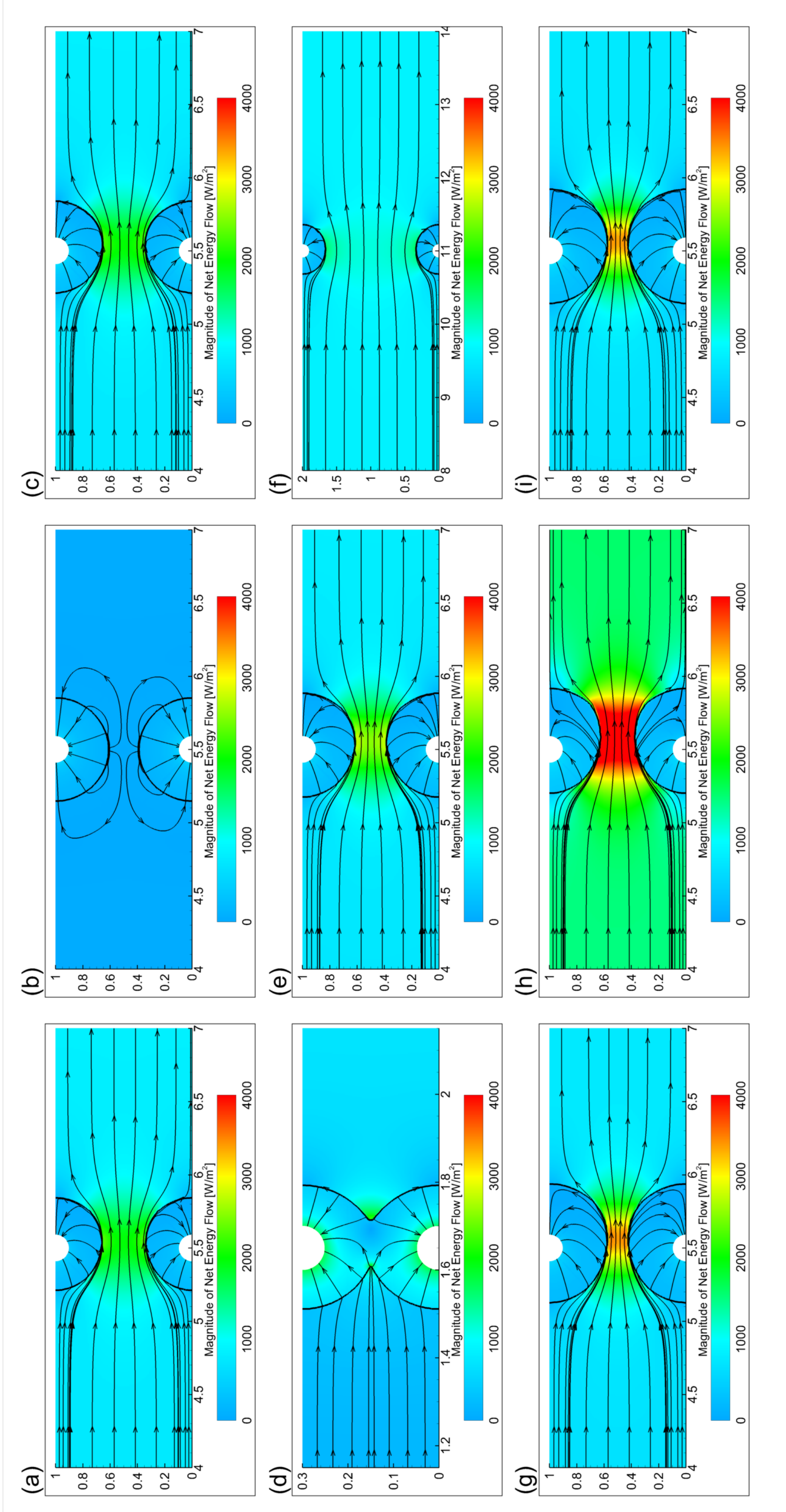

Figure 5.8 – The progression of the frozen body after 3 [day] of freezing under various design and operating parameters: (d), (e), and (f) highlight the effect of pipes spacing; (b), (e), and (h) represent the impact of groundwater seepage; (a), (e), and (i) show the influence of freeze pipes coolant's temperature; and (c), (e), and (g) display the effect of the seepage temperature. Individual plots describe certain parameter: (a) coolant's temperature of -20 [°C]; (b) no-seepage condition; (c) seepage temperature of 15 [°C]; (d) spacing of 0.3 [m]; (e) spacing of 1.0 [m] (**base case**); (f) spacing of 2.0 [m]; (g) seepage temperature of 5 [°C]; (h) seepage of 0.1[m/d]; and (i) coolant's temperature of -30 [°C].

5.5.2 Spacing between freeze pipes

The distance between freeze pipes is one of the main design parameters in any AGF system, which requires particular attention during the design stage. In this study, three typical freeze pipes' spacing in underground mines were selected (see Table 5.2). Fig. 5.7 (d), (e), and (f) reveals the effect of the distance between two freeze pipes on the development of the frozen body. The x-axis and y-axis are the lengths in meters. The figures show the temperature contours and the velocity streamlines of each case after three days of continuous freezing. The radius of the frozen body reduces while spacing between two pipes increases. This is to be expected for two reasons: (i) the fact of having two heat sinks (i.e., the freeze pipes), and (ii) the size of the ground structure that needs to be frozen, which is characterized by the distance between the pipes. If a freezing system has a single freeze pipe, one can predict a similar growth rate under similar operating conditions. In our case, however, there are two freeze pipes. The contribution of the neighbor freeze pipe to the growth of the frozen body is inversely proportional to the distance between the pipes at the same time frame. The corresponding heatlines are observed in Fig. 5.8 (d), (e), and (f). The heatlines of the 0.3 [m] case, as indicated in Fig. 5.8 (d), are pointed directly to the freeze pipes, showing that the groundwater seepage has a negligible effect on the progression of the frozen wall. As defined in Eqn. (5.10), the conductive part of the net energy flow is inversely proportional to the characteristic length, L, of the medium ($q \propto 1/L$). This leads us to the fact that at the same operating conditions, the contribution of the conductive heat transfer to the net energy flow reduces with increasing the distance between the freeze pipes.

5.5.3 Velocity of the groundwater seepage

The groundwater seepage is one of the main challenges that face any AGF process. It increases the time needed to create a closed, frozen wall. In certain conditions, the flow could prevent the hydraulic sealing between two freeze pipes. Fig. 5.7 (b), (e), and (h) and Fig. 5.8 (b), (e), and (h) demonstrate the impact of the groundwater seepage on the evolution of the frozen body after three days of continuous freezing. Clearly, the thickness of the frozen wall is identical in the three cases. The elongation in the flow direction, however, is greater at higher seepage velocity. While discussing the seepage velocity and the growth of the frozen wall, it is instructive to introduce here the Péclet number, which is a dimensionless number that is used in calculations involving convective heat transfer.

$$Pe = \frac{\text{heat transport by convection}}{\text{heat transport by conduction}} = \frac{uL}{\alpha} \tag{5.16}$$

where ($\alpha = k/(\rho c_p)$) is the thermal diffusivity. Based on the definition of the Péclet number, Pe, and the formulation of the energy flow in Eq. (5.10), one can anticipate that, at the same operating conditions, increasing the seepage velocity will boost the magnitude of the net energy flow in the unfrozen area. Thus, affecting the growth and the shape of the frozen body by dragging some heatlines away from the freeze pipes, which can be observed in Fig. 5.8 (e) and (h).

5.5.4 Temperature of the coolant

The temperature of the coolant is one of the key operating parameters that determine the thickness of the frozen body. The sub-zero temperature is required to overcome the sensible and latent heat of the groundwater in the porous ground structure. In this study, three brine's temperatures are analyzed: -20, -25, and -30 [°C]. The results of these three cases are shown in the diagonal plots in Fig. 5.7 (a), (e), and (i) and Fig. 5.8 (a), (e), and (i). Several features are apparent in these plots, notably that the frozen body gets thicker when wall's temperature is colder. The dominating mechanism in the frozen area is conduction. The conductive heat transfer, q, has a proportional relationship with the temperature difference, $q \propto \Delta T$. Thus, at lower brine's temperature, the frozen body should be thicker, taking into consideration similar design and operating conditions. Moreover, because the frozen body is thicker at lower coolant's temperature, the free aisle between the frozen areas is narrower. Thus, the seepage velocity increases, as illustrated previously, forcing the frozen body to prolong in the direction of the flow.

5.5.5 Temperature of the seepage

The temperature of the groundwater flow has the least effect on the thickness and the shape of the frozen body, as compared to the other parameters, as depicted in Fig. 5.7 (c), (e), and (g) and Fig. 5.8 (c), (e), and (g). Note, however, that the frozen body at seepage temperature of 5 [°C] is somewhat thicker than the frozen wall at 15 [°C], as inferred from Fig. 5.7 (g) and (c), respectively. This behavior can be attributed to the enthalpy of the seepage, which is directly related to the flow temperature; ($\delta h = c_p \delta T$). At higher enthalpy, the freeze pipes require more energy to overcome convective energy of the warm flow. The physical reasoning behind the stretch of the frozen body in the direction of the flow is similar to the previous discussion.

5.5.6 Closure time

Thus far, we have examined the impact of design and operating parameters on the progression of the frozen body, and now we address the effect of the parameters on the closure time, which is defined as the time needed to create a closed, frozen wall between two freeze pipes with a core temperature of -5 [°C].

Figure 5.9(a) shows the closure time at different spacing. At 0.3 [m] spacing, the closure time is around 2.2 [day]. The symmetrical freezing growth of this case, as inferred in Fig. 5.11(d), shows that the groundwater seepage has a negligible effect on the AGF process when the freeze pipes are close to each other. At 1.0 [m] spacing, the time increases to a value around 9.1 [day]; 4.5 times higher than the 0.3 [m] case. The closure time increases substantially to 72.1 [day] at 2.0 [m] spacing. This increase is due to the fact that the ground domain per pipe's unit length increases dramatically, while the heat sink in all cases stay the same: two freeze pipes with coolant temperature of -25 [°C]. The domain size per pipe's unit length increases from (0.3 [m] $\times$ 3.3 [m]), (1.0 [m] $\times$ 11.0 [m]), to (2.0 [m]$\times$ 22.0 [m]). The width of the domain increases to satisfy the boundary-condition independence that has been discussed previously. Even if the ground domain has the same width of 3.3 [m], still, the size of the domain increases from 1 [m^3], to 3.3 [m^3], and to 6.6 [m^3]. Hence, higher sensible and latent energy, and higher convective flux associated with the 10 [°C] groundwater flow have to be extracted by the same freeze pipes. Thus, the closure time increases substantially with freeze pipes spacing. Furthermore, the downstream part of the frozen body tends to elongate in the direction of the seepage. Ideally, a single freeze pipe creates a circular frozen body. However, the warm groundwater seepage forces the frozen body to lengthen in the same direction of the flow. The elongation has a proportional relation with the spacing, as shown in Fig. 5.11(e) and (f). As discussed previously, the freeze pipes require more time to create a closed, frozen body when the spacing is larger; hence the seepage has more influence on the shape of the frozen body at 2.0 [m] spacing, as compared to 0.3 [m] case.

In the case of no-seepage, the time needed to create a closed body is around 6.4 [day], as shown in Fig. 5.9 (b). The main heat sink is the freeze pipes. Therefore, the shape of the frozen body is symmetrical in x and y directions, as shown in Fig. 5.11 (b). In the case of 0.05 [m/d] seepage, it took the freeze pipes 9.1 [day] to create the required frozen body. One can observe from Fig. 5.11 (e) that the frozen body is slightly shifted in the direction of the flow. However, the heat flux through the freeze pipes is large enough to overcome the energy of the flow. Now, in the case of 0.1 [m/d] the freeze pipes require more energy to overcome the total energy of the flow. The closure time, in this case, increases to almost 12 [days]. It is notable here that the width of the downstream part of the frozen body increases from 0.5

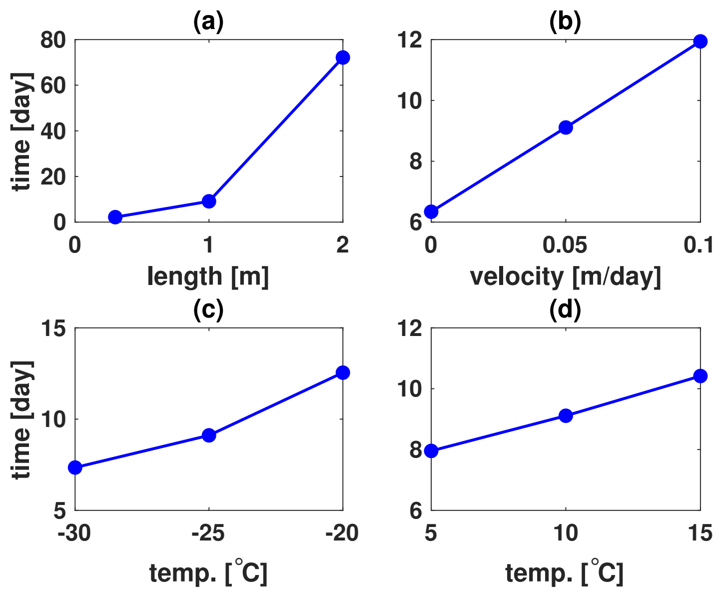

Figure 5.9 – The influence of the freeze pipes' spacing, seepage velocity, freeze pipe coolant's temperature, and seepage temperature on the closure time

[m] at the no-seepage scenario, to 1 [m] in the highest velocity case (see Fig. 5.11 (e) and (f)). This is due to the higher convective energy of the flow.

Before addressing the effect of coolants' and seepage's temperatures, we return our attention to the interaction between groundwater seepage and freeze pipes' spacing with a view to the impact on the closure time. Fig. 5.10 demonstrates the influence of groundwater seepage on the closure time at different pipes' spacings. One can observe that the closure time at 0.3 [m] spacing is way shorter than the other two cases, in spite of the existence of the seepage. Moreover, the closure time jumped suddenly from around 4.5 [hr], with no-seepage, to around 2 [day], although the seepage velocity is as low as 0.01 [m/day]. This demeanor emphasizes the significant impact and the important role of the groundwater seepage on the formation of the frozen wall. On the other hand, at the pipes' spacing of 1 and 2 [m], it is observed from the figure that the seepage hinders the formation of a closed, frozen wall at velocities higher than 0.1 and 0.05 [m/day], respectively. These results highlight the importance of developing proper design parameter prior to actual construction takes place. Fig. 5.9(c) shows the influence of the coolant's temperature on the closure time. At brine's temperature of -30 [°C], the freeze pipes require 7.4 [day] to create a frozen wall. The time increases to 9.1 and 12.6 [day] while coolant's temperature increases to -25 and -20 [°C], respectively. This is to be expected since the brine's temperature is directly and proportionally related to the heat flux through the freeze pipes. Lower coolant's temperature means higher ΔT

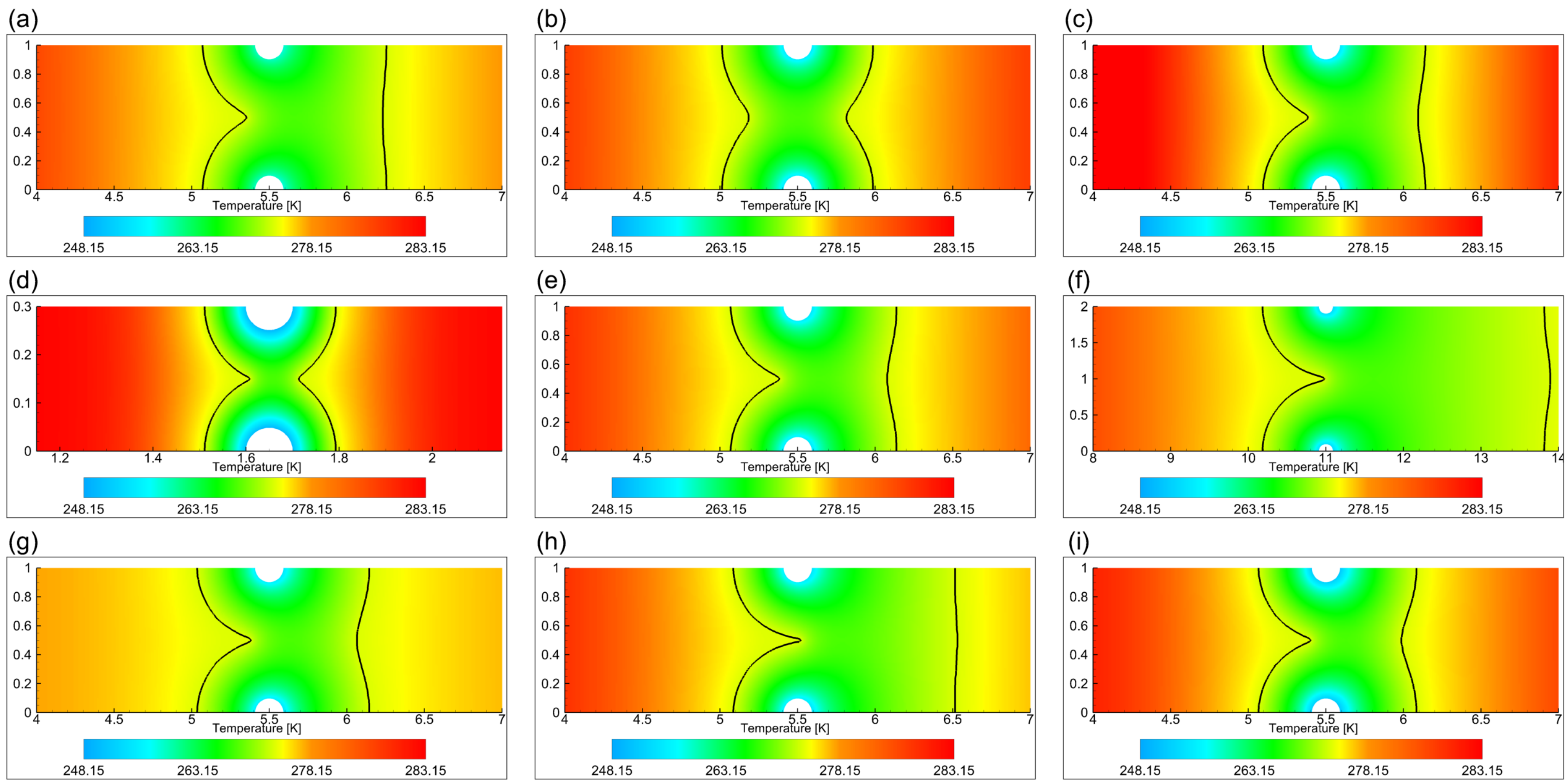

Figure 5.11 – Temperature contours of AGF process at different design and operating conditions. The frozen bodies are represented here with the zero iso-therm. horizontal plots (d), (e), and (f) highlight the effect of pipes spacing; vertical plots (b), (e), and (h) represent the impact of groundwater seepage; the diagonal plots (a), (e), and (i) show the influence of coolant's temperature; and the other diagonal plots (c), (e), and (g) display the effect of the seepage temperature. Individual plots describe certain parameter: (a) coolant's temperature of -20 [°C]; (b) no-seepage condition; (c) seepage temperature of 15 [°C]; (d) spacing of 0.3 [m]; (e) spacing of 1.0 [m] (**base case**); (f) spacing of 2.0 [m]; (g) seepage temperature of 5 [°C]; (h) seepage of 0.1[m/d]; and (i) coolant's temperature of -30 [°C].

between the pipe and the ground, which yields a higher heat transfer rate. Consequently, less time is required to overcome the ground's and seepage's energy. Fig. 5.11(A), (E), and (I) illustrate the effect of the brine's temperature on the thickness and shape of the frozen body. Although the total width of the frozen body in the coldest freeze pipe case is the lowest, which is in certain cases undesirable, the time needed to reach this stage is less than the time in the coolant's temperature of -20 [°C] case. Therefore, at the same time t, the width of the coldest freeze pipes at -30 [°C] will be larger than the width at -20 [°C] brine's temperature case. The seepage temperature has the smallest impact on the closure time, as compared to

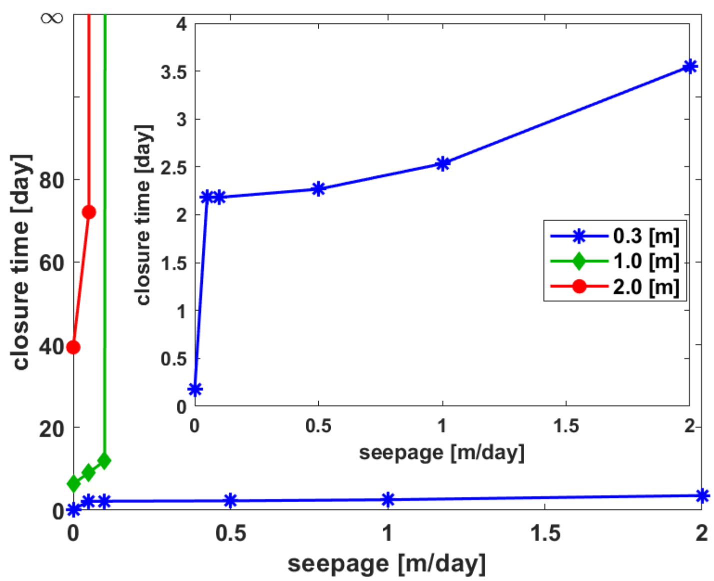

Figure 5.10 – The effect of the groundwater seepage on the closure time at different freeze pipes' spacing; 0.3, 1.0, and 2.0 [m].

the other parameters. The closure time increases from 8 [day] at flow temperature of 5 [°C] to 9.1 [day] and to 12 [day] in the case of flow at 10 [°C] and 15 [°C], respectively, which can be discerned from Fig. 5.9 (d). Also, the change of the frozen body width and shape is negligible as compared to the other cases, as inferred in Fig. 5.11 (c), (e), and (g). The discussion of the effect of this parameter on the AGF process has been illustrated previously in Section 5.5.5.

5.6 Conclusions

A mathematical model of an artificial ground freezing process under various seepage velocity has been derived, analyzed, and validated. A computational study, has been carried out with a view to studying how various design and operating parameters affect the overall performance of the AGF process. The concept of heatlines has been introduced to provide a deeper understanding of the impact of the groundwater seepage along with other design and operating parameters on the development of the frozen body between two freeze pipes.

It has been shown that a range of parameters - freeze pipes' spacing, seepage velocity, coolant's temperature, and seepage temperature - affect the overall performance of the AGF process in terms of closure time, frozen body thickness, and shape of the frozen wall. It should also be mentioned that the spacing between two freeze pipes has the highest influence on the freezing time and the shape of the frozen body. On the contrary, the seepage temperature has the least influence among the other parameters on the performance of AGF process.

The computational study presented here can be extended to, e.g., optimize the design and operating condition based on the analysis of the heatlines and the entropy generation, which will be our future work.

References

[1] Manon Vitel, Ahmed Rouabhi, Michel Tijani, and Frédéric Guérin. Thermo-hydraulic modeling of artificial ground freezing: Application to an underground mine in fractured sandstone. *Computers and Geotechnics*, 75:80–92, 2016.

[2] Yongshui Kang, Quansheng Liu, Yong Cheng, and Xiaoyan Liu. Combined freeze-sealing and new tubular roof construction methods for seaside urban tunnel in soft ground. *Tunnelling and Underground Space Technology*, 58:1–10, 2016.

[3] E Pimentel, S Papakonstantinou, and G Anagnostou. Numerical interpretation of temperature distributions from three ground freezing applications in urban tunnelling. *Tunnelling and Underground Space Technology*, 28:57–69, 2012.

[4] S Amuno, A Jamwal, B Grahn, and S Niyogi. Chronic arsenicosis and cadmium exposure in wild snowshoe hares (lepus americanus) breeding near yellowknife, northwest territories (canada), part 1: Evaluation of oxidative stress, antioxidant activities and hepatic damage. *Science of The Total Environment*, 618:916–926, 2018.

[5] Iskandar K. Iskandar. Effect of freezing on the level of contaminants in uncontrolled hazardous waste sites. part 1. literature review. *Cold Regions Research and Engineering Laboratory*, 86(19):1–33, 1986.

[6] Iskandar K. Iskandar. Ground freezing controls hazardous waste. *Military Engineer*, 79:455–456, 1987.

[7] Mahmoud A Alzoubi, Aurelien Nie-Rouquette, and Agus P Sasmito. Conjugate heat transfer in artificial ground freezing using enthalpy-porosity method: Experiments and model validation. *International Journal of Heat and Mass Transfer*, 126:740–752, 2018.

[8] FJ Sanger and FH Sayles. Thermal and rheological computations for artificially frozen ground construction. *Engineering Geology*, 13(1-4):311–337, 1979.

[9] Xiangdong Hu, Zequn Hong, and Tao Fang. Analytical solution to steady-state temperature field with typical freezing tube layout employed in freeze-sealing pipe roof method. *Tunnelling and Underground Space Technology*, 79:336–345, 2018.

[10] Xiang-dong Hu, Tao Fang, and Yan-guang Han. Mathematical solution of steady-state temperature field of circular frozen wall by single-circle-piped freezing. *Cold Regions Science and Technology*, 148:96–103, 2018.

[11] Xiang-dong Hu, Tao Fang, and Luo-yu Zhang. Analytical solution to temperature distribution in frozen soil wall with wavy boundaries by single-row-and double-row-piped freezing. *Cold Regions Science and Technology*, 145:208–228, 2018.

[12] Ting Li, Yang Zhou, Xiang-you Shi, Xiao-xue Hu, and Guo-qing Zhou. Analytical solution for the soil freezing process induced by an infinite line sink. *International Journal of Thermal Sciences*, 127:232–241, 2018.

[13] Andrew C Fowler and William B Krantz. A generalized secondary frost heave model. *Siam Journal on Applied Mathematics*, 54(6):1650–1675, 1994.

[14] Shibing Huang, Yunlin Guo, Yanzhang Liu, Lihua Ke, Guofeng Liu, et al. Study on the influence of water flow on temperature around freeze pipes and its distribution optimization during artificial ground freezing. *Applied Thermal Engineering*, 135:435–445, 2018.

[15] Klas Hansson, Jirka Simunek, Masaru Mizoguchi, Lars-Christer Lundin, and Martinus Th Van Genuchten. Water flow and heat transport in frozen soil. *Vadose Zone Journal*, 3(2):693–704, 2004.

[16] Jeffrey M McKenzie, Clifford I Voss, and Donald I Siegel. Groundwater flow with energy transport and water–ice phase change: numerical simulations, benchmarks, and application to freezing in peat bogs. *Advances in Water Resources*, 30(4):966–983, 2007.

[17] WB Yu, WB Liu, YM Lai, L Chen, and X Yi. Nonlinear analysis of coupled temperature-seepage problem of warm oil pipe in permafrost regions of northeast china. *Applied Thermal Engineering*, 70(1):988–995, 2014.

[18] Wenyu Song, Yaning Zhang, Bingxi Li, and Xinmeng Fan. A lattice boltzmann model for heat and mass transfer phenomena with phase transformations in unsaturated soil during freezing process. *International Journal of Heat and Mass Transfer*, 94:29–38, 2016.

[19] Ahmed Marwan, Meng-Meng Zhou, M Zaki Abdelrehim, and Günther Meschke. Optimization of artificial ground freezing in tunneling in the presence of seepage flow. *Computers and Geotechnics*, 75:112–125, 2016.

[20] Manon Vitel, Ahmed Rouabhi, Michel Tijani, and Frédéric Guérin. Modeling heat and mass transfer during ground freezing subjected to high seepage velocities. *Computers and Geotechnics*, 73:1–15, 2016.

[21] AD Brent, VR Voller, and KTJ Reid. Enthalpy-porosity technique for modeling convection-diffusion phase change: application to the melting of a pure metal. *Numerical Heat Transfer, Part A Applications*, 13(3):297–318, 1988.

[22] Mahmoud Jourabian, Mousa Farhadi, and AhmadAli Rabienataj Darzi. Constrained ice melting around one cylinder in horizontal cavity accelerated using three heat transfer enhancement techniques. *International Journal of Thermal sciences*, 125:231–247, 2018.

[23] Vaughan R Voller and C Prakash. A fixed grid numerical modelling methodology for convection-diffusion mushy region phase-change problems. *International Journal of Heat and Mass Transfer*, 30(8):1709–1719, 1987.

[24] Andreas König-Haagen, Erwin Franquet, Eric Pernot, and Dieter Brüggemann. A comprehensive benchmark of fixed-grid methods for the modeling of melting. *International Journal of Thermal Sciences*, 118:69–103, 2017.

[25] S Kimura and A Bejan. The "heatline" visualization of convective heat transfer. *Journal of Heat Transfer*, 105(4):916–919, 1983.

[26] Pallab Sinha Mahapatra, Achintya Mukhopadhyay, Nirmal K Manna, and Koushik Ghosh. Heatlines and other visualization techniques for confined heat transfer systems. *International Journal of Heat and Mass Transfer*, 118:1069–1079, 2018.

[27] Manar Al-Jethelah, Syeda Humaira Tasnim, Shohel Mahmud, and Animesh Dutta. Melting of nano-pcm in an enclosed space: Scale analysis and heatline tracking. *International Journal of Heat and Mass Transfer*, 119:841–859, 2018.

[28] Thiago Parente Lima and Marcelo Moreira Ganzarolli. A heatline approach on the analysis of the heat transfer enhancement in a square enclosure with an internal conducting solid body. *International Journal of Thermal Sciences*, 105:45–56, 2016.

[29] Mahmoud A Alzoubi, Agus P Sasmito, Ali Madiseh, and Ferri P Hassani. Intermittent freezing concept for energy saving in artificial ground freezing systems. *Energy Procedia*, 142:3920–3925, 2017.

[30] E Pimentel, A Sres, and G Anagnostou. Modelling of ground freezing in tunnelling. In *Underground Space-the 4th Dimension of Metropolises, ITA and World Tunnel Congress, Prague*, pages 331–336, 2007.

[31] E Pimentel, A Sres, and G Anagnostou. Large-scale laboratory tests on artificial ground freezing under seepage-flow conditions. *Geotechnique*, 62(3):227, 2012.

[32] Maasoud Kaviany. *Principles of heat transfer in porous media.* Springer Science & Business Media, 2012.

[33] C Beckermann and R Viskanta. Natural convection solid/liquid phase change in porous media. *International Journal of Heat and Mass Transfer*, 31(1):35–46, 1988.

[34] Tingting Tang and JM McDonough. A theoretical model for the porosity–permeability relationship. *International Journal of Heat and Mass Transfer*, 103:984–996, 2016.

[35] Nan Zhang and Zhaoyu Wang. Review of soil thermal conductivity and predictive models. *International Journal of Thermal Sciences*, 117:172–183, 2017.

[36] Al M Morega and A Bejan. Heatline visualization of forced convection laminar boundary layers. *International Journal of Heat and Mass Transfer*, 36(16):3957–3966, 1993.

[37] Anton Sres. *Theoretische und experimentelle Untersuchungen zur künstlichen Bodenvereisung im strömenden Grundwasser*, volume 18378. vdf Hochschulverlag AG, 2010.

Chapter 6

On the concept of the freezing on demand (FoD) in artificial ground freezing systems

Contents

Preface (Linking Paragraph)

The artificial ground freezing systems are well-known for their intensive energy consumptions. The conventional design of these systems is based on the continuous operation, mainly to satisfy safety concerns. This chapter introduces a novel operational concept of the freezing-on-demand (FoD) with a view to minimizing the energy consumption without compromising the effectiveness of the AGF system. The experimental apparatus that discussed in Chapter 4 is employed in the analysis of this chapter to demonstrate the proof-of-concept of the freezing-on-demand procedure. The framework of the mathematical model from Chapters 4 and 5 along *with the recommendations concerning the groundwater seepage from the previous chapter are implemented in the current study. The below article has been submitted based on the discussion of this chapter:*

Alzoubi, M. A., Nie-Rouquette, A., Sasmito, A. P., Madiseh, A., and Hassani, F. P. (2018). *On the concept of the Freezing on demand (FoD) in artificial ground freezing systems*, submitted to Applied Energy, 2018, under review.

Abstract

The non-stop operational practice of artificial ground freezing systems leads to intensive energy consumption. A reliable technique is then needed to diminish the depletion of energy while providing sufficient structural stability and safe operation. This paper discusses the principle of the freezing on demand (FoD) by means of experiment and mathematical model. A lab-scale rig that mimics the AGF process is conceived and developed. The setup is equipped with more than 80 thermocouples, flow-meters, and advanced instrumentation system to analyze the performance of the AGF process under the FoD concept. A mathematical model has been derived, validated, and utilized to simulate the AGF under three scenarios: (i) continuous freezing, (ii) FoD starting at a certain temperature of the center of the frozen body, and (iii) FoD starting at a specific time. Each scenario examines the effect of several designs and operating parameters on the ground's response and the energy consumption. The results suggest that the overall energy saving notably depends on the start point of the FoD cycles, which, in turn, is affected by the pipes' spacing and the coolant's temperature. Indeed, applying the FoD concept in an AGF system will lead to a significant drop in the energy consumption. The implementation, however, requires careful consideration of the design and operating parameters.

6.1 Introduction

The artificial ground freezing systems are typically designed to operate continuously. The lifetime of these systems depends on the applications' need; it could range from several months in civil applications [1–3], 20 to 40 years in underground uranium mines [4, 5], as depicted in Fig. 6.1(a), or perpetuity in hazardous waste management, such as arsenic contamination in Giant mine in Yellowknife Canada [6], as shown in Fig. 6.1(b), or controling the groundwater contamination at the Fukushima Daiichi nuclear plant, Okuma, Fukushima Prefecture, Japan [7]. The continuous-freezing procedure is usually implemented to improve the ground structure and overcome the safety concerns, by maintaining a certain thickness of the frozen body. In order to sustain these conditions, a vast AGF system is required. For instance, the remediation plan to permanently freeze the underground arsenic trioxide dust chambers in the Giant mine will cost about a billion dollars, with extra two million dollars per year to maintain the system forever [8]. Furthermore, an annual cost of 17 million dollars is estimated to run the AGF system at the Fukushima nuclear plant [7]. These expenses could put great pressure on the available resources and arouse cost-effective concerns regarding the AGF systems, especially for such long-term projects [7, 9]. Therefore, proposing effective and reliable approaches to reduce the energy consumption, while sustaining the primary objectives of AGF systems, are of great interest to specialists in this field. Inspired by the concept of ventilation on demand [10, 11] and the intermittent space heating/cooling [12], the principle of the freezing on demand (FoD) is proposed as an operational technique that determines a time-scale or a temperature range of the frozen body as reference points of the intermittent cycles. The fundamental notion behind the FoD is to provide freezing

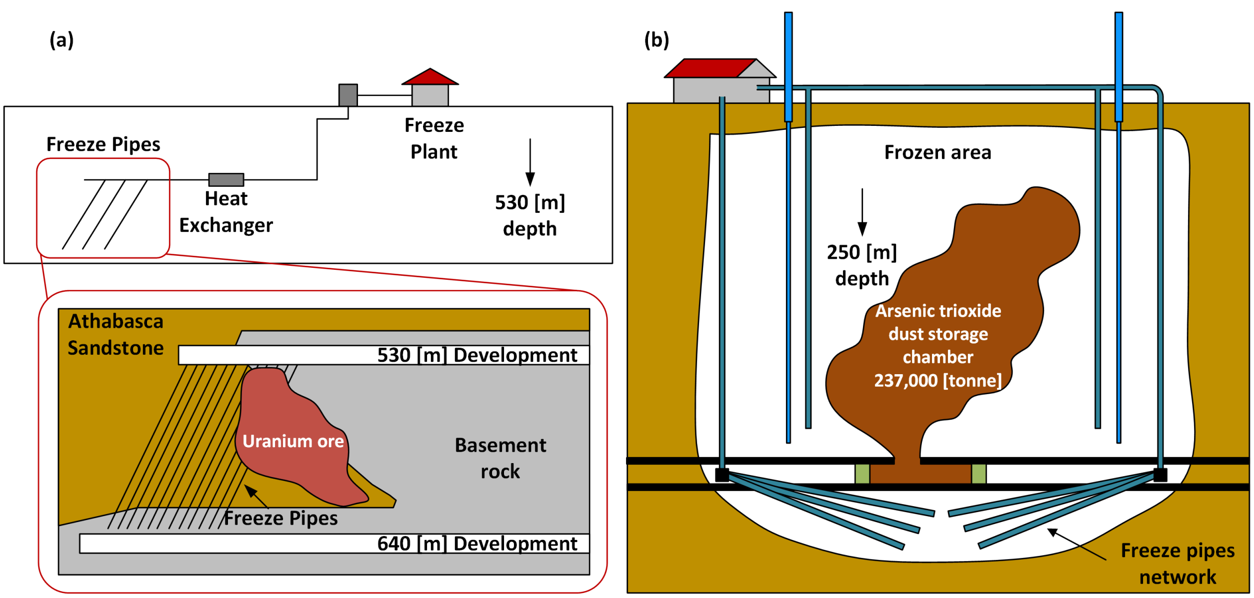

Figure 6.1 – Schematic diagram of the AGF system at (a) McArthur River uranium mine, Saskatchewan, Canada (after [4]); and (b) Giant mine, Yellowknife, NT, Canada (after [8]).

only when it is needed. The sub-zero brine is fed to the freeze pipes' network to create a thick, merged frozen body encircling the working area. Whenever the barrier achieves particular, predetermined temperature and thickness, the AGF system is compelled to stop. While the system is switched off, the frozen body is capable of maintaining its thickness and its core temperature to a certain limit (called here the upper limits). Once the upper limits are attained, the AGF begins to supply the coolant into the pipes' network [13, 14]. Implementing this idea, however, is not trivial and requires rigorous assessment during the design process. Due to geothermal heat flux that impacts the frozen ground behavior, the most critical aspect is that the upper limits should never exceed the safety limits determined by the system's requirements.

The concept of an intermittent operation is discussed in several studies as a tool to improve the performance of geothermal latent-heat storage [15–18] and to regulate the thickness of the frozen soil [19–26]. Jessberger and Makowski [19] studied the effect of intermittent freezing on the growth rate of the frost heave. Passive freezing with a constant time interval of 24 [hr] was applied. The frost heave reduced from 105 [mm] into 15 [mm]. Stevens [20, 21] discussed the impact of the intermittent cycles' time length on the heat transfer rate between the freeze pipe and the surrounding ground. The results showed that the heat transfer is higher at the beginning of the intermittent cycles and decreases with time. Also, the cycle-averaged heat transfer decreases monotonously with decreasing intermittent cycle's period. Thus, the highest overall heat transfer can be achieved by running the AGF continuously. Lackner et al. [22] addressed the effect of the intermittent freezing on the growth of the frozen body. The freezing process was divided into two sequential parts: (i) six days of continuous freezing at a coolant temperature of -30 [°C] in order to create a frozen body to a required thickness, and (ii) intermittent freezing for another eight days to maintain the thickness of the frozen body. The freezing process in the second part was reduced to 1, 3, and 5 [hr/day]. They concluded that the time span of the intermittent freezing showed a limited effect on the thickness of the frozen body. Also, they highlighted that the continuous growth of the frozen body could result in an undesirable frost heave that could lead to serious damage to the surface infrastructure. Gao et al. [23] examined the impact of various intermittent intervals on the growth of the frozen body. Ratios of 40:60, 35:65, and 60:40 between the running and stopping cycles where implemented. They concluded that the intermittent intervals' ratios are important factors regarding the optimization of the freezing process. Zhou and Zhou [25] performed lab-experiments to analyze the effect of intermittent freezing on the frost heave. Constant-time intermittent cycles were implemented in their experiment. They found out that the frost heave is effectively reduced by using the intermittent freezing mode.

As stated previously, the purpose of applying the intermittent freezing in AGF process is mainly to control the growth of the frozen body for short-time applications. Here, we propose a novel concept of freezing on demand (FoD) with the ultimate goal to reduce the energy consumption. To the best of our knowledge, no prior study has been reported that studied the FoD experimentally or numerically as an energy saving approach for AGF system. Therefore, the objectives of the work presented here are 3-fold: (i) to design and build a laboratory scale AGF rig to quantify the ground's behavior towards the FoD concept; (ii) derive and develop a mathematical three-dimensional, conjugate-heat-transfer model and validate it against the experimental data; and (iii) study the effect of various design and operating parameters - spacing between two freeze pipes, brine's temperature, and ground's initial temperature - on the amount of energy saving.

In the following, a brief description of the experimental setup is discussed in the first part. The model development along with its validation and the numerical illustrations is followed in the second part; it comprises conservation equations of mass, momentum, and energy of phase-change phenomenon in a porous medium. In the results and discussion section, the experimental results along with the mathematical model's outcomes are used for a proof-of-concept analysis. After that, the results of a parametric study that highlights the influence of the design and operating parameters of an AGF system is carried out. Finally, conclusions are drawn with emphasis on the impact of the FoD on the energy consumption as compared to a typical, continuous-freezing, long-term AGF systems.

6.2 Physical model

A laboratory-scale AGF experimental rig has been designed and built at the Mine Multi-physics laboratory, McGill University, as illustrated in Fig. 6.2. The apparatus is basically a vertical cylinder with a diameter of 0.55 [m] and hight of 1.64 [m] that contains fully saturated sand and two vertical freeze pipes; the dimensions of the physical model and the sand properties are shown in Table 6.1 and Table 6.2, respectively. The rig is equipped with more than 80 thermocouples to measure the flow's and the ground's temperatures. Three panels of thermocouples are installed at three levels to measure the ground's temperature surrounding the freeze pipes, as explained in Fig. 6.3. The freeze pipes are connected to a supply chiller that is capable of providing the system with coolant's temperature as low as -30 [°C]. The rig is equipped with advanced instrumentation systems to control the chiller and the pump's VFD, as well as recording the data of the temperature and flow rates. The tank and the connection pipes are insulated with sufficient insulation materials to reduce the heat gain from the surrounding environment. Full details about the physical setup and materials' properties can be obtained from [27]. The FoD procedure is conducted based on the core temperature of the frozen body. The readings of thermocouple no. 3 (See Fig. 6.3) are used to set the upper and lower limits of the intermittent cycles. Initially, the system freezes the ground continuously until the core temperature reaches predetermined values. At that point, the intermittent operation of the supply chiller started based on specific uppermost and lower perimeters. In this study, the temperatures of -10 [°C] and -5 [°C] are set as the

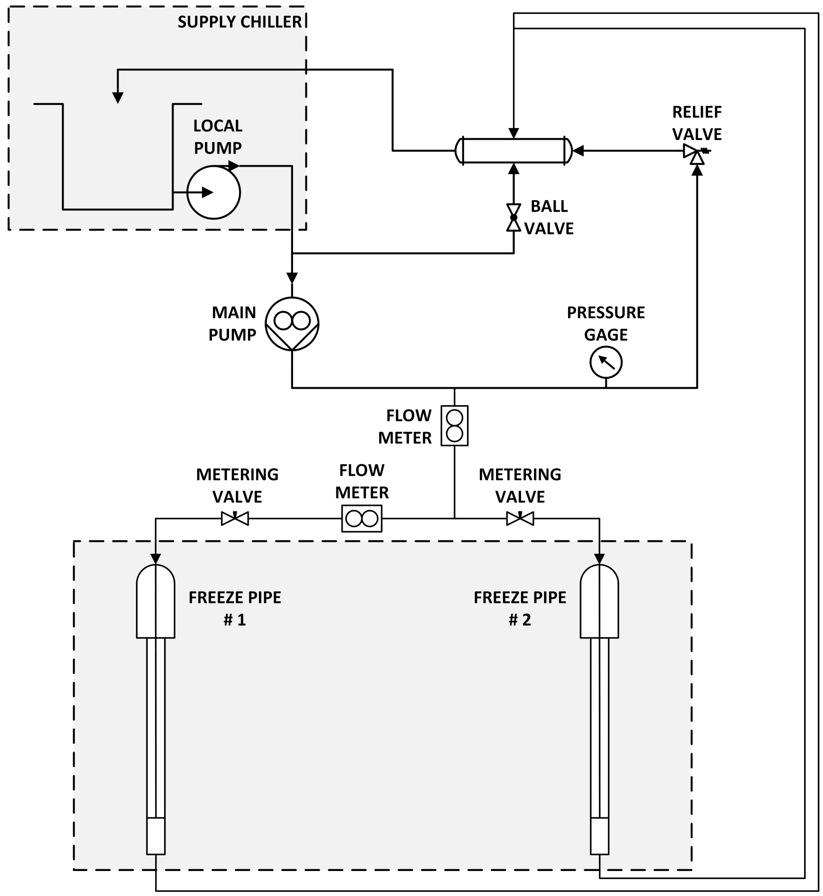

Figure 6.2 – Flowchart of the experimental setup showing the main components (after [27]).

boundaries of the intermittent cycles.

6.3 Mathematical model

The mathematical model comprises two conjugate domains: the coolant's flow in the bayonet tube freeze pipes, and the surrounding, saturated ground structure. The adjoined domains are coupled, thermally, by the wall of the freeze pipes. The flow is assumed to be incompressible, single-phase, and turbulent flow. The ground structure, on the other hand, is assumed to be fully saturated with water, where the soil particles are presumed to be rigid.

6.3.1 Governing equations

In this paper, a three-dimensional, cylindrical-coordinates model is solved for the flow in the freeze pipes and the porous ground structure. Detailed description of all parameters can be

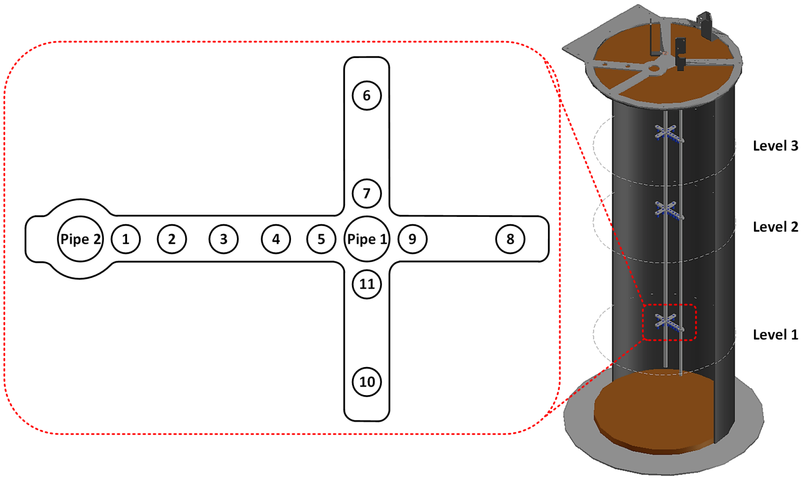

Figure 6.3 – The structure of the experimental rig showing thermocouple positions within the tank.

Table 6.1: Dimensions of the tank and the freeze pipes

	Value
Tank	
Total hight [m] (in)	1.64 (64.500)
Sand hight [m] (in)	1.55 (61.125)
Outer diameter [m] (in)	0.55 (21.625)
Wall thickness [cm] (in)	0.64 (0.250)
Base thickness [cm] (in)	0.95 (0.375)
Freeze pipe	
Length [m] (in)	1.4 (55.125)
Annulus tube outer diameter [cm] (in)	1.3 (0.500)
Inner tube outer diameter [cm] (in)	0.64 (0.250)
Clearance length [cm] (in)	1.3 (0.500)
Outer tube thickness [mm] (in)	0.89 (0.035)
Inner tube thickness [mm] (in)	0.89 (0.035)
Clearance cap thickness - outer tube [mm] (in)	1.60 (0.063)

found in the Nomenclature.

Table 6.2: Properties of the sand particle that is used in this study

Quantities	Value
Particle diameter (D_{50}) [mm]	0.212
Quartz content [%]	90.5
Thermal conductivity [W/(m.K)]	3.73
Density [kg/m^3]	2,634.50
Specific heat capacity [J/(kg.K)]	945.92
Porosity [%]	37
Permeability [m^2]	4.94×10^{-12}

Flow in the freeze pipes

In the freeze pipes, the conservation equations of mass, momentum, and energy are given as [28]:

— Conservation equation of mass:

$$\frac{\partial}{\partial t}(\rho) + \nabla \cdot \left(\rho \overline{\mathbf{U}}\right) = 0 \tag{6.1}$$

— Conservation equation of momentum:

$$\frac{\partial}{\partial t}\left(\rho \overline{\mathbf{U}}\right) + \nabla \cdot \left(\rho \overline{\mathbf{U}}\ \overline{\mathbf{U}}\right) = \nabla \cdot \left((\mu + \mu_t)\left(\nabla \overline{\mathbf{U}} + \nabla \overline{\mathbf{U}}^T\right)\right) - \nabla P + \rho \mathbf{g} \tag{6.2}$$

— Conservation equation of energy:

$$\frac{\partial}{\partial t}(\rho h) + \nabla \cdot \left(\rho h \overline{\mathbf{U}}\right) = \nabla \cdot \left[\left(k + \frac{c_p \mu_t}{Pr_t}\right) \nabla T\right] \tag{6.3}$$

where the velocity, $\overline{\mathbf{U}}$, is the averaged velocity. The standard k-epsilon formulation is used in the current study. More details of the turbulence formulation could be found in [29].

Heat transfer in the ground

The thermal and hydraulic aspects of the AGF process in a porous ground structure are formulated based on the following assumptions:

- The local volume averaging technique is used to formulate the governing equations.
- The superficial velocity is implemented in the model (i.e. $\mathbf{u} = \psi \mathbf{u}_\ell$).
- The soil particles and the solid water (ice) are rigid (i.e. $\mathbf{u}_s = \mathbf{u}_p = 0$).
- The buoyancy forces due to the natural convection are small enough to be neglected.
- The presence of the groundwater seepage is neglected.

- The soil particles, liquid water, and solid water are in local thermal equilibrium (i.e. $T_p = T_\ell = T_s$).

Under the above assumptions, the governing equations could be written as below:

— Conservation equation of mass:

$$\frac{\partial \rho}{\partial t} + \nabla \cdot (\rho \mathbf{u}) = 0 \tag{6.4}$$

— Conservation equation of momentum [30]:

$$\frac{1}{\psi}\frac{\partial (\rho_\ell \mathbf{u})}{\partial t} + \frac{1}{\psi^2}\left[\nabla \cdot (\rho_\ell \mathbf{u} \otimes \mathbf{u})\right] = \frac{1}{\psi}\nabla \cdot \left(\mu_\ell \left(\nabla \mathbf{u} + \nabla \mathbf{u}^T\right)\right) - \nabla p + \rho_\ell \mathbf{g} - \left[\frac{\mu_\ell}{K}\mathbf{u} - \mathbf{u}C_m \frac{(1-\xi)^2}{\xi^3}\right] \tag{6.5}$$

The buoyancy source term is used to induce the natural convection within the voids. The last two terms are Darcy and mushy source terms, respectively. Darcy source term characterizes the bulk resistance to the flow. The permeability, K, accounts for the interstitial surface area, the path of the fluid flow, and other related hydrodynamic characteristics of the porous medium. For a spherical backed soil structure, the permeability, K, is defined as a function of the porosity, ψ, and the mean diameter of the sand, d_p, based on the Carman-Koseny definition:

$$K = \frac{\psi^3}{180\,(1-\psi)^2} d_p^2 \tag{6.6}$$

The mushy source term is basically a modified Darcy source term that affects the momentum balance as follows. In the liquid zone, the mushy source term takes a value of zero; the single-phase momentum equation is then approximated by Darcy law. Within the freezing zone (i.e., mushy zone), the source term increases from zero to a large value as the local liquid fraction, ξ, decreases from its liquid value of 1 to its solid value of 0. As the local liquid fraction approaches zero, the mushy source term dominates all other terms in the momentum equation, and force the velocity, $\mathbf{u}$, to a value close to 0.

— Conservation equation of energy:

$$\frac{\partial (\rho h)_e}{\partial t} + \nabla \cdot (\rho_\ell h_\ell \mathbf{u}) = \nabla \cdot (k_e \nabla T) - S_H \tag{6.7}$$

where

$$(\rho h)_e = \psi\left[\xi \rho_\ell h_\ell + (1-\xi)\,\rho_s h_s\right] + (1-\psi)\,\rho_p h_p \tag{6.8}$$

The effective thermal conductivity, k_e, is formulated using the parallel arrangement approach as [31]:

$$k_e = \psi\left(\xi k_\ell + (1-\xi)\,k_s\right) + (1-\psi)\,k_p \tag{6.9}$$

The source term, S_H, is defined as:

$$S_H = \Delta H \left[\psi \frac{\partial \xi \rho_\ell}{\partial t} + \nabla \cdot (\xi \rho_\ell \mathbf{u}) \right] \tag{6.10}$$

The contribution of the latent heat, ΔH, is included in the source term, S_H. In the liquid zone, the liquid fraction, ξ, takes a constant value of 1. Thus, the time and spatial derivatives are equal to zero (i.e. $\partial \xi / \partial t = \nabla \cdot \xi = 0$). In the mushy zone, however, the liquid fraction decreases, which, in turn, induce the contribution of the source term, S_H, to the conservation equation of energy.

6.3.2 Initial and boundary conditions

Besides specifying the basic set of conservation equations and characteristics of the thermal-hydraulic aspects of the AGF system, we need to define the initial and boundary conditions to solve the model equations during the continuous freezing, and while applying the FoD procedure. Initially, the coolant temperature is set to be in thermal equilibrium with the ground. Definition of the boundary conditions is needed for inlet, outlet, and the wall of the freeze pipes. Temperature and velocity are known parameter for the freeze pipes' inlets; pressure and gradient of the temperature are known for the freeze pipes' outlets; no-slip wall and thermally coupled condition are prescribed as the boundary conditions for the freeze pipes' wall during the continuous freezing stage and during the freezing phase of the intermittent freezing cycles. When the system is off, a zero heat flux is determined as the boundary conditions at the wall. Thus, decoupled the adjoined coolant's flow and the surrounding ground.

- *Initial condition*:

$$T_g = T_c = T_{init}, \quad \overline{\mathbf{U}} = \mathbf{u} = \mathbf{u}_{init} \tag{6.11}$$

- *Freeze pipe's inlet*:

$$\mathbf{U} = \mathbf{U}_{in}, \quad T = T_{in} \tag{6.12}$$

- *Freeze pipe's outlet*:

$$p = p_{out}, \quad \mathbf{n} \cdot \nabla T = 0 \tag{6.13}$$

- *Freeze pipe's wall*:

$$\mathbf{u}_w = 0 \tag{6.14}$$

  During freezing phase:

$$q_w = \pm k_w \frac{\partial T}{\partial x} \tag{6.15}$$

$$k_c \frac{\partial T_c}{\partial n} = k_w \frac{\partial T}{\partial n}; \quad T_c = T \tag{6.16}$$

$$k_g \frac{\partial T_g}{\partial n} = k_w \frac{\partial T}{\partial n}; \quad T_g = T \tag{6.17}$$

where **n**= normal to the surface in question.

During no-freezing phase:

$$q_w = 0 \tag{6.18}$$

6.4 Computational procedure

The computational domain was created in accordance with the dimensions of the experimental setup [27]. The domain is then meshed with a structured, hexahedral mesh, and was labeled with proper boundary conditions. Different mesh size were implemented and compared to ensure the solution's independence. In the beginning, the domain was meshed with a coarse mesh consisting of 5×10^3 elements, followed by several mesh adaptations until the difference in computed ground's temperature was below 1% with a final mesh size of 6.3×10^5.

The finite-volume solver (ANSYS Fluent 16.1) was used to solve the governing equations. Within the solver, the standard k-epsilon formulation was selected to govern the turbulence flow. The model considers a two-equation model that solves for turbulent kinetic energy and rate of dissipation. Also, the solidification/melting approach was activated to simulate the freezing in the porous ground structure; the mushy constant was calibrated at 5×10^6. A user-defined functions (UDFs) was used to specify the inlet temperature, inlet velocity, and the temperature-dependent properties of the water and the coolant. The FoD technique was implemented automatically by changing the boundary condition of the freeze pipe's wall from coupled-boundary (in the freezing phase) to a decoupled-boundary with no heat flux (in the no-freezing phase) using a logical algorithm in a scheme-language commands and journal scripting. More than 45 points were created to monitor the coolant's outlet temperature, as well as the ground's temperature at three different levels (See Fig. 6.3). The transient time step was set to ensure sufficient convergence criteria (predetermined at 1×10^{-5}). The equations were solved with the Semi-Implicit Pressure-Linked Equation (SIMPLE) algorithm and second-order upwind discretization.

6.5 Model validation

The proposed model was validated against the experimental data. The actual inlet temperature and flow rate were curve fitted and fed into the model's boundary conditions. However, the oscillation of the inlet temperature and the flow rate during the FoD were not considered in the curve-fitted inlet boundary conditions. As discussed previously, the chiller is switched off within the no-freezing phase of the intermittent cycles; this stage is simulated by decoupling the coolant's flow and the porous ground (i.e., zero heat flux). The no-freezing stage is considerably short, as compared to the lifetime of the experiment. Moreover, after 35 [hr] of continuous freezing (70 % of the experiment lifetime), one can expect a small temperature gradient across the freeze pipe's wall. Thus, decoupling the two adjoined domains with a zero heat flux boundary conditions is a valid assumption.

The intermittent cycles started once the core's temperature of the frozen body reached -10 [°C], and the total time of the experiment was 50 [hr]. Good agreement between the model and the experimental data was observed, which can be discerned from Fig. 6.4.

6.6 Results and discussion

Thus far, we have discussed the development of the lab-scale setup, the derivation of a three-dimensional conjugate model, and the validation of this model against the experimental data. In the following, we turn our attention to the analysis of the experimental and numerical outcomes. In the beginning, a proof-of-concept evaluation is presented based on the results of the lab-scale experiment and the mathematical model. After that, the framework of the model is extended to typical design and operating conditions of an AGF system used in underground and remediation mines [32, 33]. The extended model examines the effect of particular parameters - spacing between two freeze pipes, coolant's temperature, and ground's initial temperature - on the performance of AGF system within the first four years, as presented in Table 6.3. The impact of these factors is examined under various freezing procedures: (i) continuous freezing; (ii) freezing-on-demand temperature-based, where the intermittent cycles begin once the core temperature reaches a predetermined lower limit (we use -15 [°C]); and (iii) freezing-on-demand time-based, which means that the intermittent cycles start after a certain period of time (in this study we use one year).

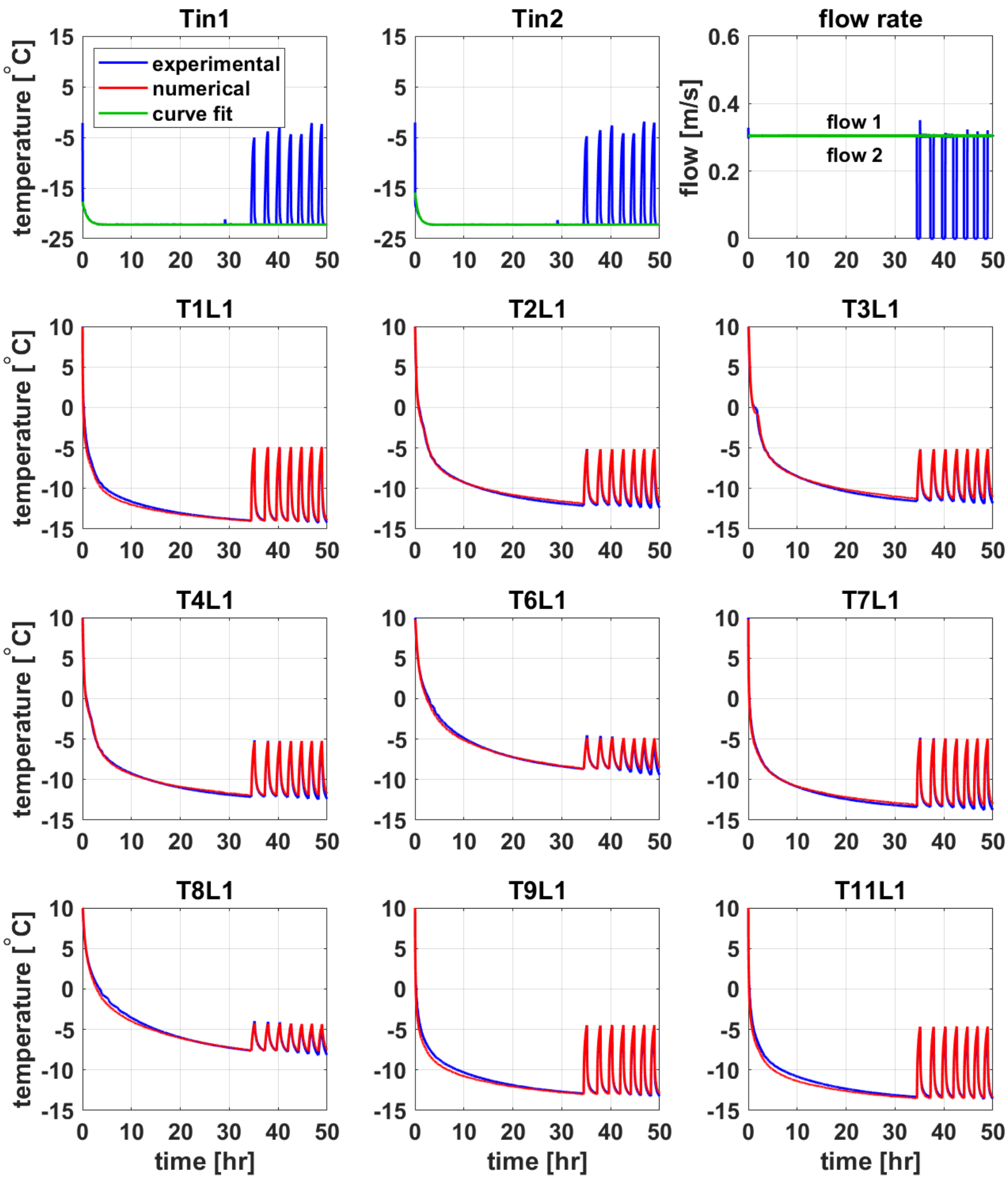

Figure 6.4 – Validation of the mathematical model against the experimental data at level 1, and the curve fit of the inlet temperatures and flow rates.

Table 6.3: Design and operating parameters at three levels

Spacing [m]	Coolant's Temp. [°C]	Ground's Temp. [°C]
1	-20	5
2	-25	10
3	-30	15

6.6.1 Proof of concept

Using specific thermocouples' readings at level-1 (see Fig. 6.3), along with the correlated temperature and liquid fraction from the numerical model, we have been able to demonstrate the proof-of-concept of the FoD, as illustrated in Fig. 6.5. We compared the results at the upper and lower limits of three different intermittent cycles: at the beginning (Fig. 6.5 (a) and (b)), at the middle (Fig. 6.5 (c) and (d)), and at the end (Fig. 6.5 (e) and (f)). The upper and lower limits were set at -5 and -10 [°C], respectively.

Clearly, the thickness of the frozen body increased despite the intermittent freezing cycles. It grew from 36.6 [cm] at the beginning, to 40 [cm] in the middle, and to 43.5 [cm] at the end of the experiment. This is due to the contribution of the frozen body during the earlier, continuous-freezing stage, and during the freezing phases of the intermittent cycles. As mentioned in Section 6.5, the FoD started after 35 [hr] of a total 50 [hr] experiment. The stored energy in the frozen ground is adequate to maintain the thickness of the frozen body during the no-freezing phase. Furthermore, the thickness of the frozen body shows no difference during the same cycle; the intermittent cycle's time is short as compared to the total time of the experiment. Hence, the geothermal heat flux from the unfrozen ground has a minimal effect on the thickness of the frozen wall. The temperature readings, on the contrary, show more intriguing results.

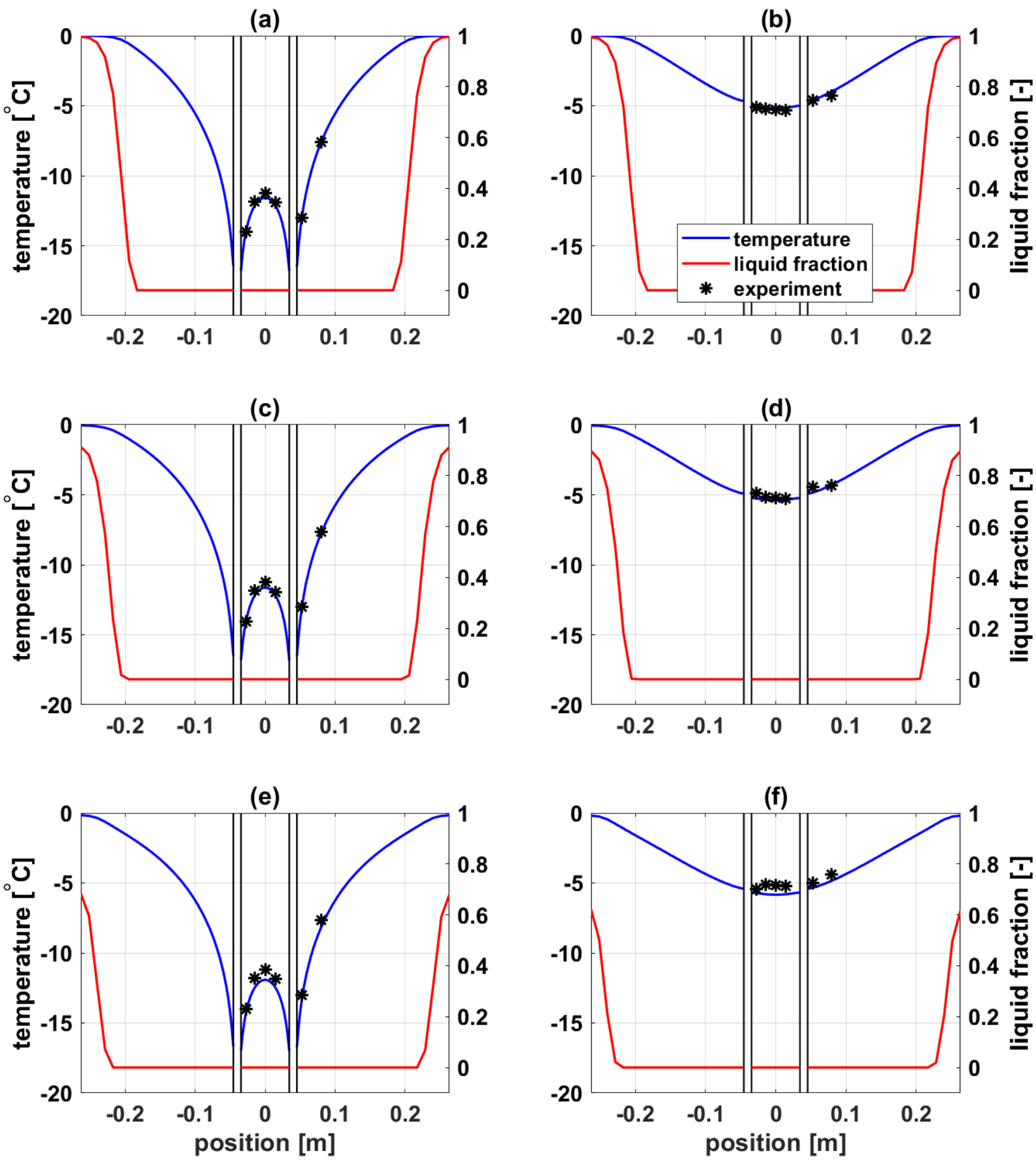

Figure 6.5 – Freezing on demand (FoD) proof of concept showing the profiles of the temperature and liquid fraction along the access of the two freeze pipes, and the experiment's measurements at: (a) the beginning of the FoD at the lower limit; (b) the end of the no-freezing phase (at the upper limit) of the first intermittent cycle; (c) the lower limit of a cycle in the middle of the FoD; (d) the upper limit of a cycle in the middle of the FoD; (e) the lower limit of the last cycle of FoD; and (f) the upper limit of the last intermittent cycle.

The upper limit of the intermittent cycles is determined based on best-practice suggestions from literature [22] and site engineers, to maintain sufficient stability within the frozen ground; that is, the temperature of the frozen body should be consistently below -5 [°C]. The lower limit, on the other hand, is chosen arbitrary based on the design and operating conditions of the current study. Certainly, one could expect that the thickness of the frozen body with a temperature reading lower than -5 [°C] will be smaller than the thickness of the overall frozen body - the growth's trend, however, should be the same. The thickness of the frozen body at the end of the freezing phases increased from 21 [cm] at the beginning, to 22 [cm] in the middle, and to 23 [cm] at the end of the experiment, as shown in Fig. 6.5 (a), (c), and (e), respectively. On the contrary, at the end of the no-freezing phases, the thickness of the frozen wall with a temperature reading lower than -5 [°C] decreased drastically. Nonetheless, the temperature between the freeze pipes did not exceed the upper limit, which is what matters most. In the real world, a typical AGF system consists of hundreds of freeze pipes that work together to create a frozen wall encircling the working area. Thus, it is essential to keep the temperature between each pair of freeze pipes below the upper limit throughout the lifetime of the system.

6.6.2 Freezing procedure

In this study, we compare the performance of AGF system under three operating schemes: classical continuous freezing, intermittent freezing based on temperature, and intermittent freezing based on time. In the following, an overall discussion on the effect of the freezing procedure on the ground's response, the thickness of the frozen body, and the energy consumption are presented. Further elaboration of the impact of individual parameter follows.

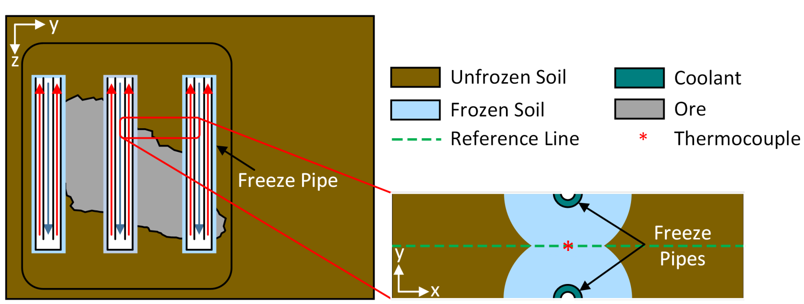

Figure 6.6 – Schematic diagram of a typical AGF system showing a cross section between two freeze pipes.

The idea of implementing the FoD is to save energy while maintaining a safe operating environment. There are, however, various parameters that influence this decision. One of the main benchmarks is when to start the procedure. Moreover, during the intermittent cycles, what are the criteria that govern the operating limits. Here, we proposed two strategies to initiate the FoD. The first one is to start the FoD once the core point of the frozen body reached -15 [°C]; the core point is located precisely between two freeze pipes, as illustrated in Fig. 6.6. The temperature value of this point is chosen based on other parameters, such as the coolant's temperature and pipes' spacing. This strategy disregards the total timeframe of the AGF process. Hence, the FoD could start as early as 13 days, as shown in Fig. 6.7(g), or after 816 days (more than two years), as observed in Fig. 6.8(c), or it could never begin within the designated time frame of the AGF process, as depicted in Fig. 6.9(c).

The other approach is to begin the FoD based on a time-scale despite the temperatures' readings. A sample of the first four years is selected to study the AGF process, where the FoD starts after one year. In some cases, the core temperature of the frozen body is much lower than -15 [°C] (the lower limit), as described in Fig. 6.7(g)-(i) and Fig. 6.8(g)-(i). In limited cases, the core temperature almost matches the lower limit after one year of freezing, as illustrated in Fig. 6.9(h). In both scenarios, the intermittent cycles are controlled only by the core's temperature of the frozen body, i.e., the time interval of the cycles is not a controlled parameter. Therefore, in each case, with time evolved, the time needed to complete one intermittent cycle increased. In general, a gradual increase in the no-freezing phase is observed, which is, at the same time, accompanied by a decrease in the freezing phase. This is to be expected, due to the contribution of the frozen body, as a heat sink, to the intermittent freezing phases. This approach is selected, in contrast to previous studies [22, 25], to satisfy the safety requirements despite the growth rate of the frozen ground.

Based on the principles of each strategy, one could expect a significant impact on the thickness of the frozen body. Surprisingly, this is not the case. As shown in Figs. 6.10, 6.11, and 6.12, the choice of the FoD method has an insignificant effect on the overall thickness of the frozen body. Further, due to the increase in the size of the frozen body throughout the freezing process, its center, at later stages, requires more time to warm up, and less time to cool down. Therefore, the influence of the intermittent freezing on the growth of the frozen body, in the late stages, is marginal.

The energy consumption is considered based on the geometry of a typical freeze pipe; 50 [m] long and a diameter of 8.9 [cm] (3.5 [inch]). The impact of implementing the FoD concept is evident. An overall glance at Fig. 6.13 shows that the continuous freezing consumes in average around 101.9 [MWhr], as compared to 75.8 [MWhr] in FoD temperature-based, and 77.1 [MWhr] FoD time-based. The first approach of FoD showed lower average energy consumption due to the fact that in most cases it starts earlier than the time-based scenario.

6.6.3 Spacing between two freeze pipes

The primary objective of this section is to examine the influence of the distance between two freeze pipes on the ground's temperature, the thickness of the frozen body, and the energy consumption. The spacing between two freeze pipes has a proportional relationship with the time interval of intermittent cycles. As depicted in Fig. 6.7, with a distance of 1 [m], one cycle needs in average 51 days, as compared to 136 days in the case of 2 [m], and 171 days with a spacing of 3 [m], as illustrated in Fig. 6.8 and Fig. 6.9, respectively. This is due to the fact that the heat flux has a proportional relationship with the volume of the ground - here the pipes' spacing. This phenomenon becomes more clear with wider spaces between the pipes. In certain scenarios of 2 and 3 [m] cases, the FoD could not start before two years, or at certain operating conditions, the pipes' spacing could prevent the initiation of the FoD, as shown in Fig. 6.9(a)-(c).

The thickness of the frozen body has a reverse relationship with the spacing between two freeze pipes. This applies to all cases, but we will discuss a particular case where the spacing is the only varying parameter; the coolant's and ground's temperatures are fixed at -30 and 5 [°C], respectively. The frozen body at the spacing of 1 [m] has a thickness of 18.4 [m]; it decreases to 18.1 [m] in the case of 2 [m], and to 16 [m] with a spacing of 3 [m], as shown in Fig. 6.10(g), Fig. 6.11(g), and Fig. 6.12(g), respectively. The growth of the frozen body is divided, essentially, into two stages. The first stage starts at the beginning of the AGF process to the point where a closed, frozen body is created. In this stage, the frozen body grows evenly around the freeze pipe. Once the second stage started, the merged frozen body begins to move away in perpendicular with the freeze pipes. Therefore, the second stage requires more time to start at spacing of 3 [m], as compared to the other two cases, which leads to a decrease in the thickness of the frozen body. However, this behavior is not universal. In particular cases, such as Fig. 6.10(a), Fig. 6.11(a) where the coolant's and ground's temperatures are fixed at -20 and 5 [°C], respectively, the thickness of the frozen body actually increases from 17.2 [m] with a spacing of 1 [m], to 18.42 [m] with a spacing of 2 [m]. In these cases, it is difficult, apparently, to determine the effect of the pipe spacing in isolation of other parameters, especially the brine's temperatures. The impact of the coolant's temperature will be discussed in the next section.

The effect of the freeze pipes' spacing on the energy consumption is evident, as depicted in Fig. 6.13. The amount of the saved energy is higher with a 1 [m] spacing case, as compared to the other two cases. For convenience, we averaged the energy consumptions of the two FoD strategies and compared them with the energy consumptions of the continuous freezing. At the spacing of 1 [m], the averaged energy consumption of FoD scenario is 35.6% lower than the continuous freezing. Also, the cases of 2 and 3 [m] spacing reduced, in average, the energy consumption by 28.6% and 18.7%, respectively, as compared to the continuous freezing scenario, as illustrated in Fig. 6.14. It is clear that the percentage of the energy saving has an inverse correlation with the pipes' spacing. The short distance between the pipes allows the FoD to start early, in case of the temperature-based scenario, or have a colder temperature, in case of the time-based scenario. On the contrary, when the distance between the pipes increases, the ground needs more time to have a merged frozen body, which means the AGF system should stay turned on for a longer time.

6.6.4 Brine's temperature

The sub-zero temperature of the brine is required to overcome the sensible and latent heat in the ground. In this work, three coolant's temperatures are studied: -20, -25, and -30 [°C]. The brine's temperature affects the FoD in two ways; in the temperature-based case, the FoD with a brine's temperature of -30 [°C] started earlier than the FoD with a brine's temperature of -25 [°C] or -20 [°C]. In the case of the FoD with the time-base scenario, the lower the brine's temperature, the lower the core temperature after one year. Within the frozen body, the dominating mechanism is conduction. The conductive heat transfer, q, has a proportional relationship with the temperature difference, $q \propto \Delta T$. Thus, at lower brine's temperature, taking into consideration similar design and operating conditions, the core of the frozen body gets colder, which reflects on the behavior of the FoD procedure. On the other hand, combining this parameter with the pipes' spacing, the core's temperature in case of 3 [m] spacing could not reach the lower limit of -15 [°C], as presented in Fig. 6.9(a)-(c).

The effect of the coolant's temperature on the thickness of the frozen body has a combined effect along with the FoD type and the spacing between freeze pipes. For instance, at the spacing of 1 [m], the thickness of the frozen body under FoD temperature-based type decreases with reducing the coolant's temperature. At the same time, the thickness of the frozen body under FoD time-based increases with reducing the brine's temperature. In order to understand this behavior, we should consult the temperature response from Fig. 6.7. By considering the FoD temp-based, the intermittent cycles start as early as 13 days when the coolant's temperature is -30 [°C], as compared to 25 days at -25 [°C] and 82 days at -20 [°C]. On the contrary, under FoD time-based, the intermittent cycles start at the same time despite the frozen body's temperature. These observations lead us to understand the effect of the FoD, in general, on the thickness of the frozen body. The longer the time that takes the FoD to start, the thicker the frozen body is. Therefore, when the FoD begins at the same time (FoD time-based), the effect of the coolant's temperature on the thickness of the frozen body is obvious. This aspect is more emphasized in the case of the 3 [m] spacing. In spite of the FoD strategy, the thickness of the frozen body decreases with decreasing the brine's temperature. Again, by observing the temperature response from Fig. 6.9, one can notice that the FoD did not have the chance to start in the case of a coolant's temperature of -20 [°C]. In the case of -25 [°C], FoD starts, despite the first cycle after one year, around the second year. In the last case of -30 [°C], it started roughly after one year. Therefore, as discussed previously, the thickness of the frozen body decreases with decreasing the coolant's temperature.

The trend of the energy consumption at different coolant's temperatures differs between continuous freezing and FoD freezing. Generally, with the continuous-freezing procedure, the energy consumption increases with decreasing the coolant temperature, as shown in Fig. 6.13. This is to be expected, due to the proportional relation between the heat flux and the temperature difference. On the other hand, the energy consumption tends to decrease with decreasing the brine's temperature, as depicted in Fig. 6.13(ii) and (iii). As discussed previously, this is due to the start time of the FoD, or the core temperature of the frozen body (when the FoD time-based technique is used).

6.6.5 Ground's initial temperature

The ground's initial temperature has a marginal effect on the thickness and temperature of the frozen body, and on the energy consumption, as compared to the other two parameters. Yet, there is an apparent effect on the temperature of the frozen body at coolants temperature of -25 [°C], pipes' spacing of 3 [m], and under the FoD time-based scenario. The FoD time-based procedure starts after one year in spite of the frozen body's temperature. However, when the ground is initially at a lower temperature (5 [°C]), considering the same thermophysical properties and same operating conditions, it should have a lower temperature after one year, as compared to the other two cases (10 and 15 [°C]). The lower core temperature is associated, ideally, with a thicker frozen wall, or larger heat sink, which help the freezing phase of the first cycle to reach the lower limit faster, as compared to the other cases, which is clearly observed in Fig. 6.9(ii).

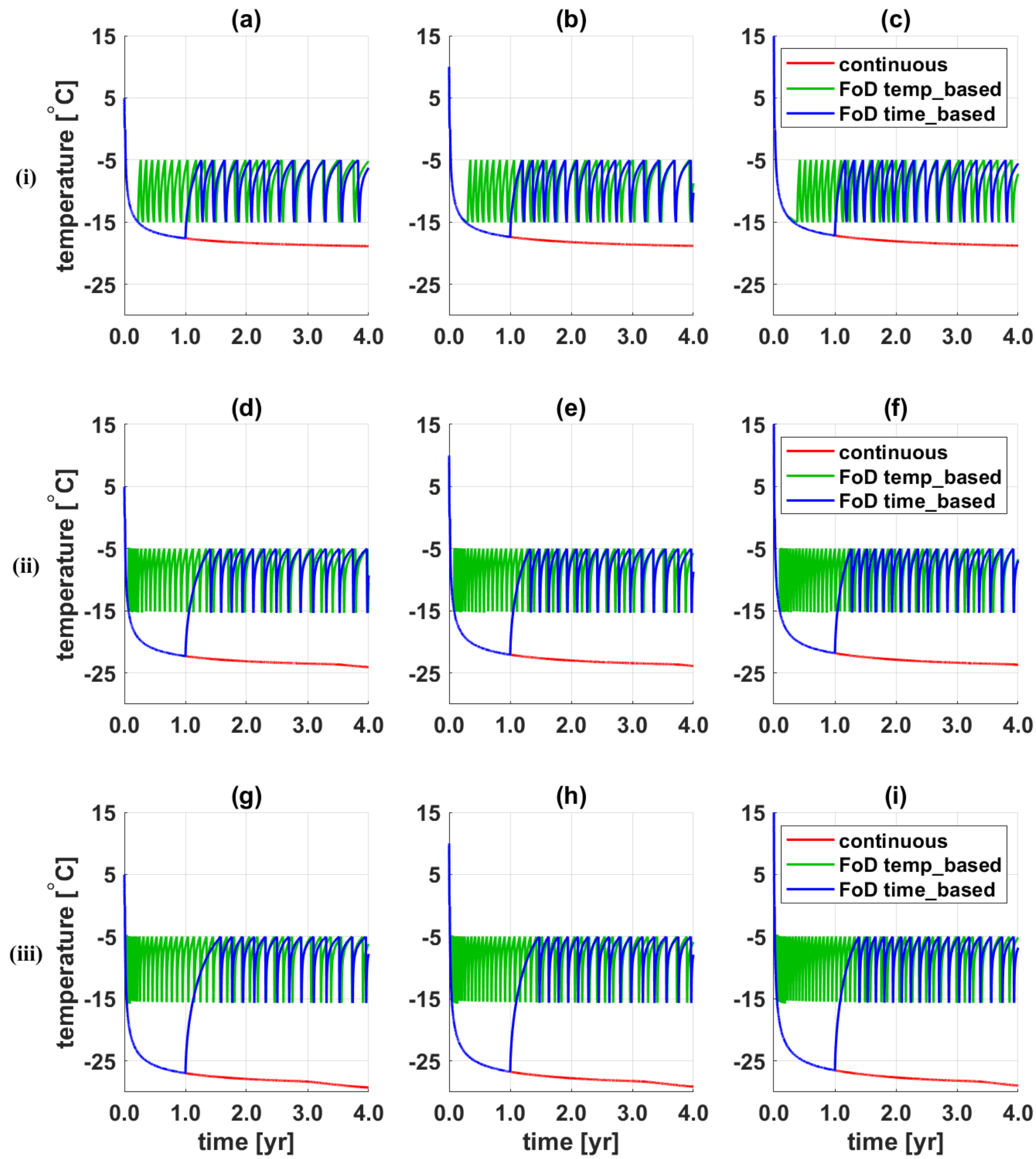

Figure 6.7 – The temperature readings at the center between two freeze pipes (See Fig. 6.6) of a spacing of 1 [m], at coolants temperature of: (i) -20 [°C]; (ii) -25 [°C]; and (iii) -30 [°C], and with a ground's temperature of: (a), (d), and (g) 5 [°C]; (b), (e), and (h) 10 [°C]; and (c), (f), and (i) 15 [°C].

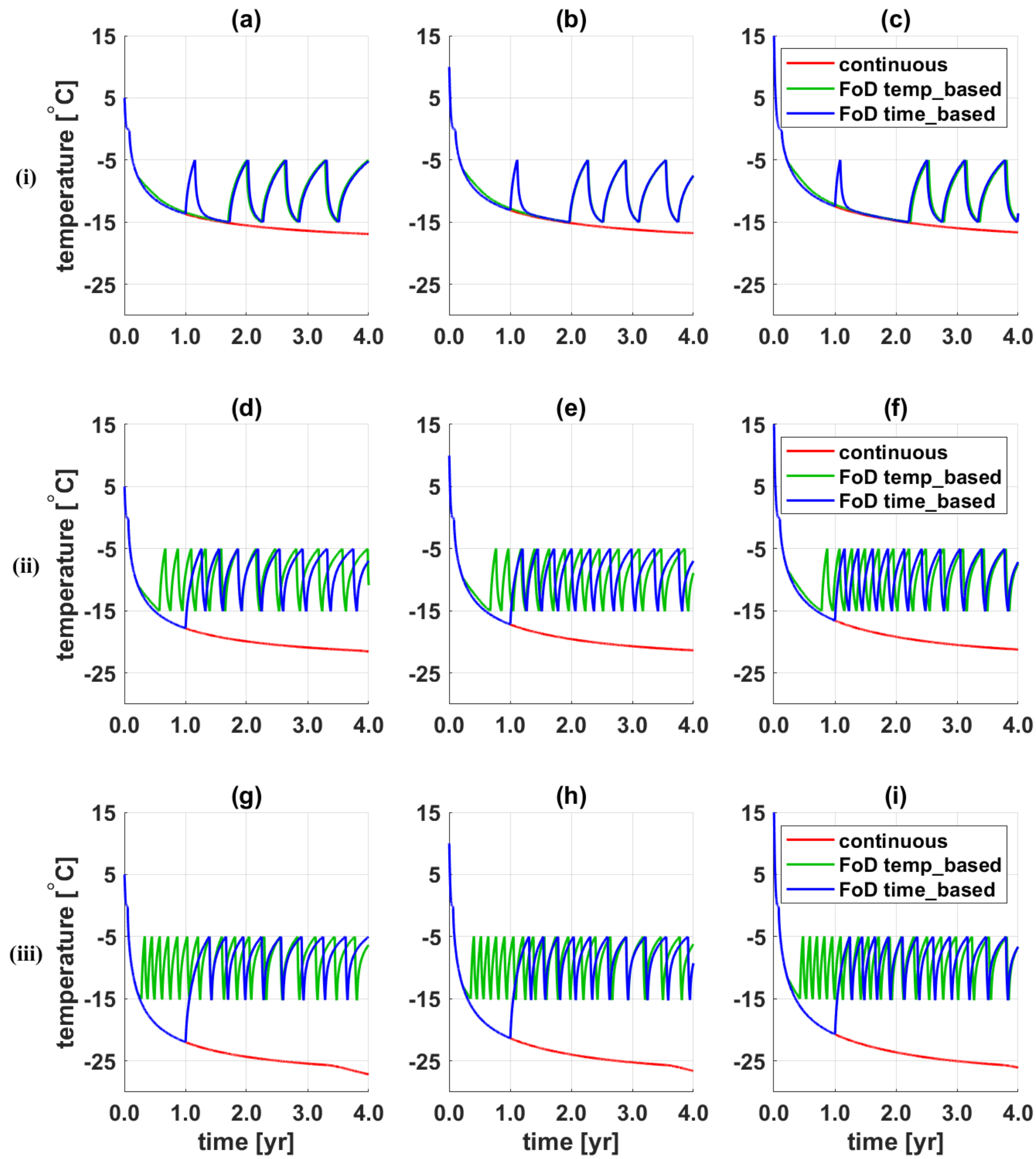

Figure 6.8 – The temperature readings at the center between two freeze pipes (See Fig. 6.6) of a spacing of 2 [m], at coolants temperature of: (i) -20 [°C]; (ii) -25 [°C]; and (iii) -30 [°C], and with a ground's temperature of: (a), (d), and (g) 5 [°C]; (b), (e), and (h) 10 [°C]; and (c), (f), and (i) 15 [°C].

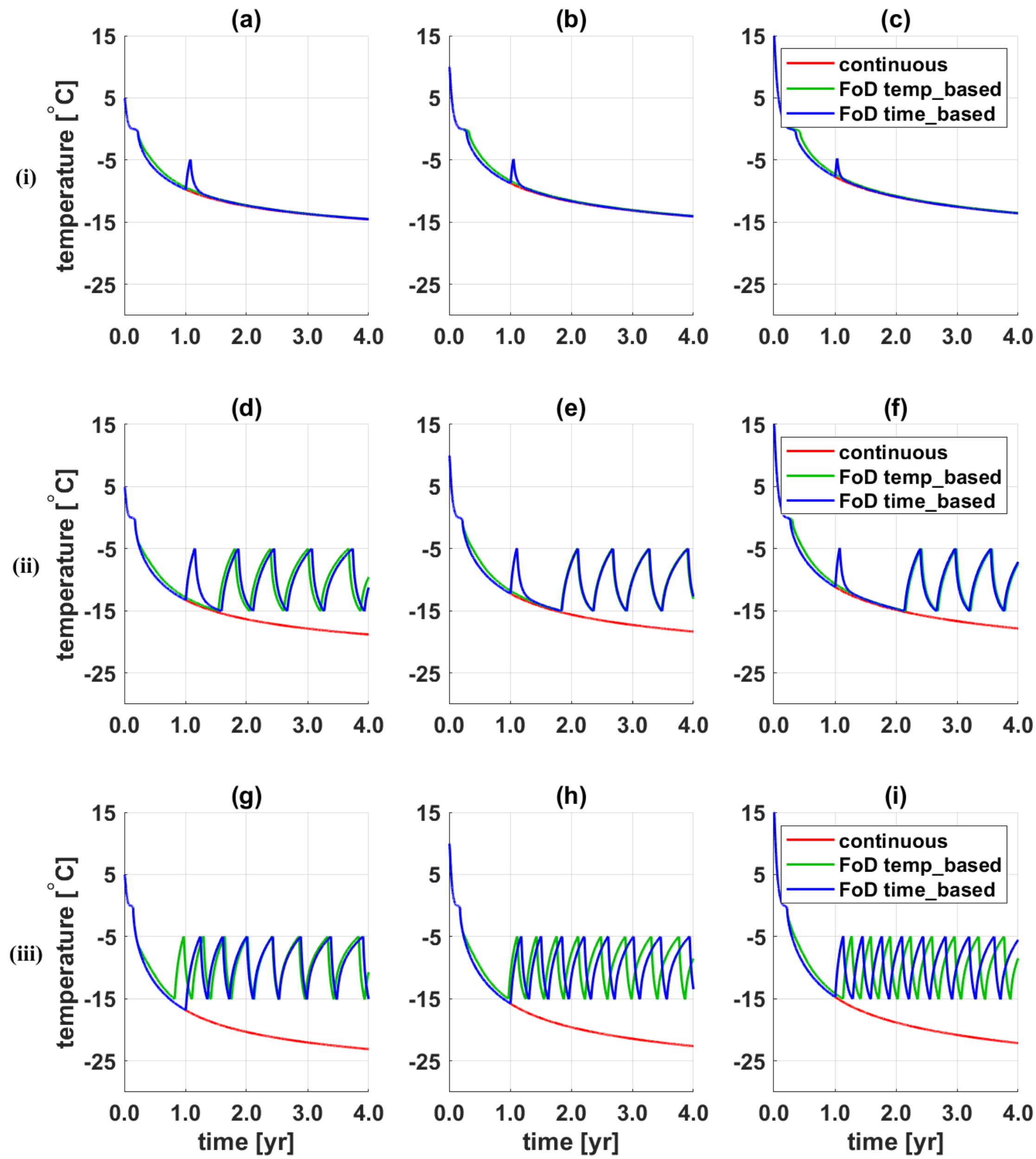

Figure 6.9 – The temperature readings at the center between two freeze pipes (See Fig. 6.6) of a spacing of 3 [m], at coolants temperature of: (i) -20 [°C]; (ii) -25 [°C]; and (iii) -30 [°C], and with a ground's temperature of: (a), (d), and (g) 5 [°C]; (b), (e), and (h) 10 [°C]; and (c), (f), and (i) 15 [°C].

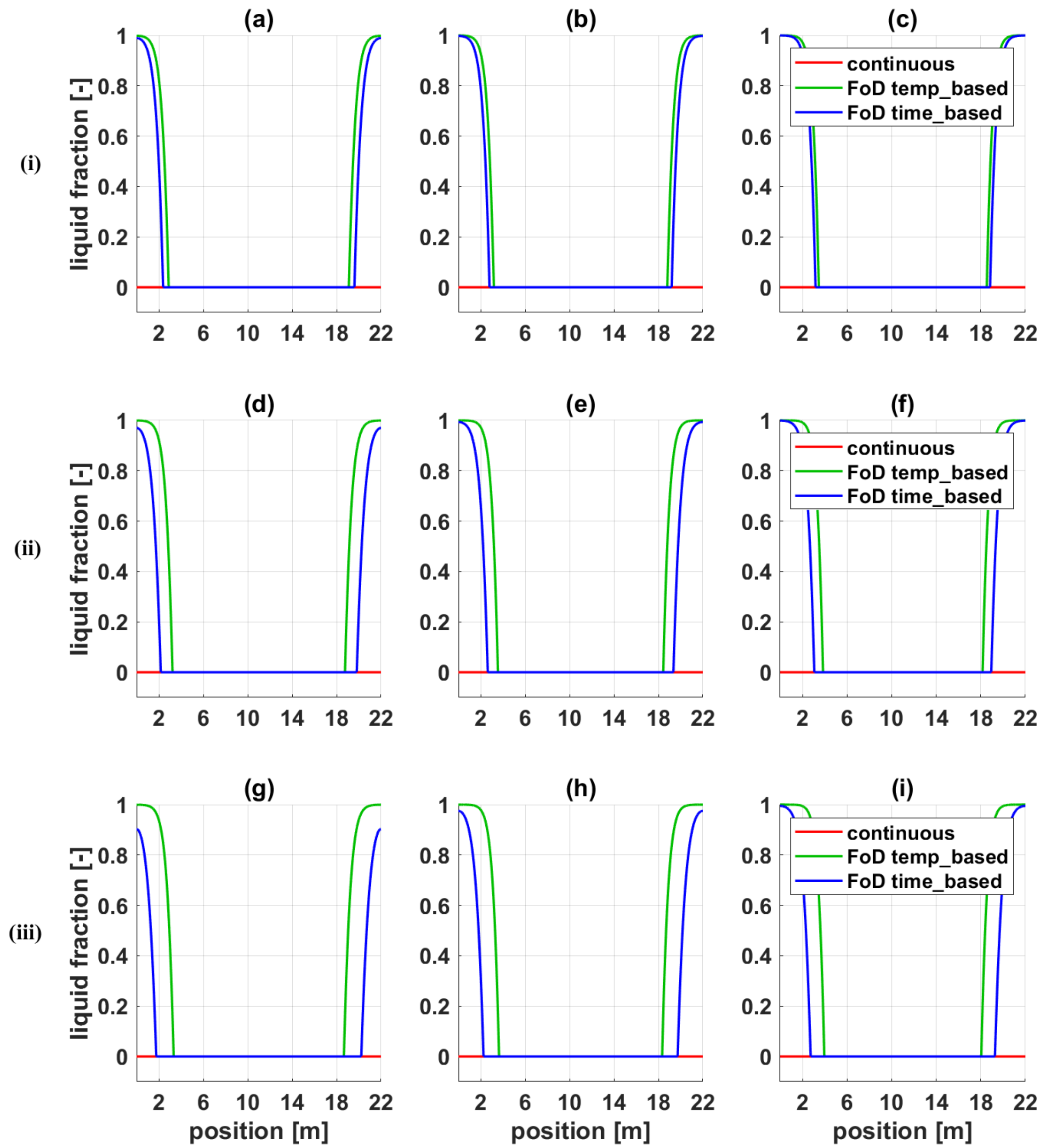

Figure 6.10 – The liquid fraction along the reference line (See Fig. 6.6) of a spacing of 1 [m] at coolants temperature of: (i) -20 [°C]; (ii) -25 [°C]; and (iii) -30 [°C], and with a ground's temperature of: (a), (d), and (g) 5 [°C]; (b), (e), and (h) 10 [°C]; and (c), (f), and (i) 15 [°C].

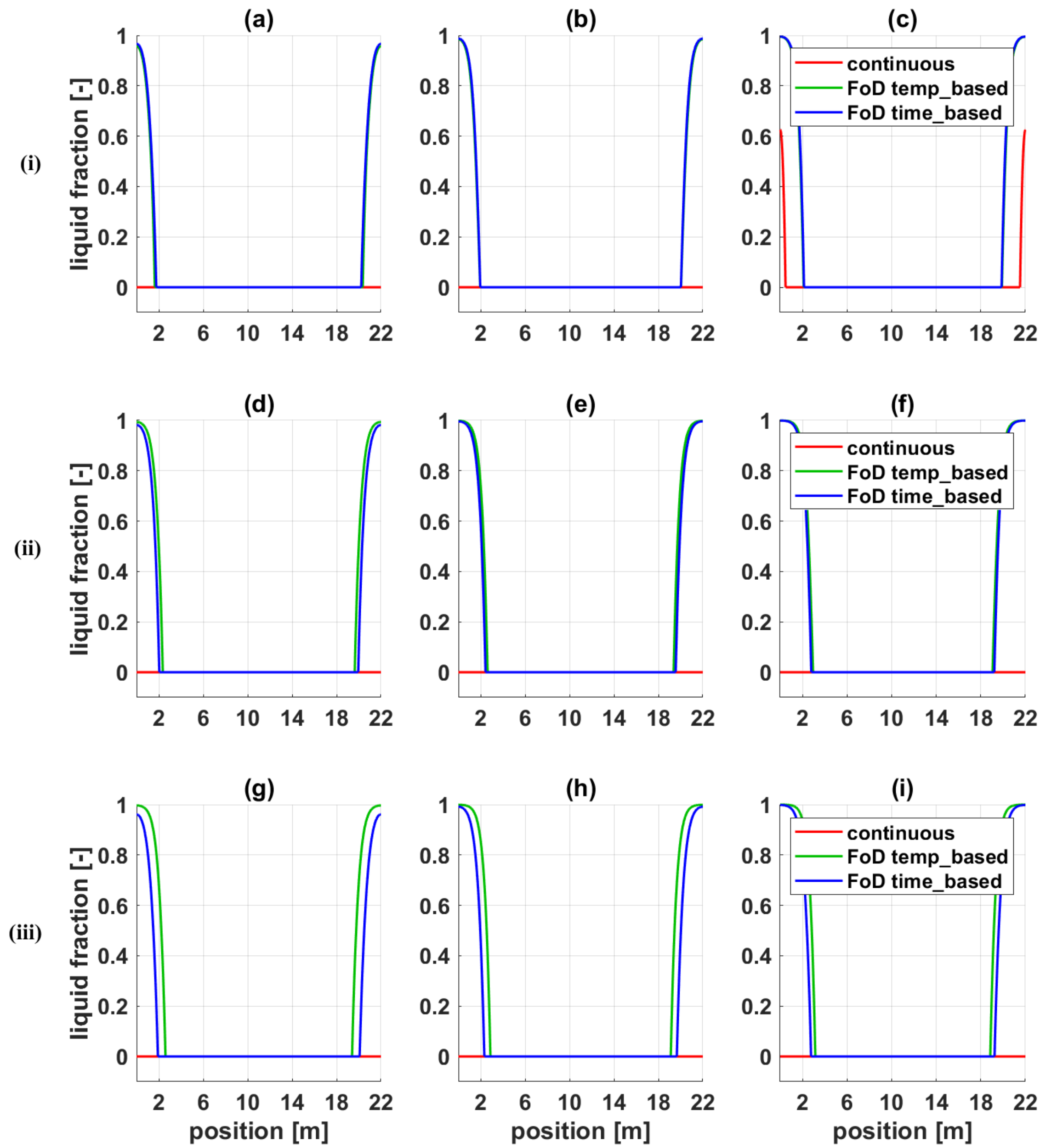

Figure 6.11 – The liquid fraction along the reference line (See Fig. 6.6) of a spacing of 2 [m] at coolants temperature of: (i) -20 [°C]; (ii) -25 [°C]; and (iii) -30 [°C], and with a ground's temperature of: (a), (d), and (g) 5 [°C]; (b), (e), and (h) 10 [°C]; and (c), (f), and (i) 15 [°C].

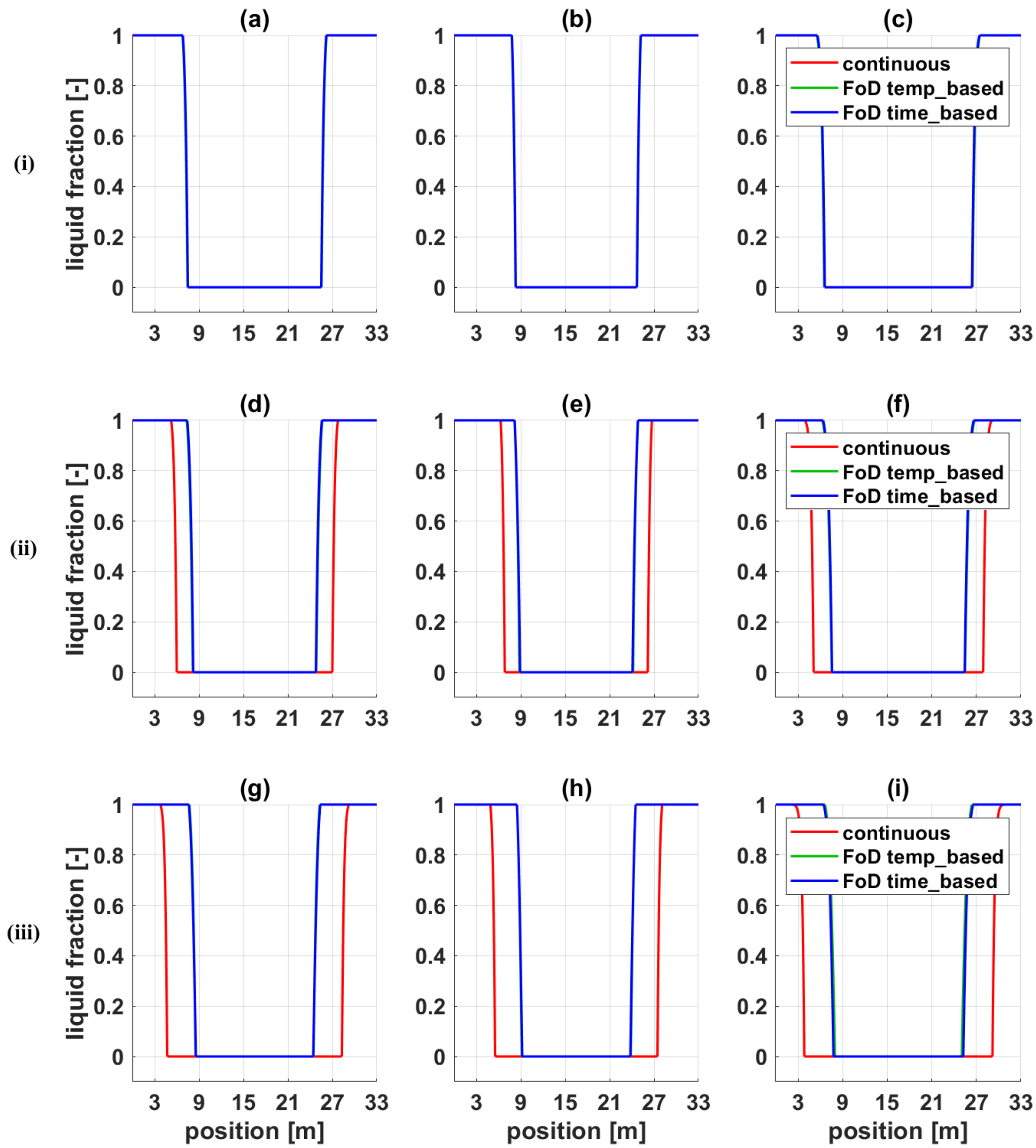

Figure 6.12 – The liquid fraction along the reference line (See Fig. 6.6) of a spacing of 3 [m] at coolants temperature of: (i) -20 [°C]; (ii) -25 [°C]; and (iii) -30 [°C], and with a ground's temperature of: (a), (d), and (g) 5 [°C]; (b), (e), and (h) 10 [°C]; and (c), (f), and (i) 15 [°C].

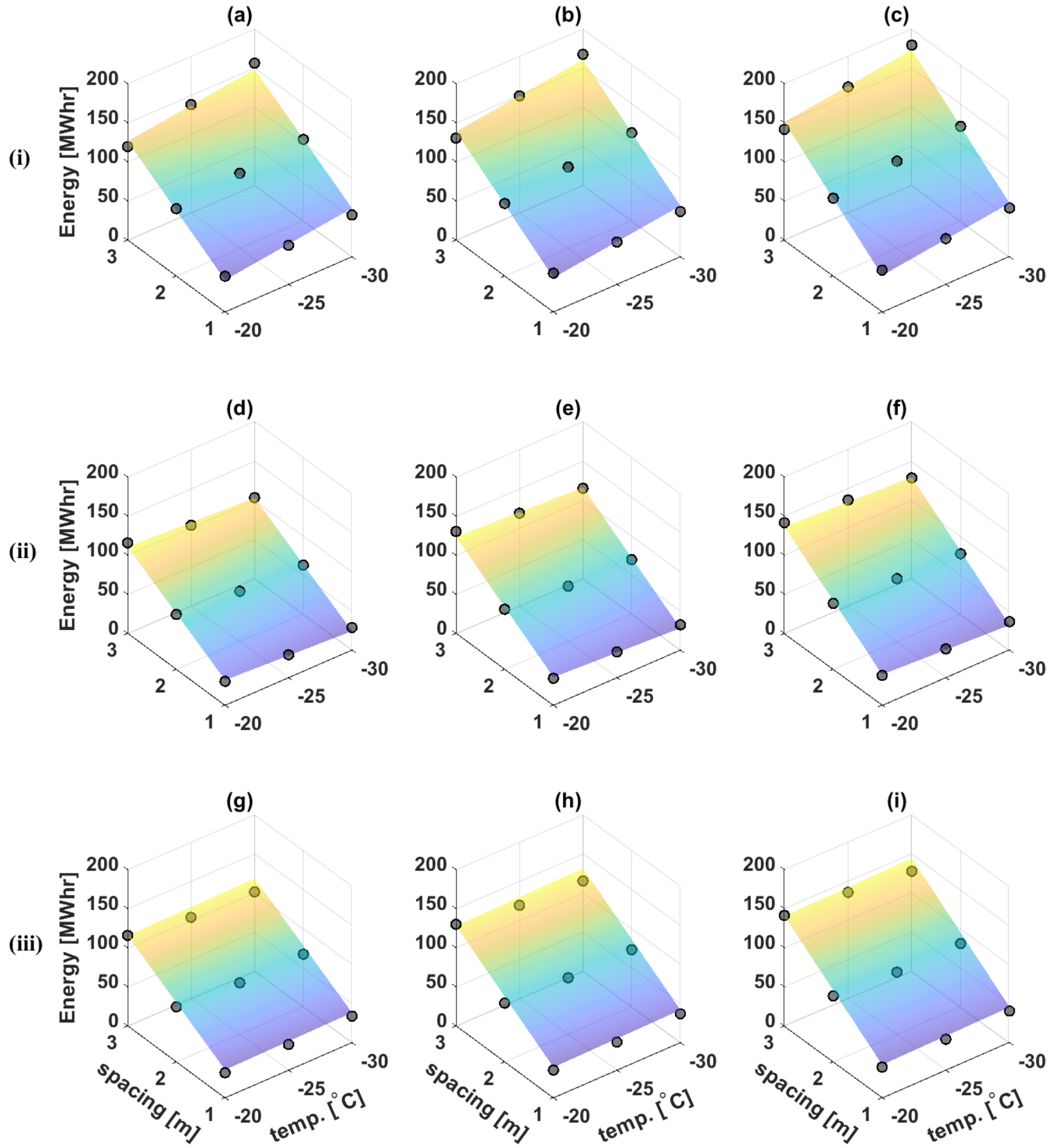

Figure 6.13 – Energy consumption of the 81 experiments at different freezing procedures: (i) continuous freezing; (ii) freezing on demand temperature-based; and (iii) freezing on demand time-based, at ground's temperature of: (a), (d), and (g) 5 [°C]; (b), (e), and (h) 10 [°C]; and (c), (f), and (i) 15 [°C].

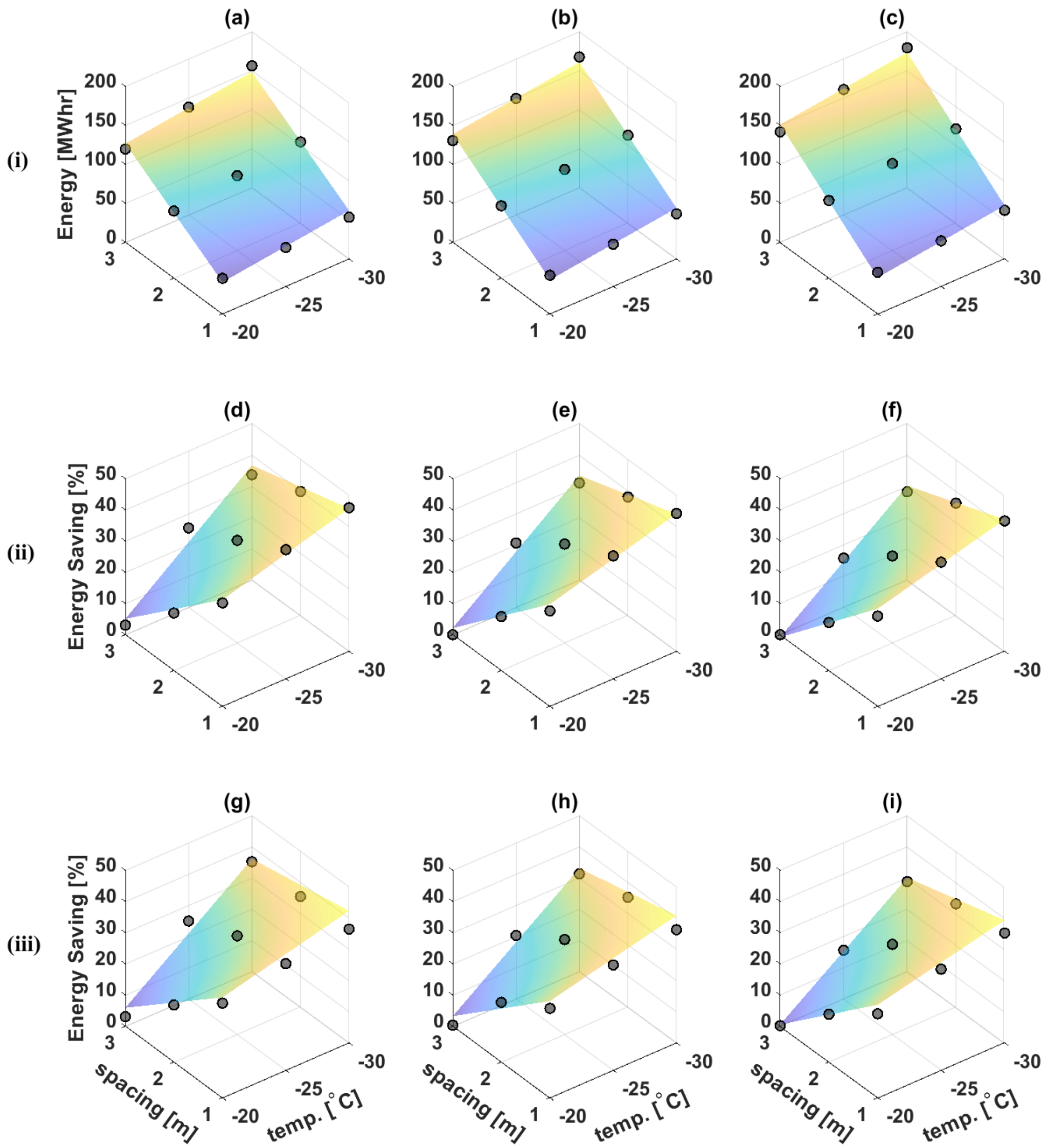

Figure 6.14 – Energy Saving of the 81 experiments at different freezing procedures as compared to the energy consumption of continuous freezing. (i) energy consumption of continuous freezing (ii) energy saving of freezing on demand temperature-based; and (iii) energy saving of freezing on demand time-based, at ground's temperature of: (a), (d), and (g) 5 [°C]; (b), (e), and (h) 10 [°C]; and (c), (f), and (i) 15 [°C].

6.7 Conclusions

An experimental and numerical investigation of a novel concept of the freezing on demand (FoD) has been illustrated in this work. A three-dimensional, conjugate model has been derived and validated against the experimental data. The framework of the mathematical model has been extended to field geometry with a view to studying how various design and operating parameters - freeze pipes' spacing, coolant's temperature, and ground's initial temperature - affect the ground response and the overall energy consumption of the AGF system. Two different approaches have been proposed to conduct the FoD technique: (i) FoD that starts once the core temperature of the frozen body reaches a particular value (named here the lower limits), and (ii)FoD that begins at a specific time despite the core temperature.

The FoD showed a significant drop in the energy consumption by up to 46%. In some cases, however, the design and operating conditions prevented the initiation of the FoD. Also, it has been shown that the ground's temperature, the thickness of the frozen body, and, as a result, the energy consumption did not follow a trivial manner in response to each parameter separately. This disparity leads us to the fact that the effect of a specific parameter on the performance of the AGF process could not be isolated from the others parameters. Therefore, a careful design has to be considered before implementing the concept of FoD is highly recommended. This study is the foundation for more investigations. Smart-freezing-on-demand strategy is among various approaches that should be examined in the future to optimize the energy consumption of the AGF system.

References

[1] E Pimentel, S Papakonstantinou, and G Anagnostou. Numerical interpretation of temperature distributions from three ground freezing applications in urban tunnelling. *Tunnelling and Underground Space Technology*, 28:57–69, 2012.

[2] Gianpiero Russo, Andrea Corbo, Filippo Cavuoto, and Silvia Autuori. Artificial ground freezing to excavate a tunnel in sandy soil. measurements and back analysis. *Tunnelling and Underground Space Technology*, 50:226–238, 2015.

[3] Xiangdong Hu, Tao Fang, Jin Chen, Hui Ren, and Wang Guo. A large-scale physical model test on frozen status in freeze-sealing pipe roof method for tunnel construction. *Tunnelling and Underground Space Technology*, 72:55–63, 2018.

[4] Greg Newman, Lori Newman, Denise Chapman, and Travis Harbicht. Artificial ground freezing: An environmental best practice at cameco's uranium mining operations in northern saskatchewan, canada. In *11th International Mine Water Association Congress–Mine Water–Managing the Challenges*, 2011.

[5] Manon Vitel, Ahmed Rouabhi, Michel Tijani, and Frédéric Guérin. Thermo-hydraulic modeling of artificial ground freezing: Application to an underground mine in fractured sandstone. *Computers and Geotechnics*, 75:80–92, 2016.

[6] Heather E Jamieson. The legacy of arsenic contamination from mining and processing refractory gold ore at giant mine, yellowknife, northwest territories, canada. *Reviews in Mineralogy and Geochemistry*, 79(1):533–551, 2014.

[7] Adrian H Gallardo and Atsunao Marui. The aftermath of the fukushima nuclear accident: Measures to contain groundwater contamination. *Science of The Total Environment*, 547:261–268, 2016.

[8] Indigenous and Northern Affairs Canada - Government of Canada. Planning the remediation of giant mine, 2014. [Online; accessed 31-August-2018].

[9] Cynthia G Jardine, Laura Banfield, S Michelle Driedger, and Christopher M Furgal. Risk communication and trust in decision-maker action: a case study of the giant mine remediation plan. *International Journal of Circumpolar Health*, 72(1):21184, 2013.

[10] Arnab Chatterjee, Lijun Zhang, and Xiaohua Xia. Optimization of mine ventilation fan speeds according to ventilation on demand and time of use tariff. *Applied Energy*, 146:65–73, 2015.

[11] Qi-fa Ge, Wei-gen Zhu, Wei-guo Zhang, Qing-gang Chen, and Zhuo-ming Yang. Ventilation-on-demand system in pulang copper mine. In *Proceedings of the 11th International Mine Ventilation Congress*, pages 116–125. Springer, 2019.

[12] Zhe Wang, Maohui Luo, Yang Geng, Borong Lin, and Yingxin Zhu. A model to compare convective and radiant heating systems for intermittent space heating. *Applied Energy*, 215:211–226, 2018.

[13] Mahmoud A Alzoubi, Agus P Sasmito, Ali Madiseh, and Ferri P Hassani. Intermittent freezing concept for energy saving in artificial ground freezing systems. *Energy Procedia*, 142:3920–3925, 2017.

[14] Mahmoud A Alzoubi, Agus P Sasmito, Ali Madiseh, and Ferri P Hassani. Freezing on demand (FoD): An energy saving technique for artificial ground freezing. *Energy Procedia*, pages –, 2018.

[15] Yan Shang, Ming Dong, and Sufen Li. Intermittent experimental study of a vertical ground source heat pump system. *Applied Energy*, 136:628–635, 2014.

[16] Chanjuan Han and Xiong Bill Yu. Sensitivity analysis of a vertical geothermal heat pump system. *Applied Energy*, 170:148–160, 2016.

[17] Chanjuan Han and Xiong Bill Yu. Performance of a residential ground source heat pump system in sedimentary rock formation. *Applied energy*, 164:89–98, 2016.

[18] Tian You, Wei Wu, Wenxing Shi, Baolong Wang, and Xianting Li. An overview of the problems and solutions of soil thermal imbalance of ground-coupled heat pumps in cold regions. *Applied energy*, 177:515–536, 2016.

[19] Hans L Jessberger and Eugen Makowski. Optimization of the freeze pipe arrangement and the necessary refrigeration plant capacity by a fem-computer program. In *Developments in Geotechnical Engineering*, volume 28, pages 175–188. Elsevier, 1982.

[20] W Stevens James. Intermittent convective heat transfer for ground-source heat pump design. In *ASME International Mechanical Engineering Congress and Exposition (IMECE)*, pages 147–153. Orlando, Florida, USA, 2000.

[21] James W Stevens. Coupled conduction and intermittent convective heat transfer from a buried pipe. *Heat Transfer Engineering*, 23(4):34–43, 2002.

[22] Roman Lackner, Andreas Amon, and Hannes Lagger. Artificial ground freezing of fully saturated soil: thermal problem. *Journal of Engineering Mechanics*, pages 117–122, 2005.

[23] Qing Gao, Ming Li, and Ming Yu. Experiment and simulation of temperature characteristics of intermittently-controlled ground heat exchanges. *Renewable Energy*, 35(6):1169–1174, 2010.

[24] Parham Eslami-nejad and Michel Bernier. Freezing of geothermal borehole surroundings: A numerical and experimental assessment with applications. *Applied Energy*, 98:333–345, 2012.

[25] Yang Zhou and Guoqing Zhou. Intermittent freezing mode to reduce frost heave in freezing soils—experiments and mechanism analysis. *Canadian Geotechnical Journal*, 49(6):686–693, 2012.

[26] Weibo Yang, Lei Kong, and Yongping Chen. Numerical evaluation on the effects of soil freezing on underground temperature variations of soil around ground heat exchangers. *Applied Thermal Engineering*, 75:259–269, 2015.

[27] Mahmoud A Alzoubi, Aurelien Nie-Rouquette, and Agus P Sasmito. Conjugate heat transfer in artificial ground freezing using enthalpy-porosity method: Experiments and model validation. *International Journal of Heat and Mass Transfer*, 126:740–752, 2018.

[28] Mahmoud A Alzoubi and Agus P Sasmito. Thermal performance optimization of a bayonet tube heat exchanger. *Applied Thermal Engineering*, 111:232–247, 2017.

[29] Agus P Sasmito, Erik Birgersson, Hung C Ly, and Arun S Mujumdar. Some approaches to improve ventilation system in underground coal mines environment–a computational fluid dynamic study. *Tunnelling and Underground Space Technology*, 34:82–95, 2013.

[30] Xiaohu Yang, Qingsong Bai, Qunli Zhang, Wenju Hu, Liwen Jin, and Jinyue Yan. Thermal and economic analysis of charging and discharging characteristics of composite phase change materials for cold storage. *Applied Energy*, 225:585–599, 2018.

[31] Xinyi Li, Ting Ma, Jun Liu, Hao Zhang, and Qiuwang Wang. Pore-scale investigation of gravity effects on phase change heat transfer characteristics using lattice boltzmann method. *Applied Energy*, 222:92–103, 2018.

[32] GP Newman and Derek Maishman. Artificial ground freezing of the mcarthur river uranium ore deposit. In *International symposium on ground freezing and frost action in soils. Belgium: Universite catholique de Louvain (UCL)*, pages 317–321, 2000.

[33] Greg P Newman. Case study: thermal analysis of artificial ground freezing at the mcarthur river uranium mine. *Geotechnical News Vancouver*, 21(2):60–62, 2003.

Chapter 7

Concluding remarks

Contents

7.1 Conclusions

This dissertation discussed the thermal and hydraulic aspects associated with the artificial ground freezing process. The framework of this thesis comprised the contribution of building a laboratory-scale experimental rig that mimics the artificial ground freezing (AGF) system under various operating parameters, and the development of a mathematical model that illustrates the multi-phase heat transfer and fluid mechanics associated with the AGF process.

In the beginning, a state-of-the-art review of the up-to-date accomplishments in the context of the AGF system has been provided. It summarized the main types of the AGF systems; it discussed the main components, the advantages and disadvantages, and the main applications of each type. After that, a detailed overview of the previous experimental research, the physical models, and the experimental procedures has been discussed. Finally, the review examined the fundamental aspects of the transport phenomena associated with the AGF process. The study concluded that the number of researches concerning the AGF system is limited, taking into consideration the complexity and the importance of such a system.

In the following chapter, a thermal analysis at a mechanistic-level regarding the design and operating parameter of a standard freeze pipe was discussed, intending to reach optimum performance in terms of pressure drop, heat transfer, entropy generation, and figure of merit. The latter is a quantity that is used to characterize the heat transfer performance of a freeze pipe with respect to its pumping power. The mathematical framework has been validated against experimental data from the literature, and then extended to a field geometry. It has been concluded that the design and operating parameters have a combined effect on the performance of the freeze pipe.

With regard to the experimental work, a lab-scale experiment has been developed with the intention to examine the AGF process under various operating conditions. The experimental research went through several stages in order to deliver robust, trustworthy results. The design of the physical model was subjected to detailed analysis, discussions, and simulations to come up with an experimental rig that is capable of employing several novel concepts at a laboratory scale and within a specific time frame without compromising the reliability of the outcomes. Moreover, the thermophysical properties of the saturated sand and the coolant have been measured, analyzed, and employed in the mathematical model. Finally, the implementation of the enthalpy-porosity method in the mathematical model provided accurate results once compared to the experimental data with an average $R^2 = 0.97$.

The mathematical models from the above mentioned two studies have been utilized to examine the impact of several operating parameters on the performance of an AGF system subjected to various groundwater seepage velocities. The concept of heatlines has been employed in this study to provide a deeper understanding of the impact of the groundwater seepage along with other parameters on the development of the frozen body between two freeze pipes. In the literature, it is mentioned, as a role of thumb, that the benchmark at which the groundwater seepage hinder the formation of the frozen body is at a velocity of 2 [m/day]. In this study, we showed that this value is valid only at a specific design and operating parameters. Based on our evaluations, a closed, frozen wall was created even at a groundwater seepage with a velocity of 3 [m/day]. This conclusion led us to the fact that the AGF process if very delicate because of the strong non-linearity of the AGF problem.

Another experimental and numerical investigation has been conducted to investigate a novel concept of the freezing on demand (FoD). The fundamental notion behind this concept is to provide freezing only when it is needed. This operational technique has been proposed to reduce the intensive energy consumption of the AGF system. The experimental rig was used to demonstrate the proof-of-concept of the FoD approach and to validate the mathematical model, while the validated model was employed to examine the impact of various parameters on the performance of the FoD technique. Two schemes have been proposed to conduct the FoD technique: (i) FoD that starts at a specific temperature, and (ii)FoD that begins after a particular time despite the core temperature. In both scenarios, the FoD showed a significant drop in the energy consumption by up to 46%. For example, one of the uranium mine in northern Canada is expanding and building a new freezing plant that comprises five compressors. Implementing the concept of FoD could potentially save the purchase of two compressors, which in turns could save few millions of dollars of capital cost and approximately million dollars of operating cost per year.

7.2 Contribution to original knowledge

Although studying the artificial ground freezing is not a new subject, this thesis has contributed to the advancements in this area of research. One of the key contributions is the development of the state-of-the-art experimental setup. To the best of our knowledge, this is the only lab-scale apparatus that is equipped with advanced measurement instrumentation and control systems. The experimental setup has been capable of producing accurate measurement (we conducted several reproducibility tests to confirm this point). Moreover, the rig has been utilized to employ novel operational concepts such as the freezing on demand (FoD) technique. This procedure aims to diminish the intensive energy consumption of the AGF system while maintaining the safe thickness of the frozen body.

On the other hand, the study of the AGF process under groundwater seepage condition utilized the concept of the heatlines to provide an accurate picture of net energy flow during AGF process under seepage condition. This concept, which is implemented for the first time in an AGF study, gave a deeper understanding of the impact of the groundwater seepage on the creation of the frozen body. Finally, the complicated, multi-physics artificial ground freezing process has been handled by developing a reliable multi-phase, conjugate heat transfer mathematical model that, in contrary to the majority of other AGF studies, utilized the enthalpy-porosity formulation, which, based on several reviews, provides more accurate results as compared to the classical apparent heat capacity approach.

7.3 Recommendations for future work

Due to the complexity of the artificial ground freezing process, the discussion of this work is limited by several assumptions and considerations. First of all, the ground structure has been assumed to be fully saturated with water. This assumption neglects the presence of air. Furthermore, the experimental setup has been designed and developed with fully-saturated sand in line with this assumption. Although this assumption is valid in several projects, such as underground tunnels, it is not necessarily applicable to other projects. Therefore, further analysis of the AGF process in an unsaturated ground structure is required in the future work.

The AGF process comprises three, nondetachable aspects: thermal, hydraulic, and mechanical. The latter, however, has been excluded from this study. The interaction between these concepts, in theory, could be broken down into two-way coupling: the impact of the thermo-hydraulic aspects on the mechanics of the ground and, in turn, the influence of the ground's mechanical properties on the thermo-hydraulic behavior of the AGF process. The first coupling is expressed solely by the impact of the ground's porosity and permeability on the thermal and hydraulic state. A complete experimental and numerical examination of the effect of these two terms is then inevitable for future considerations.

Finally, this study addressed the AGF system that is used for long-term projects such as underground uranium mines, or hazardous-waste management projects. The configuration of the freeze pipes in these applications is a wall-type configuration, where the frozen body is considered as a frozen wall. In other applications, however, circular or semi-circular shapes take place. The impact of these configurations on the implementation of new AGF approaches has yet to be studied. Therefore, it is recommended to consider these arrangements in any future analysis.

Appendix A

Supplementary Data

Contents

A.1 Supplementary data from Chapter 3

The thermophysical properties of air, that depicted in Fig. A.1, are calculated using the air equation of state (3.8) that consists of two terms: (i) ideal-gas contribution to the Helmholtz energy; and (ii) the residual contribution to the Helmholtz energy. Ideally, the equation of state consists of four terms [1]; the other two terms: base function, and critical region correction function is ignored in this study. The latter is used, however, to calculate the fluid thermal conductivity in the critical region [2]. The equations used for calculating density, viscosity, thermal conductivity, and isobaric heat capacity from the equation of state are defined as follows:

Density:

The density is calculated using the compressibility factor (Z), given by

$$Z = \frac{P}{\rho RT} = 1 + \delta \left(\frac{\partial \alpha^r}{\partial \delta} \right)_\theta \tag{A.1}$$

Viscosity:

$$\mu = \mu^0 (T) + \mu^r (\theta, \delta) \tag{A.2}$$

Thermal Conductivity:

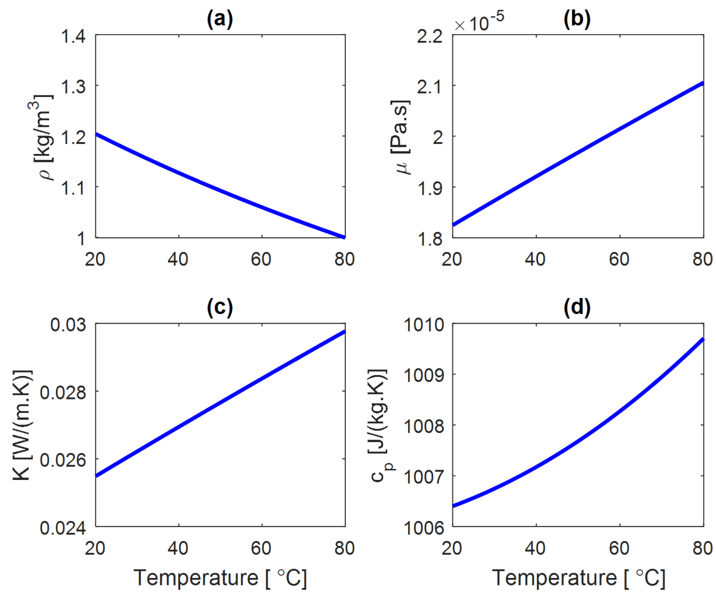

Figure A.1 – Thermophysical properties of air at atmospheric pressure: (a) density; (b) viscosity; (c) thermal conductivity; and (d) heat capacity

$$k = k^0 + k^r(\theta, \delta) + k^c(\theta, \delta) \tag{A.3}$$

Heat Capacity:

$$c_p = c_v + R\left(\frac{\left[1 + \delta\left(\frac{\partial\alpha^r}{\partial\delta}\right)_\theta - \delta\theta\left(\frac{\partial^2\alpha^r}{\partial\delta\partial\theta}\right)\right]^2}{\left[1 + 2\delta\left(\frac{\partial\alpha^r}{\partial\delta}\right)_\theta + \delta^2\left(\frac{\partial^2\alpha^r}{\partial\delta^2}\right)_\theta\right]}\right) \tag{A.4}$$

The derivations of Equations (A.1) to (A.4) are discussed in details in [3] and [2].

A.2 Supplementary data from Chapter 4

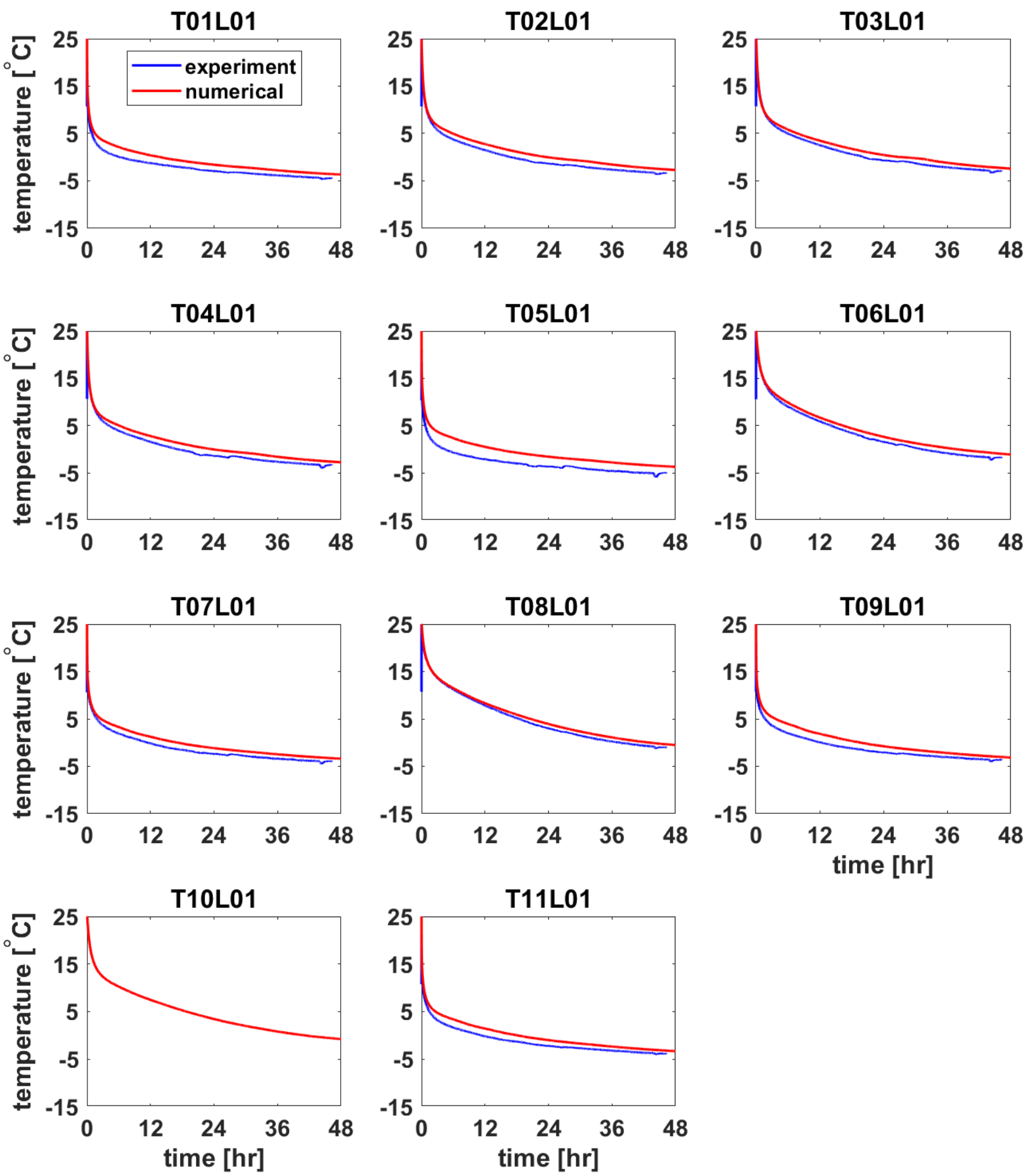

Figure A.2 – The validation of the mathematical model with experimental data at ($T_c = -10\ [°C],\ T_g = 25\ [°C],\ and\ \dot{Q} = 5\ [ml/s]$). The results show the the ground's temperature at level-01 with ($R^2 = 0.937$).

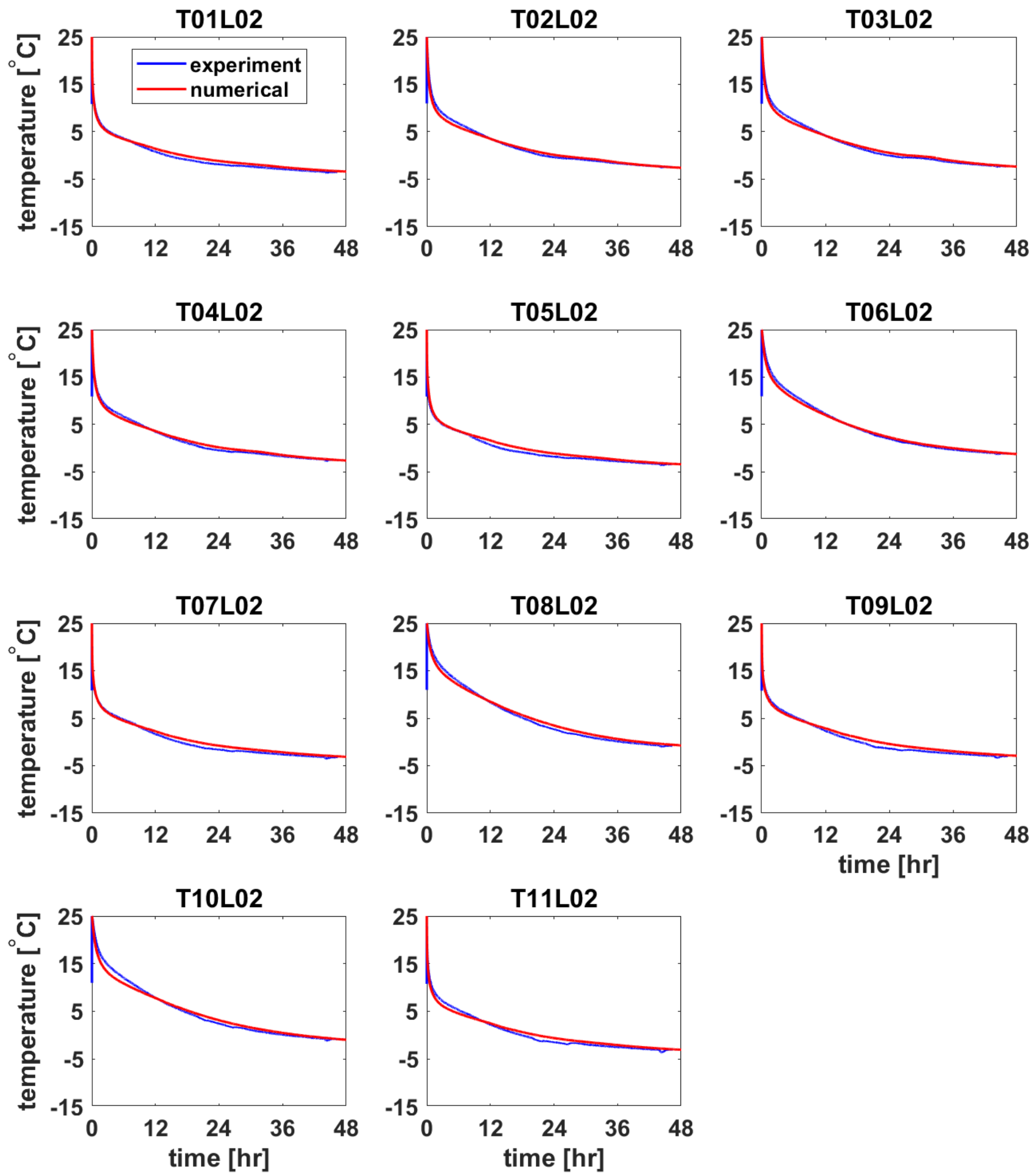

Figure A.3 – The validation of the mathematical model with experimental data at ($T_c = -10$ [$°C$], $T_g = 25$ [$°C$], $and\ \dot{Q} = 5$ [ml/s]). The results show the the ground's temperature at level-02 with ($R^2 = 0.994$).

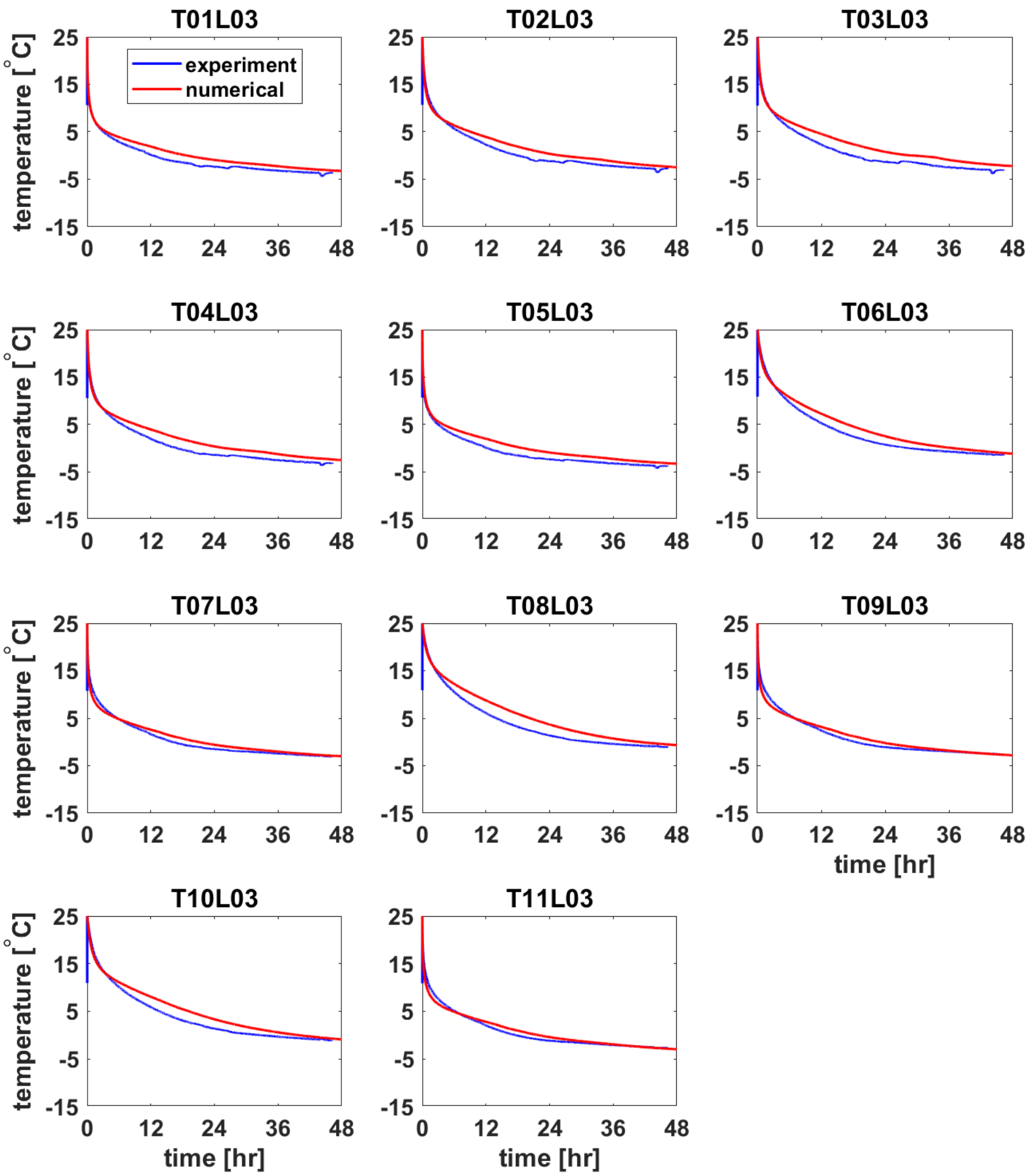

Figure A.4 – The validation of the mathematical model with experimental data at ($T_c = -10\ [°C],\ T_g = 25\ [°C],\ and\ \dot{Q} = 5\ [ml/s]$). The results show the the ground's temperature at level-03 with ($R^2 = 0.979$).

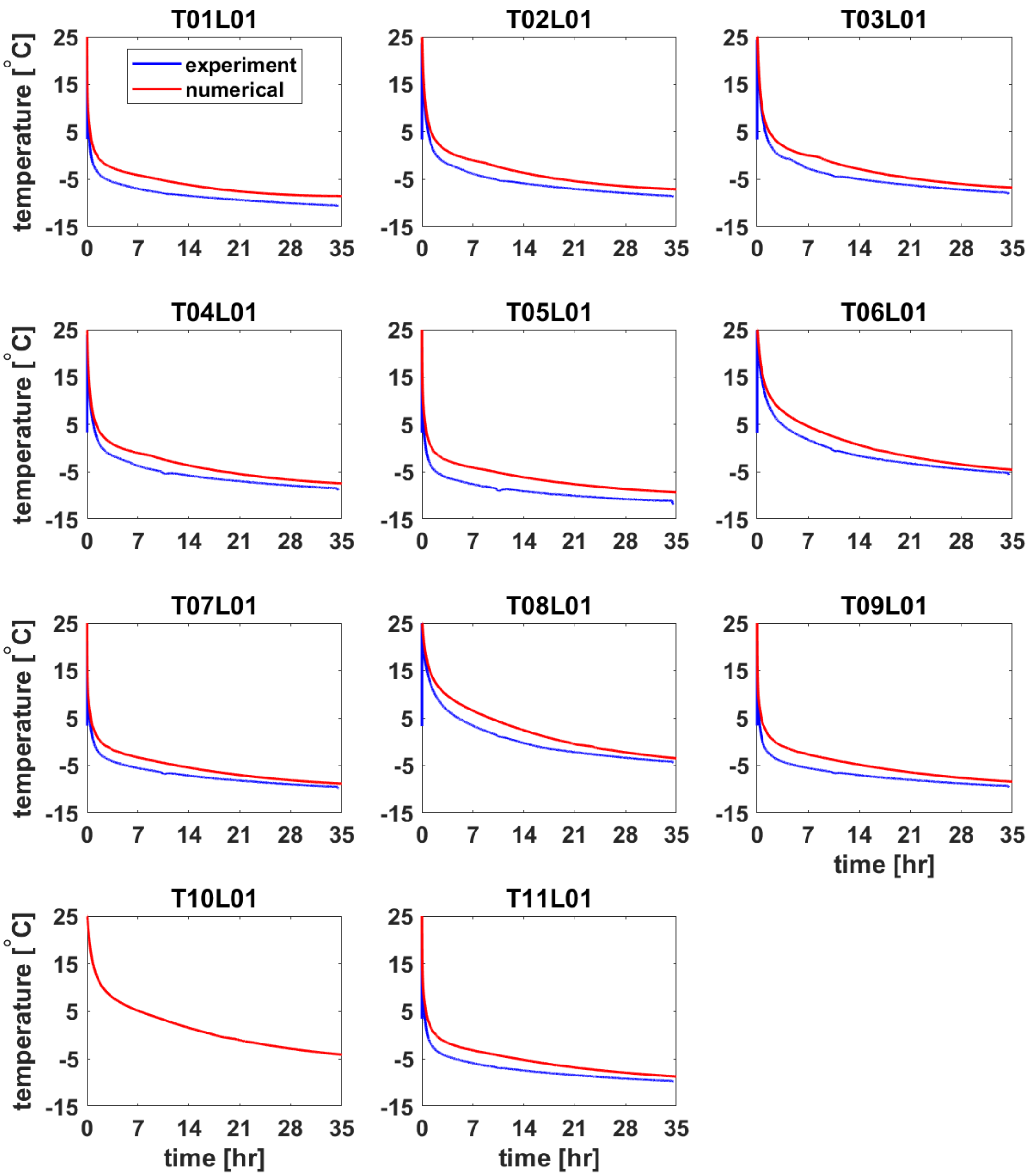

Figure A.5 – The validation of the mathematical model with experimental data at ($T_c = -20$ [$°C$], $T_g = 25$ [$°C$], $and\ \dot{Q} = 5$ [ml/s]). The results show the the ground's temperature at level-01 with ($R^2 = 0.923$).

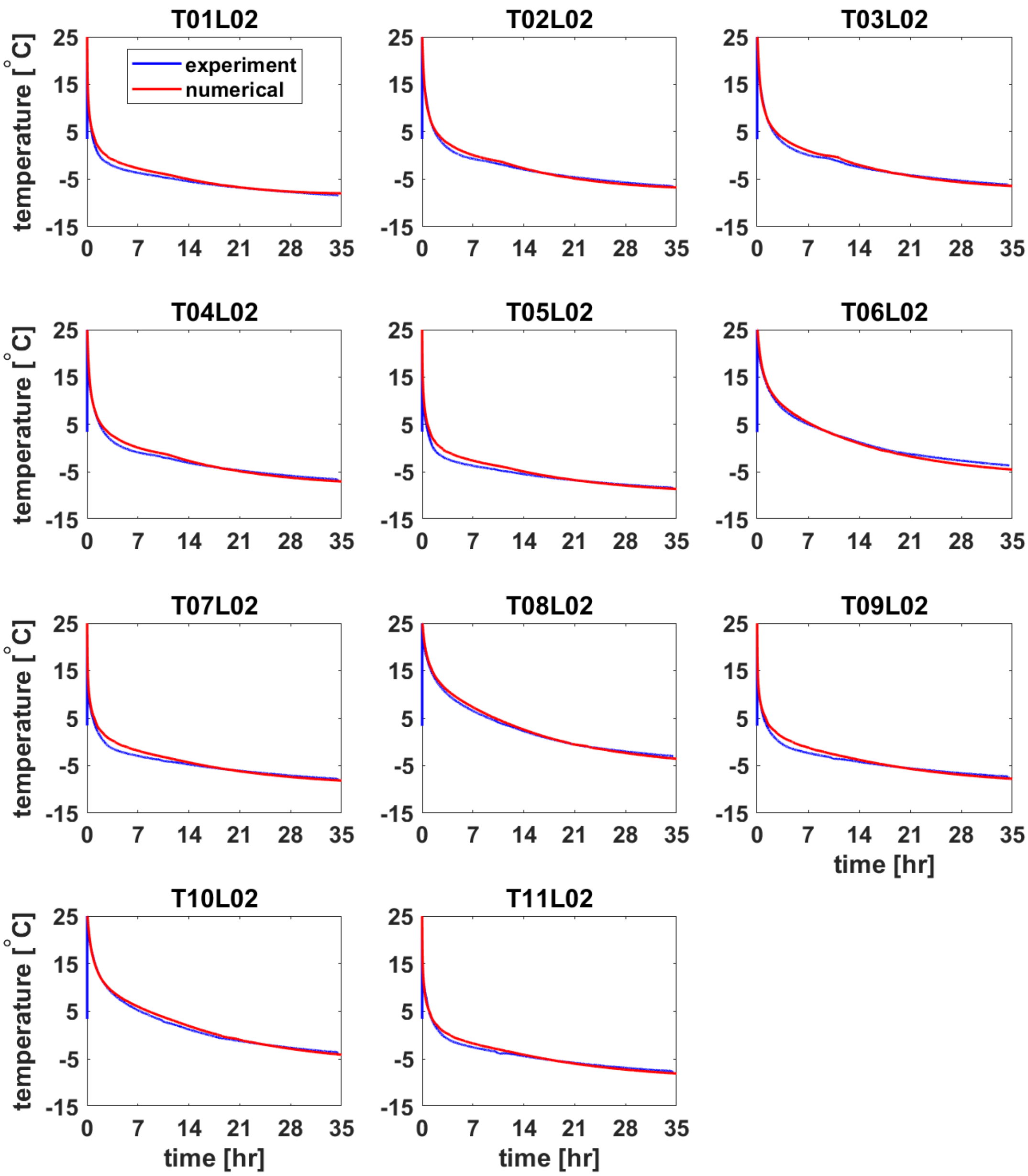

Figure A.6 – The validation of the mathematical model with experimental data at ($T_c = -20\ [°C],\ T_g = 25\ [°C],\ and\ \dot{Q} = 5\ [ml/s]$). The results show the the ground's temperature at level-02 with ($R^2 = 0.992$).

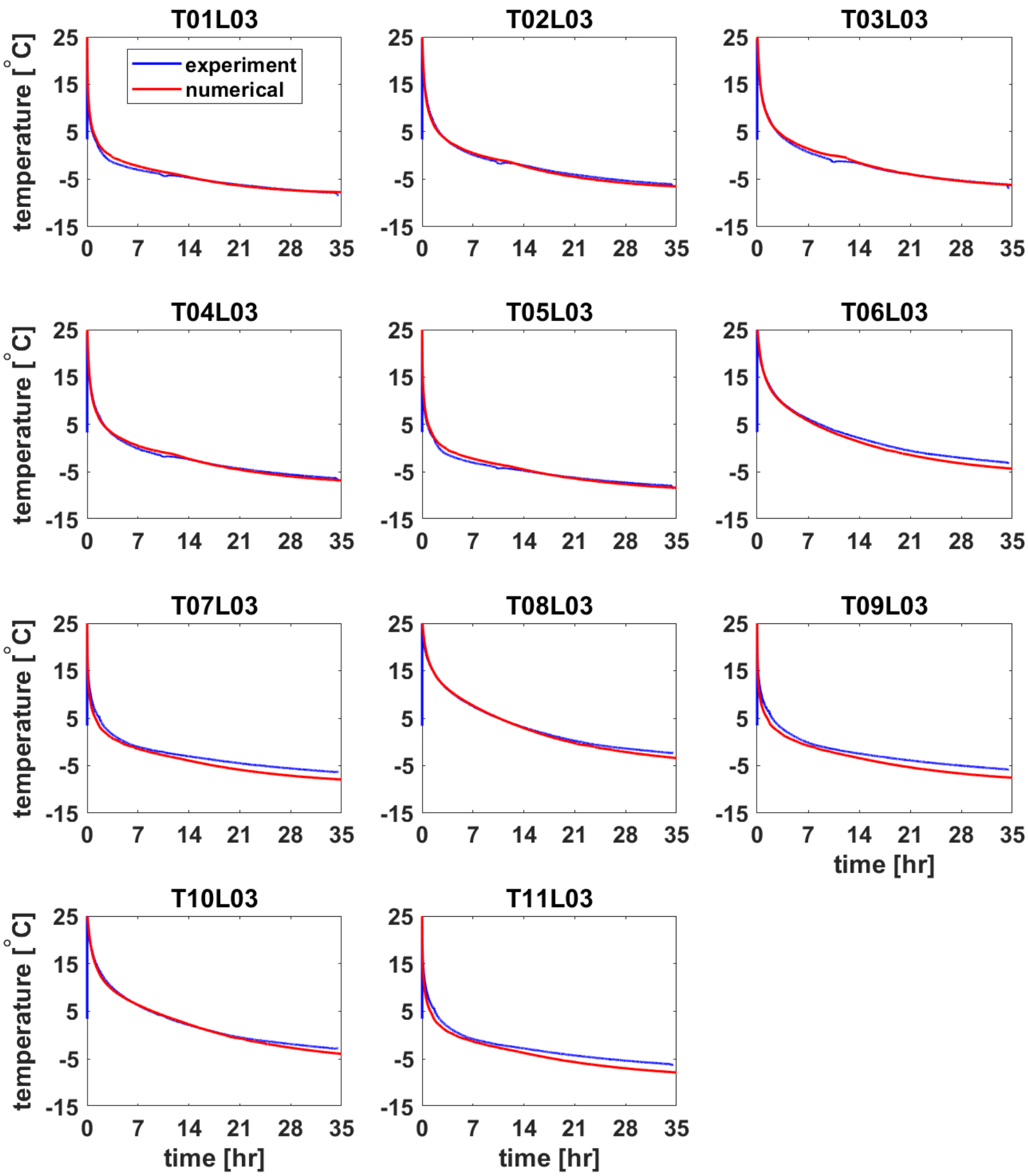

Figure A.7 – The validation of the mathematical model with experimental data at ($T_c = -20\ [°C],\ T_g = 25\ [°C],\ and\ \dot{Q} = 5\ [ml/s]$). The results show the the ground's temperature at level-03 with ($R^2 = 0.993$).

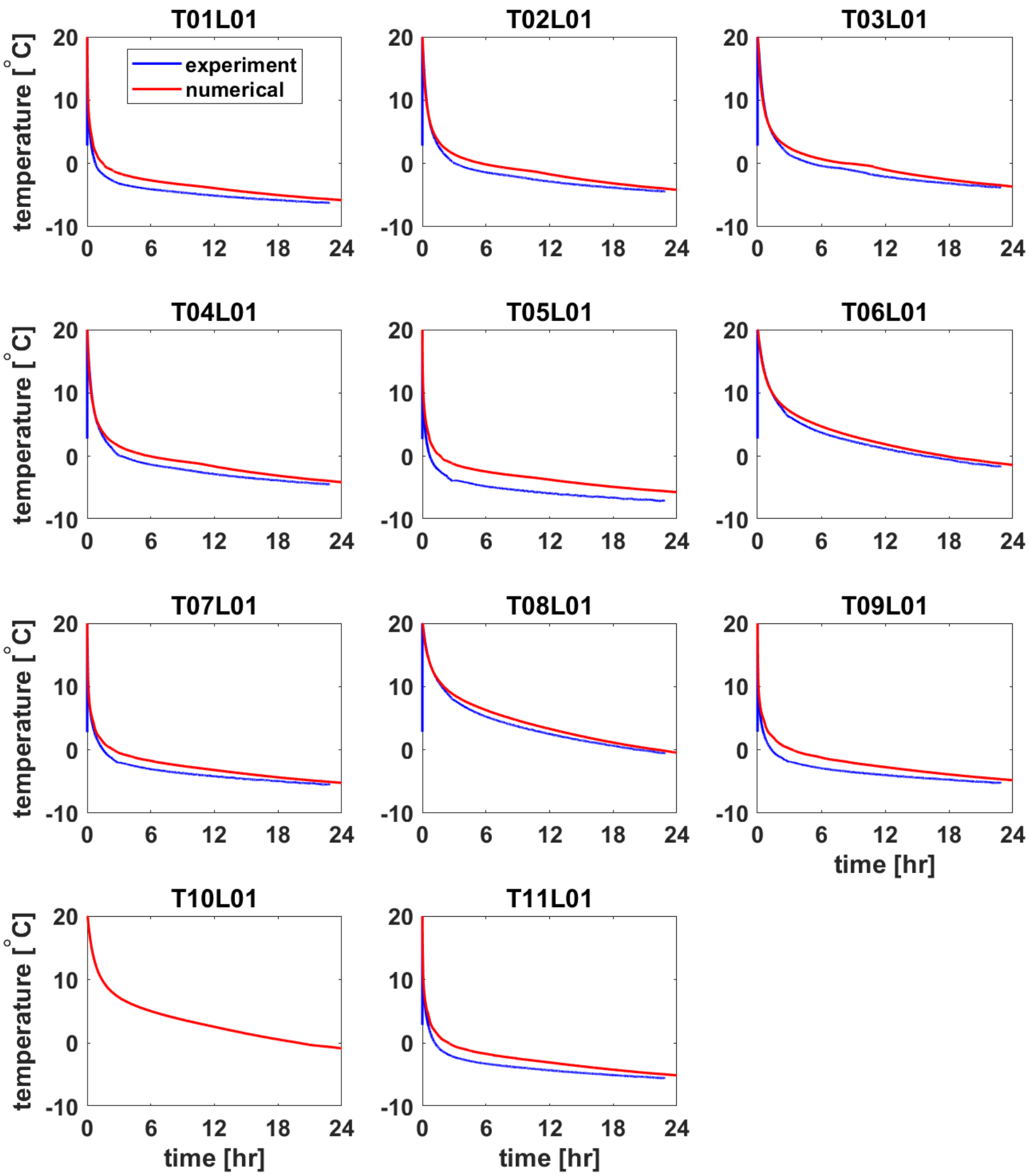

Figure A.8 – The validation of the mathematical model with experimental data at ($T_c = -15$ [$°C$], $T_g = 20$ [$°C$], $and\ \dot{Q} = 5$ [ml/s]). The results show the the ground's temperature at level-01 with ($R^2 = 0.931$).

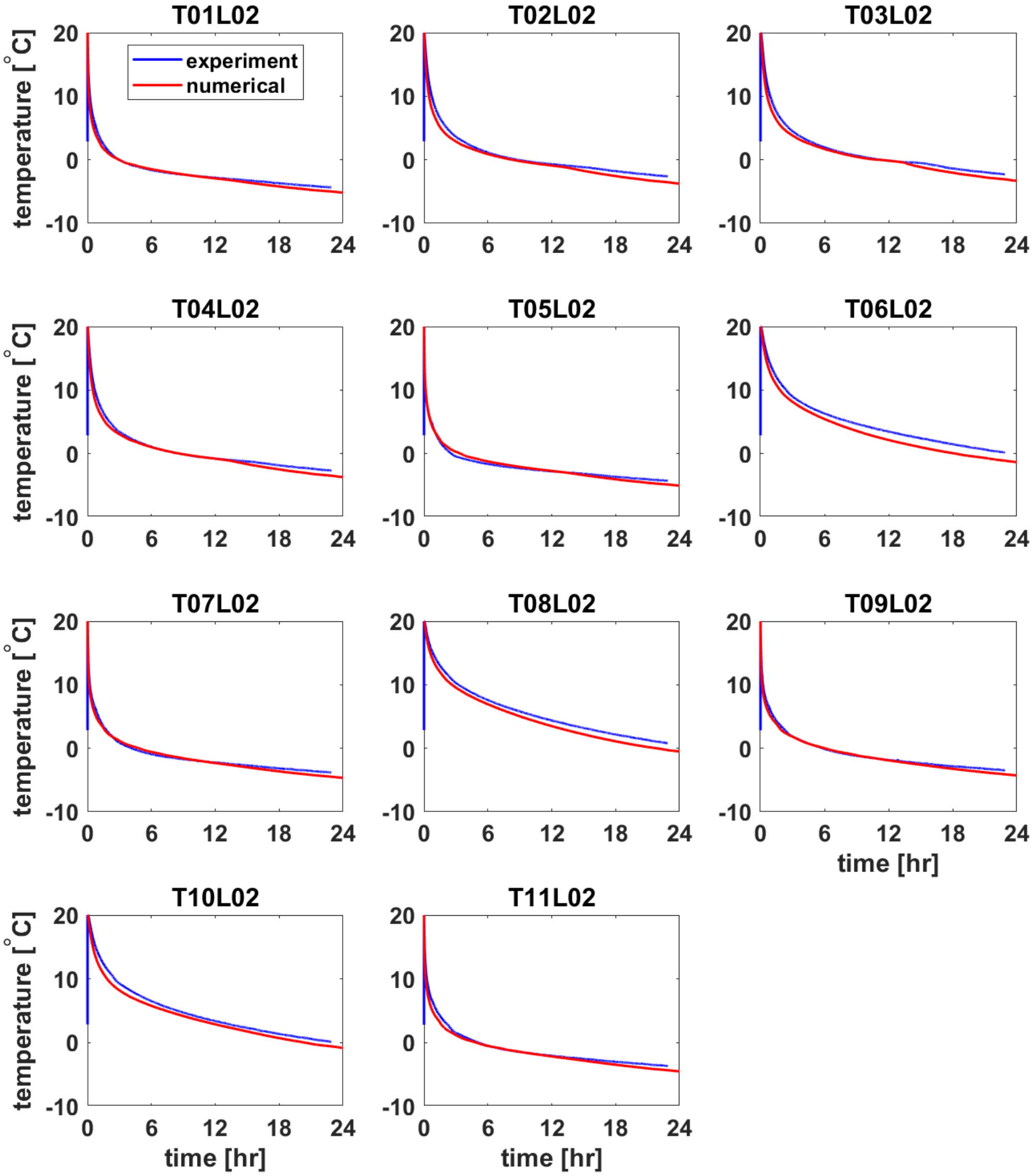

Figure A.9 – The validation of the mathematical model with experimental data at ($T_c = -15\ [°C],\ T_g = 20\ [°C],\ and\ \dot{Q} = 5\ [ml/s]$). The results show the the ground's temperature at level-02 with ($R^2 = 0.989$).

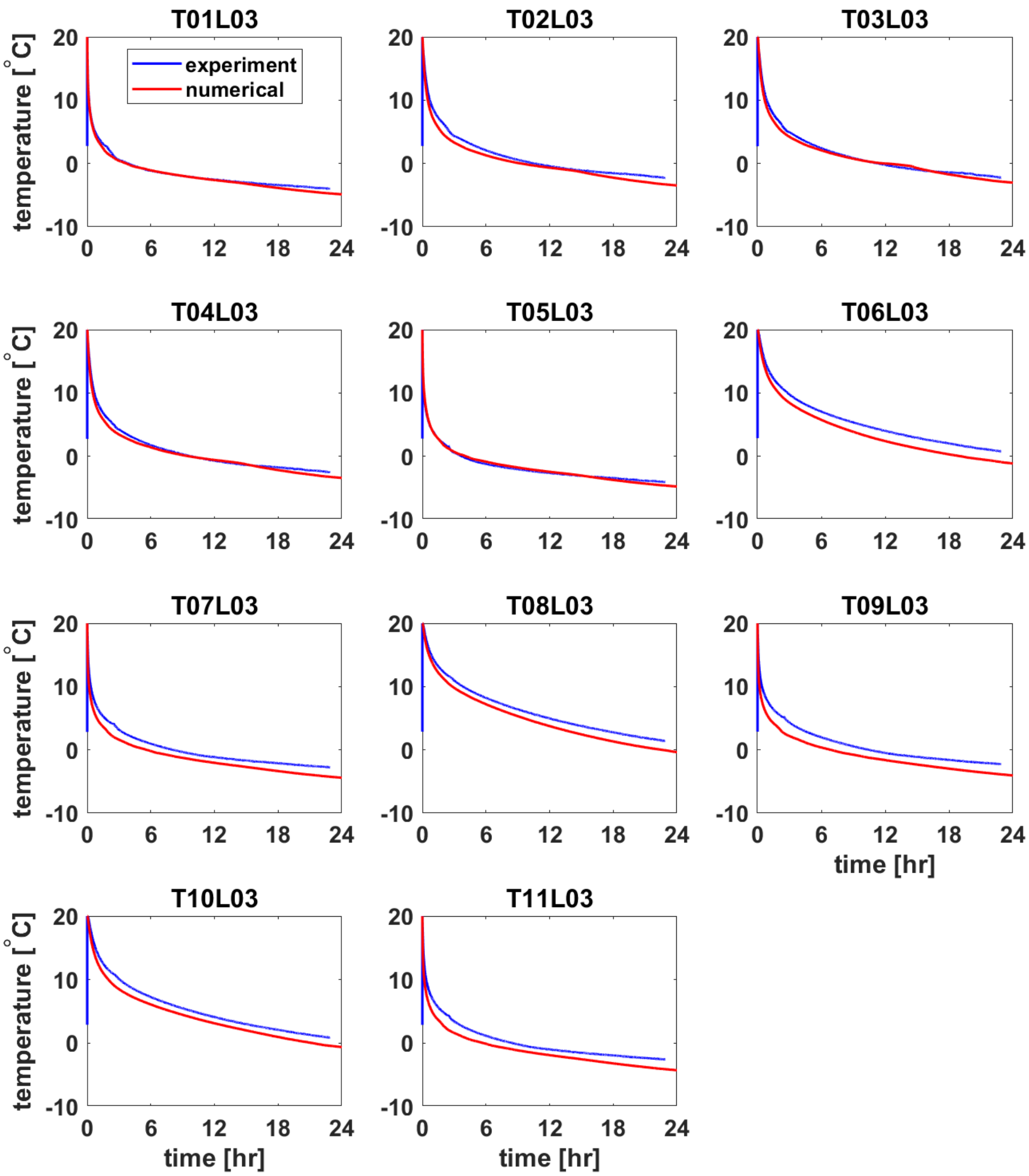

Figure A.10 – The validation of the mathematical model with experimental data at ($T_c = -15$ [$°C$], $T_g = 20$ [$°C$], $and\ \dot{Q} = 5$ [ml/s]). The results show the the ground's temperature at level-03 with ($R^2 = 0.993$).

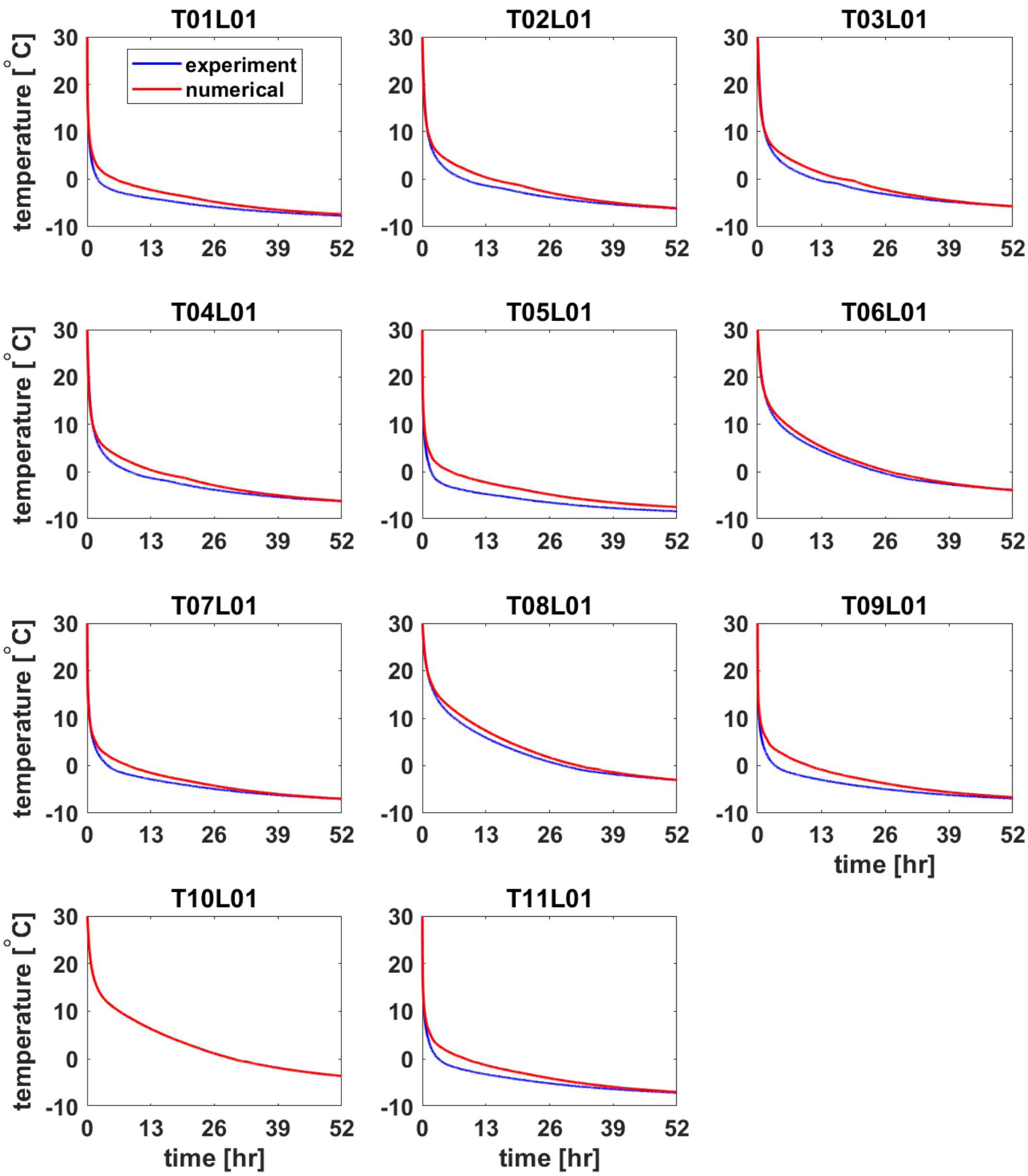

Figure A.11 – The validation of the mathematical model with experimental data at ($T_c = -15$ [$°C$], $T_g = 30$ [$°C$], $and\ \dot{Q} = 5$ [ml/s]). The results show the the ground's temperature at level-01 with ($R^2 = 0.973$).

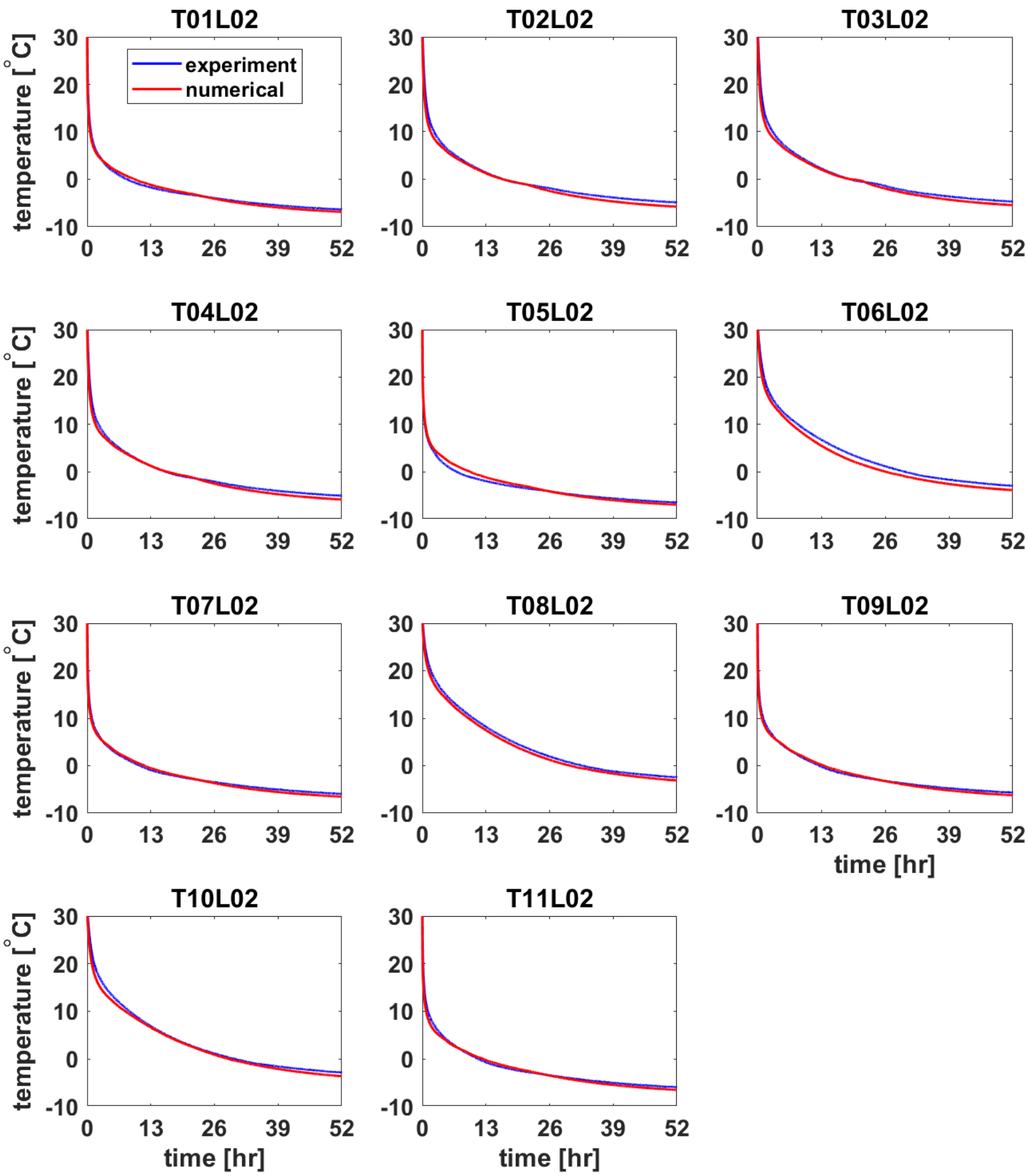

Figure A.12 – The validation of the mathematical model with experimental data at ($T_c = -15\ [°C],\ T_g = 30\ [°C],\ and\ \dot{Q} = 5\ [ml/s]$). The results show the the ground's temperature at level-02 with ($R^2 = 0.992$).

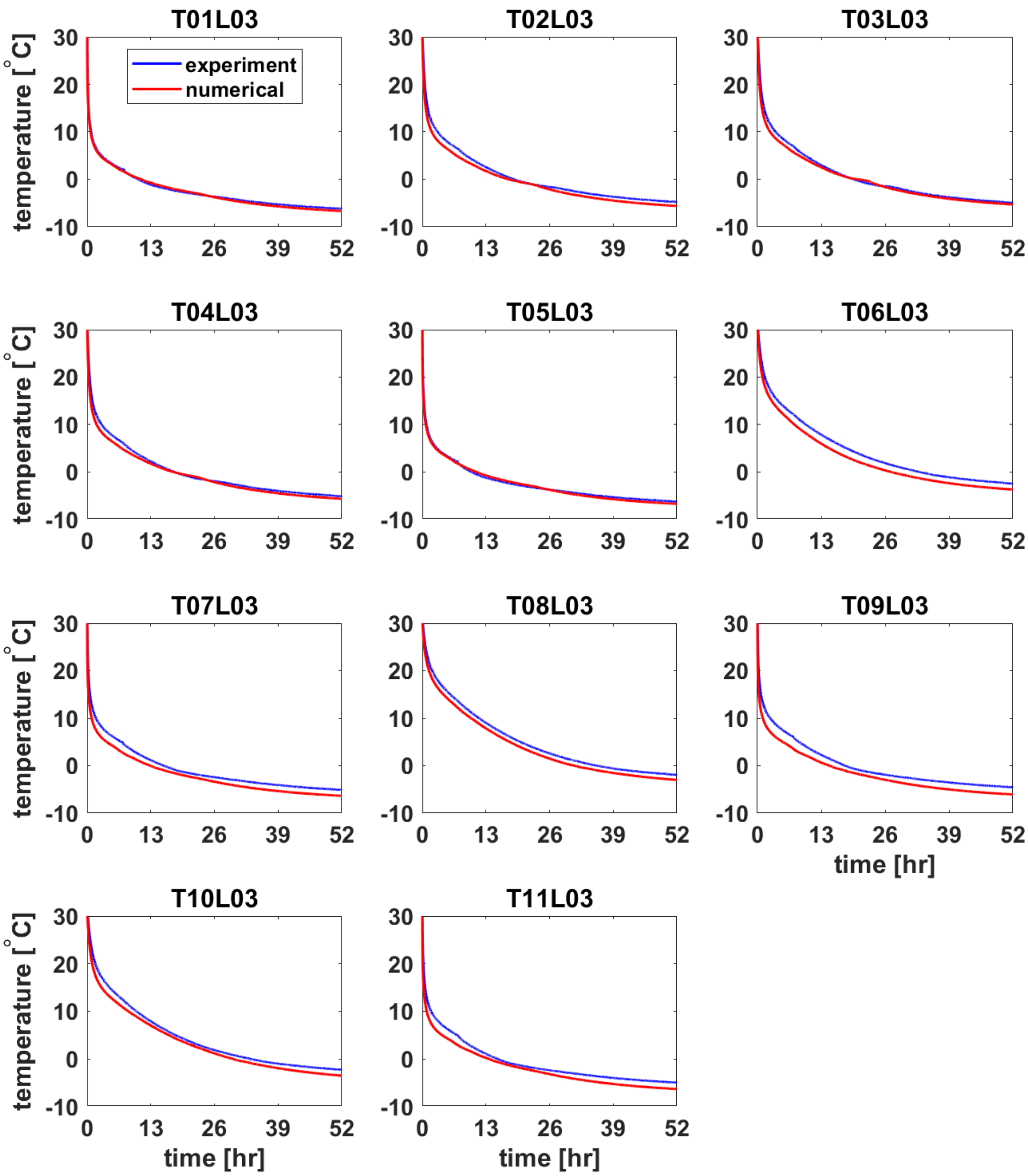

Figure A.13 – The validation of the mathematical model with experimental data at ($T_c = -15$ [$°C$], $T_g = 30$ [$°C$], $and\ \dot{Q} = 5$ [ml/s]). The results show the the ground's temperature at level-03 with ($R^2 = 0.995$).

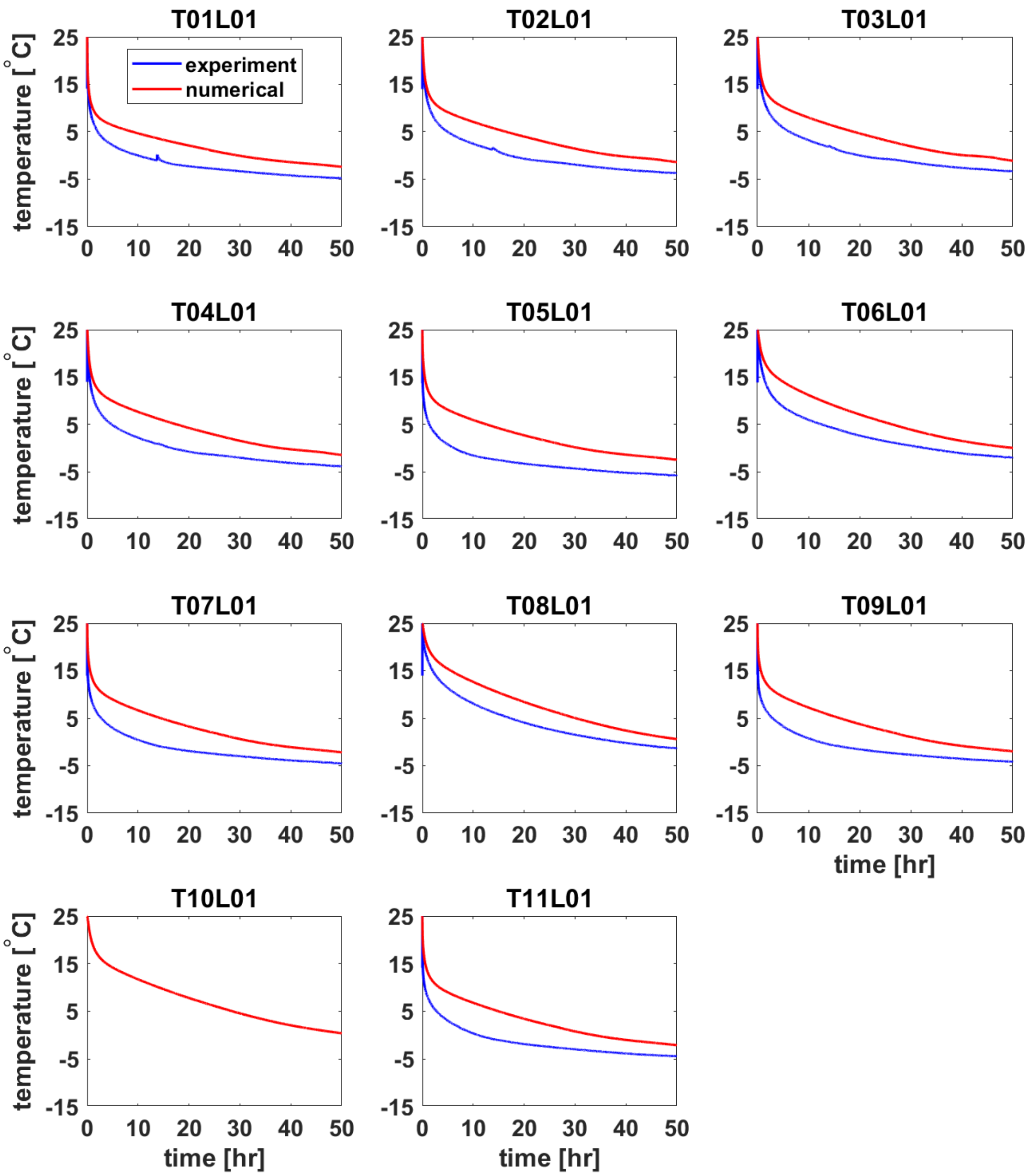

Figure A.14 – The validation of the mathematical model with experimental data at ($T_c = -15\ [°C],\ T_g = 25\ [°C],\ and\ \dot{Q} = 2.5\ [ml/s]$). The results show the the ground's temperature at level-01 with ($R^2 = 0.936$).

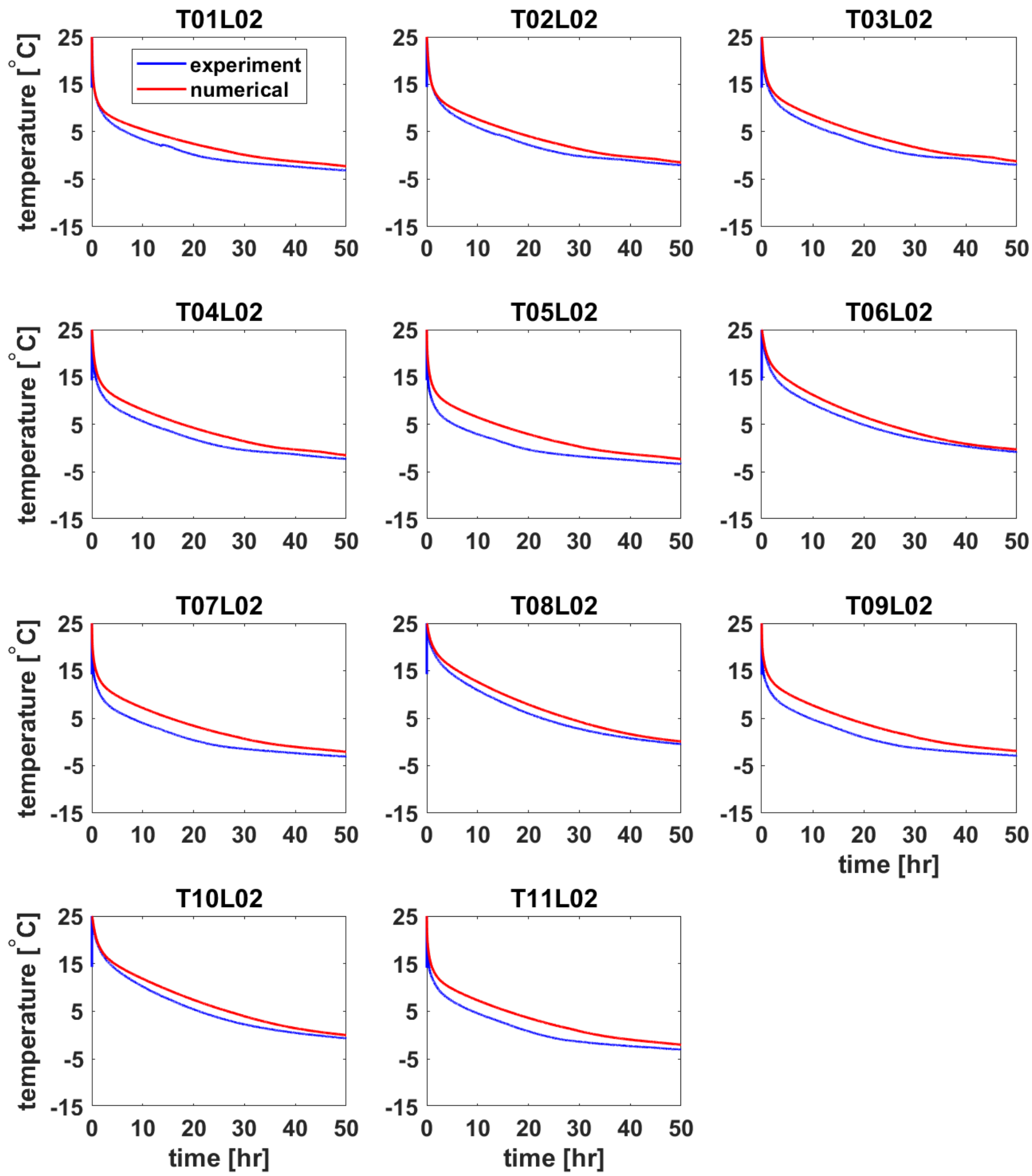

Figure A.15 – The validation of the mathematical model with experimental data at ($T_c = -15\,[°C],\ T_g = 25\,[°C],\ and\, \dot{Q} = 2.5\,[ml/s]$). The results show the the ground's temperature at level-02 with ($R^2 = 0.988$).

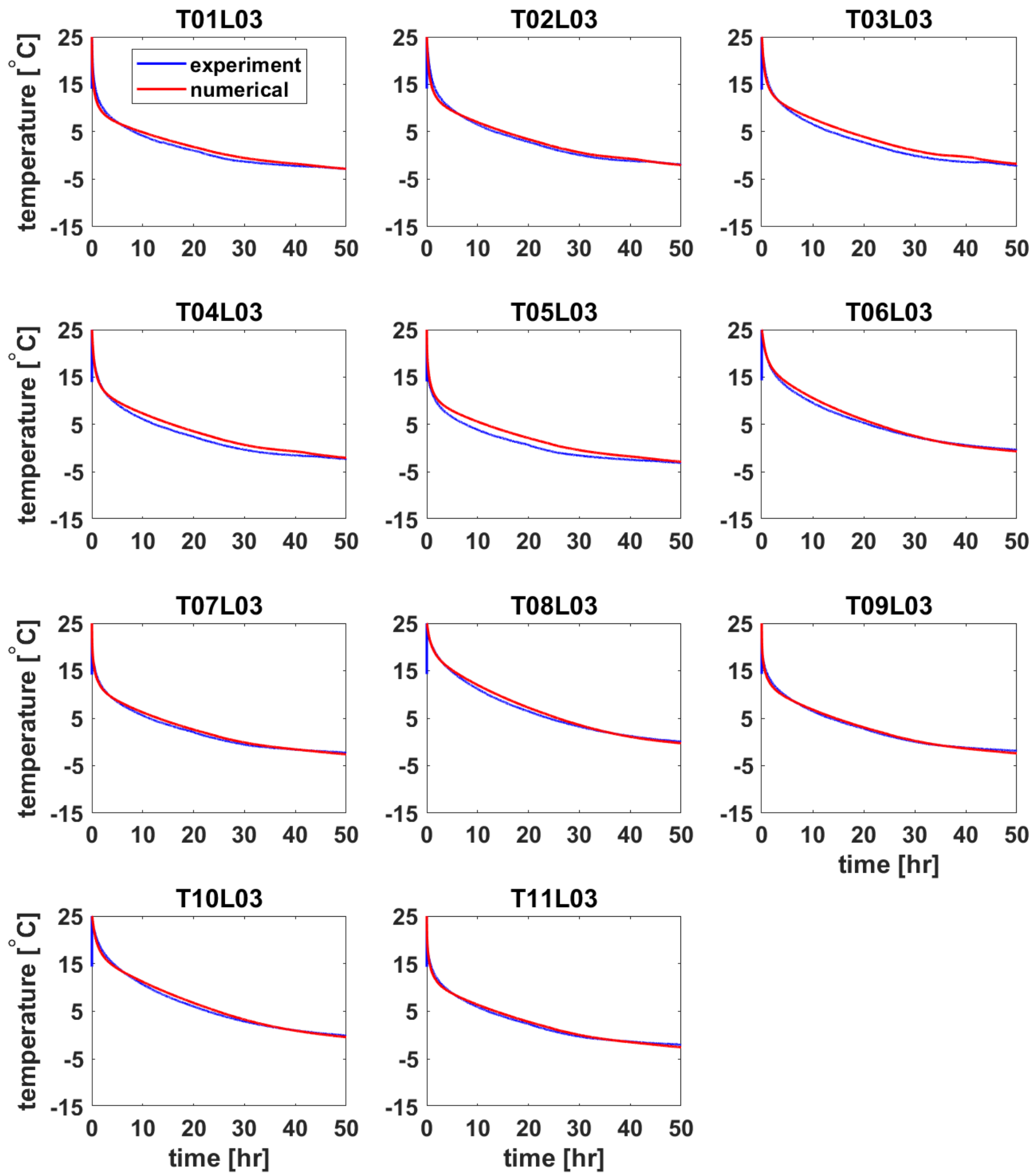

Figure A.16 – The validation of the mathematical model with experimental data at ($T_c = -15\ [°C],\ T_g = 25\ [°C],\ and\ \dot{Q} = 2.5\ [ml/s]$). The results show the the ground's temperature at level-03 with ($R^2 = 0.993$).

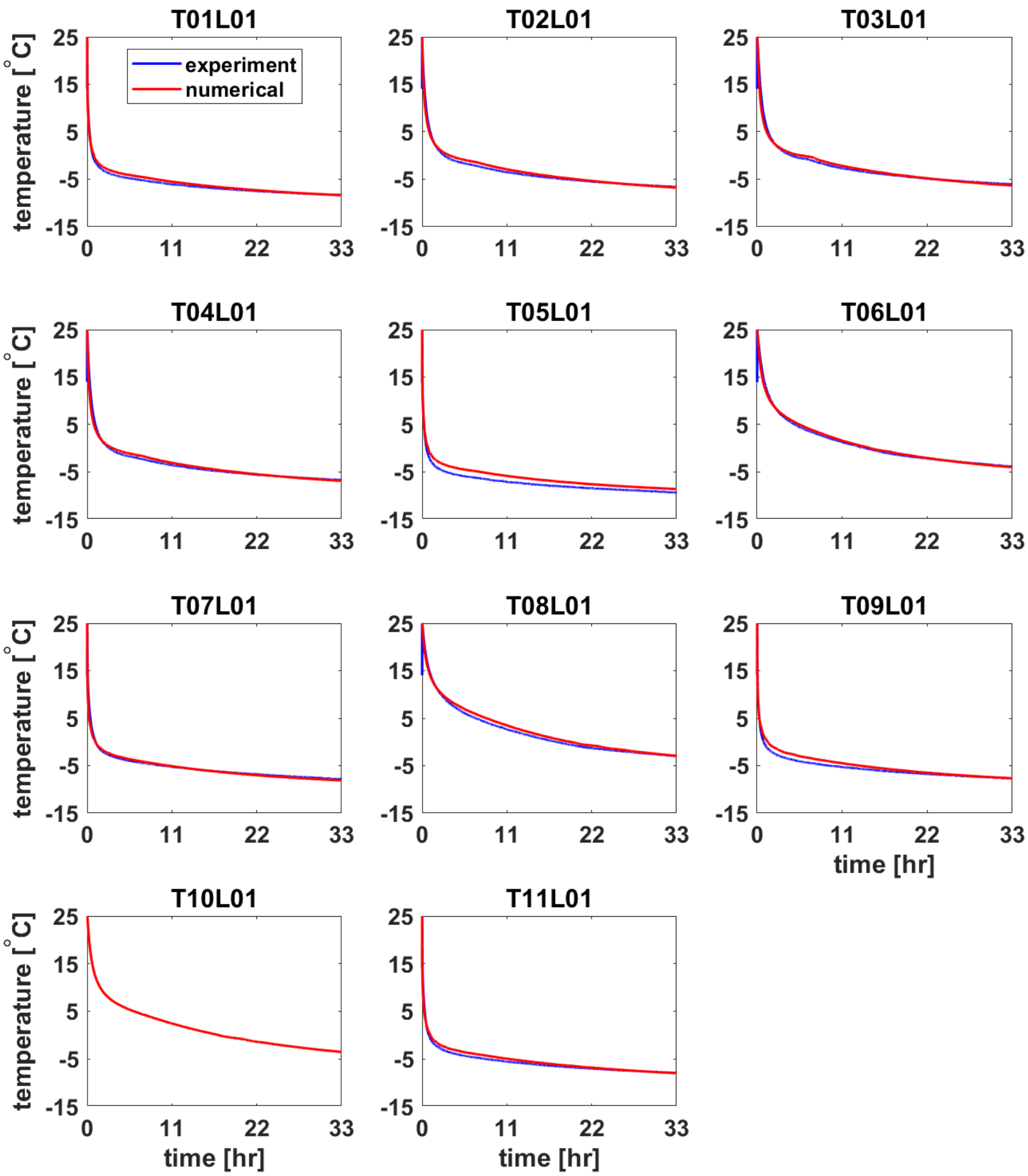

Figure A.17 – The validation of the mathematical model with experimental data at ($T_c = -15\ [°C],\ T_g = 25\ [°C],\ and\ \dot{Q} = 10\ [ml/s]$). The results show the the ground's temperature at level-01 with ($R^2 = 0.961$).

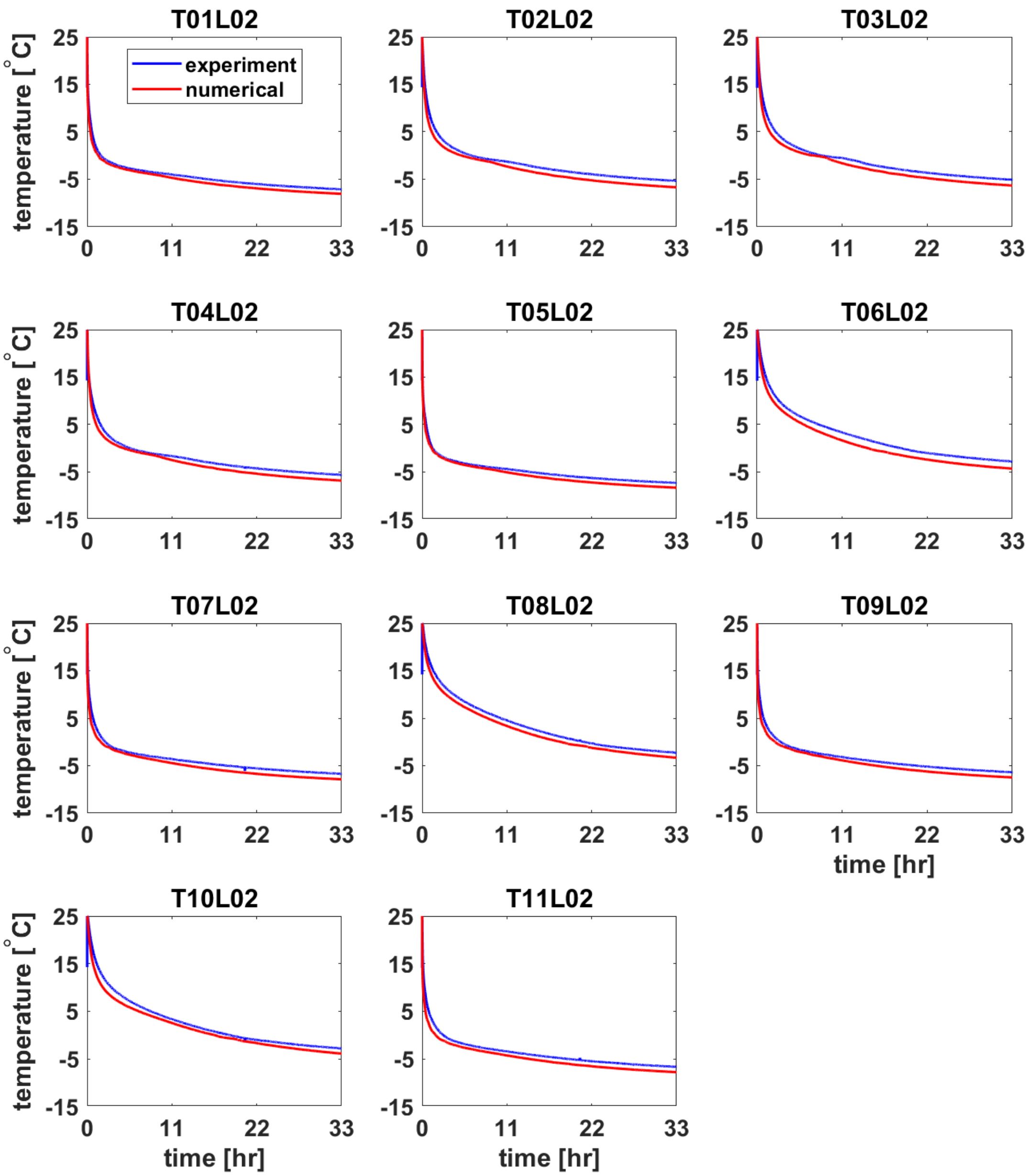

Figure A.18 – The validation of the mathematical model with experimental data at ($T_c = -15\ [°C],\ T_g = 25\ [°C],\ and\ \dot{Q} = 10\ [ml/s]$). The results show the the ground's temperature at level-02 with ($R^2 = 0.991$).

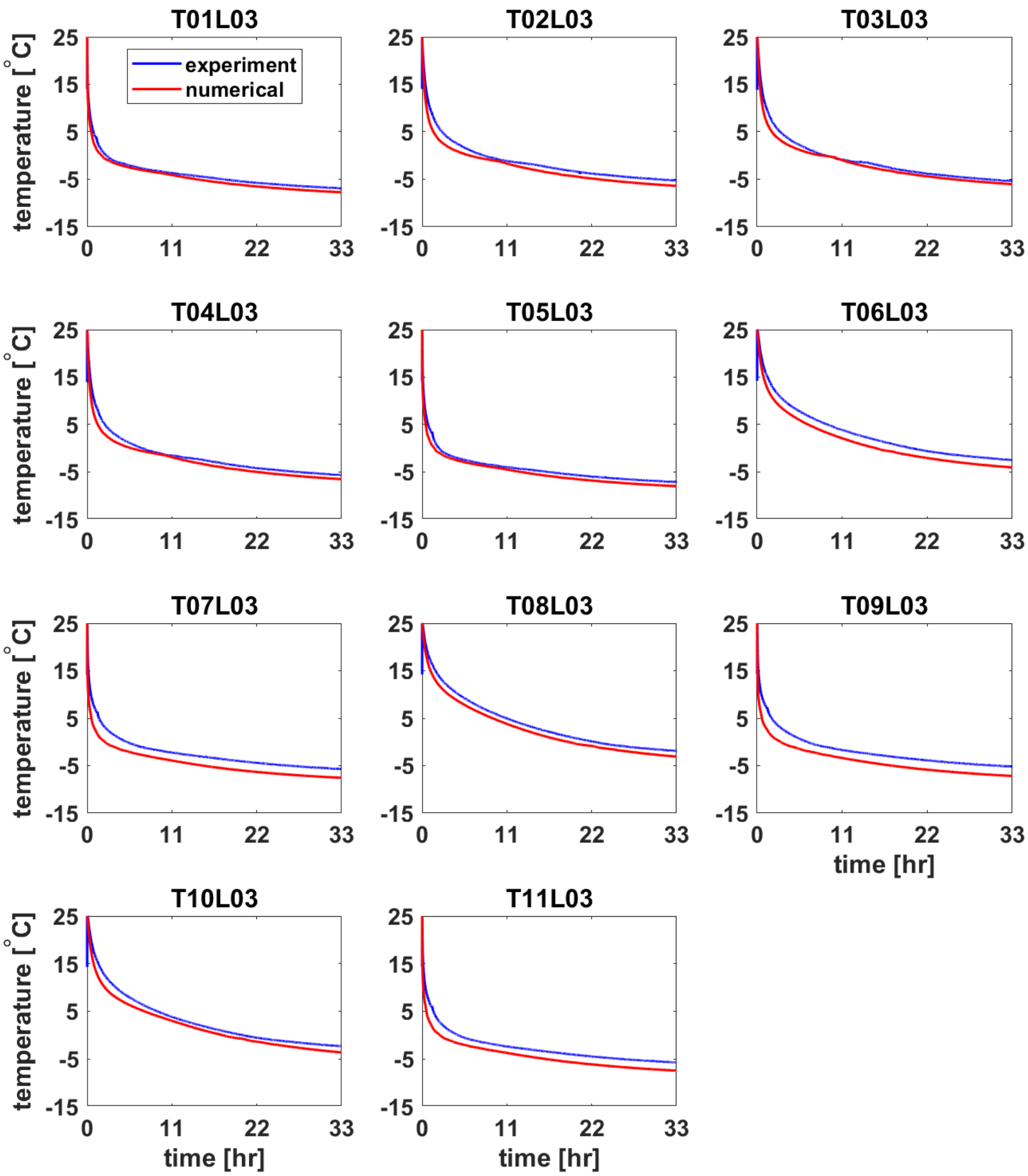

Figure A.19 – The validation of the mathematical model with experimental data at ($T_c = -15\ [°C],\ T_g = 25\ [°C],\ and\ \dot{Q} = 10\ [ml/s]$). The results show the the ground's temperature at level-03 with ($R^2 = 0.990$).

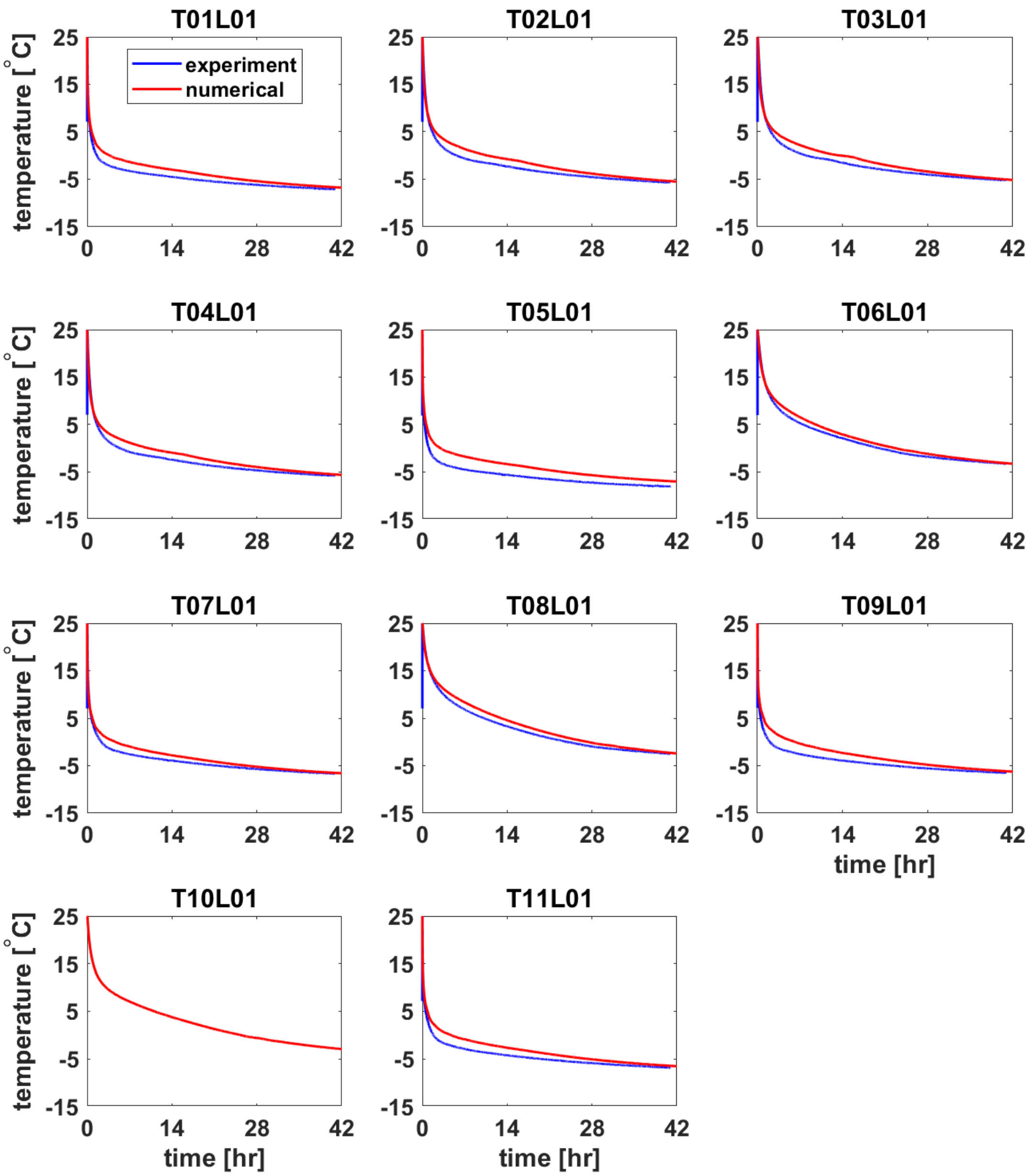

Figure A.20 – The validation of the mathematical model with experimental data at ($T_c = -15$ [$°C$], $T_g = 25$ [$°C$], $and\ \dot{Q} = 5$ [ml/s]). The results show the the ground's temperature at level-01 with ($R^2 = 0.966$).

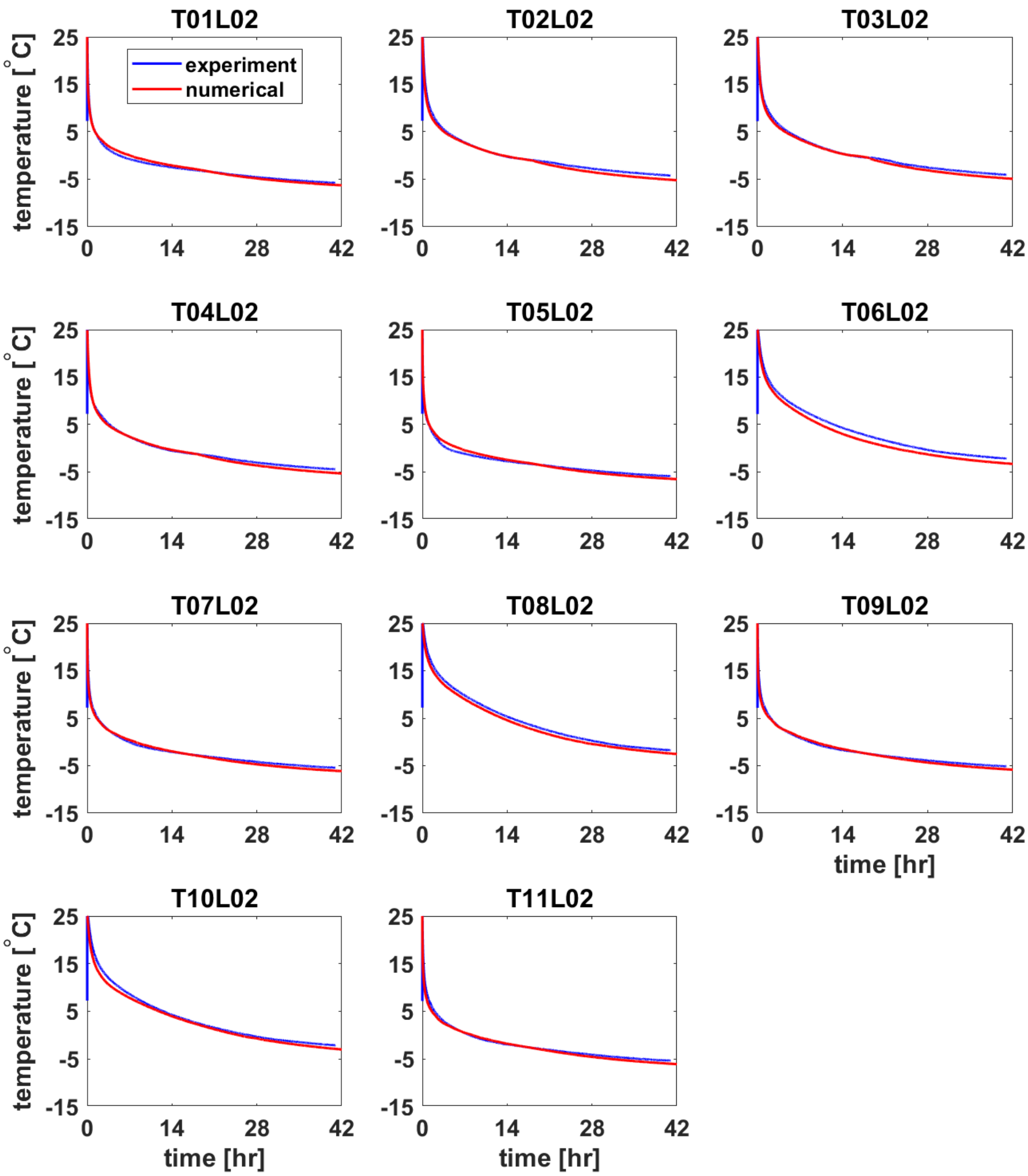

Figure A.21 – The validation of the mathematical model with experimental data at ($T_c = -15$ [$°C$], $T_g = 25$ [$°C$], $and\ \dot{Q} = 5$ [ml/s]). The results show the the ground's temperature at level-02 with ($R^2 = 0.991$).

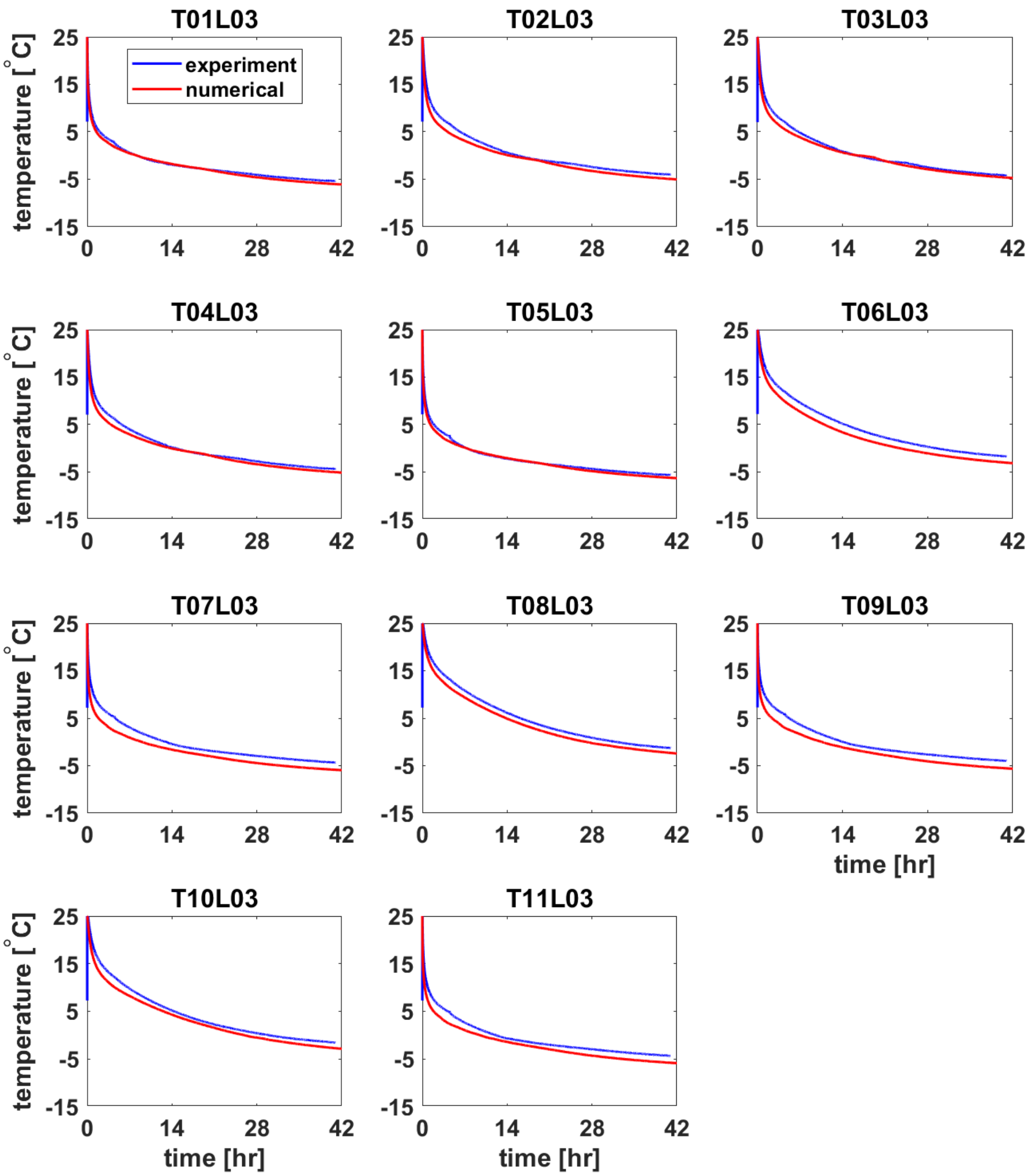

Figure A.22 – The validation of the mathematical model with experimental data at ($T_c = -15\ [°C],\ T_g = 25\ [°C],\ and\ \dot{Q} = 5\ [ml/s]$). The results show the the ground's temperature at level-03 with ($R^2 = 0.993$).

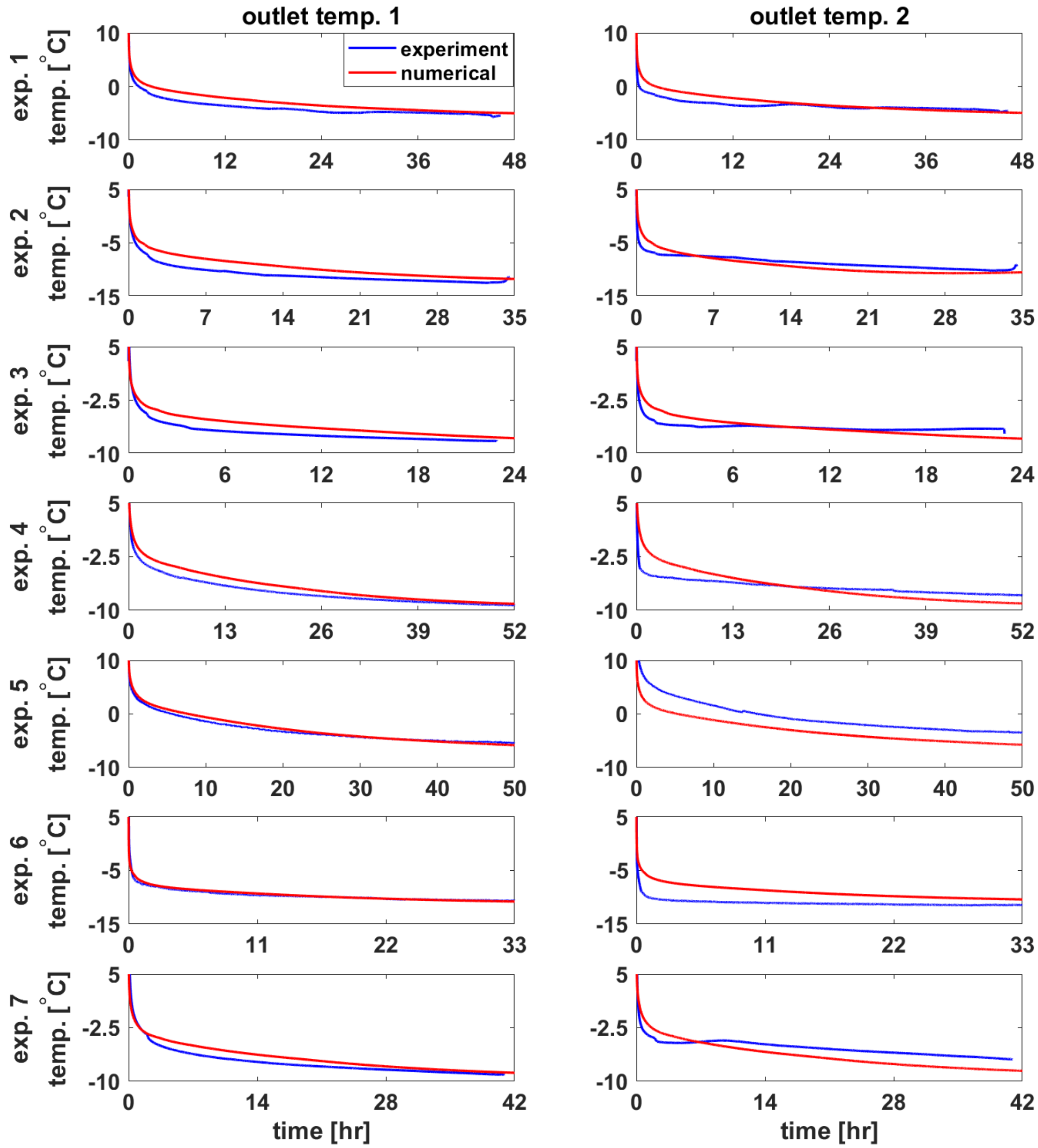

Figure A.23 – The validation of the coolant's outlet temperatures of each experiment. exp. 1: inlet temperature at -10 [°C]; exp. 2: inlet temperature at -20 [°C]; exp. 3 ground's initial tempearture at 20 [°C]; exp. 4: ground's initial temperature at 30 [°C]; exp. 5: coolant's flow rate at 2.5 [ml/s]; exp. 6: coolant's flow rate at 10 [ml/s]; and exp. 7: is the base case.

References

[1] Richard A Dobbins, K Mohammed, and Daniel A Sullivan. Pressure and density series equations of state for steam as derived from the haar–gallagher–kell formulation. *Journal of physical and chemical reference data*, 17(1):1–8, 1988.

[2] EW Lemmon and RT Jacobsen. Viscosity and thermal conductivity equations for nitrogen, oxygen, argon, and air. *International Journal of Thermophysics*, 25(1):21–69, 2004.

[3] E.W. Lemmon, R.T. Jacobsen, S.G. Penoncello, and D.G. Friend. Thermodynamic properties of air and mixtures of nitrogen, argon, and oxygen from 60 to 2000 k at pressures to 2000 mpa. *Journal of Physical and Chemical Reference Data*, 29(3):331–362, 2000.